An Experimental and Theoretical Investigation of a Fuel System Tuner for the Suppression of Combustion Driven Oscillations

A Dissertation
Presented to
The Academic Faculty

By

David E. Scarborough

In Partial Fulfillment
Of the Requirements for the Degree
Doctor of Philosophy in Mechanical Engineering

Georgia Institute of Technology
May 2010

An Experimental and Theoretical Investigation of a Fuel System Tuner for the Suppression of Combustion Driven Oscillations

Approved by:

Dr. Ben T. Zinn
Mechanical and Aerospace Engineering
Georgia Institute of Technology

Dr. Ari Glezer
Mechanical Engineering
Georgia Institute of Technology

Dr. Timothy C. Lieuwen
Mechanical and Aerospace Engineering
Georgia Institute of Technology

Dr. Peter Rogers
Mechanical Engineering
Georgia Institute of Technology

Dr. Jeff Jagoda
Aerospace Engineering
Georgia Institute of Technology

Date Approved: March 23, 2010

DEDICATION

To my parents, Henry and Hilda Scarborough, my wife, Lee Scarborough, and our children, Jonathan, Joseph, Kayleigh, Holly, Joshua, and Emily.

O LORD, our Lord, how excellent is thy name in all the earth!
who hast set thy glory above the heavens.

Out of the mouth of babes and sucklings hast thou ordained strength
because of thine enemies, that thou mightest still the enemy and the avenger.

When I consider thy heavens, the work of thy fingers,
the moon and the stars, which thou hast ordained;

What is man, that thou art mindful of him?
and the son of man, that thou visitest him?

For thou hast made him a little lower than the angels,
and hast crowned him with glory and honour.

Thou madest him to have dominion over the works of thy hands;
thou hast put all things under his feet:

All sheep and oxen, yea, and the beasts of the field;

The fowl of the air, and the fish of the sea,
and whatsoever passeth through the paths of the seas.

O LORD our Lord, how excellent is thy name in all the earth!

Psalm 8

ACKNOWLEDGEMENTS

I would like to thank Dr. Ben T. Zinn, without whom this thesis would not have been possible, for serving as my advisor, sponsor, mentor, and friend. He patiently and diligently read, corrected, and re-read every word many times. His thoughtful suggestions and penetrating questions improved every part of this work.

I am also grateful to the many undergraduates who took data, built hardware, wrote computer code, and generally assisted in every aspect of this work: Adam Knez, Javier Johnson, Bala Radharamanan, Dustin Tippens, and John Brooks.

I would also like to thank my parents, Henry and Hilda Scarborough, who first planted the seed in the mind of a 12 year old boy and encouraged him along the way. Thank you for all of the years of training, education, work, and prayers.

I would like to express my love and appreciation to my wife, Lee Scarborough, for her love, support, patience, and encouragement over many years. For her, quitting was never an option. Of you, it may be truly said: "Many daughters have done virtuously, but thou excellest them all." – Proverbs 31:29.

I would also like to express my love and appreciation to our children, Jonathan, Joseph, Kayleigh, Holly, Joshua, and Emily. Your unfailing confidence in and love for 'daddy' will never be forgotten. You will always be my greatest reward. "Lo, children are an heritage of the Lord and the fruit of the womb is his reward." – Psalm 127:3.

TABLE OF CONTENTS

ACKNOWLEDGEMENTS iv

LIST OF TABLES ix

LIST OF FIGURES x

NOMENCLATURE xxiii

SUMMARY xxix

Chapter 1: Introduction and Background 1

1.1 Introduction 1

1.2 Combustion instabilities in modern power generating gas turbine engines 3

1.3 Theoretical background of combustion instabilities 4

1.4 Prior work on techniques to control combustion instabilities 7

1.5 The need for further study 10

1.6 A Fuel System Tuner (FST) 12

1.7 Conclusions 18

Chapter 2: A Feasibility Analysis using Rayleigh's Criterion 19

2.1 The Rayleigh driving equation 20

2.2 Analysis of the Rayleigh driving equation 27

2.3 Results and predictions 32

2.4 Conclusions 44

Chapter 3: Theoretical Efforts 46

3.1 Introduction 46

3.2 Background of the nonlinear acoustic response of abrupt area changes 49

3.3 An acoustically compact area expansion 60

3.4 Comparison between the acoustic resistance of an area contraction and expansion 62
3.5 Application of the nonlinear area contraction impedance model 67
3.6 Conclusions 71
Chapter 4: Acoustic Response Measurements 72
4.1 Introduction and background 72
4.2 Study objectives 73
4.3 Two-microphone impedance tube 75
4.4 Background on area contraction studies 84
4.5 Impedance subtraction technique 92
4.6 Effective length, loss coefficient, and discharge coefficient calculations 94
4.7 The nonlinear acoustic resistance of an area change 99
4.8 'Tee' junction impedance measurements 115
4.9 Variable area valve impedance measurements 118
4.10 Area contraction in series with a valve 124
4.11 Conclusions 127
Chapter 5: Acoustic Response Modeling 129
5.1 Introduction 129
5.2 An acoustically compact area contraction 130
5.3 An area expansion 141
5.4 A 'Tee' junction 147
5.5 Variable area gate valve 151
5.6 Combined area change and gate valve 155
5.7 Overall FST acoustic model 177
5.8 Conclusions 182

Chapter 6: Combustor Model Development 183
6.1 Introduction 183
6.2 Combustor stability analysis 184
6.3 The model combustor and modeling assumptions 188
6.4 Development of the thermo-acoustic model equations 190
6.5 Quasi-linear thermo-acoustic model results 207
6.6 Conclusions 242
Chapter 7: Experimental Evaluation of the FST 244
7.1 Introduction 244
7.2 FST Performance Mapping 246
7.3 Conclusions 289
Chapter 8: Conclusions 291
8.1 Introduction 291
8.2 Discussion 291
8.3 Important contributions 297
8.4 Future work 299
Appendix A: Heat Release Transfer Function Development 300
A.1 Introduction 300
A.2 Linear heat release transfer function development 300
Appendix B: Development of heat release fluctuation parameters 305
Appendix C: The Transfer Matrix 308
Appendix D: Development of the Combustor Impedance Expressions 311
Appendix E: Supplemental Area Contraction Impedance Results 314
E.1 Area contraction from 50.8 mm to 25.4 mm diameter extension tube 314
E.2 Area contraction from 50.8 mm to 19 mm diameter extension tube 318

E.3 Area contraction from 50.8 mm to 9.5 mm diameter extension tube.....320
E.4 Area contraction from 50.8 mm to 6.35 mm diameter extension tube.....321
Appendix F: Key to FST Settings.....322
Appendix G: Model/Experiment Comparisons for Configurations 2 through 5.....325
G.1 Configuration 2.....325
G.2 Configuration 3.....327
G.3 Configuration 4.....328
G.4 Configuration 5.....329
Appendix H: Plots of Fuel System Impedance and Experimental Data for all FST Settings for Configurations 2 through 5.....330
H.1 Configuration 2.....330
H.2 Configuration 3.....332
H.3 Configuration 4.....333
H.4 Configuration 5.....334
References.....335

LIST OF TABLES

Table 2.1: Combustor geometry used in the Rayleigh analysis (see Figure 2.1). 32

Table 4.1: Experimental measurement parameters for impedance tube measurements. 101

Table 4.2: Model predicted and experimentally determined slope between real(Z)=$Z_{\delta A}$(S/ρc) and acoustic velocity amplitude. 105

Table 4.3: Reynolds' number scaling results 112

Table 5.1: Magnitude and phase of the system impedance at 250 and 400 Hz for different lengths of the tube between the area contraction and the valve. 174

Table 6.1: Combustor parameters. 208

Table 6.2: Combustor configurations tested for various FST settings. 209

Table 7.1: Combustor configurations tested for various FST settings. 247

LIST OF FIGURES

Figure 1.1: Schematic of a lean, premixed, swirl-stabilized combustor 3

Figure 1.2: Schematic of the Fuel System Tuner (FST). 13

Figure 1.3: Diagram showing the accessible region of the magnitude and phase of the FST impedance. 16

Figure 2.1: Schematic of the combustion system used in the Rayleigh analysis. 19

Figure 2.2: Magnitude of the total, real part, and imaginary parts of the impedance vs. frequency for a system with resistance. 30

Figure 2.3: Phase of the impedance vs. frequency for systems with and without resistance and driving. 31

Figure 2.4: Percent acoustic power vs. frequency for $\frac{1}{10}(\rho c)/S_{fi}$, $L_{fi} = 0.1m.$ 33

Figure 2.5: Percent acoustic power vs. frequency for $10(\rho c)/S_{fi}$, $L_{fi} = 0.1m.$ 34

Figure 2.6: Percent acoustic power vs. frequency for $(\rho c)/S_{fi}$, $L_{fi} = 0.1m.$ 35

Figure 2.7: Percent acoustic power vs. frequency for $\frac{1}{2}(\rho c)/S_{fi}$, $L_{fi} = 0.1m.$ 36

Figure 2.8: Percent acoustic power vs. frequency for $(\rho c)/S_{fi}$, $L_{fi} = 0.1m.$ In this case, equivalence ratio oscillations were turned OFF. 37

Figure 2.9: Percent acoustic power vs. frequency for $(\rho c)/S_{fi}$ and $L_{fi} = 0.2\,m.$ 38

Figure 2.10: Percent acoustic power vs. frequency for $(\rho c)/S_{fi}$ and $L_{fi} = 0.051m.$ 39

Figure 2.11: Percent acoustic power vs. frequency for a fuel system tuner with driving (i.e., the Resistance is less than zero) and with $(\rho c)/S_{fi}$, $L_{fi} = 0.1m$. 40

Figure 3.1: (a) Flow streamlines for an area contraction with flow entering the contraction. (b) Flow streamlines for an area expansion with flow leaving the contraction. 47

Figure 3.2: Diagram of a simple, acoustically compact area contraction. 52

Figure 3.3: Diagram of a simple, acoustically compact area expansion. 60

Figure 3.4: Velocity variation with time. 65

Figure 3.5: Example calculation of the average loss coefficient. 65

Figure 3.6: System including a rigid termination preceded by a sudden area change. 68

Figure 3.7: Comparison between model predictions and experimental measurements for the reflection coefficient of an abrupt area contraction. 70

Figure 4.1: Impedance tube schematic. 76

Figure 4.2: Refection coefficient error for various end conditions as a function of wavenumber for a microphone spacing of 2 inches. 80

Figure 4.3: Reflection coefficient error for various end conditions as a function of wavenumber for a microphone spacing of 9 inches. 81

Figure 4.4: Rigidly-terminated tube of length L. 82

Figure 4.5: Magnitude and phase of the reflection coefficient of a rigidly-terminated tube of length L. 83

Figure 4.6: System including a rigid termination preceded by a sudden area change. 84

Figure 4.7: Magnitude of the reflection coefficient, acoustic power, and acoustic velocity amplitude vs. Frequency for the system shown in Figure 4.4 with a 508 mm extension tube. 86

Figure 4.8: Pressure, power dissipation, and velocity amplitude vs. Frequency for the system shown in Figure 4.4 with a 508 mm extension tube. 87

Figure 4.9: Magnitude of the reflection coefficient and acoustic velocity amplitude vs Frequency for an area change at the junction of a 50.8 mm to 14 mm diameter reduction with an extension tube of length 270 mm (see Figure 4.4). 91

Figure 4.10: Impedance of the area change obtained by the impedance subtraction technique. 93

Figure 4.11: Loss coefficient and effective length calculations obtained from impedance tube measurements after applying the impedance subtraction technique. 97

Figure 4.12: Discharge coefficient vs. Acoustic velocity calculated from impedance tube measurements after applying the impedance subtraction technique. 98

Figure 4.13: Acoustic resistance vs. Reynolds # for the 50.8 mm to 25.4 mm diameter tube with a 270 mm long extension tube measured at 310 Hz. 102

Figure 4.14: Acoustic resistance vs. Reynolds # for the 50.8 mm to 19 mm diameter tube with a 270 mm long extension tube measured at 310 Hz. 103

Figure 4.15: Acoustic resistance vs. Reynolds # for the 50.8 mm to 14 mm diameter tube with a 270 mm long extension tube measured at 310 Hz. 103

Figure 4.16: Acoustic resistance vs. Reynolds # for the 50.8 mm to 9.5 mm diameter tube with a 270 mm long extension tube measured at 310 Hz. 104

Figure 4.17: Real(ξ) vs. Acoustic velocity for 50.8 mm to 14 mm diameter, 270 mm long extension tube for a range of forcing frequencies near 310 Hz....107

Figure 4.18: Real(ξ) vs. Acoustic velocity for 50.8 mm to 14 mm diameter, 92 mm long extension tube for a range of forcing frequencies near 930 Hz....107

Figure 4.19: Real(ξ) vs. Acoustic velocity for 50.8 mm to 14 mm diameter, 168 mm long extension tube for a range of forcing frequencies near 510 Hz....109

Figure 4.20: Acoustic resistance vs. Acoustic velocity amplitude. 111

Figure 4.21: Measurements of Imag(Z) for the area change vs. acoustic velocity at the junction of a 50.8 mm to 14 mm diameter reduction with an extension tube of length 92 mm. 113

Figure 4.22: Schematic of 'tee' junction of three tubes.....115

Figure 4.23: Amplitude of the reflection coefficient vs. Frequency for the 'tee' junction system shown in Figure 4.22.....117

Figure 4.24: Acoustic Pressure amplitude vs. Frequency for the 'tee' system. 117

Figure 4.25: Schematic of a commercial gate valve.....118

Figure 4.26: Schematic of a rigidly terminated duct section containing a variable area valve. 119

Figure 4.27: Magnitude and phase of the reflection coefficient vs. Frequency for the valve removed. 120

Figure 4.28: Magnitude and phase of the reflection coefficient vs. Frequency for the 100% open. 121

Figure 4.29: Magnitude and phase of the reflection coefficient vs. Frequency for the valve 2 turns open.....121

Figure 4.30: Magnitude and phase of the reflection coefficient vs. Frequency for the valve 1.0 turns open.....122

Figure 4.31: Magnitude and phase of the reflection coefficient vs. Frequency for the valve 0.5 turns open.....122

Figure 4.32: Magnitude and phase of the reflection coefficient vs. Frequency for the valve completely closed. 123

Figure 4.33: Schematic of a simple area contraction followed by a gate valve with a rigidly terminated extension tube. 124

Figure 4.34: Predictions of linear acoustic theory for the reflection coefficient of the system shown in Figure 4.33 for a range of valve settings.....125

Figure 4.35: Magnitude and phase of the reflection coefficient vs. Frequency for the system shown in Figure 4.33 for a range of valve settings.....126

Figure 5.1: System including abrupt area change.....130

Figure 5.2: Nonlinear area change model calculation procedure 132

Figure 5.3: Magnitude and phase of the reflection coefficient vs. Frequency for the system shown in Figure 5.1 with L_2=508 mm. Model/experiment comparison.....134

Figure 5.4: Schematic of the impedance tube, area contraction, and extension tube. 135

Figure 5.5: Magnitude of the reflection coefficient vs. Frequency for a speaker velocity of 1 m/s. 137

Figure 5.6: Re(Z)/|Z| and Re(Z) vs. Frequency for a speaker velocity of 1 m/s. 138

Figure 5.7: Magnitude of the reflection coefficient and area change acoustic velocity vs. Frequency for a speaker velocity of 10 m/s. 139

Figure 5.8: Re(Z)/|Z| and Re(Z) vs. Frequency for a speaker velocity of 10 m/s. 139

Figure 5.9: Acoustical network including the impedance tube with speakers, 14 mm diameter connecting tube, and the 51 mm extension tube. The area expansion is the junction of the 14 mm and 51 mm diameter tubes. 141

Figure 5.10: Magnitude and phase of the reflection coefficient at the area expansion vs. Frequency. 145

Figure 5.11: Magnitude and real part of the impedance of the area expansion vs. Frequency. 146

Figure 5.12: Schematic of 'tee' junction of three tubes. 147

Figure 5.13: Iteration procedure for the 'tee' junction 149

Figure 5.14: Comparison of tee model and measurements of the reflection coefficient taken in the impedance tube. 150

Figure 5.15: Schematic of a commercial gate valve 151

Figure 5.16: Schematic of a rigidly terminated duct section containing a gate valve located at L_v 151

Figure 5.17: Measured (o) and predicted (-) reflection coefficient vs. Frequency for the gate valve nearly closed. 153

Figure 5.18: Measured (o) and predicted (-) reflection coefficient vs. Frequency for the gate valve partially open. 154

Figure 5.19: Schematic of the system including an area contraction and a variable area gate valve followed by a rigid-walled, rigidly terminated tube. 155

Figure 5.20: Linear model predictions for the magnitude and phase of the reflection coefficient vs. Frequency just upstream of the area contraction for seven valve positions ranging from completely closed to completely open. 159

Figure 5.21: Nonlinear model predictions of the magnitude and phase of the reflection coefficient vs. frequency just upstream of the area contraction for seven valve positions ranging from completely closed to completely open. 160

Figure 5.22: Experimental measurements of the magnitude and phase of the reflection coefficient vs. frequency for a range of valve settings....161

Figure 5.23: Schematic of the system including an area contraction and a variable area gate valve followed by a rigid-walled, rigidly terminated tube. 162

Figure 5.24: Real part of the valve and system impedances vs. Frequency when the valve was open 100%....165

Figure 5.25: Real part of the valve and system impedances vs. Frequency when the valve was open 55%....166

Figure 5.26: Real part of the valve and system impedances vs. Frequency when the valve was open 25%....166

Figure 5.27: Real part of the valve and system impedances vs. Frequency when the valve was open 11%....167

Figure 5.28: Real part of the valve and system impedances vs. Frequency when the valve was completely closed....168

Figure 5.29: Phase of the valve and system impedances vs. Frequency when the valve was open 100%....169

Figure 5.30: Phase of the valve and system impedances vs. Frequency when the valve was open 55%....170

Figure 5.31: Phase of the valve and system impedances vs. Frequency when the valve was open 25%....171

Figure 5.32: Phase of the valve and system impedances vs. Frequency when the valve was open 11%....171

Figure 5.33: Phase of the valve and system impedances vs. Frequency when the valve was completely closed....172

Figure 5.34: Schematic of the FST and fuel injection system....177

Figure 5.35: Magnitude/Phase of the FST impedance vs. Frequency for FST setting 1. 179

Figure 5.36: Magnitude/Phase of the FST impedance vs. Frequency for FST setting 8. 179

Figure 5.37: Magnitude/Phase of the FST impedance vs. Frequency for FST setting 15. 180

Figure 5.38: Magnitude/Phase of the FST impedance vs. Frequency for FST setting 31. 180

Figure 6.1: Diagram of the solution procedure used to determine the frequency and growth rate of thermo-acoustic instabilities. 185

Figure 6.2: Diagram of pressure amplitude as a function of time showing the variation in saturation amplitude with linear growth rate. 187

Figure 6.3: Schematic of a swirl-stabilized combustor. 188

Figure 6.4: Schematic of the modeled combustor showing pertinent locations. 190

Figure 6.5: Schematic of the open-ended exhaust. 191

Figure 6.6: Schematic used in the development of the flame model. 192

Figure 6.7: Schematic of area change from duct section 1 to 2. 196

Figure 6.8: Schematic of the swirler location. 198

Figure 6.9: Diagram of duct sections 3 and 4 with the fuel injector. 199

Figure 6.10: A schematic of duct sections 3 and 4 with the fuel injection. 200

Figure 6.11: Network diagram of the fuel injector plenum, volume, and FST. 202

Figure 6.12: Diagram used in the grazing-bias flow interaction model. 202

Figure 6.13: Diagram of the swirler situated between the end of duct section 4 and the beginning of duct section 5. 205

Figure 6.14: Diagram of air inlet valve situated at the upstream end of duct section 5. 206

Figure 6.15: Schematic of the modeled combustor. 207

Figure 6.16: FST schematic. 208

Figure 6.17: Growth rate vs. Fuel flowrate for five different fuel injector diameters. (Combustor length = 609 mm, FST off, Combustor area/Inlet area=10, Equivalence ratio=0.8). 211

Figure 6.18: Growth rate vs. Fuel flowrate for five equivalence ratios. (Combustor length = 609 mm, FST off, Combustor area/Inlet area=10, Fuel injector hole diameter=0.83 mm) 212

Figure 6.19: Growth rate vs. Fuel flowrate for five equivalence ratios. (Combustor length = 609 mm, FST off, Combustor to Inlet area ratio=10, Fuel injector hole diameter=3.3 mm) 212

Figure 6.20: Growth rate vs. Fuel flowrate for five different equivalence ratios. (Combustor length = 914 mm, FST off, Combustor to Inlet area ratio=10, Fuel injector hole diameter=3.3 mm) 213

Figure 6.21: Growth rate vs. Fuel flowrate for seven different values of Combustor to Inlet area ratios. (Combustor length = 609 mm, FST off, Equivalence ratio=0.8, Fuel injector hole diameter=3.3 mm) 214

Figure 6.22: FST component % open vs. FST case number (see Appendix F) for reference. 216

Figure 6.23: Model predicted instability frequency vs. FST setting for Configuration 1. 218

Figure 6.24: Growth rate vs. FST setting for Configuration 1 at a fuel flowrate of 0.9 kg/hr. 219

Figure 6.25: Growth rate vs. FST setting for Configuration 1 at a fuel flowrate of 1.9 kg/hr. 220

Figure 6.26: Growth rate vs. fuel system impedance (magnitude and phase) setting for Configuration 1 at a fuel flowrate of 0.9 kg/hr. 222

Figure 6.27: Growth rate vs. fuel system impedance (magnitude and phase) for Configuration 1 at a fuel flowrate of 1.9 kg/hr. 223

Figure 6.28: Growth rate vs. FST setting for Configuration 2 at a fuel flowrate of 0.9 kg/hr. 225

Figure 6.29: Growth rate vs. FST setting for Configuration 2 at a fuel flowrate of 1.9 kg/hr. 226

Figure 6.30: Growth rate vs. fuel system impedance (magnitude and phase) for Configuration 2 at a fuel flowrate of 0.9 kg/hr. 227

Figure 6.31: Growth rate vs. fuel system impedance (magnitude and phase) for Configuration 2 at a fuel flowrate of 1.9 kg/hr. 228

Figure 6.32: Growth rate vs. FST setting for Configuration 1 at a fuel flowrate of 0.9 kg/hr at flame locations of 25.4, 50.8, and 70.2. 230

Figure 6.33: Growth rate vs. FST setting for Configuration 1 at a fuel flowrate of 1.9 kg/hr at flame locations of 25.4, and 50.8 mm. 231

Figure 6.34: Growth rate vs. FST setting for Configuration 2 at a fuel flowrate of 0.9 kg/hr at flame locations of 25.4, 50.8, and 70.2. 232

Figure 6.35: Growth rate vs. FST setting for Configuration 2 at a fuel flowrate of 1.9 kg/hr at flame locations of 25.4, 50.8, and 70.2. 233

Figure 6.36: Instability frequency vs. FST setting for Configuration 1 at a fuel flowrate of 0.9 kg/hr for average combustor temperatures of 1600, 1800, and 2000 K. 234

Figure 6.37: Instability frequency vs. FST setting for Configuration 1 at a fuel flowrate of 1.9 kg/hr for average combustor temperatures of 1600, 1800, and 2000 K. 235

Figure 6.38: Instability frequency vs. FST setting for Configuration 2 at a fuel flowrate of 0.9 kg/hr for average combustor temperatures of 1600, 1800, and 2000 K. 236

Figure 6.39: Growth rate vs. FST setting for Configuration 1 at a fuel flowrate of 0.9 kg/hr for average combustor temperatures of 1600, 1800, and 2000 K. 237

Figure 6.40: Growth rate vs. FST setting for Configuration 1 at a fuel flowrate of 1.9 kg/hr for average combustor temperatures of 1600, 1800, and 2000 K. 238

Figure 6.41: Growth rate vs. FST setting for Configuration 2 at a fuel flowrate of 0.9 kg/hr for average combustor temperatures of 1600, 1800, and 2000 K. 239

Figure 6.42: Growth rate vs. FST setting for Configuration 1 at a fuel flowrate of 0.9 kg/hr for acoustic pressure amplitudes at the fuel injector of 500, 2500, and 4000 Pa. 240

Figure 7.1: A schematic of the natural gas fueled, atmospheric pressure, swirl-stabilized combustor. 245

Figure 7.2: FST component % open vs. FST case number (see Appendix F) for reference. 249

Figure 7.3: Acoustic pressure amplitude vs. FST setting for Configuration 1 at a fuel flowrate of 0.9 kg/hr. 251

Figure 7.4: Acoustic pressure amplitude vs. FST setting for Configuration 1 at a fuel flowrate of 1.9 kg/hr. 252

Figure 7.5: P_{rms} vs. Fuel Flowrate for Configuration 1. 253

Figure 7.6: Model/Experiment comparison vs. FST setting for Configuration 1 at a fuel flowrate of 0.9 kg/hr. 256

Figure 7.7: Model/Experiment comparison vs. FST setting for Configuration 1 at a fuel flowrate of 1.9 kg/hr. 257

Figure 7.8: Acoustic pressure amplitude and Fuel system impedance (magnitude and phase) vs. FST setting for Configuration 1 at a fuel flowrate of 0.9 kg/hr. 260

Figure 7.9: Acoustic pressure amplitude and Fuel system impedance (magnitude and phase) vs. FST setting for Configuration 1 at a fuel flowrate of 1.9 kg/hr. 261

Figure 7.10: Fuel system impedance (magnitude and phase) vs. Experimental acoustic pressure amplitude for Configuration 1 operating at a fuel flowrate of 0.9 kg/hr. 262

Figure 7.11: Fuel system impedance (magnitude and phase) vs. Experimental acoustic pressure amplitude for Configuration 1 at a fuel flowrate of 1.9 kg/hr. 263

Figure 7.12: Acoustic pressure amplitude vs. FST setting for Configuration 2 at a fuel flowrate of 0.9 kg/hr. 266

Figure 7.13: Acoustic pressure amplitude vs. FST setting for Configuration 2 at a fuel flowrate of 1.9 kg/hr. 267

Figure 7.14: P_{rms} vs. Fuel Flowrate for Configuration 2. 268

Figure 7.15: Growth rate vs. FST setting for Configuration 1 at a fuel flowrate of 0.9 kg/hr. Shown are model predictions for equivalence ratios of 0.7, 0.8, and 0.9. 270

Figure 7.16: Growth rate vs. FST setting for Configuration 1 at a fuel flowrate of 1.9 kg/hr. Shown are model predictions for equivalence ratios of 0.7, 0.8, and 0.9. 271

Figure 7.17: Acoustic pressure amplitude vs. FST setting for Configuration 3 at a fuel flowrate of 0.9 kg/hr. 272

Figure 7.18: Acoustic pressure amplitude vs. FST setting for Configuration 3 at a fuel flowrate of 1.9 kg/hr. 273

Figure 7.19: P_{rms} vs. Fuel Flowrate for Configuration 3. 275

Figure 7.20: Growth rate vs. FST setting for Configuration 4 at a fuel flowrate of 0.9 kg/hr. Shown are model predictions for fuel injector hole diameters of 0.81 and 3.2 mm. 277

Figure 7.21: Growth rate vs. FST setting for Configuration 4 at a fuel flowrate of 1.9 kg/hr. Shown are model predictions for fuel injector hole diameters of 0.81 and 3.2 mm. 278

Figure 7.22: Acoustic pressure amplitude vs. FST setting for Configuration 4 at a fuel flowrate of 0.9 kg/hr. 280

Figure 7.23: Acoustic pressure amplitude vs. FST setting for Configuration 5 at a fuel flowrate of 1.9 kg/hr. 281

Figure 7.24: P_{rms} vs. Fuel Flowrate for Configuration 4. 282

Figure 7.25: Growth rate vs. FST setting for Configuration 5 at a fuel flowrate of 0.9 kg/hr. Shown are model predictions for FST u-tube lengths of 0.10, 0.55 and 1.08 m. 284

Figure 7.26: Growth rate vs. FST setting mm for Configuration 5 at a fuel flowrate of 1.9 kg/hr. Shown are model predictions for FST u-tube lengths of 0.10, 0.55 and 1.08 m. 285

Figure 7.27: Acoustic pressure amplitude vs. FST setting for Configuration 5 at a fuel flowrate of 0.9 kg/hr. 286

Figure 7.28: Acoustic pressure amplitude vs. FST setting for Configuration 5 at a fuel flowrate of 1.9 kg/hr. 287

Figure 7.29: P_{rms} vs. Fuel Flowrate for Configuration 5. 288

Figure D.1: Acoustic network model. 311

Figure E.1: Frequency response of the area change at the junction of the 50.8 mm to 25.4 mm diameter tubes with a 270 mm long extension tube attached. 315

Figure E.2: Normalized real part and imaginary part of the impedance of the area change at the 50.8 mm to 25.4 mm diameter tube junction. 316

Figure E.3: Real part of the impedance of the area change at the 50.8 mm to 25.4 mm diameter tube junction. 316

Figure E.4: Loss coefficient, effective length, and discharge coefficient for the area change at the 50.8 mm to 25.4 mm diameter tube junction with a 270 mm long extension tube. 317

Figure E.5: Normalized real part and imaginary part of the impedance of the area change at the 50.8 mm to 19 mm diameter tube junction. 318

Figure E.6: Normalized real part and imaginary part of the impedance of the area change at the 50.8 mm to 19 mm diameter tube junction. 319

Figure E.7: Loss coefficient, discharge coefficient, and effective length of the area change at the 50.8 mm to 19 mm diameter tube junction. 319

Figure E.8: Normalized real part and imaginary part of the impedance of the area change at the 50.8 mm to 9.5 mm diameter tube junction. 320

Figure E.9: Normalized real part and imaginary part of the impedance of the area change at the 2 inch to 1/4 inch diameter tube junction. 321

Figure G.1: Model/Experiment comparison vs. FST setting for Configuration 2 at a fuel flowrate of 0.9 kg/hr. 325

Figure G.2: Model/Experiment comparison vs. FST setting for Configuration 2 at a fuel flowrate of 1.9 kg/hr. 326

Figure G.3: Model/Experiment comparison vs. FST setting for Configuration 3 at a fuel flowrate of 0.9 kg/hr. 327

Figure G.4: Model/Experiment comparison vs. FST setting for Configuration 3 at a fuel flowrate of 1.9 kg/hr. 327

Figure G.5: Model/Experiment comparison vs. FST setting for Configuration 4 at a fuel flowrate of 0.9 kg/hr. 328

Figure G.6: Model/Experiment comparison vs. FST setting for Configuration 4 at a fuel flowrate of 1.9 kg/hr. 328

Figure G.7: Model/Experiment comparison vs. FST setting for Configuration 5 at a fuel flowrate of 0.9 kg/hr. 329

Figure G.8: Model/Experiment comparison vs. FST setting for Configuration 5 at a fuel flowrate of 1.9 kg/hr. 329

Figure H.1: Model/Experiment comparison vs. FST setting for Configuration 2 at a fuel flowrate of 0.9 kg/hr.....330

Figure H.2: Model/Experiment comparison vs. FST setting for Configuration 2 at a fuel flowrate of 1.9 kg/hr.....331

Figure H.3: Model/Experiment comparison vs. FST setting for Configuration 3 at a fuel flowrate of 0.9 kg/hr.....332

Figure H.4: Model/Experiment comparison vs. FST setting for Configuration 3 at a fuel flowrate of 1.9 kg/hr.....332

Figure H.5: Model/Experiment comparison vs. FST setting for Configuration 4 at a fuel flowrate of 0.9 kg/hr.....333

Figure H.6: Model/Experiment comparison vs. FST setting for Configuration 4 at a fuel flowrate of 1.9 kg/hr.....333

Figure H.7: Model/Experiment comparison vs. FST setting for Configuration 5 at a fuel flowrate of 0.9 kg/hr.....334

Figure H.8: Model/Experiment comparison vs. FST setting for Configuration 5 at a fuel flowrate of 1.9 kg/hr.....334

NOMENCLATURE

Upper case letters

A	Complex amplitude of plane acoustic traveling waves [Pa]
B	Complex amplitude of plane acoustic traveling waves [Pa]
C	Constant or coefficient
D	Diameter $[mm]$
E	Total error
H	Enthalpy $[W]$
K	Loss coefficient
L	Length or location L $[mm]$
M	Mach number
P	Pressure $[Pa]$
Q	Heat release rate $[W]$
R	Reflection coefficient
S	Area or Flame speed $[m^2]$
T	Transfer matrix
U	Volume velocity $[m^3/s]$
V	Volume
W	Matrix of coefficients
Y	Mass fraction
Z	Impedance $[kg/m^4s]$

Lower case letters

c	Speed of sound $[m/s]$
d	Diameter $[mm]$
e	Exponential
f	Frequency $[Hz]$
h	Specific enthalpy [W/kg]
i	$\sqrt{-1}$
k	Acoustic wavenumber $[1/m]$
l	Length $[mm]$
m	Mass or mass flowrate $[kg/s]$
n	Arbitrary number or counter
p	Acoustic pressure $[Pa]$
q	Oscillating heat release rate $[W/s]$
r	Acoustic resistance $[kg/m^4 s]$
s	Streamline coordinate
t	Time $[s]$
u	Velocity $[m/s]$
x	Coordinate direction

Greek letters

α	Growth or decay rate
β	Constant
δ	Small change in a given quantity
ϕ	Phase angle [*rad*]
γ	Specific heat ratio
σ	Velocity ratio
η	Volume velocity per unit length $\left[m^3/s \cdot m\right]$
ρ	Gas density $[kg/m^3]$
τ	Time delay [*s*]
ω	Angular frequency $[rad/s]$
ψ	Velocity potential
ξ	Normalized specific acoustic impedance $[\xi = ZS/\rho c]$
λ	Acoustic wavelength [*m*]
Δ	Total change in a given quantity
μ	Dynamic viscosity $[kg/m \cdot s]$
Π	Acoustic power [*W*]
T	Acoustic period [*s*]
ν	Flame speed $[m/s]$
Ψ	Mass fuel to air ratio
Φ	Equivalence ratio

Subscripts

a	Matrix element a
act	actual
b	Matrix element b
c	Matrix element c
d	Matrix element d
air	Air
i	Location
fuel	Fuel
t	Turbulent
o	Steady quantity
u	unburned
flame	flame
f	forward (right traveling)
chem	Chemical
conv	Convective
comb	Combustion
Re	Real part of a complex quantity
Im	Imaginary part of a complex quantity
stoich	Stoichiometric
blowout	Blowout
d	Duct
mix	Mixture
total	Total (fuel and air)

flame	Flame
fi	Fuel injector
1a	Location between the flame and the fuel injector
eff	Effective
forward	Forward
reverse	Reverse
rms	Root mean square of a given quantity
avg	Average of a given quantity
R	Reflection coefficient quantity
system	System quantity
ET	Extension tube
δA	Area change quantity
real	Real quantity
imag	Imaginary quantity
D	Discharge
ext	Extension or external
e	equivalent
v	Valve
ij	Interface between duct *i* and duct *j*
spkr	Speaker
oe	Open end
b	Backward
amb	Ambient
swirler	Swirler

holes	Fuel injector holes
volume	Fuel injector volume
B	Bulk
vol	Volume
valve	Valve
C	Constriction
G	Grazing

Superscripts

.	Time rate of change in a given quantity
’	Acoustic or oscillating quantity
^	Complex quantity
_	Average quantity

Mathematical Terms

Re	Real part of a complex quantity
Im	Imaginary part of a complex quantity
conj	Complex conjugate of a complex quantity
Π	Series product

SUMMARY

Manufacturers of commercial, power-generating, gas turbine engines continue to develop combustors that produce lower emissions of nitrogen oxides (NO_x) in order to meet the environmental standards of governments around the world. Lean, premixed combustion technology is one technique used to reduce NO_x emissions in many current power and energy generating systems. However, lean, premixed combustors are susceptible to thermo-acoustic oscillations, which are pressure and heat-release fluctuations that occur because of a coupling between the combustion process and the natural acoustic modes of the system. These pressure oscillations lead to premature failure of system components, resulting in very costly maintenance and downtime. Therefore, a great deal of work has gone into developing methods to prevent or eliminate these combustion instabilities.

This dissertation presents the results of a theoretical and experimental investigation of a novel Fuel System Tuner (FST) used to damp detrimental combustion oscillations in a gas turbine combustor by changing the fuel supply system impedance, which controls the amplitude and phase of the fuel flowrate. When the FST is properly tuned, the heat release oscillations resulting from the fuel-air ratio oscillations damp, rather than drive, the combustor acoustic pressure oscillations.

A feasibility study was conducted to prove the validity of the basic idea and to develop some basic guidelines for designing the FST. Acoustic models for the subcomponents of the FST were developed, and these models were experimentally verified using a two-microphone impedance tube. Models useful for designing,

analyzing, and predicting the performance of the FST were developed and used to demonstrate the effectiveness of the FST. Experimental tests showed that the FST reduced the acoustic pressure amplitude of an unstable, model, gas-turbine combustor over a wide range of operating conditions and combustor configurations. Finally, combustor acoustic pressure amplitude measurements made in using the model combustor were used in conjunction with model predicted fuel system impedances to verify the developed design rules.

The FST concept and design methodology presented in this dissertation can be used to design fuel system tuners for new and existing gas turbine combustors to reduce, or eliminate altogether, thermo-acoustic oscillations.

Chapter 1:

Introduction and Background

1.1 Introduction

Manufacturers of commercial, power-generating, gas turbine engines continue to develop combustors that produce lower emissions of nitrogen oxides (NO_x) in order to meet the environmental standards of governments around the world. Lean, premixed combustion technology is one technique used to reduce NO_x emissions in many current power and energy generating systems. However, lean, premixed combustors are susceptible to thermo-acoustic oscillations, which are pressure and heat-release fluctuations that occur because of a coupling between the combustion process and the natural acoustic modes of the system. These pressure oscillations lead to premature failure of system components, resulting in very costly maintenance and downtime. Therefore, a great deal of work has gone into developing methods to prevent or eliminate these combustion instabilities.

This dissertation presents the results of a theoretical and experimental investigation of a novel Fuel System Tuner (FST) used to damp detrimental combustion oscillations in a gas turbine combustor by changing the fuel supply system impedance, which controls the amplitude and phase of the fuel flowrate. When the FST is properly tuned, the heat release oscillations resulting from the fuel-air ratio oscillations damp, rather than drive, the combustor acoustic pressure oscillations.

This chapter presents an introduction to the problem of combustion instabilities in gas turbine engines and a survey of techniques used to control these instabilities. Next,

an approach for controlling these instabilities using a novel tunable fuel supply system is presented. Finally, the importance of the effect of acoustic oscillations on the impedance of the tunable fuel supply system and on the combustion system in general is discussed.

1.2 Combustion instabilities in modern power generating gas turbine engines

Manufacturers of commercial, power-generating, gas turbine engines continue to develop combustors that produce lower emissions of nitrogen oxides (NOx), unburned hydrocarbons, and carbon monoxide in order to meet the environmental standards of governments around the world. Lean, premixed combustion technology is one technique used to reduce NO_x emissions in many current power and energy generating systems. Figure 1.1 shows a schematic of a lean, premixed, swirl-stabilized combustor. In this type of system, the fuel is premixed with the incoming air upstream of the

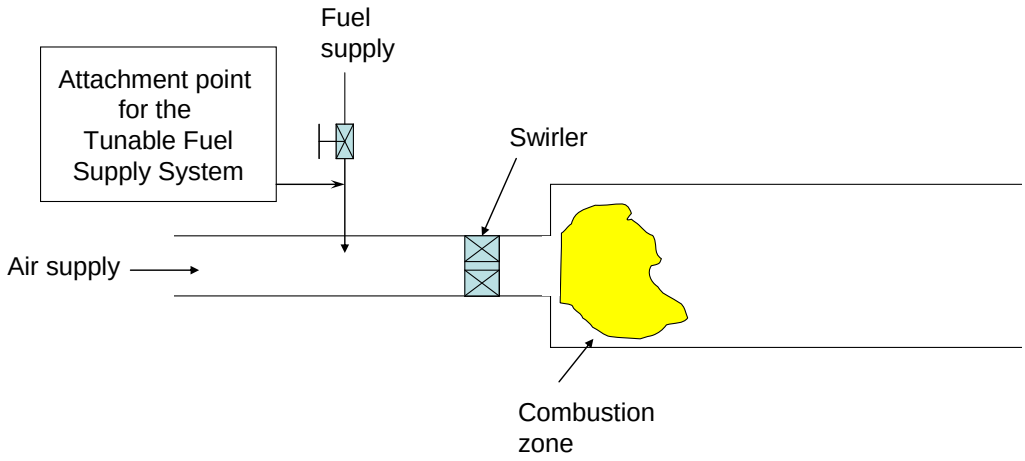

Figure 1.1: Schematic of a lean, premixed, swirl-stabilized combustor

combustion zone. As shown, the mixture passes through a 'swirler' that causes the mixture to rotate and mix prior to entering the combustion zone.

Lean, premixed combustors are susceptible to thermo-acoustic oscillations, which are pressure and heat-release fluctuations that occur because of a coupling between the combustion process and the natural acoustic modes of the system. These pressure oscillations lead to premature failure of system components, resulting in very

costly maintenance and downtime. These failures may be attributed to high cycle fatigue caused by the oscillating combustor pressure in conjunction with hot spots created by very high convective heat transfer rates due to the acoustic velocity oscillations. Therefore, a great deal of work has gone into developing passive and active methods that prevent or eliminate these combustion instabilities.

This study focuses on the investigation of a novel device that, when attached to the fuel system, e.g., at the location indicated in Figure 1.1, can be tuned to provide for stable combustor operation by altering the amplitude and phase of the flowrate of the fuel injected into the air stream. Thus, the device provides control of the amplitude and phase of the fuel-air ratio oscillations that eventually reach the combustion zone. When properly tuned, these fuel-air ratio oscillations alter the amplitude and phase of the heat release oscillations in a manner that stabilizes the combustor.

After some background on combustion instabilities is given, the methodology for developing, testing and modeling this device is presented. The discussion that follows focuses on the development and testing of this device and the development of a methodology for predicting the acoustic response of this device. Finally, this dissertation concludes with a description of a systematic method for developing a fuel supply system that can be adjusted to provide for stable combustor operation for a range of system configurations and power settings.

1.3 Theoretical background of combustion instabilities

Combustion instabilities are caused by a feedback mechanism that couples the combustion process with the ever-present pressure and velocity fluctuations in the system. In general, the frequency spectrum of the noise generated in the turbulent flow field of the combustor is broadband. However, the acoustic properties of the inlet air

system, the fuel injection system, the mixer, and the combustion chamber amplifies the fundamental acoustic mode of the system and its harmonics. In most instances, these pressure oscillations feed back into the air and fuel supply systems to cause coherent pressure and velocity oscillations in the fuel and air supply systems. These oscillations produce fluctuations in the density and velocity of the fuel and air. Therefore, the fuel-air ratio (or equivalence ratio, which is the fuel-air ratio normalized by the stoichiometric fuel-air ratio), density, and velocity of the mixture exiting the pre-mixer may cause the heat release in the combustion zone to vary with time.

As the fuel-air ratio varies with time, “packets” of fuel and air are created each having different concentrations of fuel and air. These packets are convected from the fuel injection site to the combustion zone. The time between fuel injection and the arrival of the mixture at the combustion zone is referred to as the ‘convective time delay’. Also, the heat release lags behind the arrival of these disturbances in density, velocity, and fuel-air ratio due to the so-called ‘chemical time delay’. The acoustic pressure oscillations are amplified when this periodic addition of energy, due to the heat release oscillations, is in phase with the pressure oscillations of the acoustic field[1]. These amplified acoustic pressure oscillations feed back into the air and fuel supply systems, thus completing the cycle. When the heat release oscillations are in phase with the acoustic pressure, the amplitude of the oscillations continue to build until losses, which are nonlinear, and, thus, dependent on the pressure or velocity amplitude, offset the driving of the system.

The degree of amplification, if any, depends on the magnitude of the linear and nonlinear acoustic losses in the system. For a given ‘linearly stable’ combustion system, the disturbances described above will result in no amplitude growth at all due to the presence of large acoustic losses, which offset the driving completely. However, for a

system that is not linearly stable, the magnitude of the aforementioned oscillations will increase until offset by 'nonlinear' losses, which increase in magnitude as the amplitude of the acoustic oscillations grows. For example, the acoustic losses, which are associated with the resistive part of the impedance*, generated by an abrupt area change, grow with increasing acoustic velocity amplitude and are, thus, nonlinear.

Equation (1.1) below, the so-called 'Rayleigh criterion', is an expression for the difference between the system driving and damping.

$$\underbrace{\int_t \iiint_V p'(x,t)q'(x,t)dVdt}_{\text{term 1: driving}} - \underbrace{\int_t \int_{V,S} \Psi(x,t)}_{\text{term 2: damping}} = G \qquad (1.1)$$

G is positive for an unstable system and negative or zero for a stable system. Term 1 represents the driving due to the coupling between the heat release oscillations and the acoustic pressure integrated over the combustion region. This terms says that the driving is positive when the phase between the heat release oscillations and acoustic pressure is in the range of $\pm\pi/2$. Term 2 in Eq. (1.1), i.e., the damping term, is integrated over either the surface and/or volume of the system depending on whether the losses are assumed to occur at the boundaries of the system or within the fluid volume.

* The acoustic impedance is defined as the ratio of the complex acoustic pressure and volume velocity, i.e., $p_u' / (u_u' A)$. However, other definitions exist; for example, the acoustic impedance for a compact area change is given by the ratio of the acoustic pressure drop across the area change to the volume velocity through the area change, i.e. $\left(p_u' - p_d'\right) \Big/ \left(u_u' A_u\right)$.

1.4 Prior work on techniques to control combustion instabilities

Control of combustion instabilities may be categorized as either passive or active, but both techniques either increase damping or decrease driving as discussed above. Passive control generally refers to the static modification of the engine combustion systems to damp combustion instabilities. Active control refers to the class of control techniques that use a 'fast'[†] actuator to reduce the gain of the combustion system. Both techniques generally focus on one of the following: (1) altering the magnitude and phase (relative to combustor pressure oscillations) of the injected fuel oscillation, (2) altering the flow field or (3) altering one or more system boundary conditions to increase damping.

Some systems are actually hybrids of active and passive control. These control devices utilize adjustable components to modify the combustion system hardware. These components are adjusted manually or automatically. In either case these adjustments are made very slowly compared with the period of the acoustic oscillations. These hybrid control devices contain elements of both passive and active control.

Techniques for active control of combustion instabilities have been thoroughly reviewed by McManus et al.[2] To give the reader some perspective on the current topic of research, a brief discussion of the passive control of combustion instabilities follows.

Passive control of combustion instabilities refers to the use of static combustion hardware to intervene in the feedback mechanism described above to produce stable combustion by either increasing the system damping or decreasing driving. Passive control techniques differ from active control techniques in that (1) passive control

[†] The term 'fast' refers to the period of the control action being short compared to an acoustic period.

devices are typically mechanically static; (2) they may prevent the excitation of combustion instabilities altogether or utilize the presence of low amplitude acoustic oscillations, i.e., they are responsive rather than actuated, to stabilize the combustion process; (3) they do not require high-speed 'observers' to measure and process the combustor performance on the time scale shorter than the period of an acoustic oscillation; (4) they do not require fast-acting actuators, and (5) they consume little or no power to produce the desired control action.

The following are examples of various passive control methods:

1. Modification of the average convective time delay[3,4] or the convective time delay distribution.[5,6,7]
2. Axial, radial, or asymmetric fuel-air staging.[8,9,10,11,12,13]
3. Modification of the flow field.[14,15,16,17]
4. Changing the acoustics of the system with acoustic damping devices, detuning devices (e.g. Helmholtz resonators and quarter-wave tubes), bulk-absorbing liners, [7,18,19,20] or baffles.[21]
5. Modification of the fuel supply system impedance.

The remainder of this section gives some examples of the modification of the fuel supply system impedance to obtain stable combustor operation. Hobson et al.[22] have shown that the fuel supply system impedance, including the convective time delay, can have a significant impact on combustion instabilities if the natural frequency of the fuel supply system and the natural frequency of the overall system coincide. Lieuwen et al.[23] reported the predictions of a linear stability model that demonstrates that fuel line dynamics could have an impact on combustor stability if the fuel supply system is not choked. They showed that variation of the impedance of the fuel injector by changing the fuel line length could be used to extend the stable operating region of gas turbine

combustors. Richards et al.[24] demonstrated experimentally that combustion instabilities could be suppressed by modifying the length of the fuel injector feed line; Richards' fuel injector with a tunable length section was the subject of a 1998 patent.[25] Richards et al.[26] also reported that a wide range of stable operation could be achieved on a 30 kW atmospheric combustor with multiple burners by combining fuel injectors with different impedances.

Black[27] patented a fuel injector that has a high pressure drop orifice upstream of a tunable length tube and a low-pressure drop fuel injection orifice downstream of the tube. The pressure drop of the downstream orifice was designed to be the same as the pressure drop across the air supply combustion liner. The stated purpose of the injector was to eliminate equivalence ratio fluctuations in the combustion chamber. McManus et al.[28] extended this concept to include a capability to tune the upstream and downstream orifice areas. In this case, the impedance of the downstream holes was matched with the impedance of an adjustable length tube.

Goldmeer et al.[30] reported unstable combustion in a prototype MS5002E dry, low-NO_x combustion system that was not present during testing. These instabilities were linked to modifications to the fuel supply system in the prototype system. A lumped impedance model of the fuel injector was developed to represent the experimentally determined impedance of the lab system, and the prototype fuel supply system was modified so that its impedance matched that of the lab fuel supply system. The instabilities were again reduced to acceptable levels.

1.5 The need for further study

The discussion above illustrates that various passive control devices and tunable fuel injectors have been successfully used to stabilize unstable combustion systems. However, much work remains if this technique is to become viable for use on commercial gas turbines. Much of the theoretical work to this point has been conceptual in nature, and most of the experimental work has been ad hoc with little or no analysis to guide the design process. The 'cut and try' experimental methods have been successful but inefficient. A systematic method for developing a fuel supply system that can be adjusted to attain stable combustor operation for a range of system configurations and power settings is needed, and this is the subject of this research.

To achieve this goal, several issues remain to be solved. First, no current tunable fuel supply system design is capable of attaining a wide range of impedance values due to inherent geometry limitations. Second, thermo-acoustic stability modeling of combustors has not been used effectively to determine the impedance of the tunable fuel injector required for stable operation of a given combustor. In other words, little or no work has been done to study and model the effect of the impedance of the fuel injector on combustion instabilities. Third, a limited amount of work has been done to develop good acoustic models of the tunable injectors, which are often inherently nonlinear devices.

To achieve this goal, combustor stability models that include the effects of fuel supply system impedance must be coupled with sufficiently accurate fuel supply system acoustic models so that the effectiveness of a proposed fuel system tuner geometry can be evaluated without actually implementing and testing the proposed design, which can be a costly and time-consuming process. Using this methodology, several tunable

injector configurations could be designed and evaluated quickly and efficiently before prototyping and testing begins.

The success of passive control devices in controlling combustion instabilities is encouraging. However, the static designs used in the past were limited. The next section describes a system that extends the capability of past passive control schemes with a new geometry that includes the ability to tune certain critical elements. The result is a novel Fuel System Tuner.

1.6 A Fuel System Tuner (FST)

The research described here focuses on the modification of the fuel supply system impedance, to achieve stable combustor operation. According to Lefebvre,[29] it is well-established that fluctuations in the fuel flow rate are a major cause of combustion oscillations in gas turbine engines. Further, commercial combustors that were stable when tested at the factory became unstable when installed due to differences in the fuel supply system.[30]

Tunable fuel injection systems are desirable for several reasons. First, a tunable fuel injector reduces the amount of time that must be spent analyzing and testing a given fuel supply system because the required acoustical parameters of the fuel injection system could be obtained through the adjustments provided. Second, such a device could be adjusted to eliminate instabilities that arise from changes in the overall system due to long-term wear, variations in fuel composition, and variations in the humidity or temperature of the inlet air. Third, a tunable fuel supply system could be used in the engine testing phase to determine the range of fuel supply system impedances that result in stable/unstable combustor operation.

One approach would be to design a fuel supply system that has a natural acoustic response that would provide the amplitude and phase of the fuel flowrate fluctuation required for stability. Such a system could be static with no adjustment. However, this type of system would not be able to compensate for changes in system operation over time. A better approach would be to make the fuel supply system tunable so that its impedance could be adjusted. This could be accomplished by employing valves (or variable area orifices and perforated plates), tunable volume elements, and adjustable length tubing sections. Although this type of tunable system is not ‘static’

and, thus, not exactly passive; it is not considered active either because the control action occurs over a time scale that is long compared to an acoustic period.

Figure 1.2 shows a schematic of the FST connected to the injector of a model combustor. The specific system architecture, which was based on a design by Swift,[31] shown was developed to provide adjustment of the amplitude and phase between the air-line velocity oscillations in the inlet and fuel injection rate oscillations at the point of

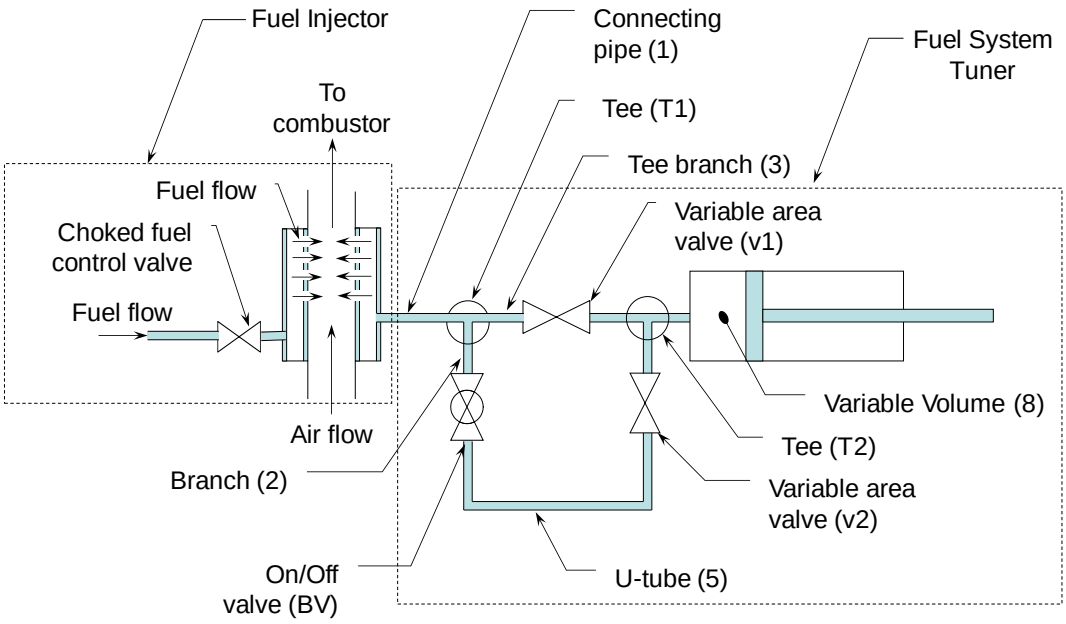

Figure 1.2: Schematic of the Fuel System Tuner (FST).

injection, thus providing control over the amplitude and phase of the equivalence ratio oscillations. These fuel-air ratio oscillations are convected downstream at the speed of the steady mean flow and cause oscillations in the combustion heat release process.

The tuning capability of the FST enables the user to select the equivalence ratio amplitude and phase that produces maximum stability. Clearly, to accomplish this level of control requires that the tuning range of the FST be made as large as possible.

The FST shown consists of a network of tubes with two variable area valves, one on/off valve, and a tunable volume. The tubes used in the FST were ½" inner diameter, smooth-walled, copper tubes. At very low frequencies, the tubes behave as mass-like inductances. However, at higher frequencies each duct behaves as a series network of mass-spring-damper systems.

The variable area valves used were common ½" gate valves, which, when fully open, present no obstruction to the steady and/or acoustic flow. As the valve handle is turned, a circular gate is forced downward across the valve opening, thus providing flow resistance. Since there is no steady mean flow, the valve's acoustic resistance is due to nonlinear damping, which will be discussed in detail in Chapter 3. As the valve approaches its fully open position, the area ratio between the valve and the tube in which it is situated approaches 1, and it ceases to provide resistance. In this case, the valve behaves acoustically like a ½" long section of straight tubing of the same diameter as the tube in which it sits. As the valve approaches its fully closed position, the valve resistance dominates, and it behaves as a rigid end-termination.

A spring-like tunable volume (8), which was a 2" inner diameter tube with a movable piston, was also provided. As the piston face was moved forward or backward, the volume within the cylinder was increased or decreased, respectively. For our purposes, the actuator rod was used to position and lock the piston face at the desired location and, therefore, the desired volume setting. The on/off valve (BV) was a commercially available ball valve, which behaved as a rigid end-termination when closed and a smooth-walled tube when open.

Adjusting the length of the U-tube or the volume of (8) changed the resonant frequency of the FST. Closing the valves (v1) or (v2) introduced acoustic resistance, which changed the real part of the complex acoustic impedance of the system.

However, it will be shown later that in the absence of steady mean flow, linear acoustic analysis yields zero real part of the impedance. In reality, nonlinear damping is present in such a system when even low amplitude acoustic velocity oscillations are present. As expected, the resistance introduced by the valves does not appreciably change the resonant frequency of the FST system.

Linear damping is introduced when steady mean flow is present. It is, therefore, reasonable to believe that introducing mean steady flow through the FST would be advantageous. In reality, this was not found to be the case. Therefore, the following discussion will center on the nonlinear behavior of the valves.

The combination shown in Figure 1.2 comprises in effect a complex Helmholtz resonator in which the first resonance is created by the volume acting as a spring and the various pipes acting as lumped masses. At sufficiently low frequencies, the pressure in the volume is uniform and the velocity along the length of an individual tube is nearly constant. At higher frequencies, the pressure in the plenum may be uniform but the velocity amplitude varies along the length of the tubes. At higher frequencies still, the pressure in the plenum varies with position as well. As mentioned previously, the FST impedance $Z_{fi} = |Z_{fi}|e^{i\phi_{fi}}$ should allow as wide a range of adjustment in the phase between the air and fuel velocity as possible.

The adjustment range of the FST is limited by its design. The maximum attainable phase range was determined as follows. It was assumed that the overall impedance of the fuel system including the FST and the fuel injector is the complex quantity Z_{fi} given by a magnitude $|Z_{fi}|$ and phase ϕ_{fi}, as shown in Figure 1.3.

For purely reactive systems, i.e., systems with no losses or damping, the real part of Z_{fi} is zero, and the phase is either 90 or -90 degrees depending on the sign of the

imaginary component. At frequencies near resonance of the FST, the sign of the imaginary component is either positive or negative depending upon whether the driving frequency is above or below the resonance frequency.

Increasing the real part of Z_{fi} from zero causes the phase to shift toward 0 degrees away from +/- 90 degrees. In a system without driving elements, e.g., a speaker, the real part of the impedance must always be positive because only damping is present in the system. Therefore, only phases in the right half plane of Figure 1.3 can be achieved.

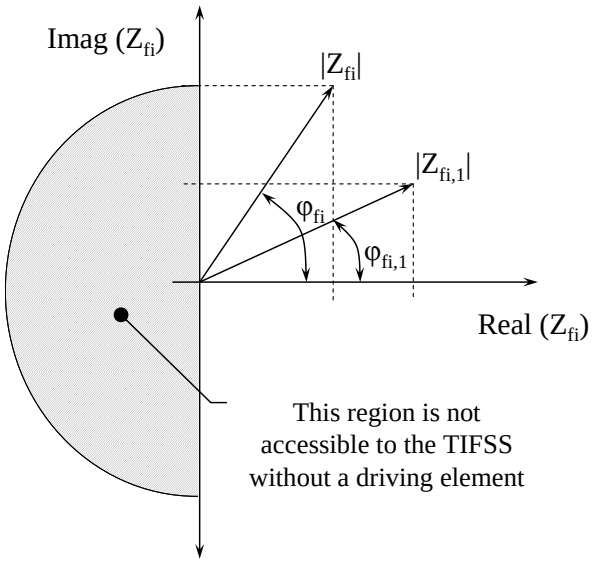

Figure 1.3: Diagram showing the accessible region of the magnitude and phase of the FST impedance.

Actual system operation over the full range of expected frequencies is quite complex and, thus, difficult to describe over the full range of frequencies. However, for very low frequencies, i.e., the wavelength is long compared to some characteristic length, the sign of the imaginary part can be obtained by tuning the resonant frequency of the FST to be above or below the frequency of the unstable mode of the combustor. The real part (resistance) of the impedance can be controlled by adjusting the variable

area valves[‡]. Based on the preceding analysis, only combustion processes requiring FST phases in the right half-plane can be stabilized using the FST. Nevertheless, even if the phase required for stability is in the left half-plane of Figure 1.3, the FST might still attenuate combustion oscillations by altering the phase such that the overall driving would be diminished.

[‡] As a matter of fact varying the setting of the valve area may, in some cases, alter the reactive part of the impedance and, thus, the resonant frequency. We neglect this effect for now for the sake of simplicity and for pedagogical reasons.

1.7 Conclusions

The stability of a given combustor depends on the impedance of the fuel supply system, and a properly designed FST can theoretically be used to adjust the impedance of the fuel supply system to attain stable combustor operation. The effectiveness of the FST can be determined by combining the FST nonlinear impedance model with a combustor acoustic response model to determine the stability of the combustor for various settings of the FST. The problem, therefore, becomes one of developing an appropriate nonlinear acoustic model for the impedance of an acoustically compact element subjected to high-amplitude acoustic velocity oscillations.

The remainder of this dissertation describes the development of a nonlinear impedance model for abrupt area changes, measurements of the nonlinear acoustic impedance of the FST and some of its components, acoustic response modeling of the FST, the development and predictions of an acoustic model for the combustor/FST system, and the evaluation of an experimental combustor/FST system.

Chapter 2:

A Feasibility Analysis using Rayleigh's Criterion

This chapter investigates the feasibility of using fuel system tuners for the suppression of combustion instabilities. To this end, Rayleigh's criterion is reduced to a simple algebraic form applicable to the study of combustion instabilities of the type described in Chapter 1 and is used to demonstrate the stabilizing effect of fuel system tuners.

Figure 2.1 shows a schematic of the simple combustor analyzed in this chapter. Air entering through the choked inlet valve at the right flows past the fuel system where fuel is injected into the air stream, and the air and fuel mix as they flow toward the "combustion zone" where both steady and unsteady heat release occurs. Hot reactants flow out of the system through the exhaust pipe.

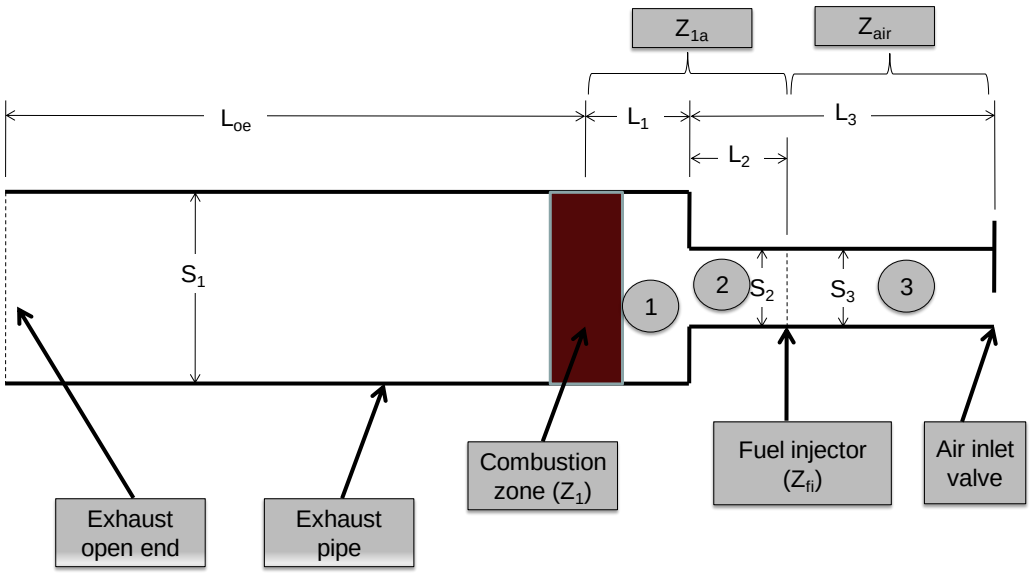

Figure 2.1: Schematic of the combustion system used in the Rayleigh analysis.

2.1 The Rayleigh driving equation

The gain of a self-excited system is the difference between the driving and the damping. Assuming constant cross-sectional area of the combustor, the driving component *D* can be computed from the Rayleigh integral as follows:

$$D = \int_x \left(\frac{S_{flame}}{\mathrm{T}} \int_{t=0}^{\mathrm{T}} \dot{q}'(x,t)\, p'(x,t)\, dt \right) dx \,. \tag{2.1}$$

The terms inside the integral of Eq. (2.1) are mathematically real quantities. Using spatially complex amplitudes to simplify the mathematics, these quantities were replaced with the equivalent form

$$\dot{q}'(x,t) = \mathrm{Re}\left[\hat{q} e^{-i\omega t} \right] \text{ and } p'(x,t) = \mathrm{Re}\left[\hat{p} e^{-i\omega t} \right] \tag{2.2}$$

so that Eq. (2.1) becomes upon substitution

$$D = \int_x \left(\frac{S_{flame}}{\mathrm{T}} \int_{t=0}^{\mathrm{T}} \mathrm{Re}\left[\hat{q} e^{-i\omega t} \right] \mathrm{Re}\left[\hat{p} e^{-i\omega t} \right] dt \right) dx \,. \tag{2.3}$$

Equation (2.3) shows that the driving can be computed once expressions for the complex heat release and complex pressure amplitudes have been obtained.

For this analysis, the change in acoustic pressure across the flame will be neglected. Therefore, the primary effect of the oscillating heat release is to accelerate the flow across the flame, i.e., to create a “jump” in the acoustic volume velocity.

However, the heat release oscillation itself is affected by the acoustic velocity, density, and fuel mass fraction fluctuations. Equations relating the heat release fluctuation to the physical acoustic parameters of the system will be developed in the following sections.

For a system with an acoustic volume velocity source having a volume velocity injection rate per unit length η', the acoustic power added to the system is given by a relation similar to Eq. (2.1) as follows:

$$\delta\Pi_{ac} = \int_x \left(\frac{1}{\mathrm{T}} \int_{t=0}^{\mathrm{T}} \mathrm{Re}\left[\hat{\eta}' e^{-i\omega t}\right] \mathrm{Re}\left[\hat{p}' e^{-i\omega t}\right] dt \right) dx, \tag{2.4}$$

which gives the increment of acoustic power added to the system by the acceleration of the flow due to the source.

Evaluating the time integral in Eq. (2.4) is facilitated by the identity

$$\frac{1}{\mathrm{T}} \int_{t=0}^{\mathrm{T}} \mathrm{Re}\left(\hat{p}' e^{-i\omega t}\right) \mathrm{Re}\left(\hat{\eta}' e^{-i\omega t}\right) dt = \frac{1}{2} \mathrm{Re}\left[\hat{p}' \cdot conj\left(\hat{\eta}'\right)\right], \tag{2.5}$$

which allows Eq. (2.4) to be written as

$$\delta\Pi_{ac} = \int_x \left(\frac{1}{2} \mathrm{Re}\left[\hat{p}' \cdot conj\left(\hat{\eta}'\right)\right] \right) dx. \tag{2.6}$$

As stated previously, for the case under investigation, the acoustic pressure was assumed constant over the extent of the flame and, therefore, over the extent of the domain of integration. This along with the complex identity

$$conj \int_x \hat{\eta}'(x)\, dx = \int_x conj\left[\hat{\eta}'(x)\right] dx \text{ for real values of x} \tag{2.7}$$

allows Eq. (2.6) to be written as

$$\delta\Pi_{ac} = \frac{1}{2} \mathrm{Re}\left[\hat{p}' \cdot conj\left(\int_x \hat{\eta}' \cdot dx \right) \right]. \tag{2.8}$$

Continuity requires that the change in acoustic volume velocity across the source region be equal to the rate of volume velocity injection as follows:

$$\int_x \hat{\eta}' \cdot dx = \delta\hat{U} = S_f \delta\hat{u}', \tag{2.9}$$

where the domain of integration is the axial extent of the source, which in this case is the combustion zone.

According to Dowling[32], a flame may be considered to be a source of volume velocity where the rate of volumetric expansion is related to the instantaneous heat release by

$$\delta\hat{U}' = S_f \delta\hat{u}' = \frac{\gamma - 1}{\gamma \bar{p}} \hat{\dot{Q}}'. \tag{2.10}$$

Substituting Eq. (2.10) into Eq. (2.8) yields

$$\delta\Pi_{ac} = \frac{1}{2}\mathrm{Re}\left[\hat{p}' \cdot conj\left(\frac{\gamma - 1}{\gamma \bar{p}} \hat{\dot{Q}}' \right) \right]. \tag{2.11}$$

Equation (2.11) allows one to compute the acoustic power added to the flame by the coupling of the heat release oscillations and acoustic pressure. However, in order to use Eq. (2.11), appropriate expressions must be developed for the heat release oscillations and acoustic pressure at the flame for the specific system under investigation. These relationships are developed in Appendices A and B.

The linear heat release transfer function Eq. (A.6), which is derived in Appendix A, is given by

$$\frac{Q'}{Q} = \left(\frac{\rho'}{\rho} + \frac{Y_i'}{Y_i} e^{i\omega\tau_{conv}} + \frac{U'}{U} \right) e^{i\omega\tau_{chem}}, \tag{2.12}$$

where $Y_i'/Y_i = Y_f'/Y_f$ is given by Eq. (B.11) or (B.12), ρ'/ρ is given by Eq. (B.1), and U'/U is given by Eq. (B.2).

Recall that the acoustic power added to the system by the coupling of the heat release oscillations and the acoustic pressure at the flame is given by

$$\delta\Pi_{ac} = \frac{1}{2}\mathrm{Re}\left[\hat{p}_1' \cdot conj\left(\frac{\gamma - 1}{\gamma \bar{p}} \hat{\dot{Q}}' \right) \right]. \tag{2.13}$$

Assuming that each of the “prime” quantities are complex quantities, the “carat” notation will be dropped from here on out. Upon substitution of Eq. (2.12), Eq. (2.13) becomes

$$\delta\Pi_{ac} = \frac{1}{2}\mathrm{Re}\left[p_1' \cdot conj\left(\frac{\gamma-1}{\gamma\bar{p}} \left(\left(\begin{array}{l} \dfrac{\rho'_{mix}}{\bar{\rho}_{mix}} + \dfrac{Y'_{fuel}}{\bar{Y}_{fuel}} e^{i\omega\tau_{conv}} \\ + \dfrac{U'_{mix}}{\bar{U}_{mix}} \end{array} \right) e^{i\omega\tau_{chem}} \right) \bar{\dot{Q}} \right) \right]. \tag{2.14}$$

Equation (2.14) gives the increment of acoustic power added to the system, integrated over the combustion volume, by the fluctuating heat release. It shows explicitly the influence of the acoustic volume velocity, density, and fuel mass fraction fluctuations.

Substituting Eqs. (B.11), (B.1), and (B.2) into Eq. (2.14) yields

$$\delta\Pi_{ac} = \frac{1}{2}\frac{\gamma-1}{\gamma\bar{p}}\bar{\dot{Q}} \cdot \mathrm{Re}\left[p_1' \cdot conj\left(C_1\right) \right], \tag{2.15}$$

where

$$C_1 = \left\{ \frac{p_1'}{\gamma_{mix}\bar{p}_1} + \left[\begin{array}{l} \dfrac{p'_{fuel}}{\gamma_{fuel}\bar{p}_{fuel}}\left(1-\bar{Y}_{fuel}\right)\cdots \\ -\dfrac{p'_{fuel}}{Z_{fi}\bar{U}_{fuel}}\left(1-\bar{Y}_{fuel}\right)\cdots \\ -\dfrac{p'_{air}}{\gamma_{air}\bar{p}_{mix}}\left(1-\bar{Y}_{fuel}\right)\cdots \\ -\dfrac{p'_{air}}{\bar{\rho}_{mix}\bar{U}_{mix}Z_{air}}\left(\dfrac{\gamma\bar{p}}{c^2}\right)_1 \end{array} \right] e^{i\omega\tau_{conv}} + \frac{p_1'}{Z_1\bar{U}_1} \right\} e^{i\omega\tau_{chem}}. \tag{2.16}$$

Note that p'_{fuel} in Eq. (2.15) is the acoustic pressure at the inlet to the FST while p_1' is the acoustic pressure at the flame location. In order to develop a useful expression for $\delta\Pi_{ac}$, the acoustic pressure at the FST was related to the acoustic pressure at the flame using the “transfer matrix” method developed in Appendix C.

Using the transfer matrix approach, the acoustic pressure at the inlet of the FST was related to the acoustic pressure and velocity at the flame as follows:

$$p'_{fuel} = p'_1\left(T_a + \frac{T_c}{Z_1}\right). \tag{2.17}$$

Substituting Eq. (2.17) into Eq. (2.16) yields

$$C_1 = \left\{\frac{p'_1}{\gamma_{mix}\bar{p}_1} + \begin{bmatrix} \dfrac{p'_1\left(T_a + \frac{T_c}{Z_1}\right)}{\gamma_{fuel}\bar{p}_{fuel}}\left(1-\bar{Y}_{fuel}\right) \\ -\dfrac{p'_1\left(T_a + \frac{T_c}{Z_1}\right)}{Z_{fi}\bar{U}_{fuel}}\left(1-\bar{Y}_{fuel}\right) \\ -\dfrac{p'_1\left(T_a + \frac{T_c}{Z_1}\right)}{\gamma_{air}\bar{p}_{mix}}\left(1-\bar{Y}_{fuel}\right) \\ -\dfrac{p'_1\left(T_a + \frac{T_c}{Z_1}\right)}{\bar{\rho}_{mix}\bar{U}_{mix}Z_{air}}\left(\dfrac{\gamma\bar{p}_1}{c^2}\right)_1 \end{bmatrix} e^{i\omega\tau_{conv}} + \frac{p'_1}{Z_1\bar{U}_1}\right\} e^{i\omega\tau_{chem}}. \tag{2.18}$$

Factoring out the acoustic pressure at the flame location yields

$$C_1 = p'_1\left\{\frac{1}{\gamma_{mix}\bar{p}_1} + \begin{bmatrix} \dfrac{\left(T_a + \frac{T_c}{Z_1}\right)}{\gamma_{fuel}\bar{p}_{fuel}}\left(1-\bar{Y}_{fuel}\right) \\ -\dfrac{\left(T_a + \frac{T_c}{Z_1}\right)}{Z_{fi}\bar{U}_{fuel}}\left(1-\bar{Y}_{fuel}\right) \\ -\dfrac{\left(T_a + \frac{T_c}{Z_1}\right)}{\gamma_{air}\bar{p}_{mix}}\left(1-\bar{Y}_{fuel}\right) \\ -\dfrac{\left(T_a + \frac{T_c}{Z_1}\right)}{\bar{\rho}_{mix}\bar{U}_{mix}Z_{air}}\left(\dfrac{\gamma\bar{p}_1}{c^2}\right)_1 \end{bmatrix} e^{i\omega\tau_{conv}} + \frac{1}{Z_1\bar{U}_1}\right\} e^{i\omega\tau_{chem}}. \tag{2.19}$$

A new constant $C_1 = p_1' C_2$ was defined as

$$C_2 = \left\{ \frac{1}{\gamma_{mix}\bar{p}_1} + \left[\begin{array}{l} \dfrac{\left(T_a + \dfrac{T_c}{Z_1}\right)}{\gamma_{fuel}\bar{p}_{fuel}}\left(1-\bar{Y}_{fuel}\right) \\ -\dfrac{\left(T_a + \dfrac{T_c}{Z_1}\right)}{Z_{fi}\bar{U}_{fuel}}\left(1-\bar{Y}_{fuel}\right) \\ -\dfrac{\left(T_a + \dfrac{T_c}{Z_1}\right)}{\gamma_{air}\bar{p}_{mix}}\left(1-\bar{Y}_{fuel}\right) \\ -\dfrac{\left(T_a + \dfrac{T_c}{Z_1}\right)}{\bar{\rho}_{mix}\bar{U}_{mix}Z_{air}}\left(\dfrac{\gamma\bar{p}_1}{c^2}\right)_1 \end{array} \right] e^{i\omega\tau_{conv}} + \frac{1}{Z_1\bar{U}_1} \right\} e^{i\omega\tau_{chem}}. \quad (2.20)$$

And, using Eq. (2.20), Eq. (2.15) was rewritten in the following form

$$\delta\Pi_{ac} = \frac{1}{2}\frac{\gamma-1}{\gamma\bar{p}}\bar{\dot{Q}} \cdot \mathrm{Re}\left[p_1' \cdot conj\left(C_2 \cdot p_1'\right)\right]. \quad (2.21)$$

The following complex identity was used to simplify Eq. (2.21):

$$\mathrm{Re}\left[conj\left(C_2 p_1'\right) p_1'\right] = \mathrm{Re}\left[conj\left(C_2\right) conj\left(p_1'\right) p_1'\right] \quad (2.22)$$

or, equivalently,

$$\mathrm{Re}\left[conj\left(C_2 p_1'\right) p_1'\right] = \left|p_1'\right|^2 \mathrm{Re}\left[conj\left(C_2\right)\right]. \quad (2.23)$$

Applying Eq. (2.23) to Eq. (2.21) yields

$$\delta\Pi_{ac} = \left(\bar{\dot{Q}}\frac{\gamma-1}{\gamma\bar{p}}\right)\frac{1}{2}\left|p_1'\right|^2 \mathrm{Re}\left[conj\left(C_2\right)\right]. \quad (2.24)$$

Now, using the identities $\mathrm{Re}\left[conj\left(C_2\right)\right] = \mathrm{Re}\left[C_2\right]$ and $p_{rms}^2 = \left|p_1'\right|^2 / 2$, Eq. (2.24) was written as

$$\delta\Pi_{ac} = \left(\bar{\dot{Q}}\frac{\gamma-1}{\gamma\bar{p}}\right) p_{rms}^2 \mathrm{Re}\left[C_2\right], \quad (2.25)$$

where

$$C_2 = \left\{ \frac{1}{\gamma_{mix}\bar{p}_1} + \begin{bmatrix} \frac{\left(T_a + \frac{T_c}{Z_1}\right)}{\gamma_{fuel}\bar{p}_{fuel}}\left(1-\bar{Y}_{fuel}\right) \\ -\frac{\left(T_a + \frac{T_c}{Z_1}\right)}{Z_{fi}\bar{U}_{fuel}}\left(1-\bar{Y}_{fuel}\right) \\ -\frac{\left(T_a + \frac{T_c}{Z_1}\right)}{\gamma_{air}\bar{p}_{mix}}\left(1-\bar{Y}_{fuel}\right) \\ -\frac{\left(T_a + \frac{T_c}{Z_1}\right)}{\bar{\rho}_{mix}\bar{U}_{mix}Z_{air}}\left(\frac{\gamma\bar{p}}{c^2}\right)_1 \end{bmatrix} e^{i\omega\tau_{conv}} + \frac{1}{Z_1\bar{U}_1} \right\} e^{i\omega\tau_{chem}} . \quad (2.26)$$

The expressions for the transfer matrix elements T_a, T_b, and T_c are developed in Appendix C.

At this point, Eqs. (2.25) and (2.26) contain the impedance at the flame zone Z_1, which depends on the impedance of everything upstream of the flame. Therefore, it was necessary to relate Z_1 to the impedance of the upstream system. This relationship between the impedances Z_1, Z_{air}, Z_{fi}, *and* Z_{1a} is developed in Appendix D.

2.2 Analysis of the Rayleigh driving equation

The set of equations making up the Rayleigh driving equation are summarized here for convenience as follows:

$$\delta\Pi_{ac} = \left(\bar{\dot{Q}}\frac{\gamma-1}{\gamma\bar{p}}\right)p_{rms}^2\,\mathrm{Re}[C_2], \tag{2.27}$$

$$C_2 = \left\{\frac{1}{\gamma_{mix}\bar{p}_1} + \begin{bmatrix} \frac{\left(T_a+\frac{T_c}{Z_1}\right)}{\gamma_{fuel}\bar{p}_{fuel}}\left(1-\bar{Y}_{fuel}\right) \\ -\frac{\left(T_a+\frac{T_c}{Z_1}\right)}{Z_{fi}\bar{U}_{fuel}}\left(1-\bar{Y}_{fuel}\right) \\ -\frac{\left(T_a+\frac{T_c}{Z_1}\right)}{\gamma_{air}\bar{p}_{mix}}\left(1-\bar{Y}_{fuel}\right) \\ -\frac{\left(T_a+\frac{T_c}{Z_1}\right)}{\bar{\rho}_{mix}\bar{U}_{mix}Z_{air}}\left(\frac{\gamma\bar{p}}{c^2}\right)_1 \end{bmatrix} e^{i\omega\tau_{conv}} + \frac{1}{Z_1\bar{U}_1}\right\} e^{i\omega\tau_{chem}}, \tag{2.28}$$

$$Z_1 = \frac{Z_{fi}\left[\frac{\left(1+e^{2ikL_3}\right)}{\frac{S_3}{(\bar{\rho}c)_3}\left(1-e^{2ikL_3}\right)}\right]}{Z_{fi}+\left(\frac{\left(1+e^{2ikL_3}\right)}{\frac{S_3}{(\bar{\rho}c)_3}\left(1-e^{2ikL_3}\right)}\right)}\left[\frac{(1-T_a)}{T_a}+1\right]-\frac{T_b}{T_a}., \tag{2.29}$$

and

$$\begin{aligned} T_a &= T_{a,1}T_{a,2} + T_{c,2}\left(T_{b,1} - ZT_{a,1}\right) \\ T_b &= T_{d,2}\left(T_{b,1} - ZT_{a,1}\right) + T_{a,1}T_{b,2} \end{aligned}. \tag{2.30}$$

Equation (2.27) states that power is added to or removed from the acoustic field by the unstable combustion process and that it increases linearly with steady heat

release. It also states that the acoustic power increases quadratically with the root mean squared acoustic pressure.

These equations also show that no acoustic power is added to the system when C_2 is purely reactive, i.e., an imaginary quantity. Consistent with Rayleigh's criterion, this is equivalent to saying that the added acoustic power was zero when the heat release and acoustic pressure oscillations are 90 degrees out of phase with each other. However, the conditions for this to occur depend on the details of the acoustic network upstream of the flame.

Physically, the Rayleigh driving equation is an expression for the amount of acoustic energy added per cycle to the acoustic field by the oscillating combustion process. As long as the driving exceeds the damping, energy continues to be added to the acoustic field until the damping in the system balances the driving, which is referred to as limit-cycle. Typically, the damping increases with acoustic pressure or velocity amplitude. Therefore, minimizing Eq. (2.27) is tantamount to minimizing the pressure amplitude in the combustor at limit-cycle. In this case, this requires minimizing the real part of C_2 in Eq. (2.27).

The above set of equations can be used to obtain an estimate of the driving for the specified system as predicted by the Rayleigh criterion. In these equations, the only unknown is Z_{fi}, which is a function of the particular geometry of the fuel injector. To better understand the effect of Z_{fi} on the response of the system, Z_{fi} was expressed as the sum of its real and imaginary parts yields

$$Z_{fi} = \frac{\rho c}{S_{fi}}\left(Z_{real} + iZ_{imag}\right), \tag{2.31}$$

where Z_{fi} has phase ϕ_Z given by

$$\phi_Z = \tan^{-1}\left[\frac{\mathrm{Im}\left(Z\right)}{\mathrm{Re}\left(Z\right)}\right]. \qquad (2.32)$$

Equations (2.31) and (2.32) show that the impedance of the fuel injector increases with the ambient density and sound speed and varies inversely with the cross-sectional area. Further, they show that the impedance is a complex quantity whose real and imaginary parts are measures of the resistance and the reactance of the system, respectively.

The resistance of the system is an indication of the amount of damping internal to the system. The higher the resistance, the more acoustic damping is present in the system. The resistance of a system can be increased by adding damping elements such as valves and screens. Speakers are driving elements represented by negative resistance values.

The reactance is a measure of the amount of energy storage within the system and is comprised of a mass-like inductance and a spring-like capacitance. The inductance of a system can be increased by adding lengths of constant area duct, which effectively add mass to the system. The inductance of the system can be increased by adding large volume elements.

Figure 2.2 and Figure 2.3 show plots of the magnitude and phase of the impedance of a system with resistance. System resonance occurs at the frequency where the impedance is minimized. For a system with no resistance, the impedance would be zero at resonance. For a system with resistance, Figure 2.2 shows that the minimum impedance at resonance is equal to the resistive part of the impedance, and that the frequency dependence of the impedance is due entirely to the reactive part of the impedance.

Figure 2.3 shows that the phase of the impedance switches from positive to negative when the resonant frequency is crossed. For systems with no resistance, the phase switches abruptly. For systems with resistance, the phase gradually rotates from $\pi/2$ through zero to $-\pi/2$. Note that phases greater that $\pi/2$ are not attainable for systems with no driving. Figure 2.3 also shows the phase for systems with driving. In this case, the phase rotates from $\pi/2$ to π before switching abruptly to $-\pi$ and rotating gradually back to $\pi/2$.

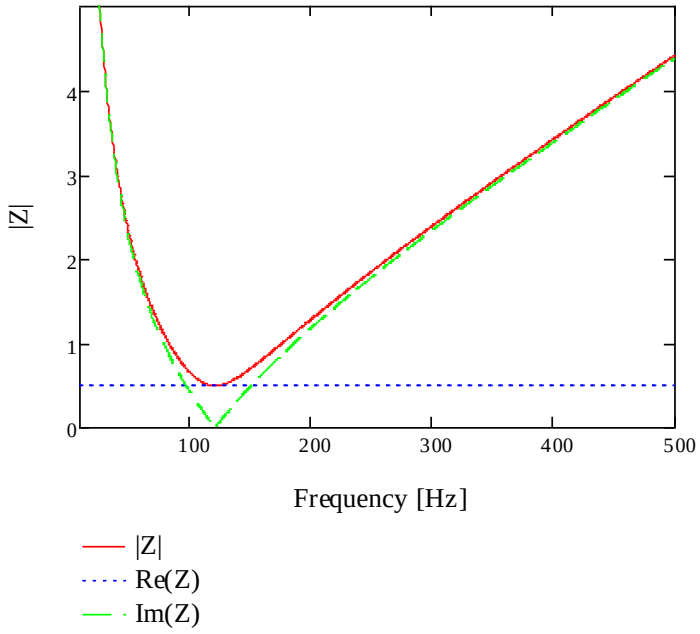

Figure 2.2: Magnitude of the total, real part, and imaginary parts of the impedance vs. frequency for a system with resistance.

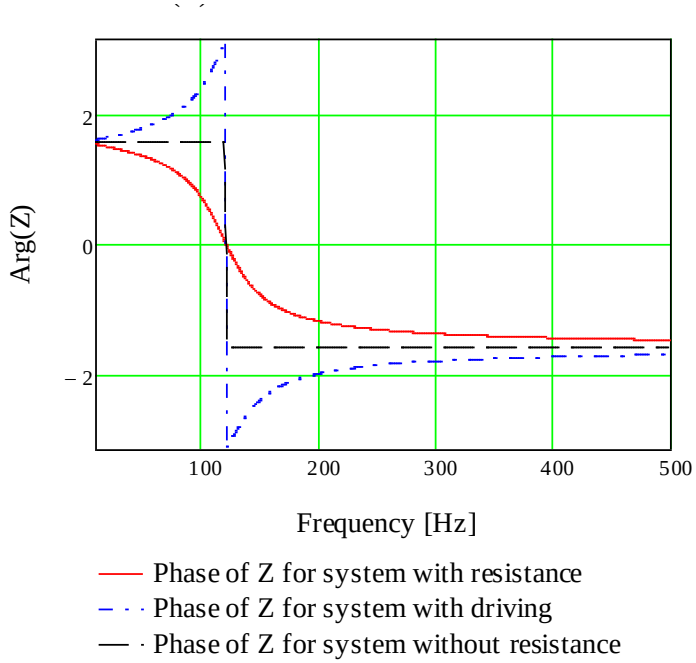

Figure 2.3: Phase of the impedance vs. frequency for systems with and without resistance and driving.

2.3 Results and predictions

In this section, the equations developed above were used to develop some trends about the impact of the FST on combustion instabilities for different values of the fuel system impedance, instability frequency, fuel injector position, and fuel injector effective diameter. Referring to Figure 2.1, Table 2.1 gives the dimensions used in the calculations that follow. The results that follow were limited to the range of frequencies between 0 and 500 Hz, since most instabilities of interest occur in this range.

Table 2.1: Combustor geometry used in the Rayleigh analysis (see Figure 2.1).

Location	Length, mm	Area, mm^2
Flame	$L_1 = 25.4$	$S_1 = 4560$
Fuel injector	$L_2 = L_{fi} = 50,\ 100,\ 200$	$S_{fi} = 253.4$
Air inlet	$L_3 = 381$	$S_3 = 506.7$

First, the effect of varying the impedance of the FST was investigated. For this analysis, the FST impedance was defined as follows

$$Z_{fi} = \sqrt{\frac{\bar{\rho}c}{S_{fi}}}\left(\sqrt{Z_{resistive}} + i\left(\sqrt{\frac{\bar{\rho}c}{S_{fi}} - Z_{resistive}}\right)\right). \tag{2.33}$$

Using this definition, the resistive part $Z_{resistive}$ of Z_{fi} was increased from 0 to $(\rho c)/S_{fi}$ while holding the magnitude of Z_{fi} constant. This is equivalent to changing the phase of the impedance from 90 to 0 degrees without changing the overall magnitude of the fuel system impedance. The fuel system impedance magnitudes used in the calculations were $\frac{1}{10}(\rho c)/S_{fi}$, $\frac{1}{2}(\rho c)/S_{fi}$, $(\rho c)/S_{fi}$, and $10(\rho c)/S_{fi}$.

Figure 2.4 through Figure 2.11 show the results of these calculations for the conditions indicated above. Note that the ratio of the fuel system to air inlet impedance is

$$\frac{(\rho c)_{fi} / S_{fi}}{(\rho c)_{ai} / S_{ai}} = 3. \tag{2.34}$$

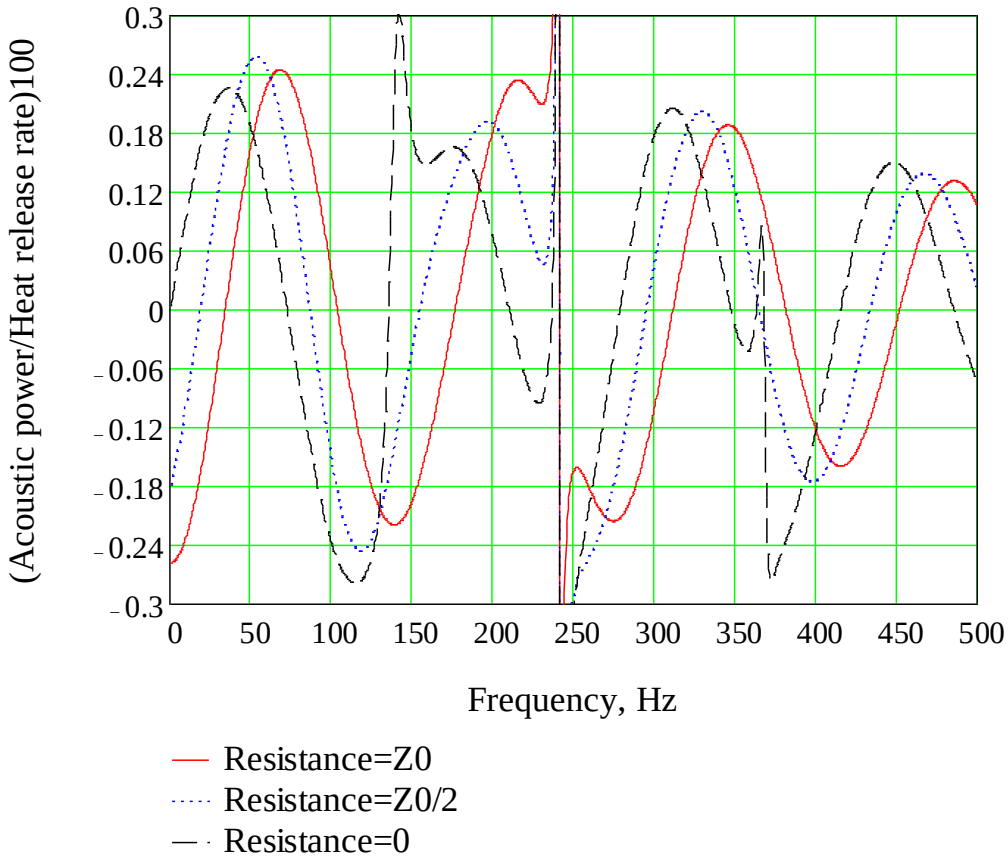

Figure 2.4: Percent acoustic power vs. frequency for $1/10 (\rho c)/S_{fi}$, $L_{fi} = 0.1m.$

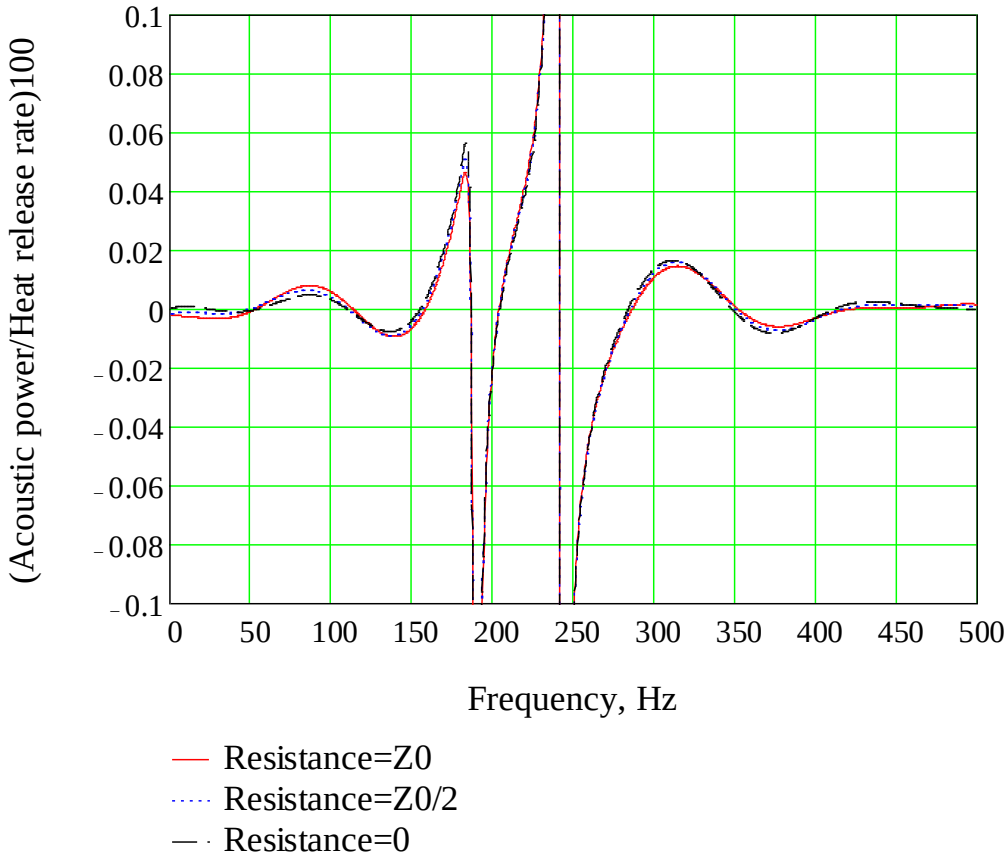

Figure 2.5: Percent acoustic power vs. frequency for $10(\rho c)/S_{fi}$, $L_{fi} = 0.1m$.

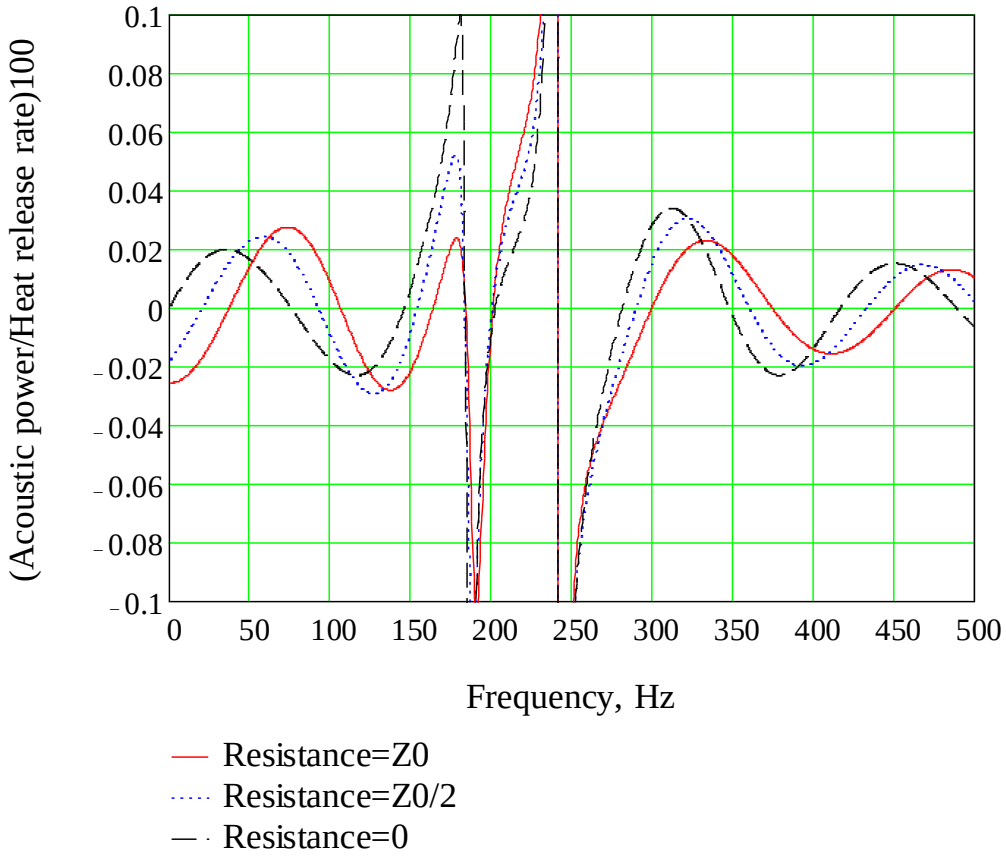

Figure 2.6: Percent acoustic power vs. frequency for $(\rho c)/S_{fi}$, $L_{fi} = 0.1m$.

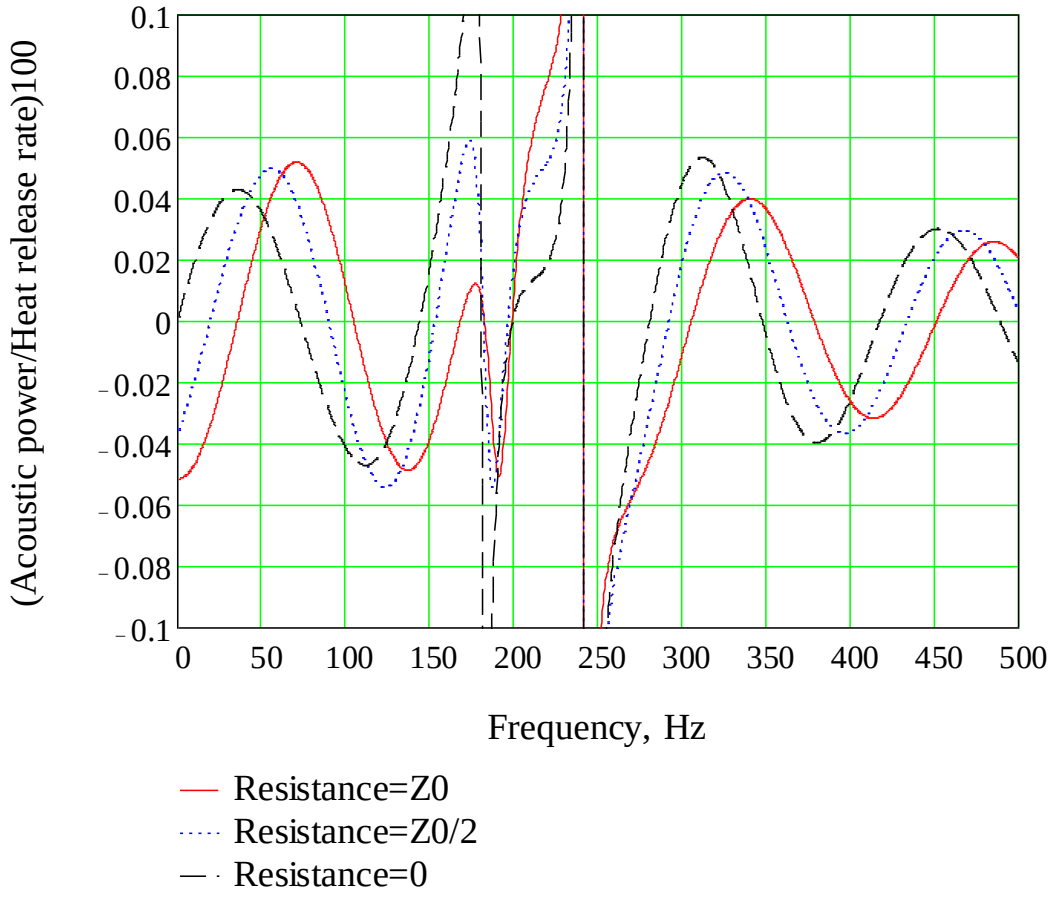

Figure 2.7: Percent acoustic power vs. frequency for $\frac{1}{2}(\rho c)/S_{fi}$, $L_{fi} = 0.1m$.

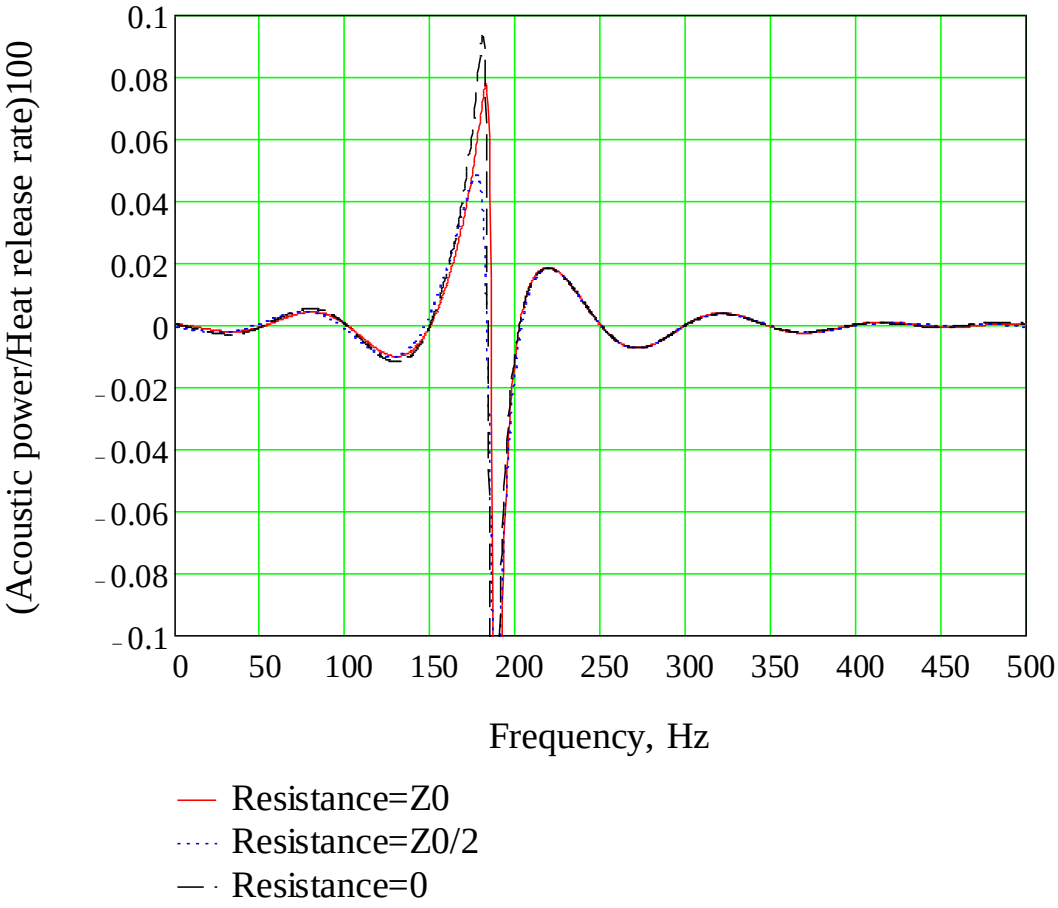

Figure 2.8: Percent acoustic power vs. frequency for $(\rho c)/S_{fi}$, $L_{fi} = 0.1m$. In this case, equivalence ratio oscillations were turned OFF.

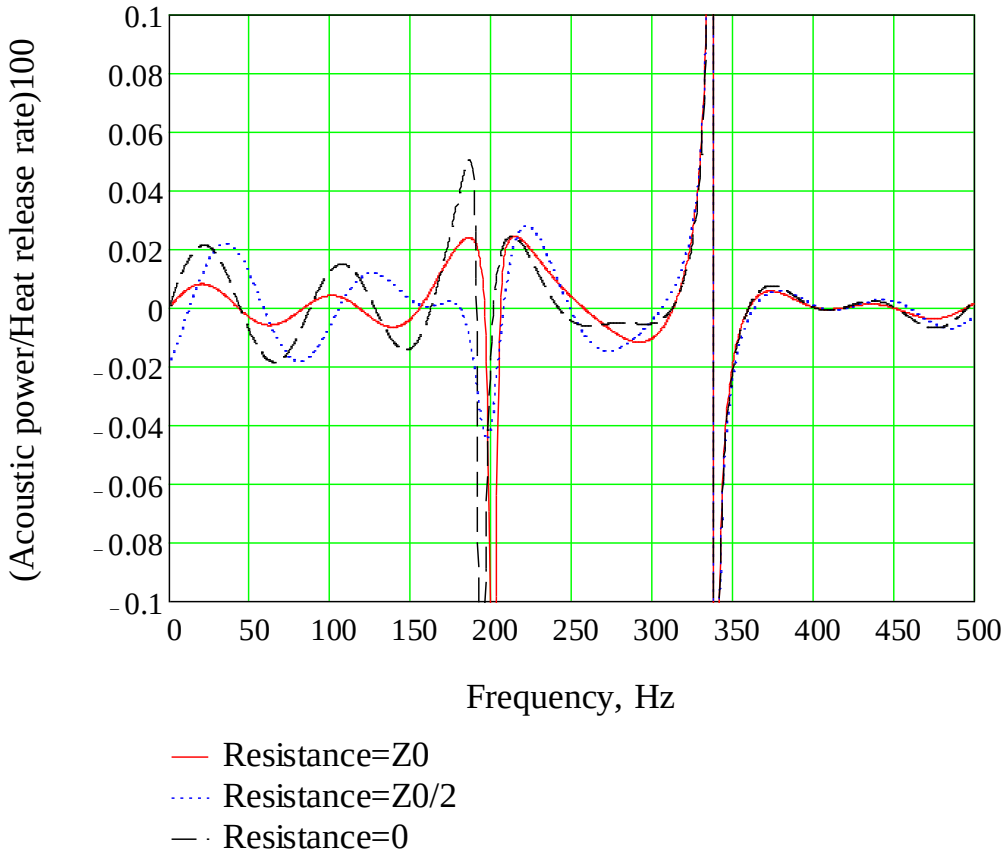

Figure 2.9: Percent acoustic power vs. frequency for $(\rho c)/S_{fi}$ and $L_{fi} = 0.2\,m$.

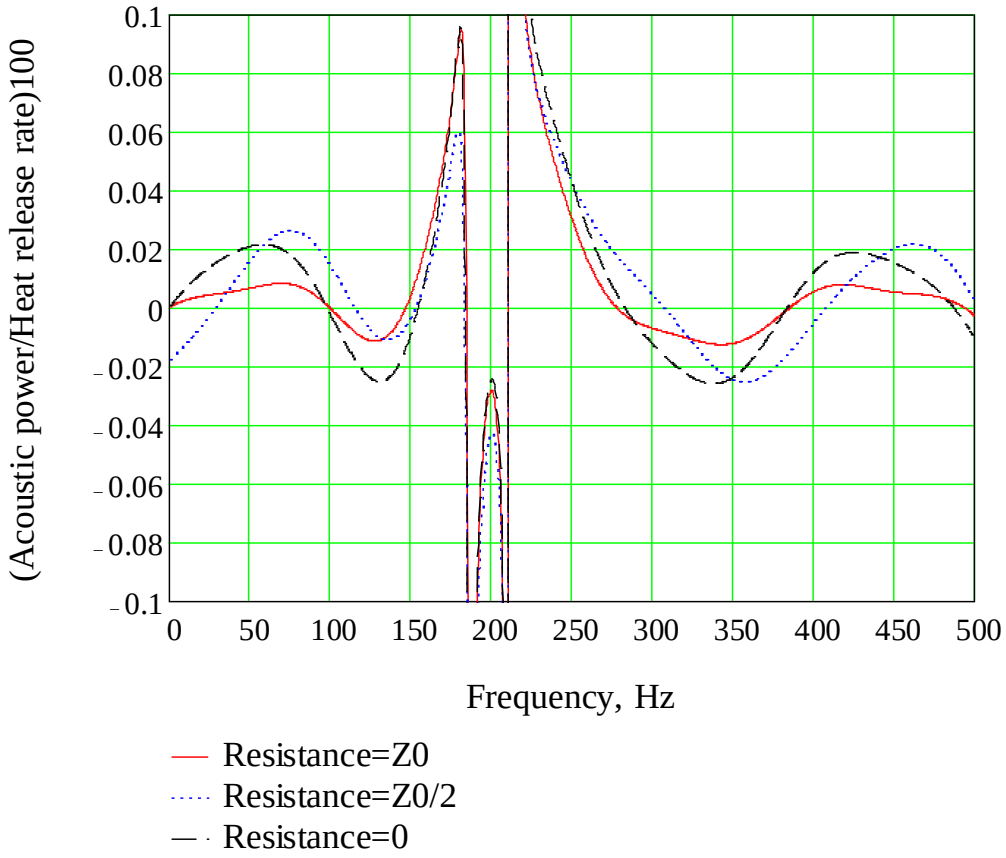

Figure 2.10: Percent acoustic power vs. frequency for $(\rho c)/S_{fi}$ **and** $L_{fi} = 0.051m.$

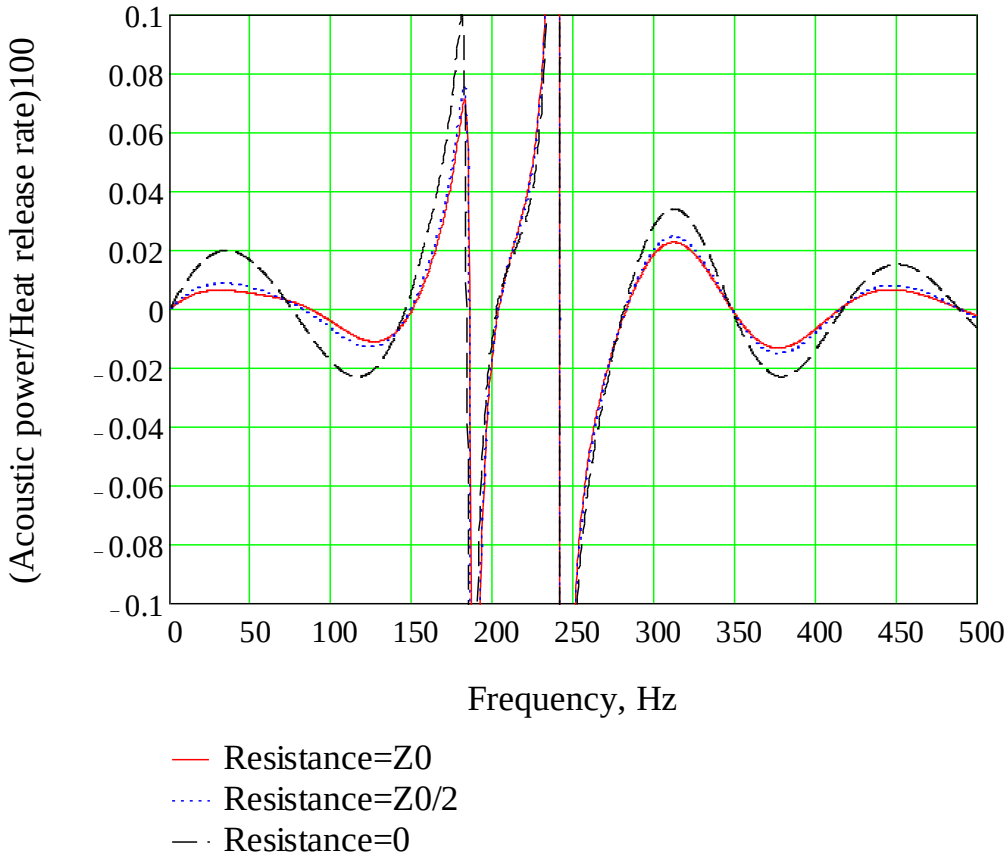

Figure 2.11: Percent acoustic power vs. frequency for a fuel system tuner with driving (i.e., the Resistance is less than zero) and with $(\rho c)/S_{fi}$, $L_{fi} = 0.1m$.

For convenience, the ratio of the acoustic power to total heat release will be referred to as the degree of instability, and large positive or negative values for the degree of instability mean that the system will be more unstable or stable, respectively. It is important to note that even when the degree of instability is positive the system will be stable if the damping exceeds the driving. Since the amount of combustion system damping (other than that in the fuel system) was unknown, this investigation centered on making the degree of instability as small as possible by varying the impedance of the fuel supply system. In practice, this is the purpose of the FST.

Figure 2.4 shows the model predictions for a fuel injector impedance magnitude of $\frac{1}{10}(\rho c)/S_{fi}$ for three different values of fuel system resistance. In all cases, the maximum degree of instability for the system is quite strong in this case compared to those shown in Figure 2.5 through Figure 2.7, indicating that the small impedance of the fuel injector has a large influence on system stability. It is also interesting that the maximum degree of instability is approximately equal for all three resistance values. Therefore, the primary effect of changing the fuel system resistance is to shift the stability curves along the frequency axis. For example, consider the 300 Hz case. When the fuel system resistance is 0, the system is quite unstable having a degree of instability of 0.18. However, the degree of instability was 0.06 and -0.1 when the fuel system increased to $Z0/2$ and $Z0$, respectively.

Clearly, at low fuel system impedances, the potential exists for very strong instabilities as well as for very stable operation depending on frequency of the instability and the phase of the fuel system impedance. Although not ideal at all frequencies, it is clear that a fuel system having a small impedance with the ability to adjust the phase of the impedance from 0 to +/- 90 degrees has the potential for large improvements in the stability of an otherwise unstable combustor.

Figure 2.5 through Figure 2.7 show the model predictions for impedance magnitudes of $10(\rho c)/S_{fi}$, $(\rho c)/S_{fi}$, and $\frac{1}{2}(\rho c)/S_{fi}$, respectively. Figure 2.5 shows that for very large impedances, varying the resistance had no effect on the system response. This is because very large injector impedances effectively isolate the FST from the acoustic oscillations that occur within the combustor and air inlet system. Therefore, tuning the FST, i.e., changing the resistance or reactance, cannot change the amplitude or phase of the fuel injection rate into the air stream.

Figure 2.5 also shows that the inlet system has a strong response (resonance) at 210 Hz with a weaker response at 182 Hz. Second, excluding the plot shows that the system stability oscillates between stable, i.e., positive values, and unstable, i.e., negative values, as the frequency varies from 0 to 500 Hz. The system is unstable between 50 and 115 Hz and again between 270 and 350, excluding the regions of strong response between 170 and 270 Hz. The system was stable between 110 and 170 Hz and again between 350 and 410 Hz.

Figure 2.6 and Figure 2.7 show that decreasing $(\rho c)/S_{fi}$ causes the response of the system to be very sensitive to changes in the resistance and reactance of the fuel injector. The key trends are as follows. As $(\rho c)/S_{fi}$ decreases, (1) the regions of stability and instability are broader with respect to frequency and (2) the degree of instability, i.e., how positive or negative the acoustic power to heat release rate ratio, increases.

These three figures show that it is critical that the fuel injector have sufficient area to allow the fuel system to communicate with the rest of the combustor. If not, the adjusting the resistance and reactance of the fuel injector will have no effect on combustor stability. Also, they show that the sensitivity of combustor stability to FST tuning can be controlled by, for example, adjusting the diameter of the fuel injector holes thereby causing S_{fi} to decrease. This indicates that since fuel injector holes are not usually adjustable in most practical systems, some nominal size should be selected that provides good sensitivity and controllability. This must be done in the combustor design phase.

Since the primary objective of the FST is to suppress combustion instabilities by changing the magnitude and phase of the fuel-air ratio oscillations relative to the acoustic pressure in the combustor, the effect of the FST on system stability was

investigated with fuel-air ratio oscillations turned OFF. Figure 2.8 shows the results of these calculations for the conditions indicated. First, notice that for most frequencies changing the resistance of the FST had little influence on the degree of instability of the system. Changing the resistance of the FST impedance did have some impact in the region of strong response centered at 180 Hz. However, it is clear from these figures that turning off the fuel-air ratio oscillations in the model significantly reduced the predicted effectiveness of the FST.

The positioning of the FST in the air inlet pipe was also found to have a strong impact on the effectiveness of the FST. Figure 2.6, Figure 2.9, and Figure 2.10 show the degree of instability of the system when the FST was located 0.1, 0.2, and 0.051 m from the combustor dump plane, respectively. The primary affect of relocating the FST was to change the frequency response of the system thereby frequency shifting the stable/unstable regions. Figure 2.9 shows that moving the FST to a position 0.2 m from the dump plane caused the resonance to shift to 330 Hz and the first region of stability to be between 50 and 100 Hz. Figure 2.10 shows that moving the FST closer to the combustion zone caused there to be a stable operating zone between 100 and 150 Hz. Further, it shows that the degree of instability in this region is much larger with the FST located very close to the combustion zone.

The current FST configuration under consideration has no acoustic power source, e.g., a speaker. Figure 2.11, however, shows the effect of including a driver in the FST. It shows that the first unstable band extends from 0 to 80 Hz; the first stable band extends from 80 Hz to 155 Hz. Excluding the strong response zones, there is a stable band from 375 to 450 Hz and an unstable zone between 300 and 375 Hz. Comparing these results to Figure 2.6, the stable/unstable zones are frequency shifted

and broadened, and the peak degree of stability in the first unstable zone is 33% of the peak in the first unstable zone shown in Figure 2.6.

While adding an acoustic source to the fuel system is interesting from a theoretical perspective, the predictions shown here are insufficient to justify the additional trouble and expense.

2.4 Conclusions

This analysis is straightforward to use but is capable of making important predictions about the effect of fuel system impedance on combustor stability. In this study, it yielded the following important conclusions about the use of fuel system tuners and combustor stability. First, the fuel system impedance is critical to combustor stability for acoustically open fuel systems, and that control of combustor instabilities can be accomplished using a variable impedance fuel supply system. Second, the magnitude of the fuel system impedance controls the sensitivity of combustor response to fuel system impedance. Third, restricting the fuel injector diameter, i.e., choking the fuel supply system, limits the ability of the variable impedance fuel supply system to control combustion instabilities. Fourth, the response of the combustor to changes in fuel system impedance depends on the location of the fuel system in the air supply system. Finally, and most importantly, fuel system impedance must be considered when developing new combustion systems. Otherwise, modifications will need to be made after the fact to allow for stable combustor operation.

Based on the results of these predictions, the best design for a tunable fuel system would center on keeping the fuel system impedance as low as possible while incorporating a mechanism for adjusting the fuel system resistance. In practice, the lowest fuel system impedance is obtained by tuning the fuel system to resonance at the

frequency of the expected combustor instability frequency, which minimizes the imaginary part of the fuel system impedance. By varying the fuel system resistance from 0 to a value much larger than the imaginary part of the fuel system impedance, the phase of the impedance can be varied from 0 to +/- 90 degrees.

Larger fuel system impedance magnitudes can be obtained by tuning slightly away from resonance to increase the imaginary part while keeping the resistive part essentially constant. This also changes the phase of the fuel system impedance, so some adjustment to the fuel system resistance may be needed to retain the same phase as before.

Chapter 3:

Theoretical Efforts

3.1 Introduction

The previous chapters introduced the FST concept and its mode of operation. It was shown that the ability of the FST to create and vary the acoustic resistance and reactance of the fuel system is critical to its operation. It was also shown that acoustic resistance can be a nonlinear phenomenon that depends on the amplitude of the acoustic oscillations. Finally, it was stressed that an adequate acoustic response model of the FST was critical to its further development and implementation on a given combustion system.

As has been mentioned previously, the FST is comprised of an acoustical network of tubes, valves, 'tees', and area changes. The area change is the least complex, from an acoustics standpoint, of all of these elements. Therefore, this chapter proceeds with the development of a nonlinear acoustic impedance model for abrupt area changes. This model was necessary to provide reasonable predictions of the frequency response of the FST and its components over the range of frequencies and acoustic pressure amplitudes encountered in unstable combustors. Figure 3.1 shows an abrupt area change and its incompressible flow streamlines for conditions of inflow and outflow.

Figure 3.1(a) suggests that the flow loses little, if any, total energy as it flows through the area contraction from 1 to 2. However, the increased velocity of the flow in 2 can result in a transition from laminar to turbulent flow. The turbulence dissipates significantly more energy due to the high velocity gradients at the tube wall. Therefore,

some dissipation of energy may be seen in the case of the area contraction. Since the flow from 1 to 2 is essentially isentropic, the unsteady, incompressible Bernoulli equation may be used along with the continuity equation to develop an expression for the impedance of the area contraction.

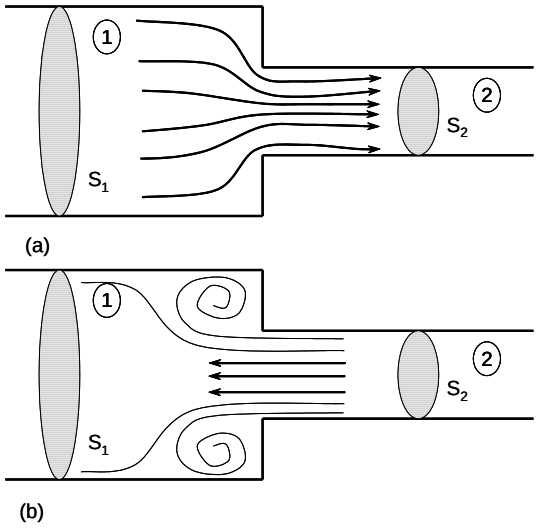

Figure 3.1: (a) Flow streamlines for an area contraction with flow entering the contraction. (b) Flow streamlines for an area expansion with flow leaving the contraction.

Figure 3.1(b) shows that the flow from 2 to 1 forms a turbulent jet as it exits the smaller tube. This jet becomes turbulent at Reynolds numbers around 100.[33] The turbulent flow from 2 separates from the lip of the area contraction, and the vortex shedding from the detached flow at the area contraction step leads to significant energy dissipation. In the case of steady flow from 2 to 1, the energy dissipated by the separated flow is proportional to $\left(V_2^2 - V_1^2\right)/2$.[34] In this case, the flow is clearly not isentropic. However, the momentum equation along with the incompressible continuity equation may be used to develop an expression for the impedance of the area expansion from 2 to 1.

In the case of acoustic oscillations with no steady mean flow or with the steady flow velocity less than the local acoustic velocity, both flow conditions exist. The flow enters the area contraction from 1 to 2 over a portion of the cycle and exits the area contraction from 2 to 1 over the remainder of the cycle. In this chapter, the acoustic impedance of the area contraction will be related to the geometry of the area contraction, the ratio of the steady to acoustic flow velocity, and the characteristic impedance of the duct.

The acoustic impedance model developed in this section captures the important relationship between acoustic velocity amplitude and acoustic resistance while maintaining simplicity. The developed model was then used to aid in the interpretation of the acoustic response measurements presented in Chapter 4, and, as described in Chapter 5, to develop an acoustic response model of the FST. The developed FST model was then used in the development of a thermo-acoustic model of a representative combustion system as detailed in Chapter 6.

3.2 Background of the nonlinear acoustic response of abrupt area changes

The acoustic response of duct systems is often of much interest in such aerospace applications as engines, wind tunnels, and exhaust ducts. Such systems may include area changes, duct sections, valves, and unchoked orifices. These elements can usually be modeled as acoustically compact for frequencies whose wavelength is much longer than the effective length of the component. To model the acoustic response of a system containing such elements, the 'lumped' acoustic impedance, which is defined as the pressure drop across the element divided by the acoustic volume velocity through the element, i.e., $Z = \left(p_1' - p_2'\right)/S_1 u_1'$, of each of these elements must be known.

Further, at low acoustic pressure amplitudes, it is conventional to neglect nonlinear effects that affect the wave propagation and the flow within these lumped elements. For most applications, these assumptions do not produce large errors while significantly simplifying the calculation of the frequency response of the system. It has been observed, however, that certain elements, such as sudden contractions, orifices, and valves, behave nonlinearly, i.e., the impedance of these elements depends on the acoustic velocity amplitude, even at very low sound pressure levels when the mean steady flow velocity is small. In fact, it will be shown herein that nonlinear effects can only be neglected for these types of elements when the acoustic velocity amplitude is small relative to the steady flow velocity, i.e., never for systems without mean flows.

Sivian[35], who was the first to note such effects, observed a nonlinear relationship between the resistance of a circular orifice and the acoustic velocity. The resistance became important at acoustic velocities around 0.5 m/s. Subsequently, Ingard[36,37] reported observations similar to Sivian's, and Ingard and Labate[36] reported that the

nonlinear effects observed in the acoustic response of orifices were closely connected to the flow patterns around the orifice itself. Ingard and Ising[38] demonstrated in 1967 that the impedance of orifices was constant at low pressure amplitudes but approached a square law relation for higher driving pressures. In 1970, Zinn[39] presented a theoretical model for the nonlinear resistance of an orifice that also incorporated a discharge coefficient to account for the vena contracta and flow coefficients. In 1976, Johnston and Schmidt[40] reported significant discrepancies between linear acoustic model predictions and the results of tests in which they attempted to measure the reflection coefficient of pipeline obstructions. They attributed these to wall radiation losses. While the above mentioned studies focused on the nonlinear acoustic response of circular orifices, similar behavior was expected for other elements that incorporated a rapid area change with little or no steady flow, such as those described above. For additional information, the reader is referred to Melling[41], who presents an excellent discussion and analysis of this subject matter.

Cummings et. al.[42] present a theoretical expression for the impedance of duct terminations similar to the one developed here. The impedance expression they developed included the effects of steady mean flow and the nonlinear effect of the acoustic velocity, both of which depend on the ratio of the flow area of the duct and the effective area of the orifice. They note but do not account for the fact that the losses are different when the oscillatory flow was into and out of the contraction.

As discussed above, the fluid mechanical behavior of the area change is complex and depends on the velocity of the flow in and out of the area change. Figure 3.1 shows a schematic of the steady flow streamlines of flows into and out of the shown area contraction. It is well-known that the losses for case (b) are greater than those for

case (a) for the same flow velocity because of the presence of the recirculation regions, which lead to viscous dissipation of the flow's kinetic energy.

Acoustic analysis of systems containing abrupt area changes requires either measurements or models for the acoustic response, i.e., acoustic impedance, of the area change to acoustic forcing. A model for the acoustic impedance of an area change must account for the fact that the impedance of the area change may be nonlinear. The model must also account for the fact that over a fraction of the period of the oscillation, the flow is aligned with the direction of the mean flow and in the opposite direction for the remaining fraction of the cycle. The duration of each phase of the flow generally depends on the ratio of the acoustic velocity amplitude to the magnitude of the steady flow velocity. Therefore, the degree of dissipation will, in general, depend on the amplitudes of the oscillations and the steady velocity component. For sufficiently high steady mean flow velocities, there will be no flow reversal. However, nonlinear effects may be neglected well before this occurs.

The nonlinear model developed here was similar to those noted above. However, this model accounts explicitly for the fact that the actual pressure losses may be greater or less than predicted using the actual ratio of the duct and contraction areas. This theoretical model was used to effectively model area contractions, area expansions, a variable area valve, and a junction of three ducts.

3.2.1 An acoustically compact area contraction

This section presents the derivation of an expression for the acoustic impedance of an acoustically compact area change (see Figure 3.2) accounting for the effects of: (1) the amplitude of the oscillations, (2) the presence of mean flow, and (3) the difference in the flow characteristics when the gradient of the acoustic pressure across the area change is positive and negative.

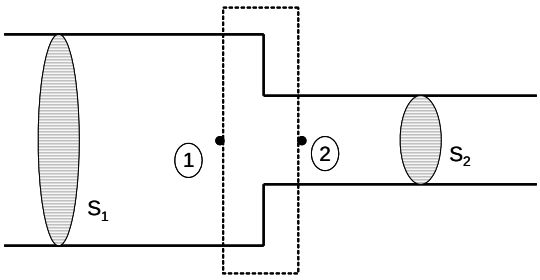

Figure 3.2: Diagram of a simple, acoustically compact area contraction.

The derivation of the expression for the impedance used the unsteady, incompressible Bernoulli equation to relate conditions between points 1 and 2 in Figure 3.2, because the flow may be assumed to be incompressible when the wavelength of the oscillations is much larger than the characteristic dimension of the investigated flow region.[43,44] The unsteady Bernoulli equation, is given by[45]:

$$-\frac{d\psi}{dt}+\frac{u^2}{2}+\int\frac{dp}{\rho}=C(t), \tag{3.1}$$

where $C(t)$ is a function of time only and ψ is the velocity potential; i.e., $\psi=-\int u\,ds$ where s is the streamline coordinate. Substituting this expression for ψ into Eq. (3.1) yields

$$\underbrace{\rho\int\frac{du(s)}{dt}ds}_{1}+\rho\frac{u^2}{2}+p=C(t)\,. \tag{3.2}$$

Following Ingard[46], the velocity $u(t,s)$ was expressed as a product of space and time dependent functions; i.e.,

$$u(t,s) = u(t)c(s) = (u_0 + u' \cdot e^{-i\omega t})c(s), \tag{3.3}$$

where u_0, u' and $c(s)$ are the magnitude of the mean axial velocity, the amplitude of the axial acoustic velocity, and a function that describes the spatial dependence of the axial velocity, respectively. Differentiating Eq. (3.3) with respect to time and substituting the result into the first term in Eq. (3.2) yields

$$\rho \int \frac{du(s)}{dt} ds = \rho(-i\omega)u' \cdot e^{-i\omega t} \underbrace{\int c(s)\, ds}_{L_e}, \tag{3.4}$$

where L_e is an equivalent length that may be determined experimentally or by further analysis[46].

Next, substituting Eq. (3.4) into Eq. (3.2), evaluating the resulting expression at points 1 and 2 in Figure 3.2, and subtracting the results from one another yields

$$\rho(-i\omega)u_1' \int_1^2 c(s)\, ds + \left(\rho \frac{u^2}{2} + p \right)_1 - \left(\rho \frac{u^2}{2} + p \right)_2 = 0. \tag{3.5}$$

It should be noted that Eq. (3.5), which is quite general and can be used to study flow changes between two points across other components, e.g., valves and orifices, does not account for pressure losses associated with the flow between the investigated points. To account for these pressure losses, Eq. (3.5) was rewritten in the following form[47]

$$\rho(-i\omega)u_1' \int_1^2 c(s)\, ds + \left(\rho \frac{u^2}{2} + p \right)_1 - \left(\rho \frac{u^2}{2} + p \right)_2 = K_L \frac{1}{2} \rho u_1^2, \tag{3.6}$$

where the pressure losses were expressed as the product of the time averaged loss coefficient K_L, which in its present form accounts for both steady and unsteady effects.

Since the investigated flow consists of steady and unsteady (i.e., acoustic) components, the pressure p is given by $p = p_0 + p'$ and the square of the velocity is given by:

$$u^2 = \left(u_0 + u'\right)^2 = {u_0}^2 + 2u_0 u' + u' \cdot u' . \tag{3.7}$$

Substituting the above expressions for p and u^2 into Eq. (3.6) yields, after rearrangement, the following equation:

$$\begin{aligned} &\underbrace{\rho(-i\omega)u_1' \int_1^2 c(s)\,ds + \left(\rho u_0 u' + \frac{\rho u' \cdot u'}{2} + p'\right)_1 - \left(\rho u_0 u' + \frac{\rho u' \cdot u'}{2} + p'\right)_2}_{\text{unsteady}} \\ &+ \underbrace{\left(\rho \frac{{u_0}^2}{2} + p_0\right)_1 - \left(\rho \frac{{u_0}^2}{2} + p_0\right)_2}_{\text{steady}} = \underbrace{K_{L,0} \frac{1}{2} \rho {u_{0,1}}^2}_{\text{steady}} \\ &+ \underbrace{K_L \frac{1}{2} \rho \left(2u_0 u' + u' \cdot u'\right)_1}_{\text{unsteady}} \end{aligned} . \tag{3.8}$$

Equation (3.8) includes both linear and nonlinear unsteady terms as well as steady flow terms. Since an expression for the acoustic impedance is desired, consider only the unsteady part of Eq. (3.8), which was rewritten in the following form:

$$\begin{aligned} &\rho(-i\omega)u_1' L_e + \left(\rho u_0 u' + \frac{\rho u' \cdot u'}{2} + p'\right)_1 - \left(\rho u_0 u' + \frac{\rho u' \cdot u'}{2} + p'\right)_2 = \\ &K_L \frac{1}{2} \rho \left(2u_0 u' + u' \cdot u'\right)_1 \end{aligned} . \tag{3.9}$$

Next, the continuity equation is used to relate the unsteady velocity components at points 1 and 2 as follows:

$$\underbrace{\frac{dm}{dt}}_{1} + \underbrace{\dot{m}_2 - \dot{m}_1}_{2} = 0 , \tag{3.10}$$

where the first term in Eq. (3.10) was set to zero because the flow was assumed incompressible within the region of investigation. Substituting the following expression for the mass flux,

$$\dot{m} + \dot{m}' = \rho u_0 S + \rho u' S + O(\rho' \cdot u') = 0, \tag{3.11}$$

into Eq. (3.10) and neglecting all but first order terms, because $\rho' = 0$ for the assumed incompressible flow, yields the following form of the continuity equation:

$$\underbrace{S_1(\rho u_0)_1 - S_2(\rho u_0)_2}_{steady} + \underbrace{S_1(\rho u')_1 - S_2(\rho u')_2}_{unsteady} = 0. \tag{3.12}$$

Finally, treating the steady and unsteady parts of Eq. (3.12) independently, the following relationships between the velocities at points 1 and 2 in Figure 3.2 were obtained:

$$\frac{u_{0,1}}{u_{0,2}} = \frac{u_1'}{u_2'} = \frac{S_2}{S_1}. \tag{3.13}$$

Substituting Eq. (3.13) into Eq. (3.9), dividing the resulting expression by $S_1 u_1'$ and multiplying and dividing the right hand side by the speed of sound, c, yields the following expression for the acoustic impedance of the investigated area change:

$$\frac{Z}{\rho c} = \frac{p_1' - p_2'}{\rho c \cdot S_1 u_1'} = \underbrace{\frac{i\frac{\omega}{c}L_e}{S_1}}_{1} + \underbrace{\left(\frac{u_0}{c} + \frac{|u_1'|}{2 \cdot c}\right)\frac{\overbrace{\left[\left(\frac{S_1}{S_2}\right)^2 + K_L - 1\right]}^{3}}{S_1}}_{2}. \tag{3.14}$$

Accounting for the possibility that the loss coefficient K_L differs for the steady and unsteady portions of the flow yields,

$$\frac{Z}{\rho c} = \frac{p_1' - p_2'}{\rho c \cdot S_1 u_1'} = \underbrace{\frac{i\frac{\omega}{c}L_e}{S_1}}_{1} + \underbrace{\frac{u_0}{c}\frac{\left(\frac{S_1}{S_2}^2 + K_{L,u_0} - 1\right)}{S_1}}_{2} + \underbrace{\frac{|u_1'|}{2 \cdot c}\frac{\left[\left(\frac{S_1}{S_2}\right)^2 + K_{L,u'} - 1\right]}{S_1}}_{3}. \tag{3.15}$$

Tracing the origin of the various terms on the right hand side of Eq. (3.15) reveals that Term 1 is the reactive part associated with the oscillating mass between points 1 and 2 in Figure 3.2, and Terms 2 and 3 are the linear and nonlinear components of the

resistance, respectively. It is noteworthy that the linear component is associated with the steady flow and the nonlinear component is associated with the oscillatory component of the flow and that the additional flow losses associated with $K_{L,u_1'}$ in Term 3 in Eq. (3.15) have the same effect upon the impedance, Z, as the area change, S_1/S_2. Thus, these flow losses may be regarded as an "equivalent" increase in the area ratio.

Considerations of the flow at the investigated area change suggest that as long as the flow reverses direction, i.e., when the amplitude of the oscillatory velocity component is larger than the magnitude of the mean flow, the magnitudes of K_{L,u_0} and $K_{L,u'}$ will differ. The difference between K_{L,u_0} and $K_{L,u'}$ is expected, however, to vanish as the magnitude of the mean flow increases and/or the amplitude of the oscillatory velocity decreases so that the flow no longer reverses direction.

By defining an effective discharge coefficient C_D, Eq. (3.14) can be rewritten in a modified form as

$$\xi = \frac{ZS_1}{\rho c} = \frac{(p_1' - p_2')S_1}{\rho c \cdot S_1 u_1'} = ikL_e + \left(\frac{u_0}{c} + \frac{|u_1'|}{2 \cdot c}\right)\frac{(1 - C_D^2)}{C_D^2} \tag{3.16}$$

where

$$C_D = \frac{S_{eff}}{S_1} = \frac{u_1}{u_{eff}} = \frac{u_1'}{u_{eff}'} = \frac{1}{\sqrt{\left(\frac{S_1}{S_2}\right)^2 + K_L}} \tag{3.17}$$

and S_{eff} is an effective area that must be obtained either from further analysis or experimental measurements. This expression was used to obtain an estimate for C_D from impedance tube measurements, which are described later in the thesis.

Equation (3.16) is a preferable form for the impedance of, for example, an open-ended pipe. In this case, S_{eff} is the effective area into which the open-ended pipe radiates.

3.2.2 Energy considerations

Referring to Figure 3.2, neglecting steady flow the acoustic power reflected or dissipated by the area change $\Delta\Pi$ is equal to the difference between the acoustic power incident on the area change and the acoustic power leaving the area change, which, in equation form, was expressed as

$$\Delta\Pi = \frac{S_1}{2}\mathrm{Re}\left[p_1' \cdot conj\left(u_1'\right)\right] - \frac{S_2}{2}\mathrm{Re}\left[p_2' \cdot conj\left(u_2'\right)\right]. \tag{3.18}$$

Writing the acoustic pressure at location *i* in terms of the acoustic impedance Z_i and the acoustic velocity yields

$$\Delta\Pi = \frac{S_1}{2}\mathrm{Re}\left[u_1' S_1 Z_1 \cdot conj\left(u_1'\right)\right] - \frac{S_2}{2}\mathrm{Re}\left[u_2' S_2 Z_2 \cdot conj\left(u_2'\right)\right], \tag{3.19}$$

or

$$\Delta\Pi = \frac{S_1^{\,2}}{2}\left|u_1'\right|^2 \left\{\mathrm{Re}\left[Z_1 - Z_2\right]\right\}. \tag{3.20}$$

Assuming Z_2 to be purely reactive as would be the case for any lossless acoustical system, the real part of Z_2 is zero and Eq. (3.20) becomes

$$\Delta\Pi = \frac{S_1^{\,2}}{2}\left|u_1'\right|^2 \left\{\mathrm{Re}\left[Z_1\right]\right\}. \tag{3.21}$$

Equation (3.21) indicates that the acoustic power dissipated by the area change only depends on the resistive part of the impedance at location 1 assuming that Z_2 is purely reactive. In addition, if Z_2 is purely reactive, the real part of the impedance at location 1 must equal to the real part of the impedance of the area change, so that Eq. (3.21) may be written in the following equivalent form

$$\Delta\Pi = \frac{S_1^{\,2}}{2}\left|u_1'\right|^2 \left\{\mathrm{Re}\left[Z_{\delta A}\right]\right\}, \tag{3.22}$$

where $Z_{\delta A}$ is assumed given by Eq. (3.14). Substituting the real part of Eq. (3.14) into Eq. (3.22) yields

$$\Delta\Pi = \frac{S_1^{\,2}}{2}\left(\rho c\right)_1 \left|u_1'\right|^2 \left(\frac{u_0}{c} + \frac{\left|u_1'\right|}{2\cdot c}\right) \frac{\left[\left(\frac{S_1}{S_2}\right)^2 + K_L - 1\right]}{S_1}. \tag{3.23}$$

Equation (3.23) states that the acoustic power reflected by the area change depends quadratically on the acoustic velocity amplitude at location 1 when the acoustic velocity amplitude is small compared to the steady flow velocity and cubically on the acoustic velocity when the acoustic velocity amplitude is large compared to the steady flow velocity. It also indicates that large area contractions lead to higher power dissipation than smaller area contractions.

3.3 An acoustically compact area expansion

This section presents the derivation of an expression for the nonlinear acoustic impedance of an acoustically compact area change (see Figure 3.2), which accounts for the effects of acoustic velocity amplitude, area ratio, and the presence of mean flow.

Here it is assumed that the mean and fluctuating flow exits the smaller area section into the larger one as a 1-D, axial flow leading to flow separation. Because the flow at the exit is purely axial, the pressure across the face of the dump plane and interface 1 is assumed uniform because of negligible lateral velocity.

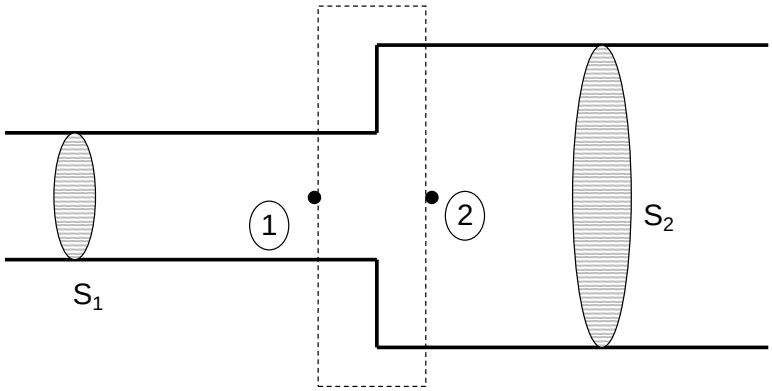

Figure 3.3: Diagram of a simple, acoustically compact area expansion.

Considering only the component of momentum in the x-direction, the integral momentum equation can be written as:

$$\frac{\partial}{\partial t}\int_{cv}\left(\rho\bar{V}\right)dV+\left(\rho V_x A V_x\right)_2-\left(\rho V_x A V_x\right)_1=p_1A_1-p_2A_2+F_x. \qquad (3.24)$$

Analysis of the forces acting on the control surface due to the presence of the duct shows that $F_x=p_1\left(A_2-A_1\right)$. Substituting this expression into Eq. (3.24) yields

$$\frac{\partial}{\partial t}\int_{cv}\left(\rho\bar{V}\right)dV+\rho\left[\left(V_xAV_x\right)_2-\left(V_xAV_x\right)_1\right]=A_2\left(p_2-p_1\right). \qquad (3.25)$$

Linearizing Eq. (3.25) and neglecting the volume integral and terms of $O\left(M^2\right)$ yields

$$A_2\left(p_2' - p_1'\right) + 2\rho\left(V_{0,2}A_2v_2' - V_{0,1}A_1v_1'\right) + \rho\left(A_2v_2'^2 - A_1v_1'^2\right) = 0, \quad (3.26)$$

where the subscripts 1 and 2 denote the respective region interfaces.

The incompressible continuity equation applied to this situation yields

$$\rho_0\left(v_2'A_2 - v_1'A_1\right) = 0 \text{ and } \rho_0\left(V_{0,2}A_2 - V_{0,1}A_1\right) = 0 \quad (3.27)$$

or

$$\frac{V_{0,2}}{V_{0,1}} = \frac{v_2'}{v_1'} = \frac{A_1}{A_2}. \quad (3.28)$$

Using Eq. (3.28), Eq. (3.26) was rearranged to obtain

$$A_2\left(p_2' - p_1'\right) + \rho\left(2V_{0,1} + v_1'\right)\left(\frac{A_1}{A_2} - 1\right)v_1' = 0. \quad (3.29)$$

Defining the ratio of the pressure drop between interfaces 1 and 2 and the acoustic volume velocity at interface 1 as the acoustic impedance, i.e.,

$$Z^e_{\delta A_{12}} = \frac{p_1' - p_2'}{v_1'A_1}, \quad (3.30)$$

and adding a reactive term ikL^e_{eff} to account for the oscillating mass at the opening of the area expansion, yields the following expression:

$$Z^e_{\delta A_{12}} = \frac{p_1' - p_2'}{v_1'A_1} = \frac{\rho c}{A_1}\left\{ikL^e_{eff} + \left(\frac{2V_{0,1} + v_1'}{c_1}\right)\left(\frac{A_1}{A_2}\right)^2\left[1 - \frac{A_2}{A_1}\right]\right\}, \quad (3.31)$$

which is the acoustic impedance of an abrupt area expansion.

3.4 Comparison between the acoustic resistance of an area contraction and expansion

It is interesting to compare the resistive part of the impedance of the sudden area contraction and expansion. The resistive part of the area contraction impedance is given by

$$\frac{\Delta p'}{v_1' A_1} = Z^c_{\delta A_{12}} = \frac{(\rho_0 c_0)}{A_1}\left\{\frac{V_{0,1}}{c_0}\left[\left(\frac{A_1}{A_2}\right)^2 - 1\right]\right\}. \tag{3.32}$$

The resistive part of the impedance of the area expansion is given by

$$Z^e_{\delta A_{12}} = \frac{p_1' - p_2'}{v_1' A_1} = \frac{\rho c}{A_1}\left\{2\frac{V_{0,1}}{c_1}\left(\frac{A_1}{A_2}\right)^2\left[1 - \frac{A_2}{A_1}\right]\right\}. \tag{3.33}$$

Forming the ratio of Eqs. (3.32) and (3.33) yields the ratio of the pressure drop between interfaces 1 and 2 assuming the volume velocity for each case, as given below

$$\frac{Z^{cont}_{\delta A_{12}}}{Z^{\exp}_{\delta A_{12}}} = \frac{\left(\frac{p_1' - p_2'}{v_2' A_2}\right)^{cont}}{\left(\frac{p_1' - p_2'}{v_1' A_1}\right)^{\exp}} = \frac{\frac{\rho c}{A_2}\frac{V_{0,2}}{c}\left[1 - \left(\frac{A_2}{A_1}\right)^2\right]}{2\frac{\rho c}{A_1}\frac{V_{0,1}}{c}\left(\frac{A_1}{A_2}\right)^2\left[1 - \frac{A_2}{A_1}\right]}. \tag{3.34}$$

Note that the steady velocity at interface 2 for the contraction is equal to the steady velocity at interface 1 for the contraction, i.e., $V^{cont}_{0,1} = V^{\exp}_{0,2}$. Further, for the area contraction, A_1 and A_2 are the larger and smaller areas, respectively, whereas for the area expansion, the situation is reversed, or

$$A_1^{cont} = A_2^{\exp} = A_{big} \text{ and } A_2^{cont} = A_1^{\exp} = A_{small}, \tag{3.35}$$

so Eq. (3.34) can be written as

$$r_p = \frac{\left(p_1' - p_2'\right)^{cont}}{\left(p_1' - p_2'\right)^{\exp}} = \frac{\dfrac{1}{A_{small}}\left[1 - \left(\dfrac{A_{small}}{A_{big}}\right)^2\right]}{2\dfrac{1}{A_{small}}\left(\dfrac{A_{small}}{A_{big}}\right)^2\left[1 - \dfrac{A_{big}}{A_{small}}\right]} = -\frac{1}{2}\left(1 + \frac{A_{big}}{A_{small}}\right), \quad (3.36)$$

where r_p is defined as the pressure drop ratio. For $A_{big}/A_{small} = 4,\ |r_p| = 5/2$ and for $A_{big}/A_{small} = 16,\ |r_p| = 17/2,$ which shows that the pressure drop for an area contraction is much larger than for an area expansion under similar flow conditions.

This analysis shows that the acoustic impedance of the area expansion may be neglected compared to the area contraction for contraction/expansion systems having an area ratio greater than 4.

3.4.1 The net impedance of the area contraction

Given that the predicted resistance depends on whether the velocity is into or out of the area contraction, a method for determining the net impedance Z_{net} was needed. Referring to Figure 3.4, the net impedance Z_{net} was defined as

$$Z_{net} = \frac{\frac{1}{T}\left[\int_0^{t_{forward}} Z_{forward}\left(u'_{forward}\right)^2 dt + \int_{t_{forward}}^{T} Z_{reverse}\left(u'_{reverse}\right)^2 dt\right]}{\left(u'_{rms}\right)^2}, \qquad (3.37)$$

where the first time integral from 0 to $t_{forward}$ was taken over the period when the oscillatory velocity was in the direction of the mean flow and the second time integral over $t_{reverse}$ was taken over the period when the direction of the oscillatory velocity was in a direction opposite that of the steady flow. $Z_{forward}$ is the impedance when the oscillatory flow was in the same direction as the steady flow and $Z_{reverse}$ is the loss coefficient when the oscillatory flow reversed direction. Equation (3.37) shows that as the magnitude of the steady mean flow increases, the magnitude of the duration of the reverse flow gradually diminishes until $Z_{net} \cong Z_{u_0}$.

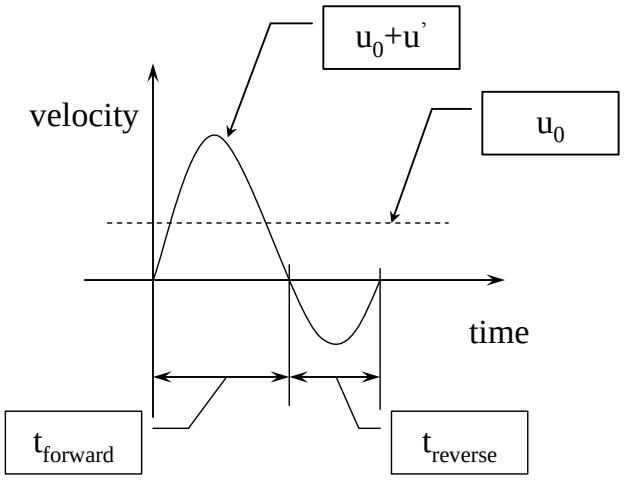

Figure 3.4: Velocity variation with time.

As an example, Figure 3.5 shows a plot of Z_{net} as a function of steady flow velocity for an acoustic velocity amplitude of 10 m/s, $Z_{forward} = 1$, and $Z_{reverse} = 0$. In this plot, the steady flow velocity increased from zero at the left to the amplitude of the acoustic velocity at the right.

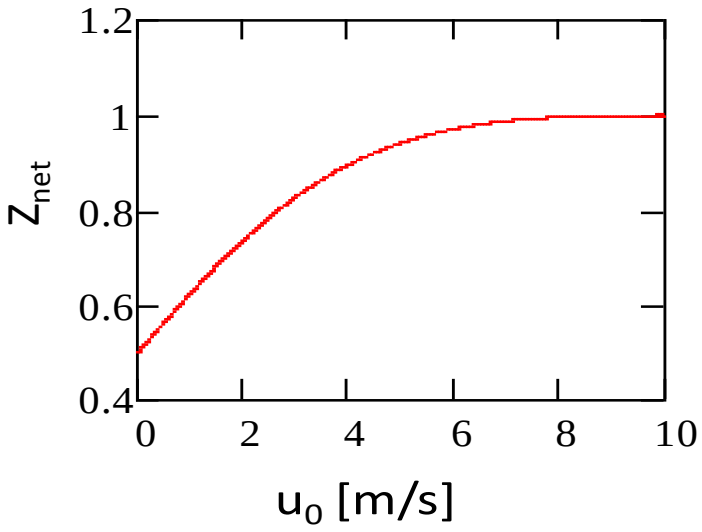

Figure 3.5: Example calculation of the average loss coefficient.

As expected, the value of Z_{net} increased from a minimum when the steady flow velocity was zero to a maximum value when the steady flow velocity was equal to the acoustic velocity. When the steady flow velocity was zero, the amount of inflow time was equal to the amount of outflow time. For this case, the average loss coefficient was equal to the average value of the forward and reverse loss coefficients. However, as the steady flow increases, outflow occurred during a greater portion of the period. Therefore, the average loss coefficient increased to reflect this skew toward outflow. When the steady flow velocity was equal to or greater than the acoustic velocity, the outflow time was equal to the period, so the average loss coefficient saturated at the value of the loss coefficient for outflow.

3.5 Application of the nonlinear area contraction impedance model

This section demonstrates the application of the above impedance model to elements of the FST employing modeling techniques commonly used in plane wave models of duct systems. The key contribution here is the use of the nonlinear impedance relation given by Eq. (3.14) together with an iterative solution technique to obtain a more realistic understanding of the acoustic behavior of these elements. This approach was used to develop an overall FST acoustic model that was incorporated into a combustor stability model for determining the performance of the FST.

The example calculation procedure presented in this section is for a system having a "rigid" end-termination preceded by a sudden area change (see Figure 3.6). It incorporates the nonlinear impedance model in an otherwise linear acoustic response model. The following analysis was used to determine the reflection coefficient at location 1, which accounts for the impedance of the system comprised of the area change and duct 2.

From classical acoustics, the pressure perturbation and the acoustic velocity in a duct are given by

$$p' = Ae^{ikx} + Be^{-ikx}, \tag{3.38}$$

$$u' = \frac{1}{\rho c}\left(Ae^{ikx} - Be^{-ikx}\right). \tag{3.39}$$

This system must satisfy two boundary conditions: $p'=P_{ext}$ at location 1 (P_{ext} is the measured acoustic pressure) and $u'=0$ at $x=L$. Applying these boundary conditions yields at $x=0$

$$A_1 + B_1 = P_{ext}, \tag{3.40}$$

and at $x=L$

$$A_2 e^{ikL} - B_2 e^{-ikL} = 0 \tag{3.41}$$

where A and B are the complex amplitudes of the oscillations in ducts 1 and 2, respectively.

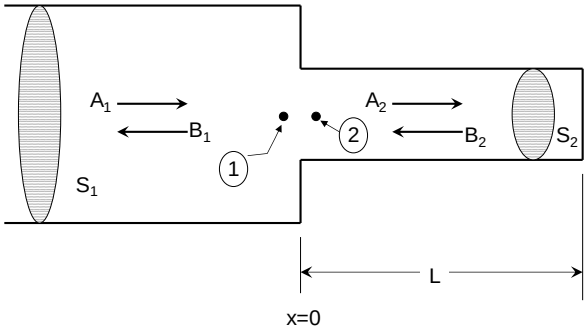

Figure 3.6: System including a rigid termination preceded by a sudden area change.

The impedance, Z, of the area change interface relates the pressure drop between locations 1 and 2 to the velocity at location 1 as follows,

$$p_1' - p_2' = Z \cdot S_1 u_1', \tag{3.42}$$

where Z is given by Eq. (3.14). The subscripts 1 and 2 in Eq. (3.42) refer to locations just upstream and downstream of the area change, respectively. It is important to note that the separation distance between locations 1 and 2 is of vanishing length when compared to the acoustic wavelength. Substituting the appropriate expressions for the acoustic pressures and velocity into Eq. (3.42) yields

$$A_1\left(1 - Z\frac{S_1}{Z_0}\right) + B_1\left(1 + Z\frac{S_1}{Z_0}\right) = A_2 + B_2, \tag{3.43}$$

where $Z_0 = \rho c$ is the characteristic impedance of the medium.

The continuity equation requires that the acoustic volume velocity $V_j' = u_j' S_j$ be continuous across the area change from duct 1 to duct 2 yielding

$$A_1\left(\frac{S_1}{Z_0}\right)-B_1\left(\frac{S_1}{Z_0}\right)=A_2\left(\frac{S_2}{Z_0}\right)-B_2\left(\frac{S_2}{Z_0}\right). \tag{3.44}$$

To determine the complex pressure amplitudes, A_1, A_2, B_1, and B_2, the nonlinear set of Eqs. (3.40), (3.41), (3.43), and (3.44) (using Eq. (3.14) for *Z*) were solved simultaneously. Having determined the complex pressure amplitudes, the acoustic velocities and pressures within the cavity were computed from Eqs. (3.38) and (3.39).

Since *Z* was a function of the acoustic velocity, the set of equations above were nonlinear and therefore could not be solved directly. Instead, an iterative solution procedure was used. This solution procedure starts by assuming values for the constant K_L and $\left|u_1'\right|/c$ and substituting them into Eq. (3.14) to estimate the impedance *Z*. This value together with the imposed pressure, P_{ext}, was then substituted into Eqs. (3.40), (3.41), (3.43), and (3.44), which were then solved for the four unknown amplitudes. From the calculated amplitude, a new value for the acoustic velocity was obtained and the process repeated until convergence was achieved.

Figure 3.7 shows the predicted frequency dependence of the reflection coefficient $R=B_1/A_1$ for an area contraction with a 508 mm long extension tube attached, i.e., L=508 mm. It should be noted that a single value K_L was used to predict *R* for all frequencies. For reference, this figure also shows reflection coefficient measurements taken in an impedance tube. The details of these measurements will be discussed in Chapter 4.

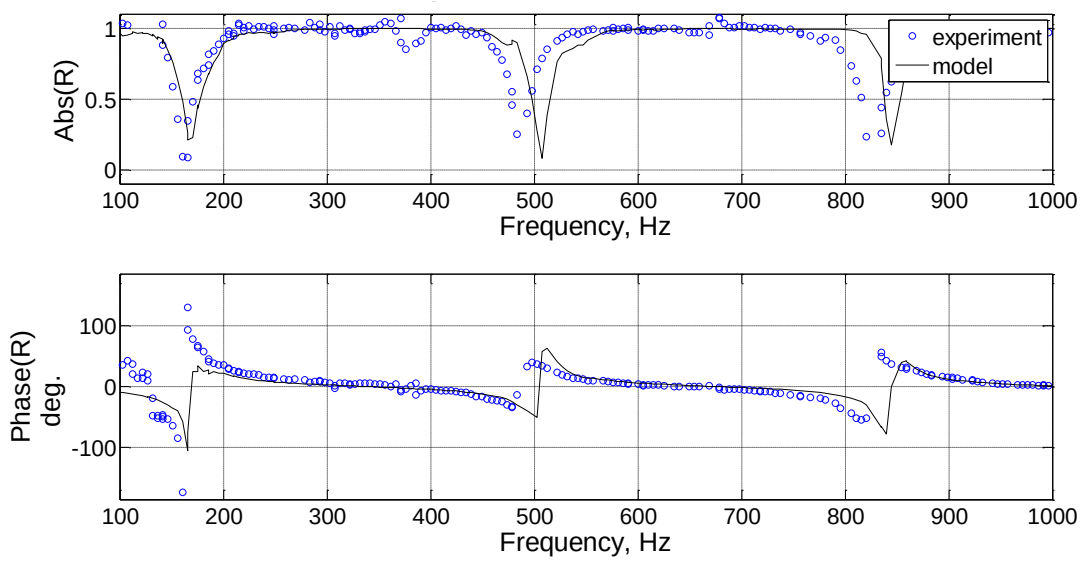

Figure 3.7: Comparison between model predictions and experimental measurements for the reflection coefficient of an abrupt area contraction.

Linear acoustics with zero losses predicts that R=1 everywhere, even at frequencies in the vicinity of resonance, while linear acoustic with losses due to mean flow rate would predict R<1 everywhere. It is interesting to note that the reflection coefficient was neither less than nor equal to one for all frequencies. The reason for this is that the extension tube forced a zero acoustic velocity boundary condition at x=L. Therefore, changing the frequency causes the location of the other acoustic velocity node(s) and anti-node(s) to shift. When the velocity node was at the location of the area change (x=0), the reflection coefficient tended to one. When the acoustic velocity was non-zero at the area change, the reflection coefficient deviated from one as shown in the figure.

Figure 3.7 shows that the absolute value of the reflection coefficient R was nearly one over most of the frequency spectrum, except for small frequency ranges where the acoustic velocity was relatively high in and around the location of the area change. This

indicates that the nonlinear losses were due to the high oscillating velocity amplitude that occurs near the quarter wave resonance frequencies of the extension tube.

3.6 Conclusions

This chapter presented the development of nonlinear acoustic impedance models for acoustically compact area contractions and expansions. These models captured the important trends and provided a convenient relationship for correlating experimental data. In addition, the developed models can be conveniently incorporated into acoustic network models. Finally, the development and predictions of an acoustic response model of an acoustic network containing an area contraction were presented.

Chapter 4:

Acoustic Response Measurements

4.1 Introduction and background

A theoretical model was presented in the previous chapter that relates the acoustic impedance of an acoustically compact area contraction to the steady flow velocity, the acoustic velocity amplitude, and the area ratio of the contraction. This chapter reports the experimental results of an investigation into the factors affecting the impedance of several types of acoustically compact elements that comprise the FST, some of which could not be easily modeled theoretically. These include area contractions, 'tee' junctions, gate valves, and area expansions. In particular, the nonlinear acoustic resistance of these elements was needed to develop an adequate acoustic response model of the FST.

This experimental study demonstrates that the developed model includes the necessary parameters to accurately predict or correlate the acoustic resistance of the FST components with acoustic velocity amplitude and validates the theoretical prediction that frequency should not play a role in the acoustic resistance. The influence of each of the parameters listed above on the acoustic resistance of the FST components was determined for a wide range of frequencies and acoustic pressure amplitudes. Previous studies on acoustic waves incident on orifices performed by Ingard et. al.[48,49], Cummings[50], Cummings and Eversman[51], Salikuddin[52], Salikuddin and Brown[53], Salikuddin and Ahuja[54], and others mentioned in Chapter 3 were used to gain insight into the physical mechanisms involved.

4.2 Study objectives

In this investigation, the nonlinear impedance of a number of different components of the FST was studied over a range of frequencies and acoustic velocity using a two-microphone impedance tube. In particular, this study experimentally determined the nonlinear acoustic impedance of five different diameter area contractions, an area expansion, an open-ended tube, and a variable area valve. In addition, the influence of high intensity sound waves on the reflection coefficient of various combinations of these elements was studied. In these studies, the reflection coefficient at the 'tee' junction of three ducts and the reflection coefficient of a combination of an area contraction followed by a variable area valve were measured. Although these measurements did not permit the direct measurement of the acoustic impedance of the individual elements of the system, they clearly demonstrate the inherent nonlinear behavior of the acoustic impedance of these components.

These studies differ from the previous studies in that (1) they were made in an acoustic impedance tube excited by a single-frequency, standing wave field rather than an inherently transient impulsive wave field and (2) these measurements were made over a large range of acoustic velocities. In addition, the previous studies limited their attention to thin orifices in high intensity sound fields situated in large diameter pipes. Therefore, the effects of the area contraction and expansion on the acoustic impedance of the orifice could not be studied separately, and the flow field created by the sudden contraction influenced the flow field of the sudden area expansion and vice versa. In this study, the effects of the area contraction and area expansion were studied separately. For example, the abrupt area contraction was followed by a length of tubing having the same diameter as the opening (see Figure 4.6) so that the nonlinear impedance of the area contraction alone could be measured.

In all of these studies, the emphasis was placed on the nonlinear *real* part of the acoustic impedance, i.e., acoustic resistance, of these various elements. Their imaginary parts were assumed small due to the fact that each of these elements was acoustically compact, i.e., their physical dimensions were small compared with an acoustic wavelength. In addition, based on the theoretical results, nonlinear effects were not expected to significantly affect the imaginary part of the acoustic impedance.

The focus of this study was on measuring the impedance of these elements under conditions similar to those in an acoustically unstable combustion system. Therefore, the acoustic pressure amplitude in this investigation was higher than those used in most of the previous studies, close to the acoustic pressure amplitude in unstable combustors.

First, this chapter presents the development of a two-microphone impedance tube used to measure the nonlinear acoustic impedance of area contractions, 'tees', and valves. This is followed by a discussion of the nonlinear acoustic resistance measurements of the FST elements. Then, experimental measurements of the frequency response of some simple systems incorporating the FST elements are presented. And, finally, frequency response measurements of the FST itself are discussed.

4.3 Two-microphone impedance tube

To meet the goals of this study, a reliable acoustic frequency response model for the FST was needed. To test the predictions of this model, it was necessary to measure the acoustic impedance of several elements of the FST (e.g., area changes, valves, and "tee" junctions). Also, measurements of the input acoustic impedance of the FST (as a unit) were required to validate the predictions of the overall FST frequency response model. Consequently, a system for measuring the acoustic response of these elements had to be developed.

Acoustic impedances can be measured using, e.g., (1) the two-microphone technique, (2) the probe tube technique of measuring the standing wave ratio, and (3) the direct measurement technique using a microphone and a hot-wire anemometer. In this study, an impedance tube employing the two-microphone technique was used.

Figure 4.1 shows a schematic of the two-microphone impedance tube developed for this study. Pressure oscillations of known frequency were generated using two speakers attached to the side wall of the tube about 10 tube diameters from the location of the investigated impedance. According to the technique, the pressure amplitude was measured at two locations L_1 and L_2, each a known distance from the measured impedance location and from each other.

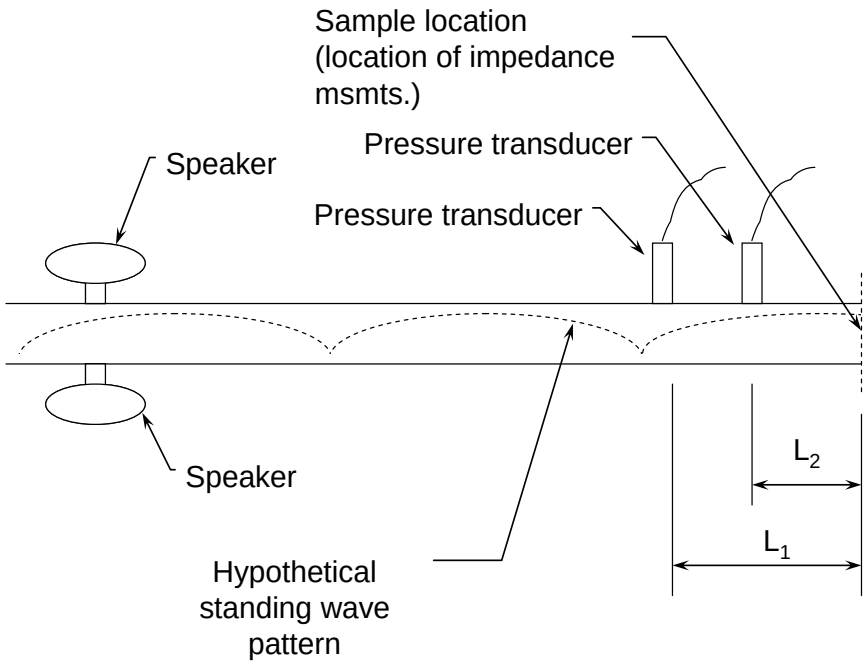

Figure 4.1: Impedance tube schematic.

An expression for the complex reflection coefficient $\hat{R}$ was obtained assuming no losses, plain wave oscillations, non-zero steady flow and linear acoustics (see Munjal[55] for a slightly different form of the equation, also Chung and Blaser[56]) as follows:

$$\hat{R} = \frac{P_{reflected}}{P_{incident}} = \frac{\frac{P_1}{P_2} e^{ik_f L_2} - e^{ik_f L_1}}{e^{-ik_r L_1} - \frac{P_1}{P_2} e^{-ik_r L_2}}, \tag{4.1}$$

where the wavenumber in the positive *x*-direction was given by

$$k_f = \frac{\omega}{c - u} \tag{4.2}$$

and in the negative *x*-direction by

$$k_r = \frac{\omega}{c + u}. \tag{4.3}$$

P_1 and P_2, c, and u are the complex amplitudes, sound speed, and steady flow velocity, respectively. The complex acoustic impedance $\hat{Z}$ in terms of the complex reflection coefficient $\hat{R}$, the density ρ and the sound speed c is given by[57]

$$\hat{Z} = \rho c \frac{1+\hat{R}}{1-\hat{R}}. \tag{4.4}$$

Since the frequency range of longitudinal combustion instabilities in most gas turbine engines is between 100 Hz and 1000 Hz, the tube was designed to accurately measure reflection coefficients at these frequencies. The impedance tube was tunable to maintain a high level of acoustic pressure at the measurement location.

Because the measurement of the reflection coefficient is based on the difference in amplitude and phase of the pressure signals at locations 1 and 2, each pressure transducer was calibrated against a known standard. Although the data is not presented here for brevity, measurements of the reflection coefficients of a rigidly terminated pipe and an open-ended pipe compared favorably with well-known theoretical results.

The error associated with measuring the reflection coefficient of a given end-termination depends on the error associated with measuring several variables. These variables include the ratio of the two measured complex pressures, the frequency, and the microphone spacing. Assuming that the errors associated with measuring these parameters were fixed, the allowable error in reflection coefficient would then determine the practical frequency range of the impedance tube. Of course, this usable frequency range could be shifted or extended by altering the absolute spacing between microphones.

The purpose of the following analysis was to determine analytically the sensitivity of the calculated reflection coefficient of a given end-termination to errors in the above discussed measurements. Using this information, an estimate of the error associated

with calculating the reflection coefficient of a given end-termination was obtained as a function of frequency. This error estimate was then used to determine the usable frequency range of the impedance tube for a given microphone spacing.

The total error associated with measuring the reflection coefficient was obtained by taking the total differential of the reflection coefficient as follows, assuming that the error in measuring the microphone locations was negligible. The total error is given by

$$E_R = \underbrace{\frac{d\hat{R}}{dk}\delta k}_{\substack{\text{Error in reflection coefficient due to error in measuring the wavenumber.}}} + \underbrace{\frac{d\hat{R}}{dP_R}\delta P_R}_{\substack{\text{Error in reflection coefficient due to error in measuring the complex pressure ratio.}}} . \qquad (4.5)$$

The $\hat{R}$ derivatives in the above equation were obtained by differentiating Eq. (4.1) and the variables δk and δP_R are estimates of the error in measuring the frequency and complex pressure ratio, respectively. Differentiating Eq. (4.1) yields the following expressions for the first and second terms on the right side of Eq. (4.5):

$$E_R = \left[\frac{i\left(L_1 \cdot e^{ikL_1} - L_2 \cdot P_R \cdot e^{ikL_2}\right)}{P_R \cdot e^{-ikL_2} - e^{-ikL_1}} + \frac{i\left(e^{ikL_1} - P_R \cdot e^{ikL_2}\right)\left(L_2 \cdot P_R \cdot e^{-ikL_2} - L_1 \cdot e^{-ikL_1}\right)}{\left(P_R \cdot e^{-ikL_2} - e^{-ikL_1}\right)^2} \right] \delta k \qquad (4.6)$$

and

$$E_R = \left[\frac{-e^{ikL_2}}{P_R \cdot e^{-ikL_2} - e^{-ikL_1}} - \frac{\left(e^{ikL_1} - P_R \cdot e^{ikL_2}\right)\left(e^{-ikL_2}\right)}{\left(P_R \cdot e^{-ikL_2} - e^{-ikL_1}\right)^2} \right] \delta P_R . \qquad (4.7)$$

These two “error terms” were then summed to obtain an estimate of the combined error in calculated reflection coefficient assuming a certain error in measuring the frequency and complex pressure ratio as a function of frequency and pressure ratio for a given end-termination. The error estimate given by this sum is complex. The

absolute value of this error represents the error in the magnitude of the reflection coefficient, and the angle represents the error in the phase of the reflection coefficient.

To obtain a bound for the total error, three end condition reflection coefficients were considered: $\left|\hat{R}\right| = 0,\ 1,\ and\ -1$. The results of these calculations are shown in Figure 4.2 and Figure 4.3 for two different microphone spacings. The error in the phase of the reflection coefficient is constant across the entire range of frequencies for a given microphone spacing for $\hat{R} = 1$ and $\hat{R} = -1$ and is a linear function of frequency for $\hat{R} = 0$. Since these results were not helpful in determining the useable frequency range of the impedance tube, only the results for the magnitude of the reflection coefficient are shown below.

Figure 4.2 shows a plot of the absolute value of the reflection coefficient error for a microphone spacing of $L_1 = 25.4\ \text{mm}$ and $L_2 = 101.6\ \text{mm}$ and an error in measuring the complex pressure ratio and frequency of 1%. If the allowable reflection coefficient error was assumed to be 10%, the lowest allowable measurement frequency for assumed $\hat{R} = 1$ was found to be about 200 Hz and the highest was well beyond the frequency of interest for this study. For $\hat{R} = -1$, the lower frequency was about 150 Hz. For $\hat{R} = 0$, the estimated error was lower than the allowable error for all frequencies of interest.

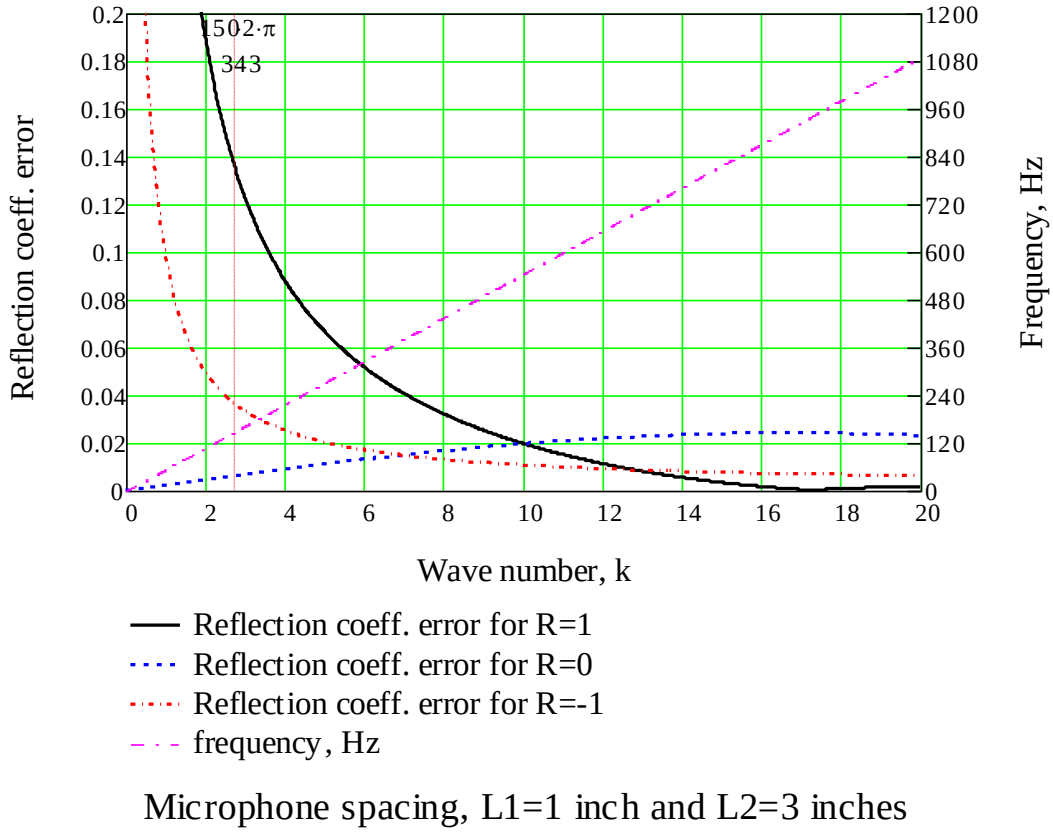

Figure 4.2: Refection coefficient error for various end conditions as a function of wavenumber for a microphone spacing of 2 inches.

Figure 4.3 shows a similar plot for microphones located 25.4 and 254 mm, respectively, from the impedance measurement location. This microphone arrangement extended the lower usable frequency to below 100 Hz for all cases, but the error for higher frequencies increased to an unacceptable level. In fact, the highest usable frequency for an allowable error of 5% was reduced to 750 Hz, which was far below the desired upper measurement frequency.

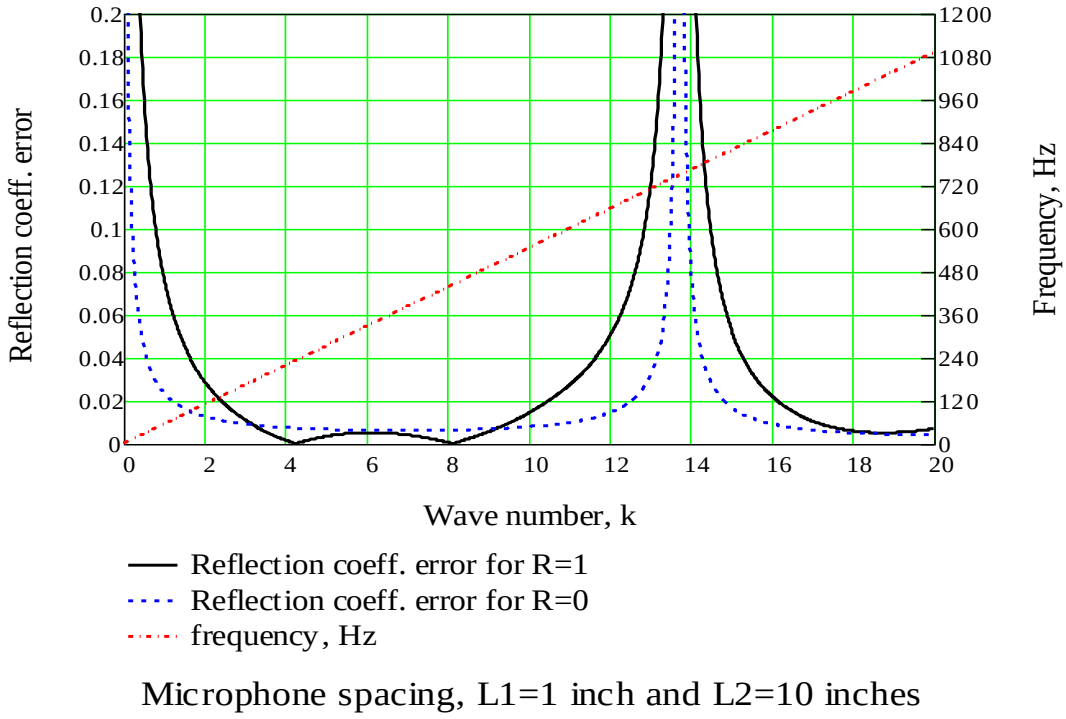

Figure 4.3: Reflection coefficient error for various end conditions as a function of wavenumber for a microphone spacing of 9 inches.

Guided by these results, microphones positioned 25.4 and 75.2 mm, respectively, from the impedance measurement location were used for all measurements discussed in the following sections. A final note regarding the two-microphone method is that the method is not to be used at or near the resonant frequencies of the system.[58] The method is singular at the resonant frequency, and the error in the two-microphone method increases dramatically near the resonances.

The FST described in Chapter 1 was made up of a number of compact acoustic piping elements, e.g., 'tee's, valves, area expansions, and area contractions. In order to develop an accurate model of the acoustic response of the FST, sufficiently accurate models for each of these subcomponents were needed. In order to validate these models, measurements of the acoustic reflection coefficient for each of these subcomponents were required.

A simple study was conducted to verify that the impedance tube measurements were consistent with the known impedance of a rigidly-terminated length of tubing. A schematic of the system measured is shown in Figure 4.4. In this case, the length of the tube L was 247.7 mm.

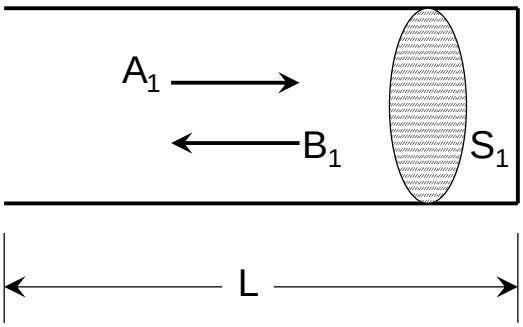

Figure 4.4: Rigidly-terminated tube of length L.

Measurements of the reflection coefficient for this case are shown as the circles (o) in the magnitude and phase plots in Figure 4.5. The reflection coefficient predicted from purely linear acoustic analysis was one for all frequencies and is shown in the figure as the solid line. The phase predicted from linear analysis was given by $\tan(kL)$, which is shown as the solid line in the phase plot of Figure 4.5.

For frequencies greater than 150 Hz, the measurements agreed well with the predictions from linear acoustics. However, there was some loss of acoustic energy at the higher frequencies presumably due to wall radiation from the thin-walled tube. At frequencies lower than 150 Hz, the deviation was larger and was not attributable to wall radiation. As discussed above, these errors were most probably due to the close proximity of the microphones in the impedance tube.

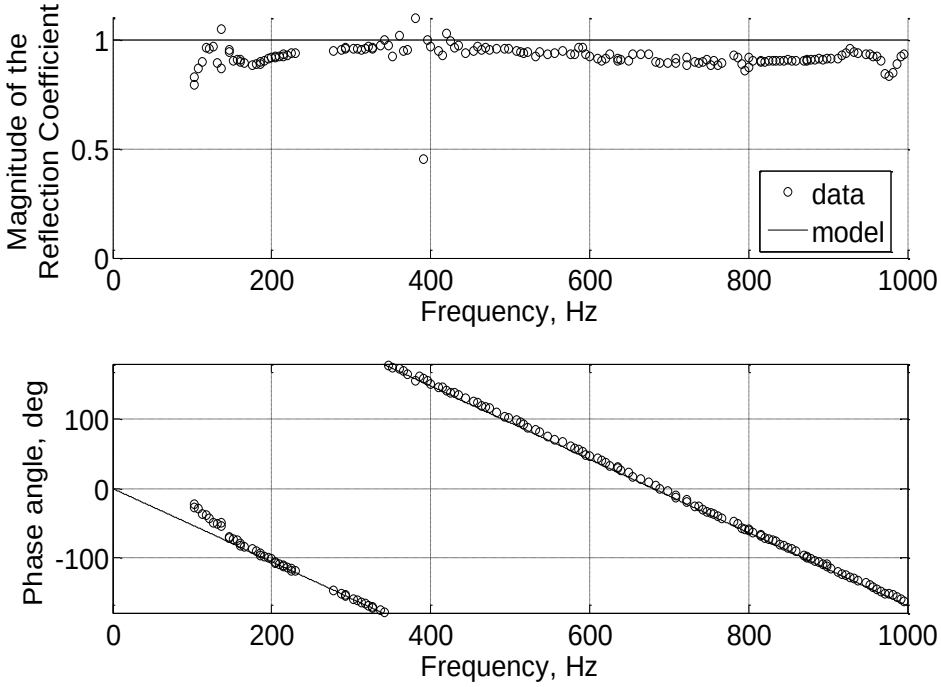

Figure 4.5: Magnitude and phase of the reflection coefficient of a rigidly-terminated tube of length L.

In all, these measurements show that the impedance tube performed quite well in the frequency range of interest. Therefore, the system was used to measure the impedance of the elements of the FST. The next chapter presents the results of these measurements.

4.4 Background on area contraction studies

The simple, abrupt area contraction was considered first because it is one of the simplest of all of the acoustical elements considered here and lends itself well to theoretical study. Further, the area contraction is a common element in many acoustical duct systems and is an element of the FST.

The system studied is shown in Figure 4.6. The acoustic forcing originates far to the left of the location marked *x=0* in the figure. There was a sudden contraction from the larger diameter pipe to the smaller diameter tube at the location *x=0*, followed by a length of tubing terminated by a rigid wall at the location marked end location.

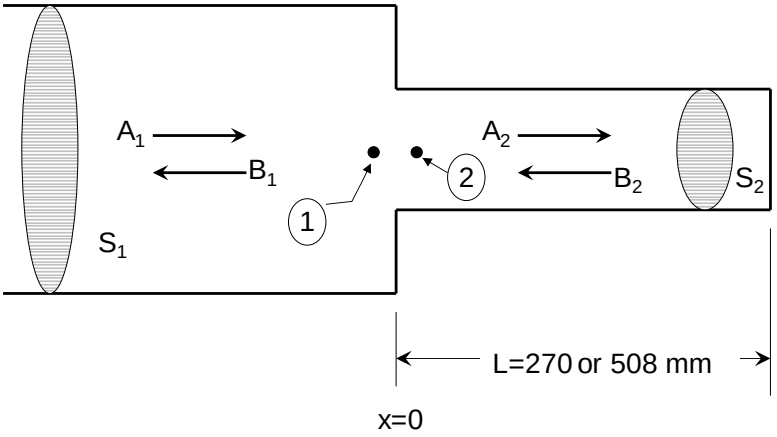

Figure 4.6: System including a rigid termination preceded by a sudden area change.

In the interpretation of the measurements, a few points from linear acoustic theory were considered. First, linear acoustics tells us that in the absence of damping, the impedance will be purely imaginary and the magnitude of the reflection coefficient measured at any point in the system will be one because in the absence of dissipation of acoustic energy, all of the incident acoustic energy entering must be reflected. If any sort of acoustic loss mechanism is present within the duct, the impedance will have a real and imaginary component and the magnitude of the reflection coefficient will be

smaller than one. When the reflection coefficient is zero, all of the energy entering the plane of measurement leaves the system completely.

Next, linear acoustic theory tells us that in the absence of damping the phase of the impedance measured just upstream of the area contraction must be $\pm\pi/2$. This is because the acoustic pressure and velocity must always be 90 degrees out of phase with each other for the power dissipation to be zero. If damping is present in the system, the phase between the acoustic pressure and velocity will shift toward zero degrees depending on the amount of damping in the system. In this case, one may think of a system of forward and reverse traveling waves, which carry no energy into or out of the system and a third traveling wave that carries acoustic energy out of the system.

As an example, Figure 4.7 shows a plot of the frequency dependence of amplitude and phase of the measured reflection coefficient of an area contraction system. In this case, the larger diameter tube was 50.8 mm, the smaller diameter tube was 14 mm, and the length of the small diameter tube was 508 mm. For a system with no losses, the magnitude of the reflection coefficient is expected to be one over large ranges of frequency. It can be clearly seen from this figure that the reflection coefficient deviated significantly from unity for large portions of the spectrum. This deviation indicates that a significant loss of acoustic energy occurred within this system, presumably at the area reduction since there were no losses in the rest of the system, assuming that viscous losses and wall radiation is neglected. Also, the fact that the magnitude of the reflection coefficient did not vary monotonically with frequency indicates that the reflection coefficient was dependent on the variation of some acoustic variable other than frequency, i.e., acoustic pressure or velocity amplitude. The observed behavior of the reflection coefficient was due to the frequency dependence of

the acoustic pressure and velocity fields.

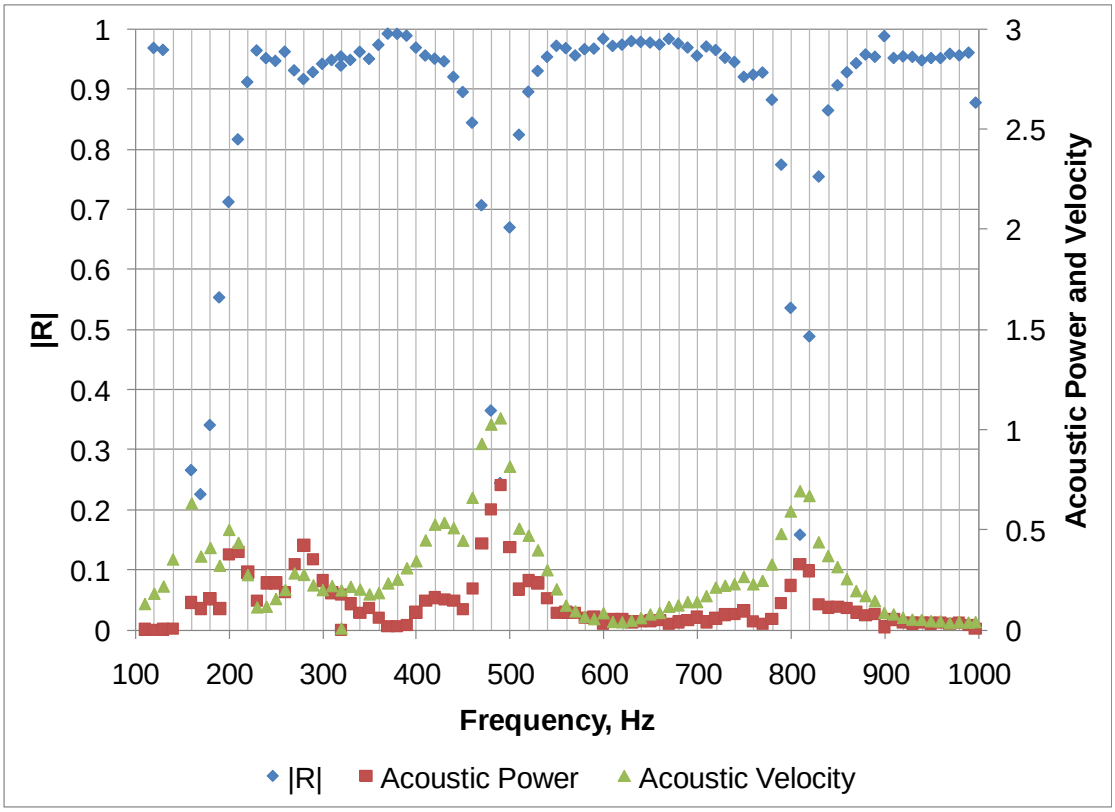

Figure 4.7: Magnitude of the reflection coefficient, acoustic power, and acoustic velocity amplitude vs. Frequency for the system shown in Figure 4.4 with a 508 mm extension tube.

Figure 4.8 shows a plot of the acoustic pressure, velocity, and power dissipation measured at location 1 for the area contraction system. Due to the acoustical properties of the system, the pressure and velocity amplitudes varied significantly over the range frequencies tested. For the 508 mm tube length, pressure anti-nodes occurred at the location of the area change at the following frequencies: 322, 645, and 965 Hz. Also, velocity anti-nodes occur at the area change for the following frequencies: 161, 482, and 804 Hz. When pressure anti-nodes occur at the area change, the velocity was low, as can be seen from the figure. Therefore, losses due to velocity oscillations at these frequencies were expected to be low.

This is also indicated in Figure 4.7 by the fact that the $|\hat{R}|$ was very nearly equal to one at these frequencies. However, at the frequencies for which velocity anti-nodes occur at the area change, losses due to velocity oscillations were high. For these frequencies, the $|\hat{R}|$ was low and the acoustic velocity and the power dissipation were both high.

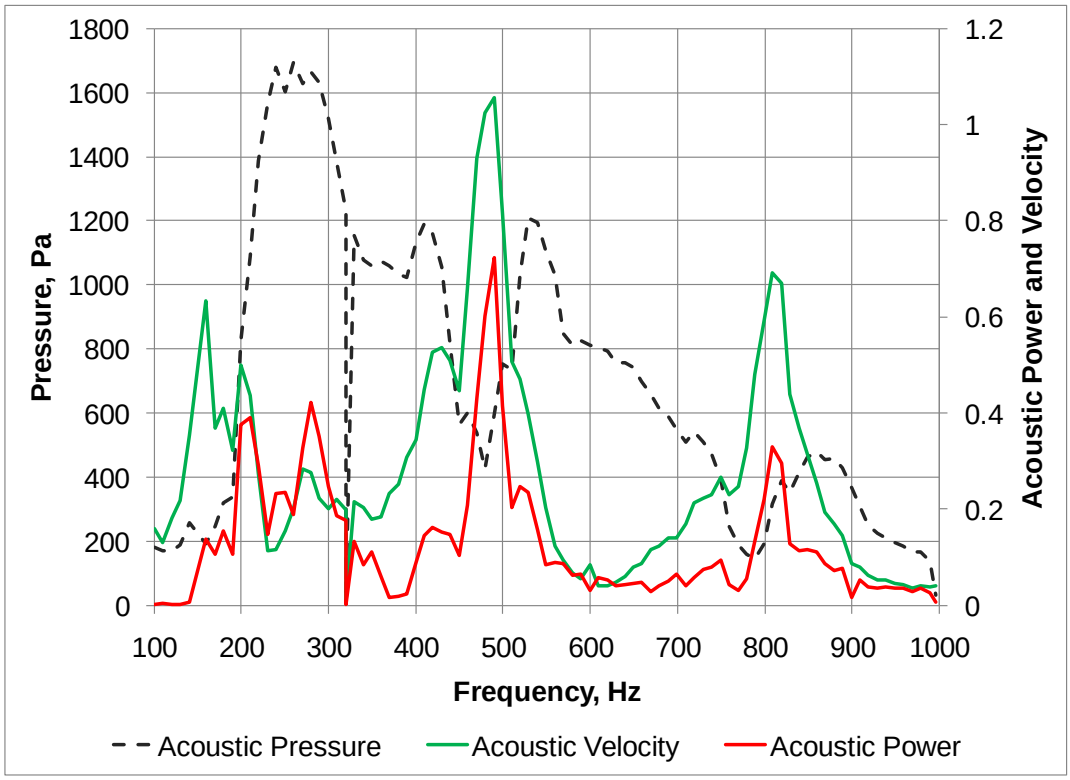

Figure 4.8: Pressure, power dissipation, and velocity amplitude vs. Frequency for the system shown in Figure 4.4 with a 508 mm extension tube.

The frequency dependence observed in Figure 4.7 was not due to frequency dependence of the impedance of the area change itself, which was acoustically compact. It was due to the fact that the acoustic impedance of the area change was sensitive to the magnitude of the acoustic velocity oscillations. At certain frequencies, the velocity anti-node was situated at the location of the area change. At other frequencies, the velocity node was situated there. The specific frequencies at which this

occurred was due entirely to the acoustical properties of the extension tube, in this case, its length.

Returning to Figure 4.7, when $\left|\hat{R}\right|$ approached zero, there was no wave reflected from the area discontinuity. This means that all of the acoustic energy impinging on the area discontinuity passed out of the system without reflection. This is shown in the acoustic power plot in Figure 4.7. Whenever the reflection coefficient was low, i.e., approaching zero, the acoustic power dissipation was high. This is because the real part of the impedance of the area change increased as discussed in Chapter 3.

Whenever the magnitude of the reflection coefficient was zero, no resonance occurred in either the extension tube or in the impedance tube. This explains why the pressure amplitude at location 1 was low at the corresponding frequencies. It is consistent with acoustic theory to expect the pressure amplitude to be low when there is no feedback from a reflected wave. However, when the reflection coefficient is near one, no acoustic energy was lost. For these frequencies, the pressure amplitude was high, as expected.

For an extension tube of length L, there exist two sets of critical frequencies. The first set corresponds to cases where there was a pressure anti-node at both ends of the extension tube. This occurred when the driving frequency was

$$f = \frac{nc}{2L} \text{ where n=0, 1, 2, 3, } \cdots \qquad (4.8)$$

For the 508 mm extension tube, these frequencies were: 0, 322, 643, and 965 Hz. Figure 4.8 shows that at these frequencies the pressure amplitude at the area change was quite high while the velocity amplitude was rather low. At these frequencies, the impedance of the area change tends toward infinity because the velocity amplitude was nearly zero and the pressure amplitude was high.

Because of the very low acoustic velocity at the frequencies of 322, 643, and 965 Hz, they were not suitable frequencies for obtaining good measurements of the impedance of the area change. As mentioned in Chapter 4, the error in measuring the impedance using the two-microphone method grows rapidly near resonances of the system. Better impedance measurements can be obtained when the velocity anti-node occurs at the area change, i.e., locations of high acoustic power dissipation.

At these frequencies, the velocity amplitude was high, and the pressure amplitude was also nonzero. When the real part of the impedance was low, the phase between the pressure and velocity was very nearly 90 degrees. Therefore, the velocity must be nearly zero whenever the pressure was near a maximum. However, the presence of damping causes the phase between the pressure and velocity to be somewhat less than 90 degrees.

In the presence of damping, the pressure amplitude can be nonzero when the velocity amplitude was near a maximum. This is also seen from Figure 4.2, which shows that the error in measuring the reflection coefficient was smaller when the reflection coefficient tended toward zero than when it was nearly one.

The other set of critical frequencies correspond to cases where there was a velocity anti-node at the area change. This situation occurs when the driving frequency was

$$f = \frac{(1+2n)c}{4L} \text{ where n=0, 1, 2, 3, } \cdots \qquad (4.9)$$

For the 508 mm extension tube, these frequencies were 161, 482, and 804 Hz. Figure 4.8 shows that at these frequencies the velocity amplitude was high. Figure 4.7 shows that the reflection coefficient was low at these frequencies indicating that the impedance of the area change was sensitive to the high velocity oscillations at the area change.

Figure 4.8 shows that there is significant power dissipation at the frequencies 160, 480, and 800 Hz while the power is nearly zero at the frequencies given above. The reason for this is that, as discussed in Chapter 3, there is no acoustic power dissipation when the real part of the impedance is equal to zero. Therefore, locations of high power dissipation are locations where the real part of the impedance is also high.

A brief second example demonstrates the effect of changing the length of the extension tube from 508 mm to 270 mm. For this new extension tube length, the critical frequency between 0 and 1000 Hz for the pressure anti-node case was 635 Hz, and for the velocity anti-node case the critical frequency was 318 Hz. Therefore, the resistance of the area contraction was expected to be large at 318 Hz. Also, measurements near 635 Hz were disregarded due to the large measurement errors near resonance.

Figure 4.9 shows the results of these measurements. Clearly, the area change reflection coefficient was low whenever the acoustic velocity at the area change was high resulting in high power dissipation at these frequencies. This figure also shows that the reflection coefficient was nearly one at the frequency of 635 Hz, which corresponds to the case where the pressure anti-node was situated at the area change. This is another indication that the impedance of the area change was not affected by pressure oscillation amplitude but by high acoustic velocity oscillations as at 310 Hz.

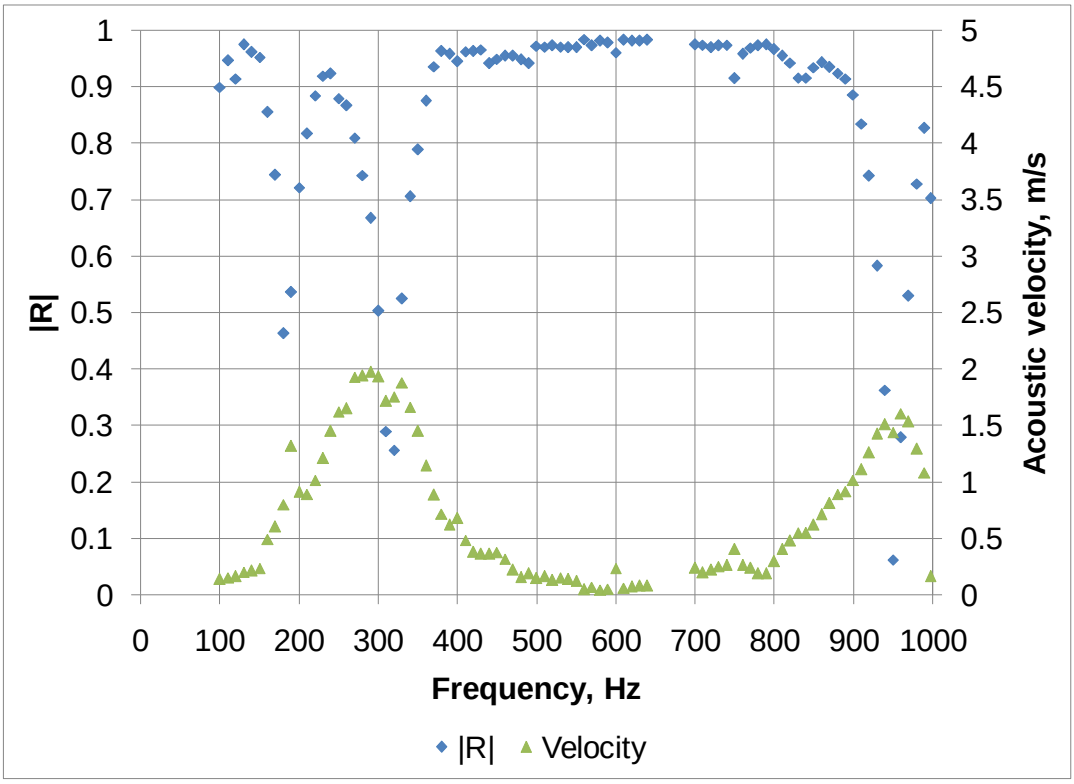

Figure 4.9: Magnitude of the reflection coefficient and acoustic velocity amplitude vs Frequency for an area change at the junction of a 50.8 mm to 14 mm diameter reduction with an extension tube of length 270 mm (see Figure 4.4).

4.5 Impedance subtraction technique

As noted, the reflection coefficient measured at location 1 in Figure 4.6 includes not only the effects of the abrupt area change but also the purely reactive response of the rigidly-terminated tube beyond that location. Since the impedance of the area change alone was desired, some method for removing the effect of the length of the tube was needed. Since the area change and tube were acoustically in series with one another, the impedance of the tube measured at location 2 just downstream of the area change could be subtracted from the impedance measured at location 1 just upstream of the area change.

The acoustic impedance of the rigidly terminated extension tube of length L_{ET}, assuming linear plane wave propagation in the tube, is given by

$$Z_{ET} = \frac{(\rho c)_{ET}}{S_{ET}} \frac{\left(1+e^{2ikL_{ET}}\right)}{\left(1-e^{2ikL_{ET}}\right)}. \tag{4.10}$$

The impedance of the entire system, which includes both the area contraction and the extension tube, Z_{system} was obtained from measurements in the impedance tube. The impedance of the area change $Z_{\delta A}$ was found by subtracting the impedance of the extension tube Z_{ET} from the impedance of the entire system Z_{system}. This gives the following expression for the impedance of the area change:

$$Z_{\delta A} = \frac{p'S}{(\rho c)U'} = \frac{S}{(\rho c)}\left(Z_{system} - Z_{ET}\right). \tag{4.11}$$

Figure 4.10 shows the magnitude of the area change impedance $Z_{\delta A}$ for the system with the 508 mm long extension tube. The real and imaginary parts of $Z_{\delta A}$ clearly vary significantly with frequency but not monotonically as would be the case if

$Z_{\delta A}$ were dependent on frequency. As should be the case, the real part of the impedance was nearly zero near the frequencies where the velocity amplitude at the area change was very low.

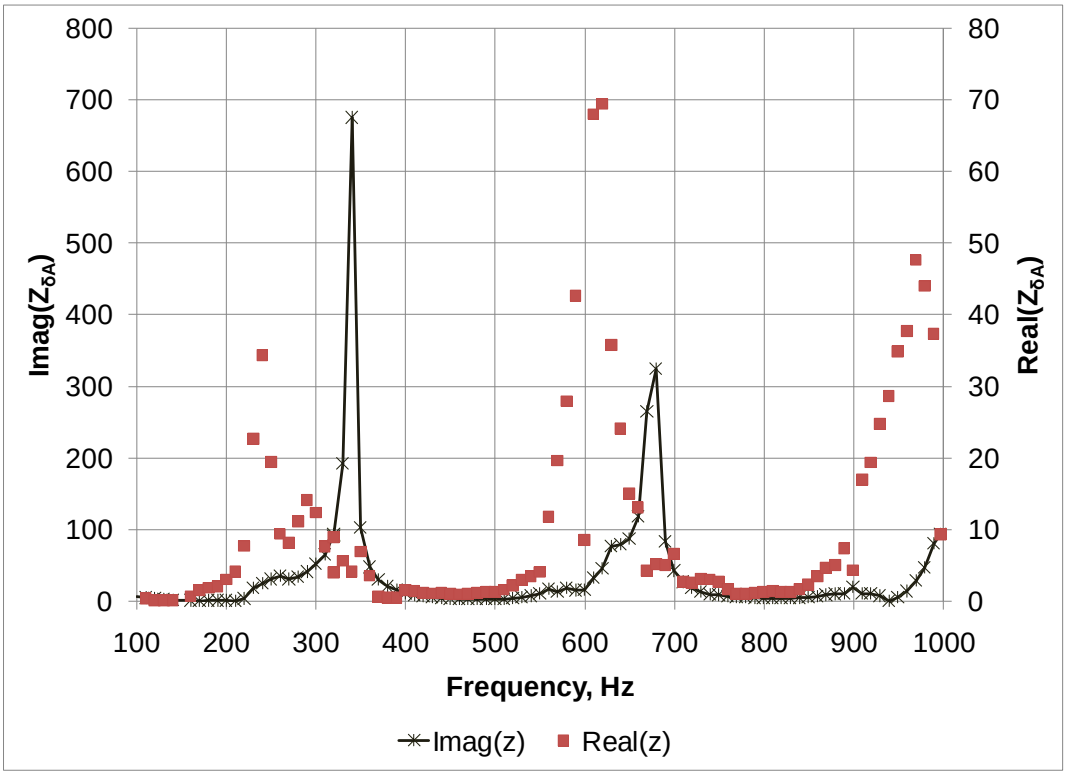

Figure 4.10: Impedance of the area change obtained by the impedance subtraction technique.

As described above, the spikes in the both the real and imaginary parts of the acoustic impedance of the area change were expected for frequencies where the velocity node occurs at the area change. For this reason, as well as the other stated previously, these are poor frequencies for determining the impedance of the area change. Instead, it is better to determine the impedance of the area change at frequencies for which the velocity anti-node was at the location of the area change.

It is important to understand that, assuming small wall radiation and viscous effects, the acoustic field in the extension tube downstream of the area contraction is linear and lossless and that the measured real part of the impedance of the area

contraction is independent of the impedance of the extension tube. This is not the case, however, for the imaginary part.

4.6 Effective length, loss coefficient, and discharge coefficient calculations

The theory developed in Chapter 3 utilized a loss coefficient K_L, an effective length L_{eff}, and a discharge coefficient C_D. These quantities can be determined from further analysis or from experimental measurements. This section presents a method for determining the values of these parameters from impedance tube measurements using the theory developed in Chapter 3.

Equation (3.14) defines the real part of the area change impedance as

$$Z_{real} = \frac{(\rho c)_{IT}}{S_{IT}} \frac{\left(u + \frac{|u'|}{2}\right)}{c} \left[\left(\frac{S_{IT}}{S_{ext}} \right)^2 + K_L - 1 \right], \tag{4.12}$$

where Z_{real} was obtained from impedance tube measurements as described above using the impedance subtraction technique. Solving Eq. (4.12) for K_L leads to the following expression for the loss coefficient

$$K_L = \frac{Z_{real} S_{IT}}{(\rho c)_{IT}} \frac{c}{\left(u + \frac{|u'|}{2}\right)} - \left[\left(\frac{S_{IT}}{S_{ext}} \right)^2 - 1 \right]. \tag{4.13}$$

Positive values of K_L represent an increase in the apparent area ratio while negative values represent a decrease in the apparent area ratio. In the event that the magnitude of Z_{real} was greater than zero when the acoustic velocity was near zero, this value must be subtracted from Z_{real} prior to applying Eq. (4.13). Also, computed values of K_L near

zero acoustic velocities may result in erroneous values of K_L due to the difficulty in measuring the impedance at very low acoustic pressure amplitudes and, hence, acoustic velocities.

Equation (3.14) can also be used to define the imaginary part of the area change impedance as

$$Z_{imag} = \frac{(\rho c)_{IT} kL_{eff}}{S_{IT}}, \tag{4.14}$$

where Z_{imag} was obtained from impedance tube measurements as well. Solving Eq. (4.14) for L_{eff} leads to the following expression for the effective length

$$L_{eff} = \frac{Z_{imag} S_{IT}}{(\rho c)_{IT} k}. \tag{4.15}$$

However, this expression for L_{eff} is based on calculating the impedance of the area change using the acoustic velocity in the larger 50.8 mm tube. By convention, the effective length is computed using the impedance calculated from the pressure and acoustic velocity in the smaller duct. This was done by multiplying Eq. (4.15) by the area ratio so that Eq. (4.15) becomes

$$L_{eff} = \frac{Z_{imag} S_{IT}}{(\rho c)_{IT} k}\left(\frac{S_{ext}}{S_{IT}}\right). \tag{4.16}$$

Equation (3.16) was used to obtain an expression for the discharge coefficient, which was

$$C_D = \frac{S_{eff}}{S_{IT}} = \sqrt{\frac{1}{\frac{2\xi c}{|u'_{IT}|} + 1}}. \tag{4.17}$$

In this case as in calculating K_L any “linear” losses must be subtracted from the measured impedance prior to calculating C_D.

Using Eqs. (4.13) and (4.15), the effective length and loss coefficients were computed for the system shown in Figure 4.6 (with the 270 mm extension tube attached) and were based on the impedance tube measurements at 310 Hz for a range of acoustic forcing amplitudes. Figure 4.11 shows the results of these calculations for all three tests as a function of the Reynolds' number of the area change based on the diameter difference between the 50.8 mm tube and the 14 mm tube. Both the effective length and loss coefficient were constant across the range of acoustic Reynolds' numbers tested.

The value of the effective length obtained using this method differs from that predicted using the linear theory for acoustic radiation for a flanged, open-ended pipe, which is

$$L_{eff} = \left(\frac{8}{3\pi} \right) \frac{d_{ext}}{2} . \qquad (4.18)$$

L_{eff} computed from Eq. (4.18) for $d_{ext} = 14$ mm at a frequency of 310 Hz was about 6 mm. (The result for an unflanged pipe was 3.8 mm or 0.15 inches.) The overall average effective length across all three test runs and all acoustic velocities was 1.4 mm (0.055 inches). However, it showed quite a bit of variation with acoustic velocity but was quite repeatable.

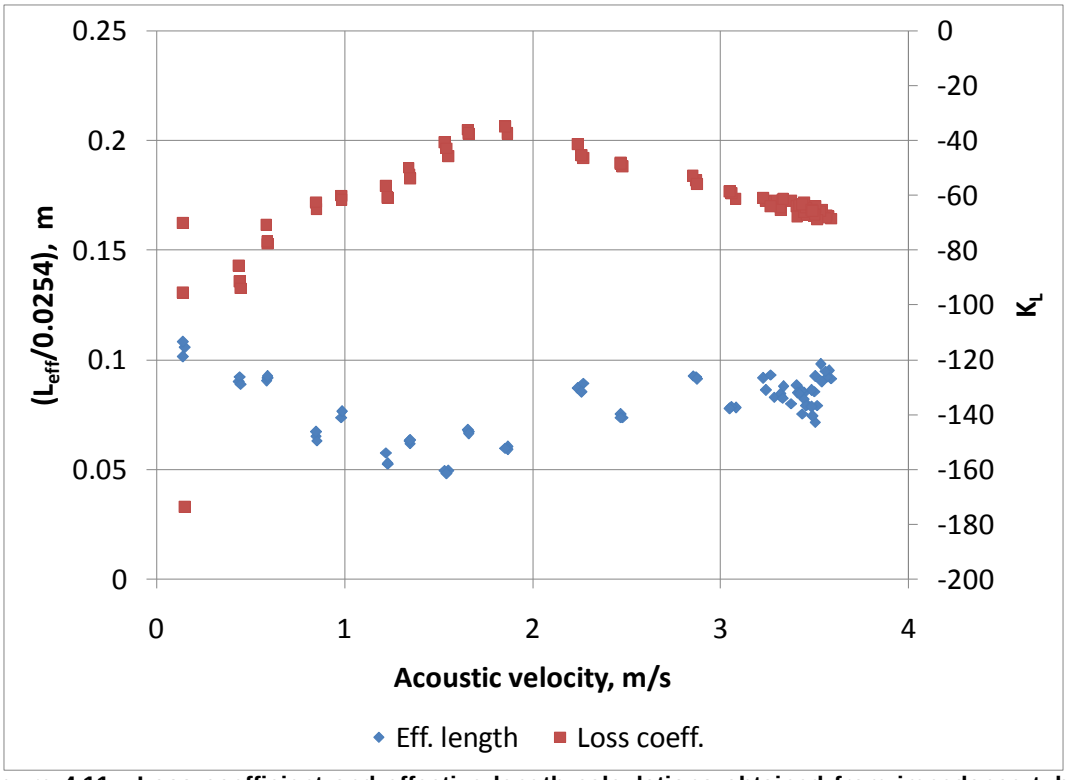

Figure 4.11: Loss coefficient and effective length calculations obtained from impedance tube measurements after applying the impedance subtraction technique.

The loss coefficient K_L for this case at low velocities was quite large being of the same order of magnitude as the area ratio squared, which equals 256. In this case, K_L increases until the acoustic velocity is about 2 m/s at which point it begins to decrease. At low acoustic velocities, the effect of K_L is to increase the sensitivity of impedance of the area change to acoustic velocity oscillations. At high acoustic velocities, the effect of K_L is to decrease this sensitivity.

Figure 4.12 shows the dependence of the discharge coefficient calculated from impedance tube data on the acoustic velocity amplitude at the area change. Clearly, the discharge coefficient varies significantly over the entire range of acoustic velocities measured. At low acoustic velocities this variation is very rapid, but at higher acoustic velocities the slope of the discharge coefficient curve drops significantly to a nearly

constant value. It does appear that the discharge coefficient becomes linear for acoustic velocities greater than 2 m/s. However, this figure indicates that the effective area of the area reduction was a strong function of the acoustic velocity.

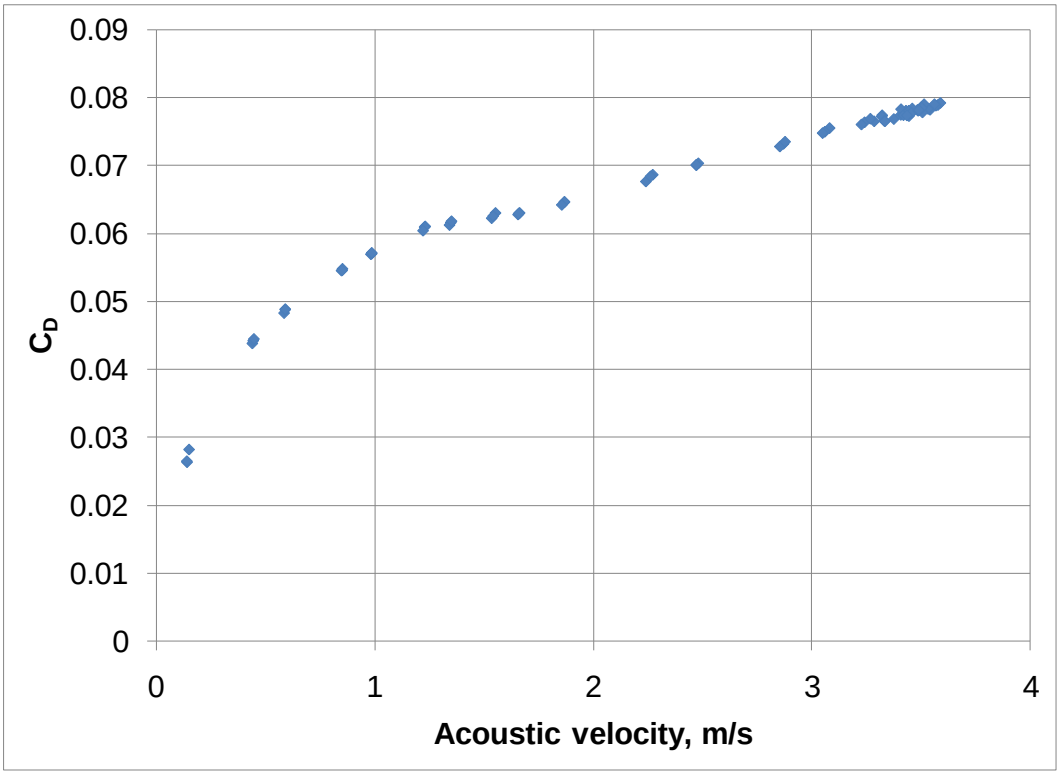

Figure 4.12: Discharge coefficient vs. Acoustic velocity calculated from impedance tube measurements after applying the impedance subtraction technique.

In this section, the acoustic impedance of the area contraction was shown to depend entirely on the amplitude of the acoustic velocity at the area contraction. The amplitude of the acoustic velocity and, therefore, the acoustic impedance, was shown to be high at certain frequencies. These frequencies were dependent on the acoustic properties of the extension tube. Finally, a method for calculating the loss coefficient, effective length, and discharge coefficient was presented. The next section presents measurements of the effect of high amplitude acoustic oscillations on the reflection coefficient and acoustic impedance of area contractions having different extension tube lengths and contraction ratios.

4.7 The nonlinear acoustic resistance of an area change

The acoustic response of an abrupt, i.e., acoustically compact, area change was needed to develop a model for the various components of the FST and the combustor itself. The model developed in Chapter 3 was used to help interpret the experimental data, and the experimental data was used to discover the limitations and shortcomings of the developed model. Experimental measurements were made for a number of different contraction ratios, extension tube lengths, frequencies, and forcing amplitudes. For future reference, the contraction ratio is defined as the ratio of the area of the larger diameter pipe to the area of the smaller diameter pipe.

In order to study the effect of varying the area ratio of the contraction shown in Figure 4.6, the following procedure was followed. First, extension tubes having diameters of 9.5 mm, 14 mm, 19 mm, and 25.4 mm were each attached to the impedance tube. Then, measurements of the impedance of the system were made for a range of frequencies to determine the response of the system over the entire spectral range of interest. Finally, measurements were made at a single critical frequency to examine the effect of varying the acoustic velocity while holding the frequency constant. When appropriate, the impedance subtraction technique was used to “remove” the effect of the 270 mm long tube extension and to calculate the impedance of the area change for each of these diameters.

The acoustic impedance depends on the acoustic velocity and the gas density. Further, the exact dependence of the nonlinear losses on the acoustic velocity was expected to be a function of the geometry of the area contraction, in particular the area or diameter ratio. The non-dimensional parameter relating these quantities is the acoustic Reynolds number, which is defined as

$$\mathrm{Re} = \frac{\rho |u'| (D_{IT} - D_{ext})}{\mu}. \qquad (4.19)$$

For the area contractions, the characteristic length used was the difference between the diameters of the large and small tubes. The acoustic velocity in the smaller diameter tube was computed from impedance tube measurements.

The real part of the impedance of the area change $Z_{\delta A}$ obtained from the impedance subtraction calculation was normalized based on Eq. (3.14) as follows:

$$\xi = \frac{real(Z_{\delta A})}{\left[\left(\frac{S_{IT}}{S_{ext}}\right)^2 - 1\right]}. \qquad (4.20)$$

4.7.1 Acoustic resistance of an area change: the effect of acoustic velocity amplitude

This section presents results for experimental studies conducted on the system shown in Figure 4.6, which contains an area contraction followed by a constant area extension tube. In these, studies, the acoustic resistance and reactance of the area contraction was determined for several different extension tube lengths, for frequencies between 100 and 1000 Hz, and for several acoustic pressure amplitudes.

As shown in Table 4.1, impedance measurements were made over a wide range of driving acoustic pressure amplitudes for extension tube diameters of 25.4, 19, 14, and 9.5 mm. In addition to the impedance, the acoustic velocity amplitude at the location of the area contraction was measured as well and was found to be high when the driving frequency was at or near 310 Hz.

The acoustic velocity amplitudes in the extension tube shown in the table were not measured directly but, rather, computed using the continuity equation. The maximum acoustic velocity amplitude was limited by the maximum acoustic forcing amplitude achievable with the equipment used.

Table 4.1: Experimental measurement parameters for impedance tube measurements.

Extension tube diameter, mm	Minimum driving pressure amplitude, dB	Maximum driving pressure amplitude, dB	Minimum acoustic velocity amplitude in the extension tube, m/s	Maximum acoustic velocity amplitude in the area contraction, m/s
25.4	100	150	0.24	22
19	106	152	5.7	38
14	106	161	0.65	46
9.5	102	159	0.48	110

Figure 4.13 through Figure 4.16 show the acoustic resistance (i.e., the real part of the area change impedance) of the area contraction as well as the normalized real part of the impedance computed from Eq. (4.20) for each case. Each of these tests was repeated several times and the results were quite repeatable. It is important to note, however, that the impedance was difficult to measure at very low acoustic pressures because the signal to noise ratio was low resulting in unacceptable data noise levels at the low end of the Reynolds numbers tested.

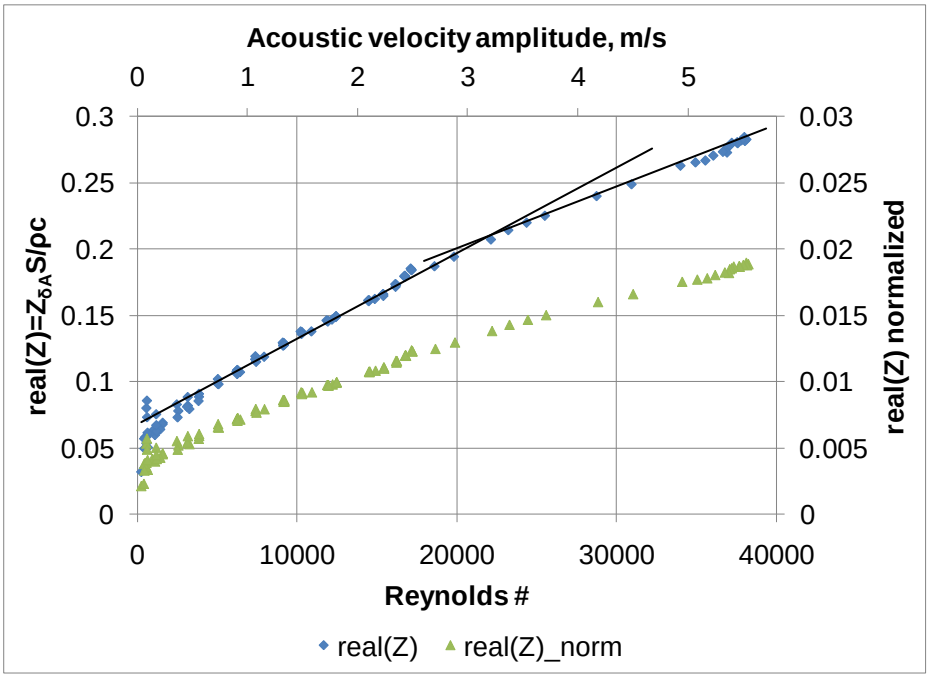

Figure 4.13: Acoustic resistance vs. Reynolds # for the 50.8 mm to 25.4 mm diameter tube with a 270 mm long extension tube measured at 310 Hz.

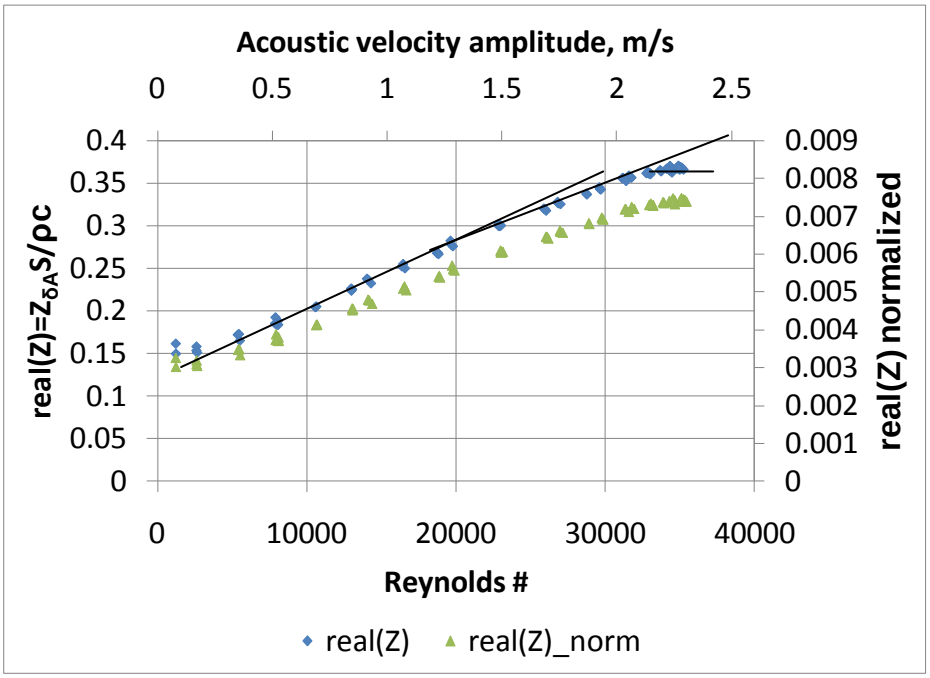

Figure 4.14: Acoustic resistance vs. Reynolds # for the 50.8 mm to 19 mm diameter tube with a 270 mm long extension tube measured at 310 Hz.

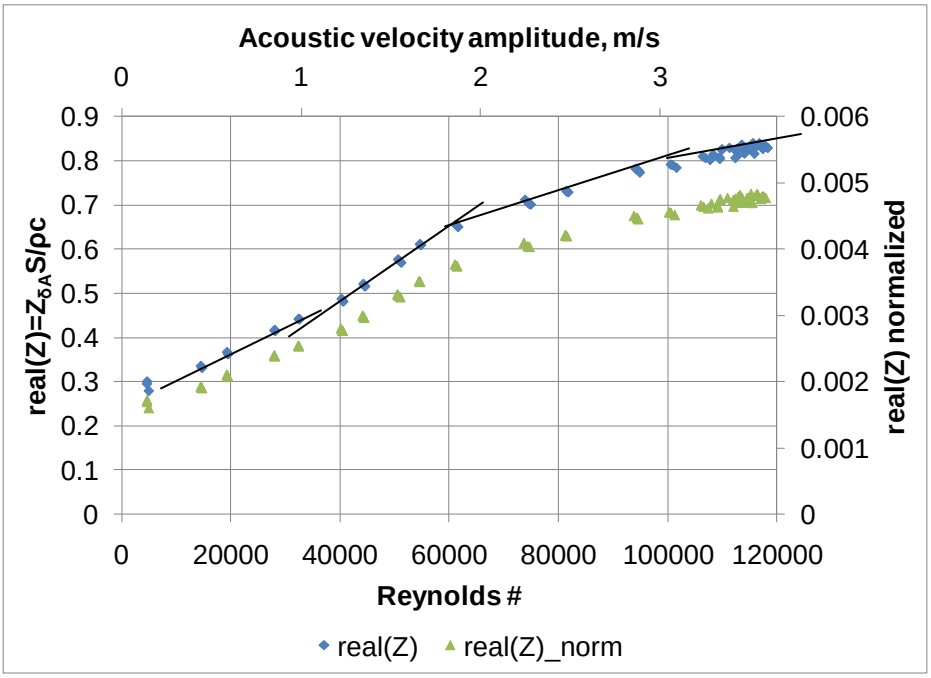

Figure 4.15: Acoustic resistance vs. Reynolds # for the 50.8 mm to 14 mm diameter tube with a 270 mm long extension tube measured at 310 Hz.

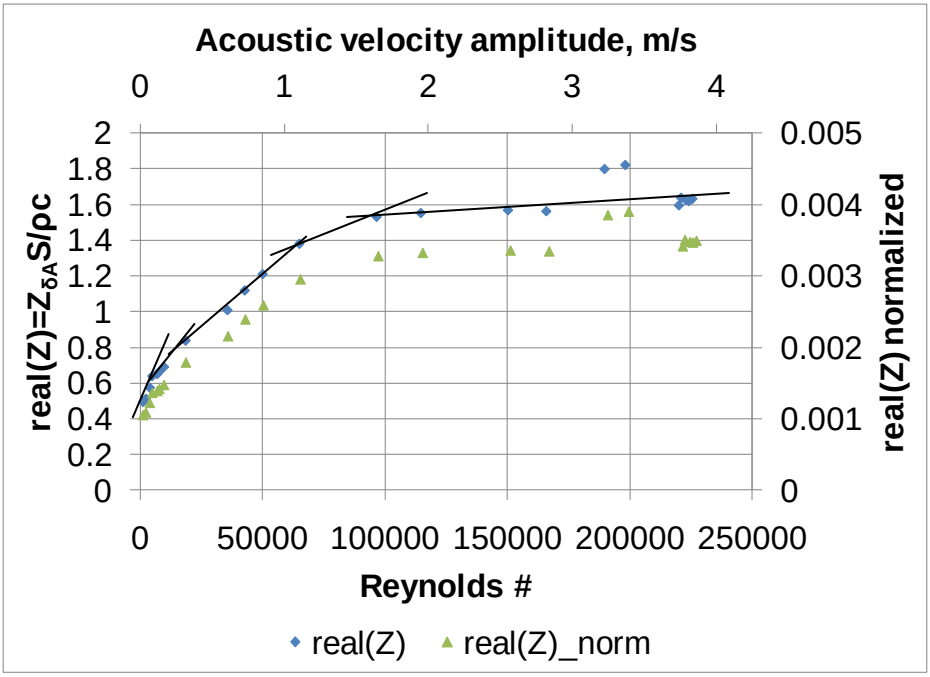

Figure 4.16: Acoustic resistance vs. Reynolds # for the 50.8 mm to 9.5 mm diameter tube with a 270 mm long extension tube measured at 310 Hz.

Figure 4.13 shows that, for the 25 mm extension tube, the acoustic resistance varied linearly with acoustic velocity for acoustic Reynolds numbers from 2,500 to around 20,000. From 20,000 to 38,000, the dependence of acoustic resistance on Reynolds number was linear but with a different slope. Figure 4.14 and Figure 4.16 show results for measurements using 14 and 9.5 mm diameter extension tubes, respectively. In both cases, slope changes occurred at Reynolds numbers around 20,000, 32,000, 60,000, and 100,000. In addition, consistent with the theory presented in Chapter 3, these results show that as the diameter of the extension tube increased, the acoustic resistance for a given acoustic velocity amplitude decreased.

The theory presented in Chapter 3 indicates that the real part of the impedance should be linearly related to velocity (or Reynolds' number). However, these results show that the behavior of the flow field around the area contraction is modal in its behavior. In other words, the flow field changes discretely at certain Reynolds numbers.

Between these Reynolds numbers, the acoustic resistance increases linearly with acoustic velocity.

The reason for the change in slope is not easily explained. However, at very high Reynolds' numbers, the effects of very intense turbulence may be responsible for the sudden change in behavior of the impedance. This type of behavior was reported by Ingard[49]. This leads to the following conclusions. (1) The acoustic resistance increases linearly with acoustic velocity amplitude for a given flow field structure. (2) The structure of the flow field depends on the acoustic Reynolds number as defined in Section 4.7. (3) The structure of the flow field at the area contraction determines the rate of increase of acoustic resistance with acoustic velocity.

The initial linear slope obtained from the experimental data, along with the slope predicted by Eq (3.14), is shown in Table 4.2. The model under-predicts the slope for small area ratios and over-predicts it for large area ratios.

Table 4.2: Model predicted and experimentally determined slope between real(Z)=$Z_{\delta A}$(S/ρc) and acoustic velocity amplitude.

Extension tube diameter, mm	Initial slope (experimental)	Predicted slope (Eq. 3.14)
25.4	0.042	0.022
19	0.114	0.073
14	0.23	0.251
9.5	0.91	1.19

4.7.2 Acoustic resistance of an area contraction: the effect of frequency

The model developed in Chapter 3 indicates that the acoustic resistance of a compact area contraction should be independent of frequency. To test this prediction, the acoustic resistance of the area contraction shown in Figure 4.4 was measured over a range of frequencies. For this study, a 14 mm diameter extension tube having lengths of 92, 168, and 270 mm was used. For these three lengths, the velocity anti-node was situated at the location of the area contraction for frequencies of 900, 500, and 310 Hz, respectively. Therefore, measurements of the acoustic resistance were made for a range of acoustic velocity amplitudes over frequency ranges of 900-970 Hz, 460-550 Hz, and 270-360 Hz for the respective extension tube lengths.

Figure 4.17 shows the variation in acoustic resistance of the area contraction with acoustic velocity for the 14 mm diameter, 270 mm long extension tube for several frequencies centered around 310 Hz. Low signal to noise ratios for acoustic velocities below 0.5 m/s led to significant variability in the acoustic resistance. However, the results above 0.5 m/s, show clearly that the acoustic resistance of the area contraction is independent of frequency for the range of frequencies tested. This is consistent with the predictions of the model developed in Chapter 3, which indicates that the acoustic resistance of the area contraction should not depend on the driving frequency.

A plot of the real part of the impedance, i.e., acoustic resistance, versus acoustic velocity for the 92 mm long extension tube is shown in Figure 4.18. As before, low signal to noise ratio explains the variability observed in the acoustic resistance measurements for acoustic velocities below 0.5 m/s. As expected, the real part of the impedance varied linearly with acoustic velocity with no dependence on frequency observed.

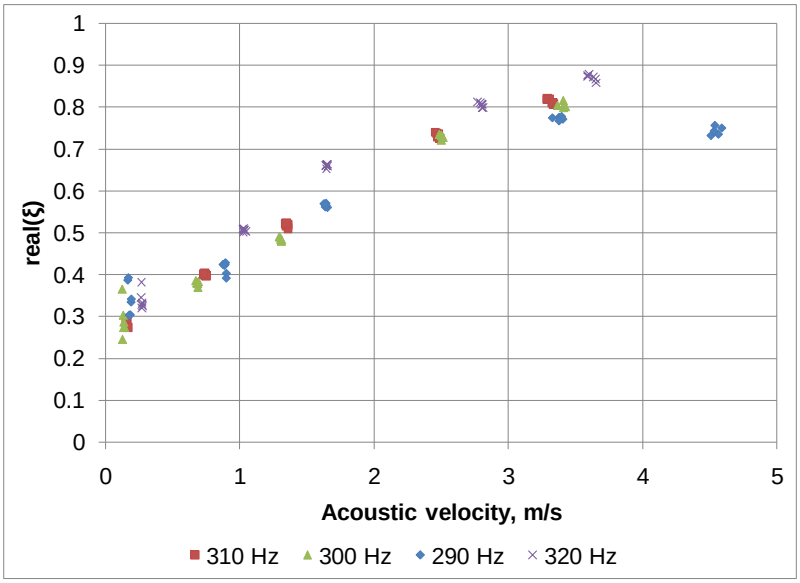

Figure 4.17: Real(ξ) vs. Acoustic velocity for 50.8 mm to 14 mm diameter, 270 mm long extension tube for a range of forcing frequencies near 310 Hz.

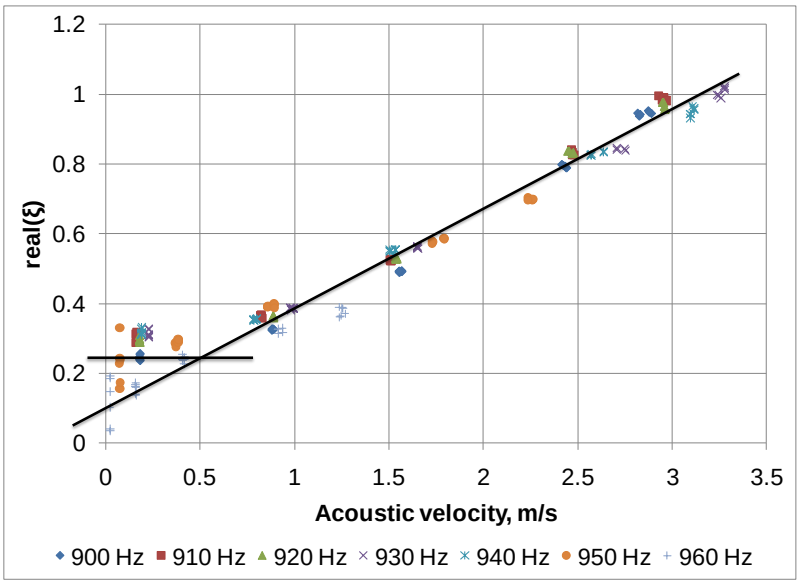

Figure 4.18: Real(ξ) vs. Acoustic velocity for 50.8 mm to 14 mm diameter, 92 mm long extension tube for a range of forcing frequencies near 930 Hz.

Figure 4.19 shows a plot of the real part of the impedance as a function of acoustic velocity for the 14 mm diameter, 168 mm long extension tube. As before, low

signal to noise ratio explains the variability observed in the acoustic resistance measurements for acoustic velocities below 0.5 m/s, and the linear relationship between the real part of the impedance and the acoustic velocity is clear. However, in this case, considerable scatter in the data was observed.

The three lines shown indicate the slope of the data shown. Line 1 matches the slope for all of the data for the 460, 470, 480, and 490 Hz cases. Line 2 matches the slope of the data for the 510 Hz case. Line 3 matches the slope for the rest 530, 540, and 550 Hz cases. The 520 Hz data is scattered between the three lines with large changes in resistance for very small changes in acoustic velocity. Further, notice that while Line 1 matches the data for the 490 Hz and some of the 520 Hz data, Line 2 matches the data for the 510 Hz case and some of the 520 Hz data. These observations indicate that the variation in slope is due to unstable flow patterns at the area contraction at these frequencies.

Earlier results showed that the flow field in and around the area contraction were heavily dependent on acoustic Reynolds number. The results presented here also imply that the modes of the flow field in and around the area contraction depend on frequency.

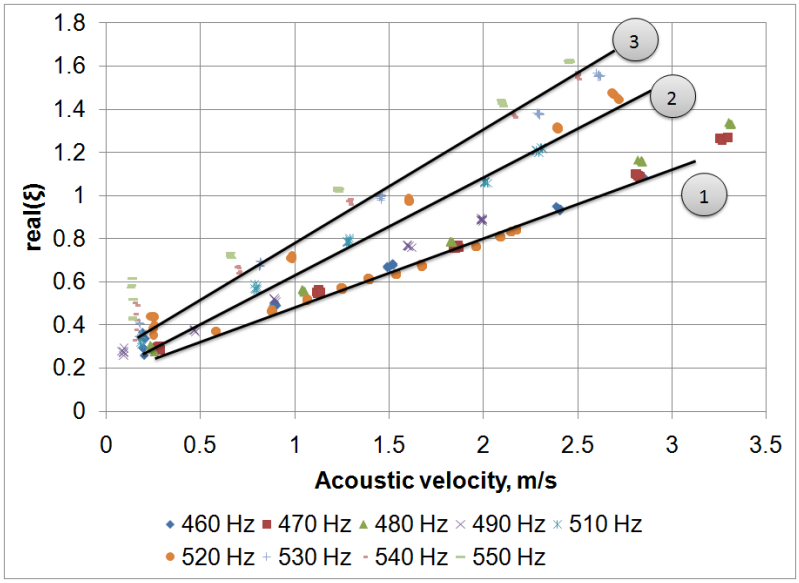

Figure 4.19: Real(ξ) vs. Acoustic velocity for 50.8 mm to 14 mm diameter, 168 mm long extension tube for a range of forcing frequencies near 510 Hz.

These results show that the acoustic resistance depends linearly on acoustic velocity over the range of acoustic velocities investigated. Further, the average slope of the acoustic resistance was nearly the same for the three frequency ranges studied, but these results are inconclusive and need further investigation. However, these results are consistent with the theoretical predictions that the acoustic resistance should be linearly dependent on velocity and independent of frequency.

4.7.3 Reynolds number scaling

The experimental study of the previous section shows that the slope of the acoustic resistance vs. acoustic Reynolds number curve decreases with increasing acoustic Reynolds number. This type of behavior is typical of a power law relationship. Therefore, the possibility that the acoustic resistance depends on acoustic Reynolds number by a power law relationship was further investigated. Ingard[48] notes that this power law relationship, in general, takes the form

$$\xi = real\left(\frac{Z_{\delta A} S_{IT}}{\rho c}\right) = C_{\xi}\left(u'_{IT}\right)^{n_{\xi}}, \tag{4.21}$$

where C_{ξ} and n_{ξ} were both constants and u'_{IT} was the acoustic velocity amplitude in the impedance tube.

Since the impedance data were linear at low acoustic velocities but decreased at higher velocities, n_{ξ} should be less than one. C_{ξ} is equal to the real part of Eq. (3.14) excluding the velocity terms. In the case of no steady mean flow, C_{ξ} was written as

$$C_{\xi} = \frac{\left[\left(\frac{S_{IT}}{S_{\delta A}}\right)^2 + K_L - 1\right]}{2c} = \frac{1}{2c}\frac{\left(1 - {C_D}^2\right)}{{C_D}^2}. \tag{4.22}$$

The exponential term n_{ξ} was found by plotting the real part of the impedance obtained from measurements against velocity raised to the power n_{ξ} and applying a linear fit to the data. The value of n_{ξ} that yielded the best linear relationship was deemed the “correct” one.

Figure 4.20 shows the results of this procedure for the 4:1 area contraction with a 1 inch diameter, 10.5 inch long extension tube. In this case, the value of n_{ξ} was found

to be 0.45 and C_ξ was found to be 0.11. The value of C_ξ calculated from Eq. (4.22) for $K_L = 0$ was 0.03. More importantly, Figure 4.20 shows that the data follow a reasonable functional relationship with acoustic velocity as predicted by the model.

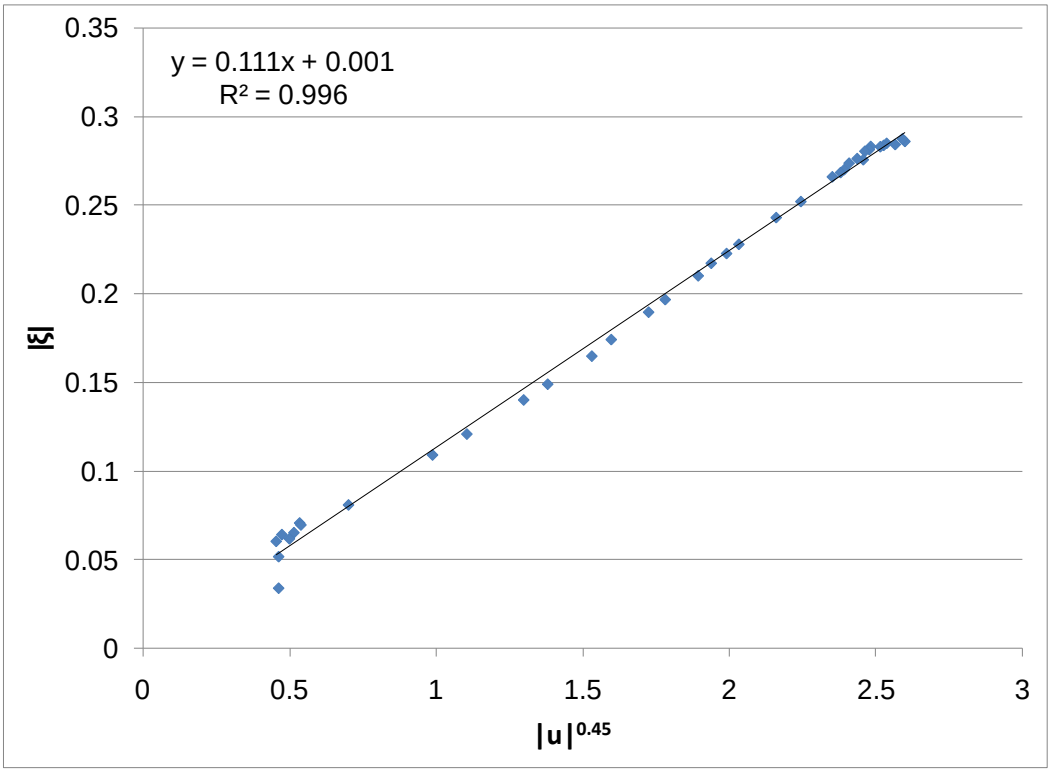

Figure 4.20: Acoustic resistance vs. Acoustic velocity amplitude.

This procedure was used for the four area ratios shown in Table 4.3, which shows the results for C_ξ and n_ξ. The first column shows the value of C_ξ obtained from a curve fit of the data for the value of n_ξ shown in the third column. The second column shows the results for C_ξ obtained using Eq. (4.22). The data show that the value of C_ξ increases with increasing area ratio and that the value of n_ξ was a function of

frequency. The values of C_ξ obtained from Eq. (4.22) differ somewhat from the values obtained from the curve fits, but the trends were similar.

The most important conclusion to be gained from this investigation was that the resistance of the area contraction did not follow a strictly linear relationship with acoustic velocity as indicated by the model of Chapter 3. Instead, the data indicate that the resistance of the area contraction more closely followed a power law relation similar to Eq. (4.21).

Table 4.3: Reynolds' number scaling results.

Case (Area ratio, tube length, freq.)	C_ξ *(from data)*	C_ξ *from Eq.* (4.22)	n_ξ
4:1, 10.5 inches, 310 Hz	0.11	.03	0.45
16:1, 20.0 inches, 490 Hz	.36	.56	.85
28:1, 10.5 inches, 310 Hz	.58	.77	.45
64:1, 10.5 inches, 310 Hz	1.7	.79	.45

4.7.4 Acoustic reactance of an area contraction

The acoustic reactance, i.e., the imaginary part of the impedance, of the area contraction, shown in Figure 4.4, for a range of acoustic velocities is shown in Figure 4.21. Contrary to the theory presented in Chapter 3, the imaginary part of the impedance shows a slight reduction as the acoustic velocity increases. In terms of effective length, this means that the amount of oscillating mass in the opening of the smaller diameter tube depends on the acoustic velocity at the opening of the area contraction. Therefore, some of the energy stored in the oscillating air mass at the exit of the smaller tube was lost at higher velocities. Most probably, these differences were due to energy lost due to interactions between oscillating mass at the area contraction and the recirculation zone in the larger diameter tube. Therefore, energy stored by the oscillating mass is lost. This lost energy appears as an increase in the real part of the impedance.[48]

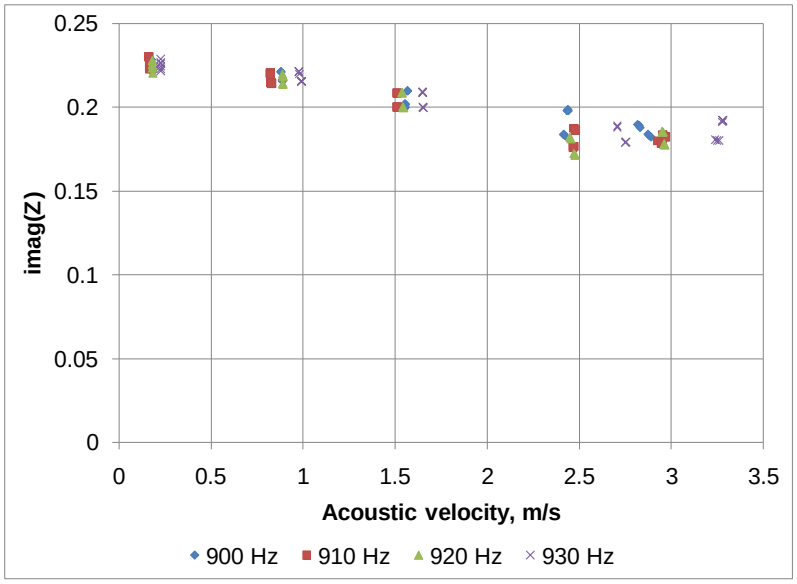

Figure 4.21: Measurements of Imag(Z) for the area change vs. acoustic velocity at the junction of a 50.8 mm to 14 mm diameter reduction with an extension tube of length 92 mm.

4.7.5 Summary of area contraction impedance measurements

Some conclusions drawn from this part of the study are as follows. First, under all circumstances, the real part of the impedance of the area change is nonlinear. That is, the acoustic resistance of an area change depends on the amplitude of the acoustic velocity oscillations. Second, the acoustic resistance of the area change varied linearly with acoustic velocity, but it was observed that the rate of change of the acoustic resistance with acoustic velocity depends on the acoustic Reynolds number. Third, at extremely high acoustic velocity amplitudes, the resistive part of the impedance exhibited a tendency to level off. Fourth, in general, the resistive part of the impedance of the area change varied in proportion to the squared area ratio. When normalized by the squared area ratio in accordance with Eq. (3.14), the acoustic resistance of all of the area contraction ratios tested was of the same order of magnitude.

The measurements in this section clearly show that the response of an abrupt area change to acoustic forcing is strongly dependent on the velocity amplitude at the location of the area change. The model developed in Chapter 3, although helpful in understanding the data, does not completely describe the acoustic response of the area change to acoustic velocity oscillations.

4.8 'Tee' junction impedance measurements

Another element, found at two locations in the FST is the 'tee' junction, an example of which is shown in Figure 4.22. In general a 'tee' junction is formed when three ducts or tubes are joined at a single location. For this study, each of these three ducts was assumed to have the same diameter.

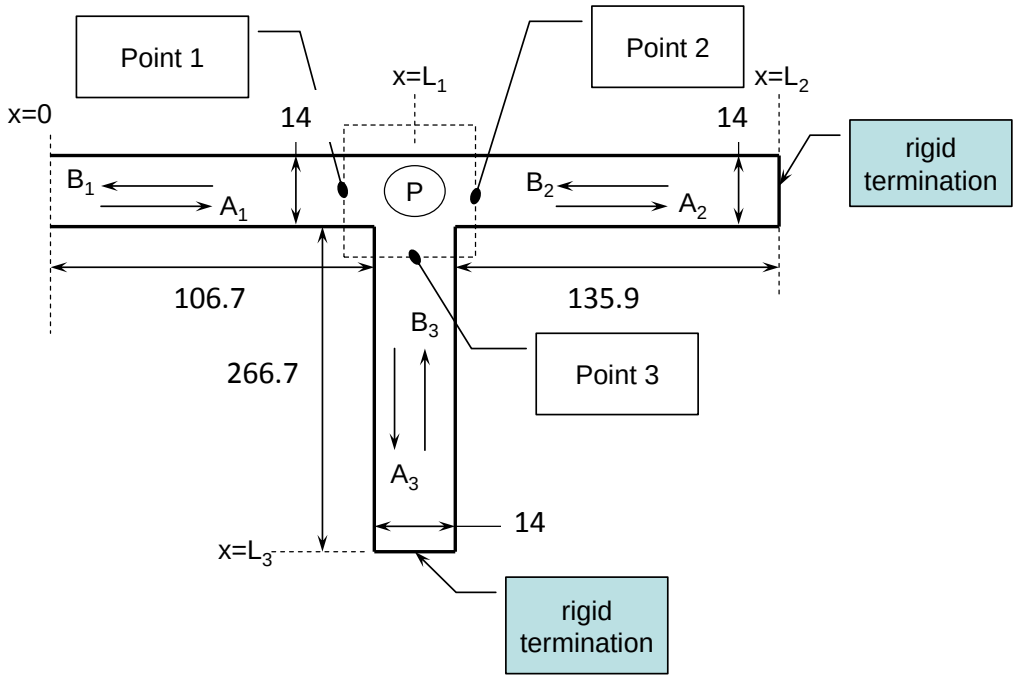

Figure 4.22: Schematic of 'tee' junction of three tubes.

The primary purpose of measuring the impedance of the 'tee' junction network shown was to determine whether or not the acoustic impedance of the 'tee' junction is nonlinear. Since there are no observed nonlinear elements in the tubes or rigid end-termination, any observed nonlinear behavior in the 'tee' network shown must be due to the presence of the 'tee' itself.

The system shown in Figure 4.22, which was used for these tests, consists of a 14 mm diameter tube leading up to the 'tee' junction at location 1. The 'tee' junction

itself was confined to the region indicated by the dotted line box. Rigid-walled, 14 mm diameter tubes with rigid end-terminations were attached to the 'tee' at locations 2 and 3. The length of each tube is indicated in the figure.

The impedance of the network at the location marked *x=0* was measured using the impedance tube. Of course, this measured impedance includes the effects of the adjoining tubes. However, this information was deemed sufficient for the purpose of determining the linear or nonlinear behavior of the 'tee' junction.

Direct measurement of the impedance of the 'tee' itself was virtually impossible for the nonlinear case because the acoustic velocity entering each branch of the 'tee' depends on the acoustic properties of its branch line. This, in turn, affects the acoustic impedance of the junction. This leads to the conclusion that the 'tee' junction was not really a simple piping element but was, in reality, a type of network itself.

Figure 4.23 shows a plot of the magnitude of the reflection coefficient of the 'tee' junction system shown in Figure 4.22. Clearly, the magnitude of the reflection coefficient deviated significantly from one at frequencies centered around 450 Hz, indicating that acoustic energy was dissipated at the 'tee' for these frequencies.

Figure 4.24 shows a plot of the pressure amplitude measured at location 1 for the 'tee' system. Due to the acoustical properties of the system, it was not practical to maintain constant pressure amplitude for each frequency, and clearly, the pressure amplitude varied significantly over the range of frequencies tested. In particular, the pressure amplitude at location 1 was lowest around 200 Hz, between 400 and 500 Hz, and again around 800 Hz. However, Figure 4.23 shows that the nonlinear damping was strongest at about 450 Hz and again at about 950 Hz. The data indicate that the damping was nonlinear due to the presence of high amplitude acoustic velocity fluctuations.

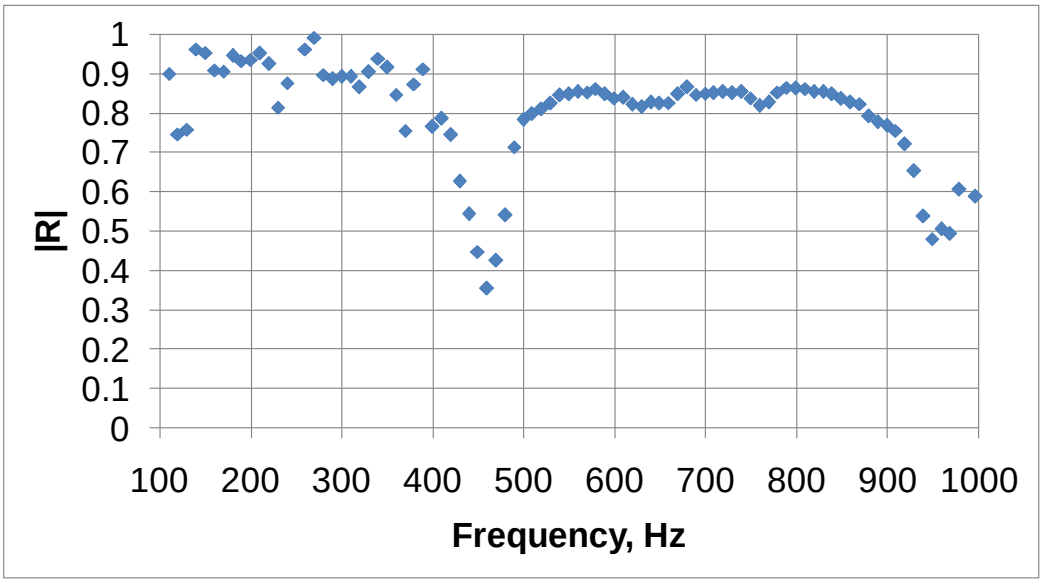

Figure 4.23: Amplitude of the reflection coefficient vs. Frequency for the 'tee' junction system shown in Figure 4.22.

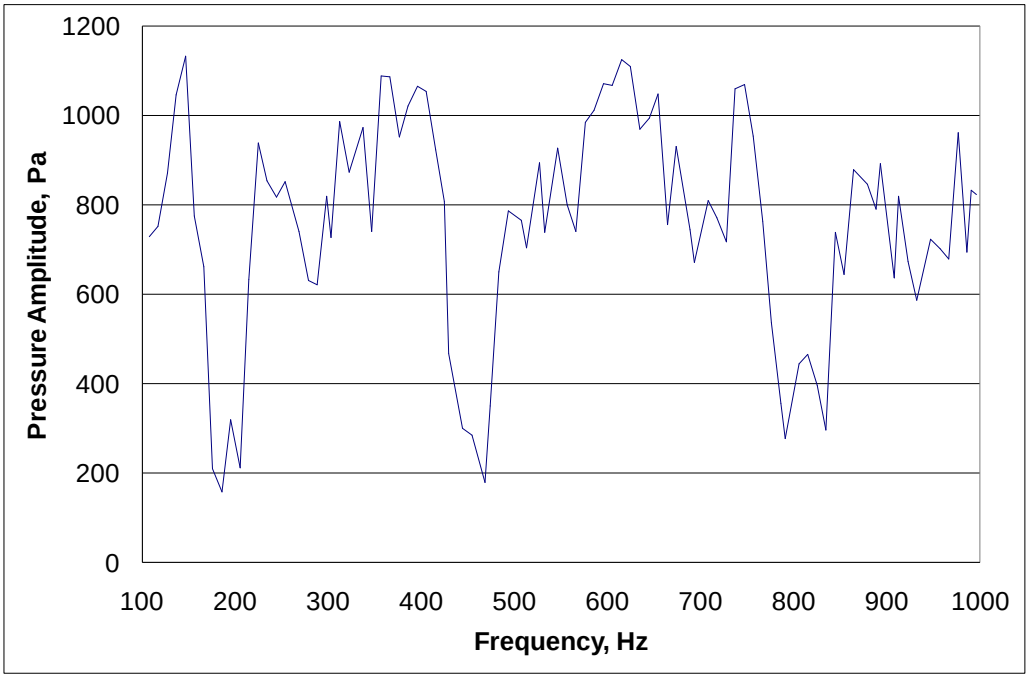

Figure 4.24: Acoustic Pressure amplitude vs. Frequency for the 'tee' system.

4.9 Variable area valve impedance measurements

The investigated FST includes two variable area, gate valves, see Figure 4.25. The purpose of the gate valve was to introduce acoustic resistance in the network, thereby providing a means for controlling the impedance of the FST network. Neglecting wall friction effects, linear acoustic theory allows for resistance only in the case in which steady mean flow is present. To help determine the magnitude of this effect, measurements of the impedance of the valve were made using the two-microphone impedance tube.

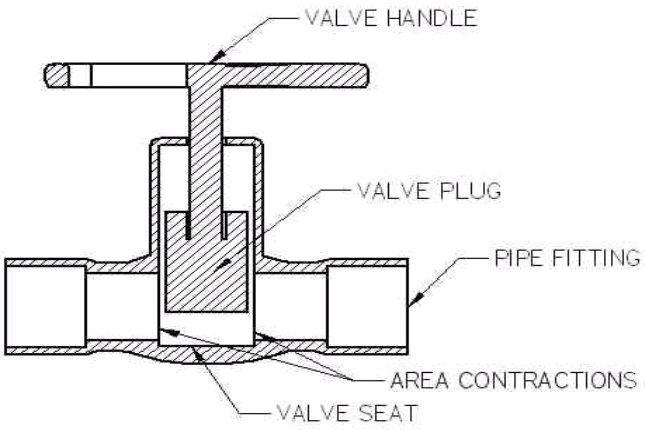

Figure 4.25: Schematic of a commercial gate valve

As before, direct measurement of the impedance of the valve as inserted into the network was not possible. Therefore, the measurements were made using the simple system shown in Figure 4.26.

The valve was located at the point labeled $x=L_1$ followed by a length of rigidly-terminated, 14 mm diameter tubing. The reflection coefficient of the valve was measured just upstream of the valve; the impedance of the valve itself was obtained by the impedance subtraction technique previously, discussed.

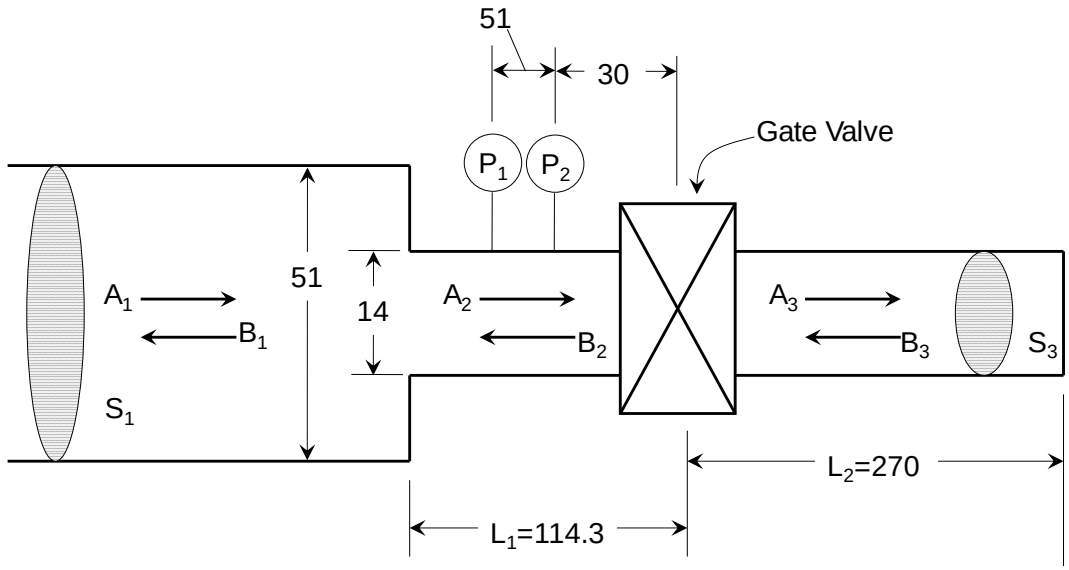

Figure 4.26: Schematic of a rigidly terminated duct section containing a variable area valve.

Figure 4.25 suggests that the valve be represented schematically in Figure 4.26; that is the valve behaved acoustically as an area contraction followed by an area expansion. Therefore, it is expected that the behavior of the valve could be approximated by an area contraction and expansion in series with each having the same area ratio as the valve throat.

Measurements of the acoustic response of the valve situated in a length of 14 mm diameter tubing as shown in Figure 4.26 were made for several different valve open areas using the two-microphone impedance tube. The reflection coefficient and impedance at the valve centerline were computed from these measurements.

Figure 4.27 through Figure 4.32 show measurements of the reflection coefficient measured at the face of the valve in the absence of steady mean flow. Figure 4.27 shows the case in which the valve was removed. This case was expected to compare closely with the case in which the valve was completely open. As expected, the $|\hat{R}|$ is

equal to one and the phase varied linearly with $k \cdot L$. In fact, the results were the same as for a straight, rigid-walled tube of the same length.

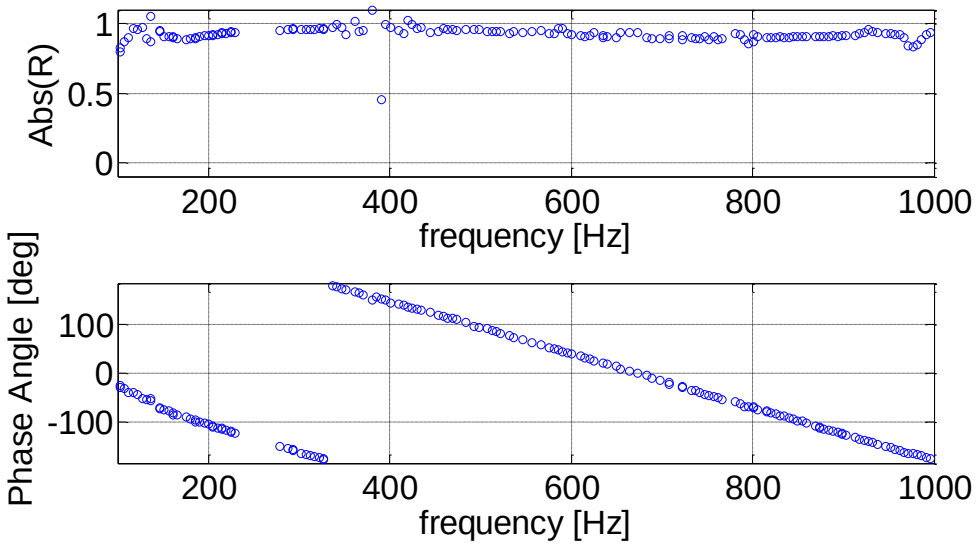

Figure 4.27: Magnitude and phase of the reflection coefficient vs. Frequency for the valve removed.

Figure 4.28 through Figure 4.32 show plots of the magnitude and phase of the reflection coefficient of the system shown in Figure 4.26 with the gate valve 100%, 57%, 28%, 14%, and 0% open, respectively.

Figure 4.28 shows the expected result that the influence of the valve was quite small when completely open. However, some acoustic resistance was indicated by the reduction in the reflection coefficient across almost all frequencies. The valve was 57% open in the results shown in Figure 4.29. In this case, the resistive effect of the valve is clearly seen in these results, as at most frequencies, the $\left|\hat{R}\right|$ deviated significantly from one.

Figure 4.30 and Figure 4.31 show results for the valve 28% and 14% open. These two cases exhibit that closing the valve causes the resistance to increase over

the entire range of frequencies. However, the effect is quite pronounced at certain frequencies, e.g. 250, 325, and 450 Hz.

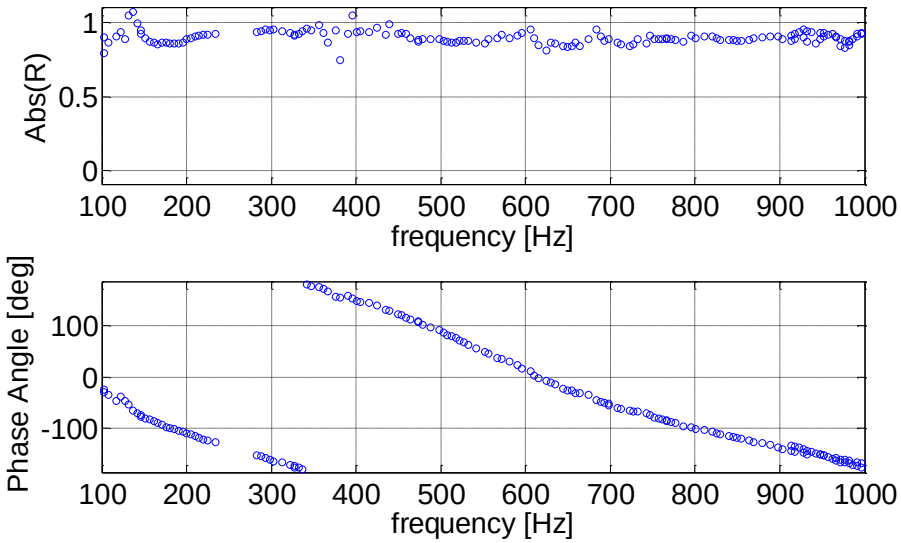

Figure 4.28: Magnitude and phase of the reflection coefficient vs. Frequency for the 100% open.

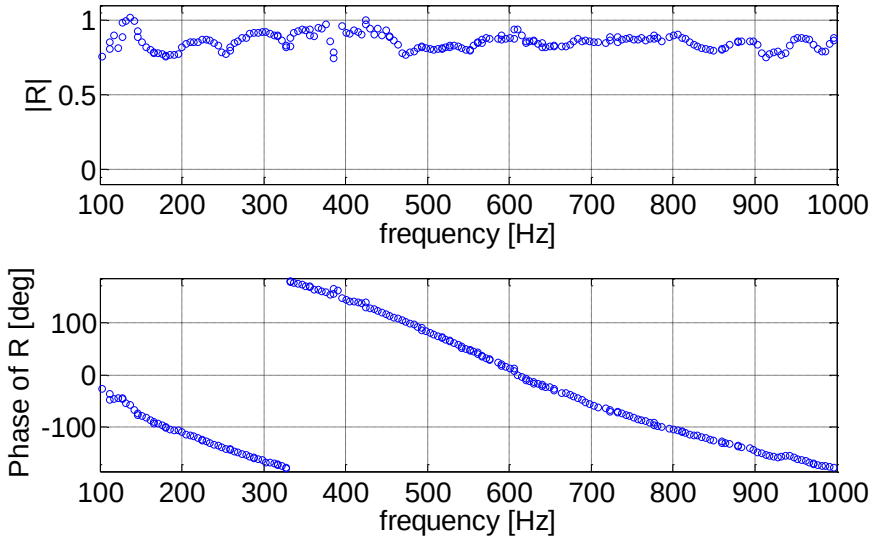

Figure 4.29: Magnitude and phase of the reflection coefficient vs. Frequency for the valve 2 turns open.

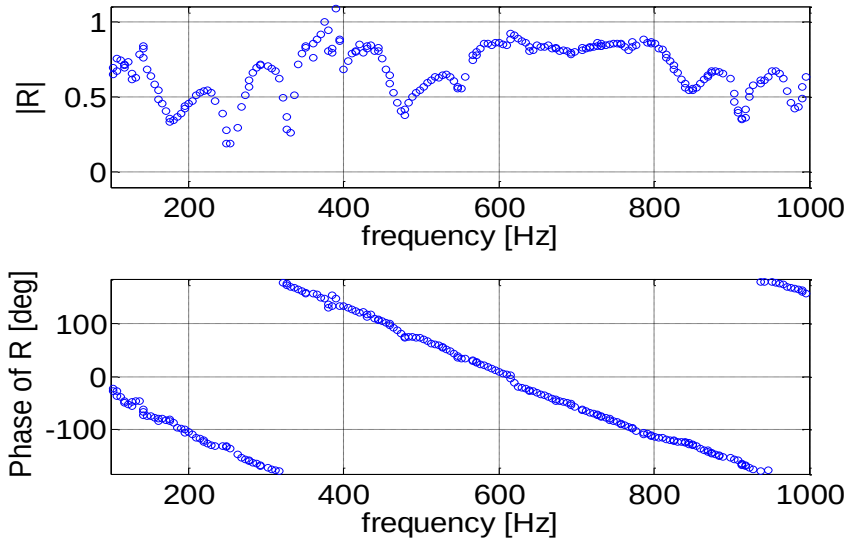

Figure 4.30: Magnitude and phase of the reflection coefficient vs. Frequency for the valve 1.0 turns open.

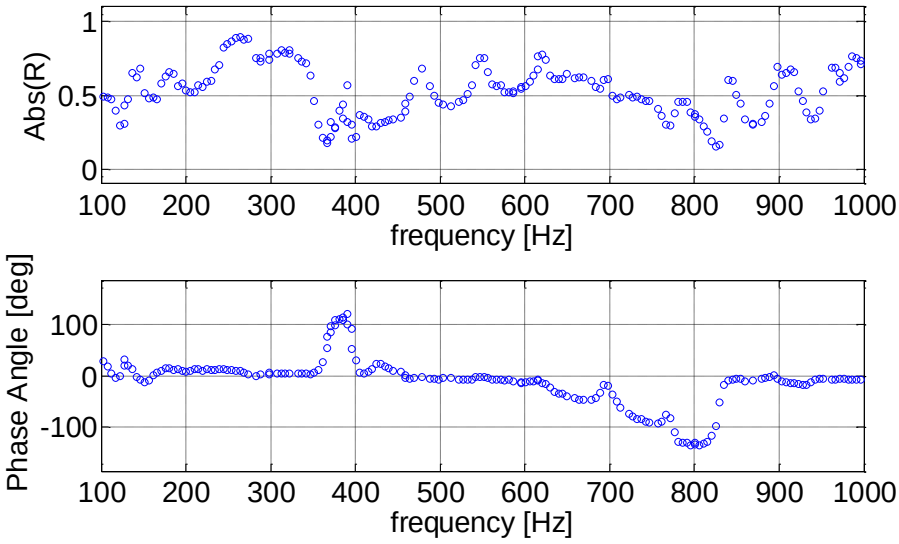

Figure 4.31: Magnitude and phase of the reflection coefficient vs. Frequency for the valve 0.5 turns open.

Closing the valve further to its completely closed condition caused the resistance of the valve to further increase so that it appeared to be a rigid wall as evidenced by the fact that $\left|\hat{R}\right|$=1 as shown in Figure 4.32. The phase plot in this figure shows that the

phase of R was 0 degrees indicating that the downstream tubing no longer affected the acoustic oscillations.

The results presented in this section show clearly that the acoustic behavior of the gate valve is complex in that its impedance depends both on frequency and valve setting. Further, the theory presented in Chapter 3 indicates that, in the absence of steady flow through the valve, nonlinear effects are important when the valve is neither completely open nor closed. Based on the predictions of this theory, the frequency dependence observed in the measurements discussed above are most likely due to variations in acoustic velocity amplitude at the valve with frequency.

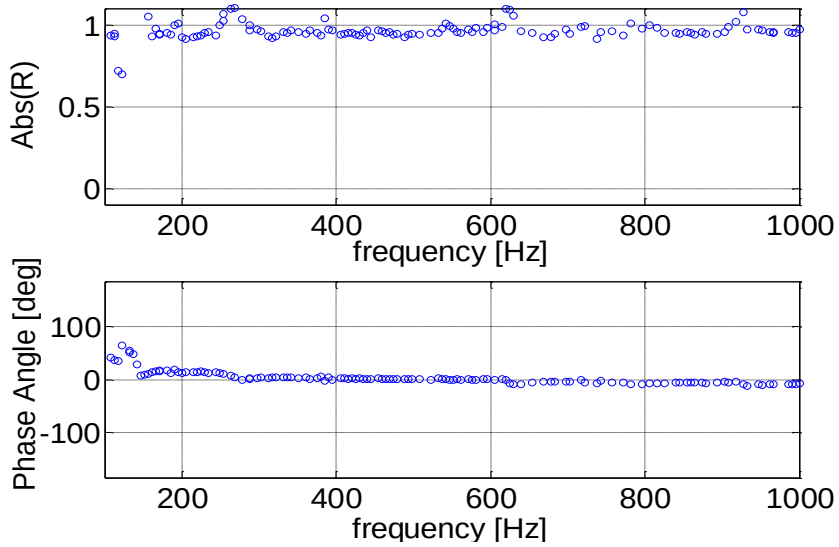

Figure 4.32: Magnitude and phase of the reflection coefficient vs. Frequency for the valve completely closed.

4.10 Area contraction in series with a valve

In addition to studying the acoustic characteristics of the simple piping components discussed in the previous sections, the acoustic properties of an abrupt area contraction followed by a valve was also studied. These results will be used in the next chapter to validate the model predictions of these simple combinations. In addition, it is important to understand the acoustical behavior of combinations of these components.

For this study, a rigidly terminated extension tube was attached to the downstream side of the valve as shown in Figure 4.33. In this study, the reflection coefficient at the area contraction was measured for six settings of the valve, ranging from the closed position to the fully open position.

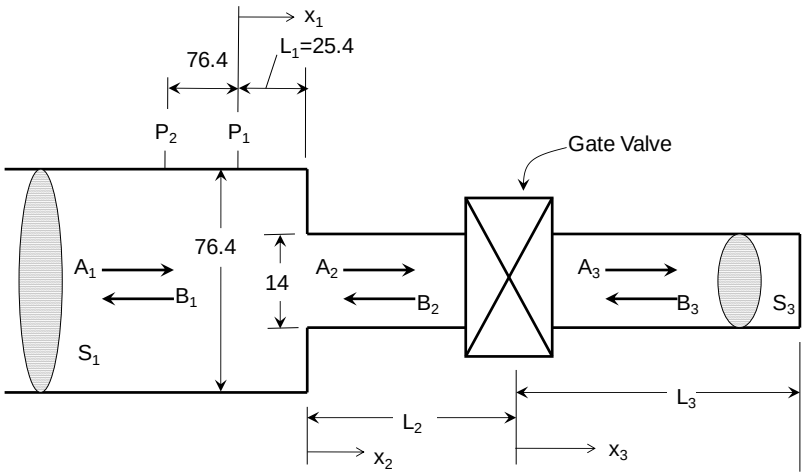

Figure 4.33: Schematic of a simple area contraction followed by a gate valve with a rigidly terminated extension tube.

The diameter of section 1 was 50.8 mm and the diameter of sections 2 and 3 was 14 mm. The length of section 2 was 3.2 mm, and the length of section 3 was 23.5 mm.

Neglecting wall friction effects, 1-D, linear acoustic theory for this system with no steady mean flow predicts that the reflection coefficient is one for all frequencies. Also, the phase of the reflection coefficient was predicted to be zero except in the vicinity of the resonant frequencies of the system. According to linear acoustic theory (see Figure 4.34), the primary effect of changing the valve position from open to closed was to change in the resonant frequencies of the system from 160 and 490 Hz to 355 Hz, respectively.

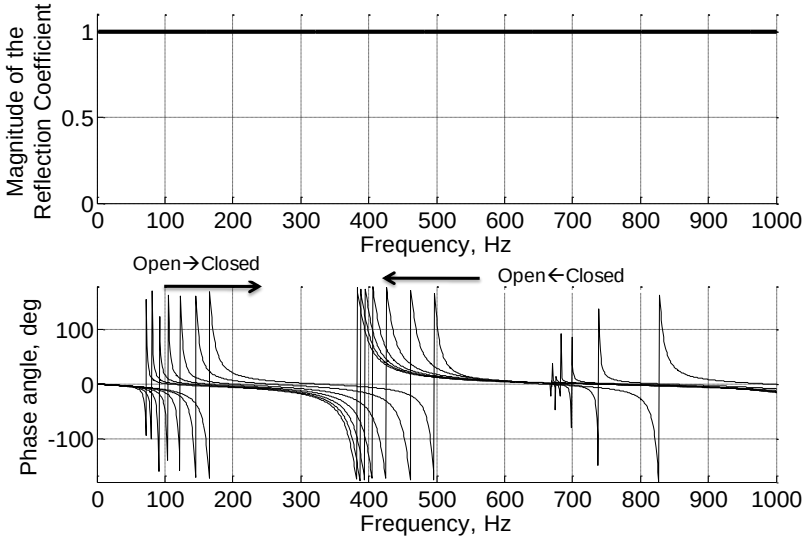

Figure 4.34: Predictions of linear acoustic theory for the reflection coefficient of the system shown in Figure 4.33 for a range of valve settings.

Using the impedance tube, the complex reflection coefficient for this system was measured at a location 3.2 mm upstream of the area contraction. The results of these measurements are shown in Figure 4.35 for the six settings of the valve. Clearly, the magnitude of the reflection coefficient deviated significantly from one depending on valve setting. When the valve was nearly open, the plot of the magnitude of the reflection coefficient resembles that of a simple area contraction followed by a rigidly terminated tube shown in Figure 4.7. Specifically, the reflection coefficient tended to zero at 150,

480, and 825 Hz and was nearly one elsewhere. However, as the valve was closed, the magnitude of the reflection coefficient tended to approach one for these frequencies and tended to zero at 350 Hz when the valve was nearly closed. When the valve was completely closed the system was identical to the case of Figure 4.6, except that the tube length extending from the area contraction was only 3.2 mm long.

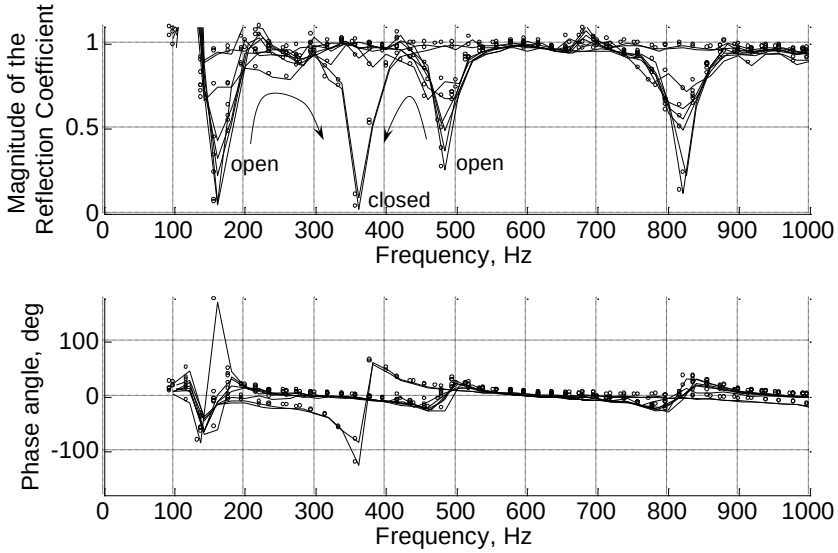

Figure 4.35: Magnitude and phase of the reflection coefficient vs. Frequency for the system shown in Figure 4.33 for a range of valve settings.

Comparing Figure 4.34 and Figure 4.35 shows that the damping introduced by the area change and the valve significantly affected the sharpness of the phase rotations as shown.

4.11 Conclusions

This chapter presented the development, sensitivity analysis, and validation of a two-microphone impedance tube used to measure the impedance of the various area contractions and valves critical to the construction and performance of the FST. The measurements presented in this chapter accomplished the following. First, the measurements extended those made by previous researchers to higher acoustic pressure and velocity amplitudes. Specifically, the acoustic resistance of an area contraction was measured over the range of acoustic velocity amplitudes from 0.25 to 110 m/s. In addition, these measurements show that the nonlinear impedance model developed in Chapter 3 correctly predicts a linear relationship between acoustic resistance and acoustic velocity amplitude for simple area contractions. However, these measurements show that the slope of the linear dependence was not constant. In fact, the measurements show that the slope changed discretely at acoustic Reynolds numbers of 15,000, 32,000, 60,000 and 100,000. It was also found that a Reynolds number scaling, or power law, model yielded good agreement with the data over the range of acoustic velocities tested.

The measurements presented also revealed that the acoustic resistance of a simple ‘tee’ junction was also nonlinear with acoustic velocity amplitude. Although typically modeled as a linear acoustic duct element, these results show that a nonlinear model for the ‘tee’ junction impedance is required to achieve accurate predictions.

The acoustic resistance of a simple gate valve was also shown to be nonlinear and that its resistance increased as the valve was closed. However, closing the valve to its 100% closed position showed that, in this case, the acoustic resistance of the valve was infinite and, therefore, dissipated no acoustic power. These results also show that the frequency response of the system containing the valve depends on valve setting.

The important conclusion from this part of the study is that achieving an accurate prediction of valve resistance is critical to predicting the acoustic impedance of the overall system.

Finally, the reflection coefficient of a combination of an area contraction, a gate valve, and a rigid-walled tube was measured for frequencies between 100 and 1000 Hz. These results show that the behavior of simple acoustic networks containing nonlinear elements have a complex acoustic response that cannot be captured by linear models.

Chapter 5:

Acoustic Response Modeling

5.1 Introduction

The ultimate goal of this part of the study was to develop an acoustic response model for the Fuel System Tuner to be used in conjunction with a thermo-acoustic combustor model to predict the effect of the FST on combustor stability. To this end, an effective technique for modeling the acoustic response of the various area contractions, tees, and valves used in the design of the FST was needed. Chapter 3 presented the development of a nonlinear acoustic impedance model for an acoustically compact area contraction. Chapter 4 showed the results of experimental measurements of the acoustic response of some common duct elements, including acoustically compact area contractions, a tee junction, and a variable area gate valve. The focus of this chapter is to demonstrate that the individual components of the FST can be successfully modeled using the nonlinear area change impedance equation developed in Chapter 3. For each component, the chapter presents the method by which each model was developed and a comparison between the predicted acoustic response and experimental measurements from Chapter 4.

This chapter also demonstrates the modeling technique used for systems containing multiple nonlinear elements, and it shows the complex acoustic response exhibited by even simple combinations of nonlinear elements. Finally, the FST model is presented along with a comparison of the FST model predictions and acoustic impedance measurements made using the two-microphone impedance tube.

5.2 An acoustically compact area contraction

Figure 5.1 shows a duct system with an area discontinuity a distance L_2 from a rigid termination. The objective of the analysis was to determine the reflection coefficient at area contraction (at the junction of duct 1 and duct 2) because this quantity was measured and reported in Chapter 4. To this end, the following analysis was used to determine the reflection coefficient at the right hand end of duct 1. From the reflection coefficient the impedance of the area change/duct 2 system can be easily determined from

$$Z = \frac{\rho c}{S}\frac{1+R}{1-R}. \tag{5.23}$$

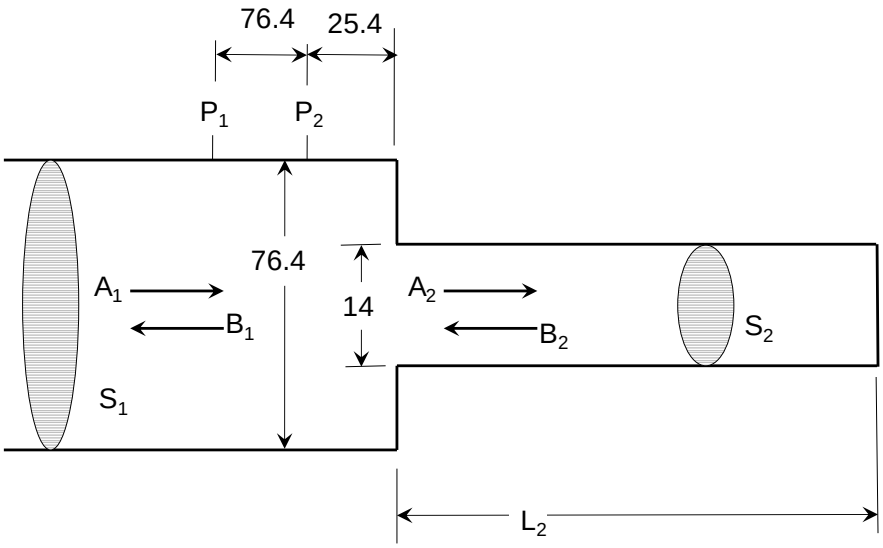

Figure 5.1: System including abrupt area change

From classical acoustics of plane standing waves, the acoustic pressure in a one dimensional duct is given by

$$p_i' = A_i e^{ikx_i} + B_i e^{-ikx_i}, \tag{5.1}$$

and the acoustic velocity is

$$u_i' = \frac{1}{(\rho c)_i}\left(A_i e^{ikx_i} - B_i e^{-ikx_i}\right). \tag{5.2}$$

The two boundary conditions for this system are (1) the acoustic pressure P_{ext} at the area contraction was imposed, i.e., it was measured, and (2) the acoustic velocity u_2' at $x = L_2$, where the cavity was rigidly terminated, is zero. Using Eq. (5.1) with $x = 0$, the first boundary condition leads to

$$A_1 + B_1 = P_{ext}\,., \tag{5.3}$$

The impedance of the area change $Z_{\delta A}$ was used to relate the pressure drop across the area contraction to the velocity at the right hand end of duct 1 as follows:

$$p_1' - p_2' = Z_{\delta A} \cdot S_1 u_1', \tag{5.4}$$

where $Z_{\delta A}$ was determined by Eq. (3.14). Substituting the expressions for the acoustic pressures and velocity into Eq. (5.4) at $x_1 = 0$ and $x_2 = 0$, respectively, yields

$$A_1\left(1 - Z\frac{S_1}{Z_0}\right) + B_1\left(1 + Z\frac{S_1}{Z_0}\right) = A_2 + B_2. \tag{5.5}$$

Continuity requires that the acoustic volume velocity $W_j' = u_j' S_j$ be continuous across the area change from duct 1 to duct 2 yielding

$$S_1 u' = S_2 u_2', \tag{5.6}$$

which upon substituting the expression for the acoustic velocity for each duct becomes

$$A_1\left(\frac{S_1}{Z_0}\right) - B_1\left(\frac{S_1}{Z_0}\right) = A_2\left(\frac{S_2}{Z_0}\right) - B_2\left(\frac{S_2}{Z_0}\right). \tag{5.7}$$

Applying the boundary condition at the rigidly terminated end of the pipe and using Eq. (5.2) gives

$$A_2 e^{ikL_2} - B_2 e^{-ikL_2} = 0. \tag{5.8}$$

The complex coefficients, A_1, A_2, B_1, and B_2 were determined by simultaneously solving the boundary condition equations given by Eqs. (5.3), (5.5), (5.7), and (5.8), using Eq. (3.14) for $Z_{\delta A}$. Having determined the complex coefficients, the acoustic velocities and pressures within the cavity were computed from Eqs. (5.1) and (5.2).

The set of equations above was nonlinear because $Z_{\delta A}$ is a function of the acoustic velocity amplitude at the area contraction. Therefore an explicit solution of these equations cannot be obtained directly; instead, the iterative solution procedure, illustrated graphically in Figure 5.2, was used. First, values for K_L and $|u'|/c$ were guessed and substituted into Eq. (3.14) to determine the impedance $Z_{\delta A}$. This value together with the imposed pressure P_{ext} was substituted into the boundary condition Eqs. (5.3), (5.5), (5.7), and (5.8), which were then solved for the four unknown complex coefficients.

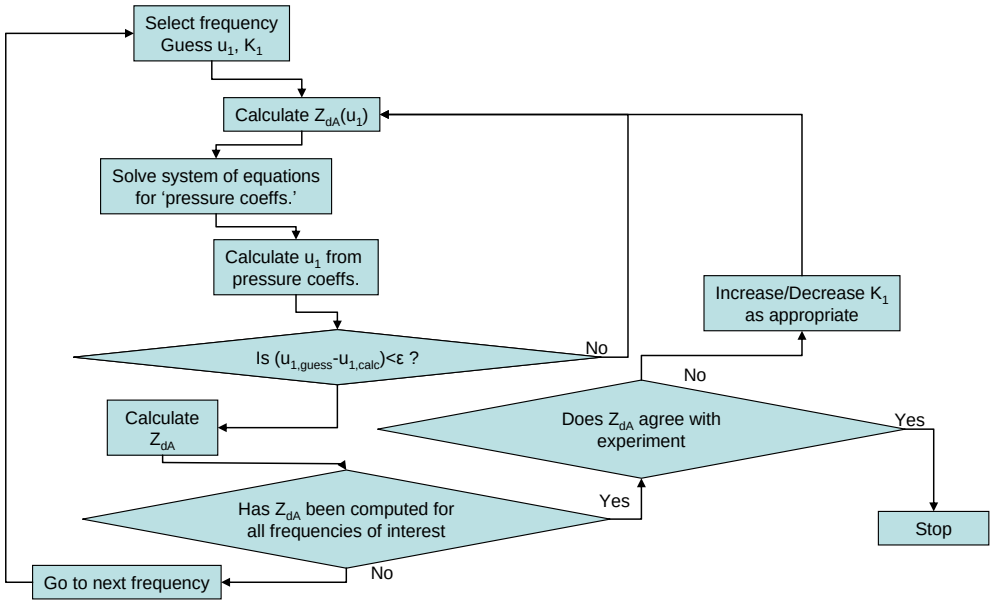

Figure 5.2: Nonlinear area change model calculation procedure

From the calculated complex amplitudes, a new value for the acoustic velocity was obtained and the process repeated until convergence was achieved. It should be noted that K_L is a property of the area contraction and not a function of frequency. Therefore, the same value of K_L was used for all frequencies. The value of K_L was determined by comparing the model predictions with the data from impedance tube measurements. The value of K_L was increased or decreased as needed, and the iteration procedure described above was repeated to achieve the best fit to the experimental data.

Figure 5.3 shows a comparison of the model predictions and impedance tube measurements of the reflection coefficient $R = B_1/A_1$, for the case $L_2 = 508$ mm. For comparison, linear acoustics with no losses would predict that *R*=1 for all frequencies, while linear acoustic with viscous losses due to steady mean flow would predict that $|R|$ is constant but less than one for all frequencies.

Figure 5.3 confirms that the model predictions are in reasonable agreement with the experimental frequency response measurements. In addition, Figure 5.3 shows that the $|R|$ was nearly one over most of the frequency spectrum, except for small frequency ranges. In these small ranges where the $|R| < 1$, the acoustic resistance of the area contraction is nonzero and dissipates acoustic energy. In this case, the only source of acoustic resistance was the nonlinear impedance of the area contraction, which was frequency dependent because the acoustic velocity amplitude at the area contraction was frequency dependent. This is consistent with the model presented in Chapter 3, which indicates that the acoustic resistance is directly proportional to the acoustic velocity amplitude.

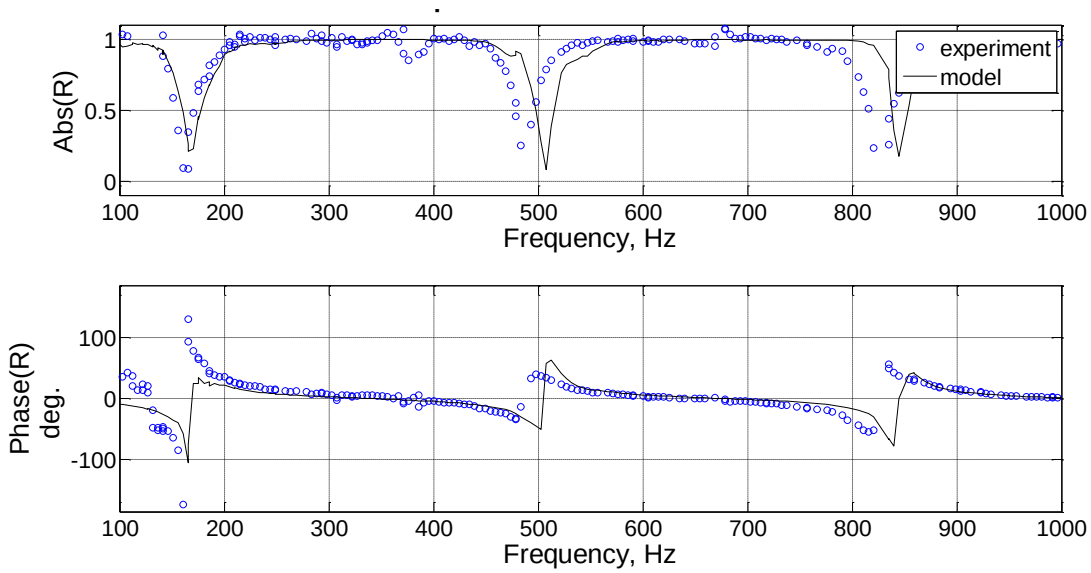

Figure 5.3: Magnitude and phase of the reflection coefficient vs. Frequency for the system shown in Figure 5.1 with L_2=508 mm. Model/experiment comparison.

A model of the system shown in Figure 5.4 was used to gain additional insight into the acoustic response of the general behavior of the acoustic network containing an area contraction. In this case, the entire impedance tube was modeled assuming that the speakers were volume velocity sources.

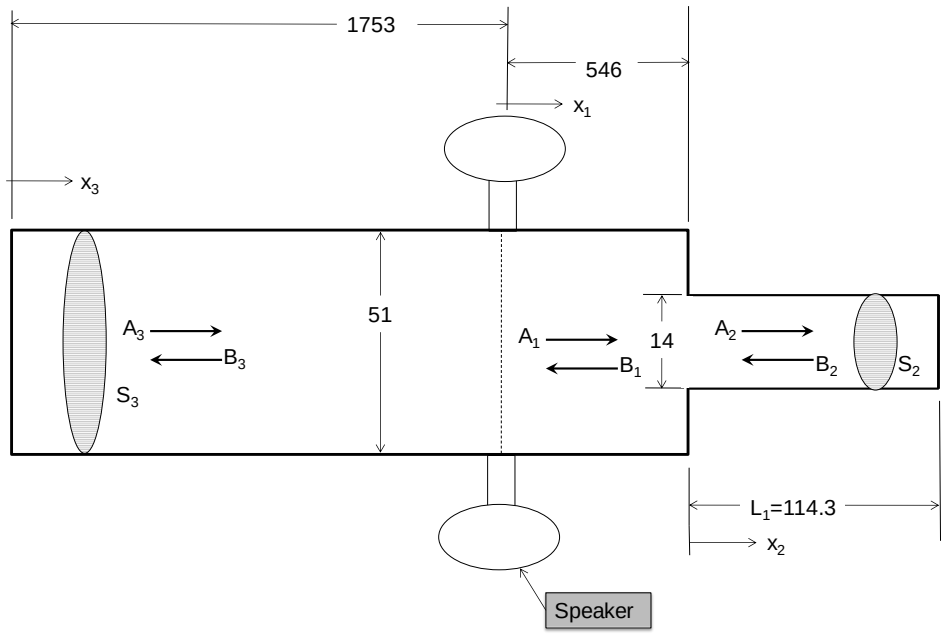

Figure 5.4: Schematic of the impedance tube, area contraction, and extension tube.

For these calculations the condition expressed by Eq. (5.3) was eliminated, and three additional equations were developed to solve for the six unknown complex amplitudes. Therefore, in addition to Eqs. (5.5), (5.7), and (5.8), the following equations were developed.

First, the acoustic velocity at the rigid end of the impedance tube at $x_3 = 0$ must vanish yielding

$$u_3(x_3 = 0) = \frac{1}{(\rho c)_3}(A_3 - B_3) = 0\,. \tag{5.9}$$

Next, the volume velocities, including the volume velocity provided by the speaker, at $x_2 = 0$ must sum to zero yielding

$$U_3(x_3 = L_3) - U_1(x_1 = 0) = -S_{spkr}u_{spkr}\,, \tag{5.10}$$

or

$$\frac{S_3}{(\rho c)_3}\left(A_3 e^{ikL_3} - B_3 e^{-ikL_3}\right) - \frac{S_1}{(\rho c)_1}\left(A_1 - B_1\right) = -S_{spkr} u_{spkr}\,. \tag{5.11}$$

Finally, the pressures at $x_2 = 0$ must be equal so that

$$p_3\left(x_3 = L_3\right) - p_1\left(x_1 = 0\right) = 0\,, \tag{5.12}$$

or

$$\left(A_3 e^{ikL_3} + B_3 e^{-ikL_3}\right) - \left(A_1 + B_1\right) = 0\,. \tag{5.13}$$

Equations (5.9), (5.11), and (5.13) along with Eqs. (5.5), (5.7), and (5.8) form the set of equations to be solved for the six complex amplitudes. In addition, the solution was subject to the constraint that the magnitude of the acoustic velocity at the area contraction (computed from the complex coefficients) and the acoustic velocity used in the nonlinear impedance formulation must be equal. The reflection coefficient and acoustic impedance were then calculated from the complex amplitudes. The results of these calculations for the case in which $L_2 = 267$ mm and assuming that $u_{spkr} = 1$ m/s, are shown in Figure 5.5 and Figure 5.6.

Figure 5.5 shows the calculated magnitude of the reflection coefficient at the area contraction as a function of frequency. It should be pointed out that very high and very low acoustic resistances result in the $|R| \simeq 1$. As Figure 5.6 shows, the reflection coefficient is minimized when $\mathrm{Re}(Z)/|Z| \sim 1$. In other words, very low values for $|R|$ are only achieved when the acoustic resistance is of the order of the characteristic impedance of the system. In addition, power is only dissipated when the acoustic resistance and the acoustic reactance of the system are of the same order of magnitude. If the acoustic reactance is much larger than the acoustic resistance, the phase between the acoustic pressure and velocity is 90 degrees, in which case no power is dissipated.

According to Figure 5.5 and Figure 5.6, these two conditions are satisfied at 310 and 950 Hz, and it is at these two frequencies that the $|R| \ll 1$.

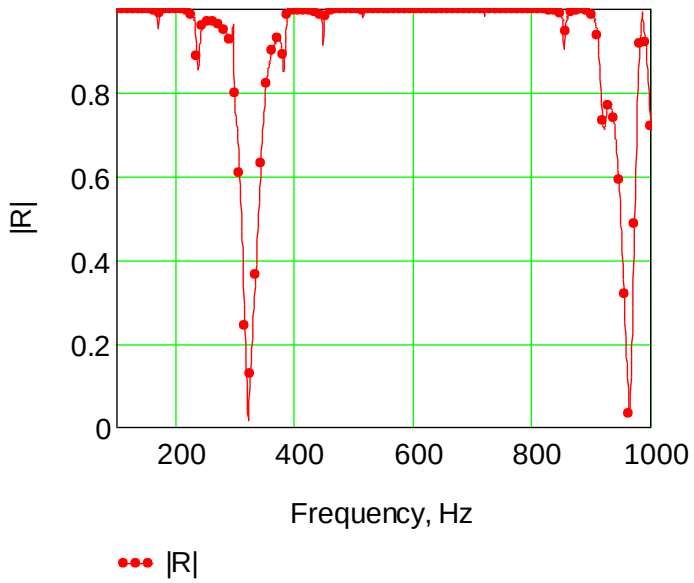

Figure 5.5: Magnitude of the reflection coefficient vs. Frequency for a speaker velocity of 1 m/s.

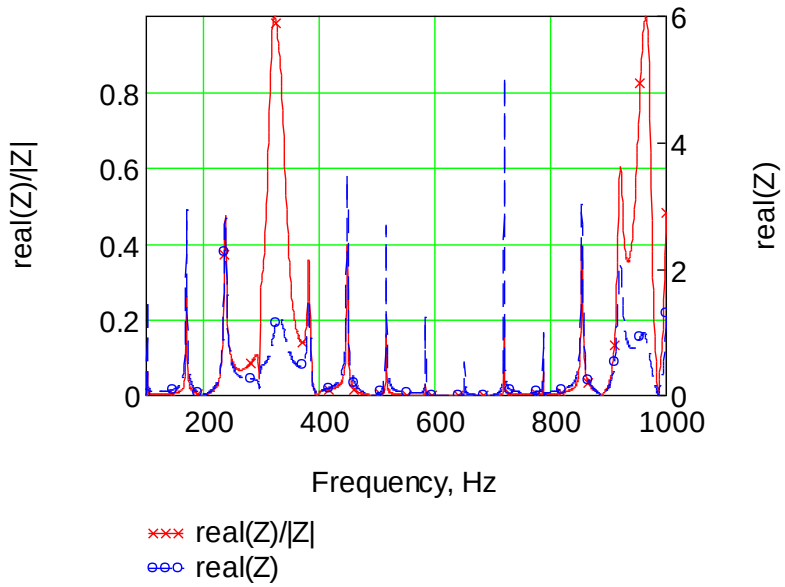

Figure 5.6: Re(Z)/|Z| and Re(Z) vs. Frequency for a speaker velocity of 1 m/s.

The effect of increasing the speaker forcing velocity to 10 m/s is seen in Figure 5.7 and Figure 5.8. Comparing these figures with those above reveals that increasing the forcing amplitude resulted in higher acoustic velocities and higher acoustic resistance. Focusing on the frequency around 310 Hz shows that the acoustic resistance of the area contraction was about 0.5 for this case compared with a value of about 0.2 for a speaker velocity of 1 m/s. At 310 Hz, the $|R|$ is actually higher for the 10 m/s speaker velocity case due to the higher resistance of the area contraction despite though the resistance being higher. In this case, the impedance is dominated by the resistance of the contraction causing the contraction to appear more like a rigid wall than a resistive junction.

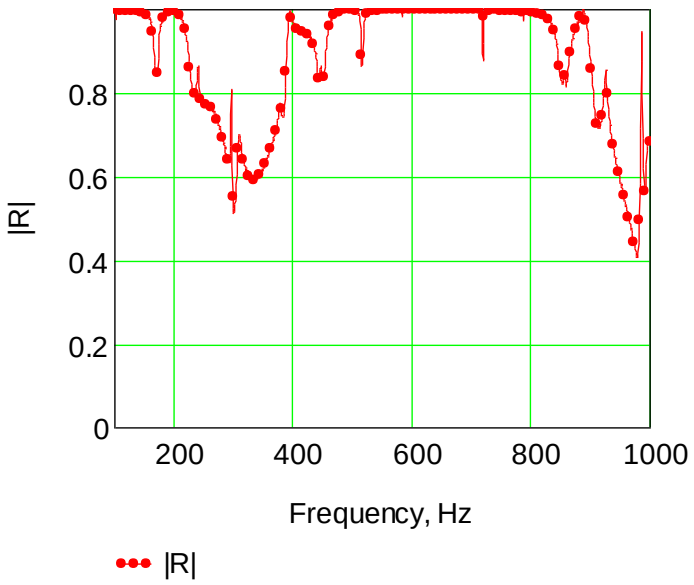

Figure 5.7: Magnitude of the reflection coefficient and area change acoustic velocity vs. Frequency for a speaker velocity of 10 m/s.

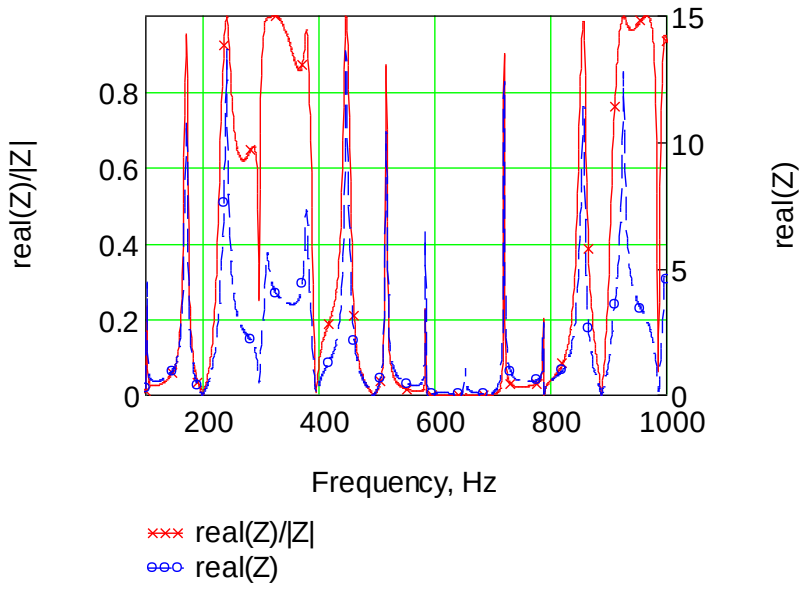

Figure 5.8: Re(Z)/|Z| and Re(Z) vs. Frequency for a speaker velocity of 10 m/s.

This analysis shows that (1) very high and very low acoustic resistances result in the $|R| \simeq 1$, (2) very low values for $|R|$ are only achieved when the acoustic resistance is of the order of the characteristic impedance of the system, (3) power is only dissipated when the acoustic resistance and the acoustic reactance of the system are of the same order of magnitude, and (4) no power is dissipated by the area contraction if the acoustic reactance of the system is much larger than the acoustic resistance.

5.3 An area expansion

The acoustically compact area expansion is another common duct element found in the FST. A schematic of this system is shown in Figure 5.9. In this case, the duct expands over some acoustically short distance from a smaller to larger duct cross-sectional area. This case differs from the case of the area contraction in that the source of acoustical energy was, in this case, assumed to originate in the duct having a small cross-sectional area. Therefore, acoustic energy was assumed lost in going from the smaller to the larger duct.

A schematic of the entire modeled system including the impedance tube is shown in Figure 5.9. The modeling approach for this case was very similar to that for the area contraction. Plane-wave, harmonic acoustic oscillations were assumed throughout with the exception of the vicinity of the area expansion, which was modeled as an area expansion using the theory developed in Chapter 3.

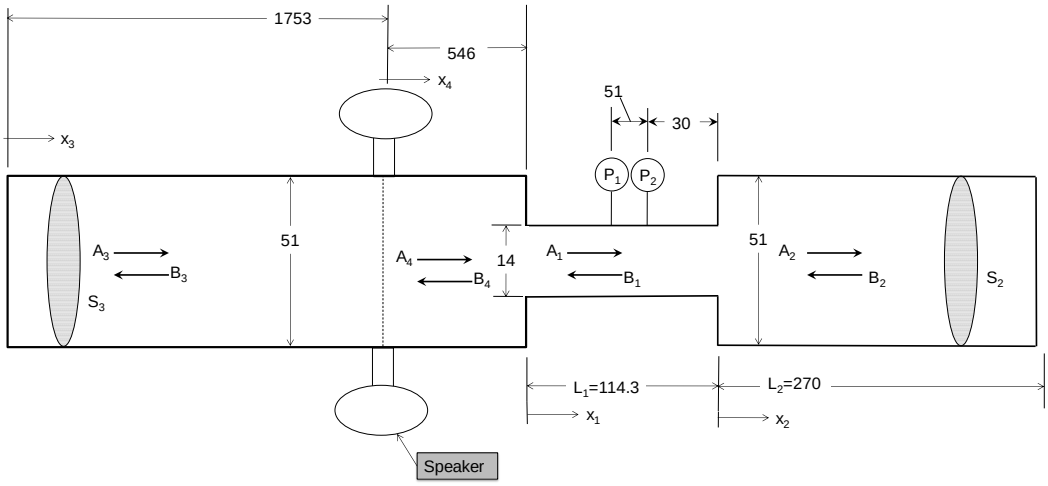

Figure 5.9: Acoustical network including the impedance tube with speakers, 14 mm diameter connecting tube, and the 51 mm extension tube. The area expansion is the junction of the 14 mm and 51 mm diameter tubes.

The modeling approach used was as follows. First, at the rigid end wall of the impedance tube, i.e., where $x_3 = 0$, it was assumed that the velocity vanished so that

$$u_3(x_3 = 0) = \frac{1}{(\rho c)_3}(A_3 - B_3) = 0\,. \tag{5.14}$$

At the location of the speakers, i.e., where $x_4 = 0$, the difference in volume velocity for sections 3 and 4 was assumed equal to the volume velocity of the speakers, assuming that the speakers behaved as a constant-amplitude, sinusoidal source of volume velocity. This requirement led to the following equation:

$$U_3 - U_4 = -U_{spkr}\,, \tag{5.15}$$

or

$$\frac{S_3}{(\rho c)_3}(A_3 e^{ikL_3} - B_3 e^{-ikL_3}) - \frac{S_4}{(\rho c)_4}(A_4 - B_4) = S_{spkr} u_{spkr}\,. \tag{5.16}$$

In addition, the pressure for tube sections 3 and 4 were assumed equal at $x_4 = 0$ so that

$$p_3 = p_4\,, \tag{5.17}$$

or

$$A_3 e^{ikL_3} + B_3 e^{-ikL_3} = A_4 + B_4\,. \tag{5.18}$$

A nonlinear impedance model was used at the area contraction, i.e., $x_1 = 0$, which led to the following expression

$$\frac{p_4(x_4 = L_4) - p_1(x_1 = 0)}{S_4 u_4(x_4 = L_4)} = Z_{41} = (\rho c)_4 \left\{ \frac{i\frac{\omega}{c}L_{e,41}}{S_4} + \left(\frac{|u_4'|}{2 \cdot c}\right) \frac{\left[\left(\frac{S_1}{S_4}\right)^2 - 1\right]}{S_4} \right\}. \tag{5.19}$$

Expression the left hand side of Eq. (5.19) in terms of left and right traveling plane waves and rearranging yields

$$A_4 e^{ikL_4}\left[1 - \frac{S_4}{(\rho c)_4} Z_{41}\right] + B_4 e^{-ikL_4}\left[1 + \frac{S_4}{(\rho c)_4} Z_{41}\right] - (A_1 + B_1) = 0\,. \tag{5.20}$$

In addition, continuity of volume velocity at the area contraction required that

$$U_4\left(x_4 = L_4\right) - U_1\left(x_1 = 0\right) = 0\,, \tag{5.21}$$

or

$$\frac{S_4}{\left(\rho c\right)_4}\left(A_4 e^{ikL_4} - B_4 e^{ikL_4}\right) - \frac{S_1}{\left(\rho c\right)_1}\left(A_1 - B_1\right) = 0\,. \tag{5.22}$$

Next, continuity of volume velocity at the area expansion requires that

$$U_2\left(x_1 = L_1\right) = U_1\left(x_2 = 0\right) \tag{5.23}$$

or

$$\frac{S_1}{\left(\rho c\right)_1}\left(A_1 e^{ikL_1} - B_1 e^{-ikL_1}\right) = \frac{S_2}{\left(\rho c\right)_2}\left(A_2 - B_2\right). \tag{5.24}$$

The impedance of the area expansion in terms of Z_{12} given by Eq. (3.32), which relates the pressure drop across the expansion and acoustic volume velocity as follows:

$$Z_{12} = \frac{p_1\left(x_1 = L_1\right) - p_2\left(x_2 = 0\right)}{S_1 u_1\left(x_1 = L_1\right)} = \frac{\left(\rho c\right)_1}{S_1}\left\{ikL_{eff}^{c} + \left(\frac{2\left|u_1\right|}{c_1}\right)\left(\frac{S_1}{S_2}\right)^2\left[1 - \frac{S_2}{S_1}\right]\right\}. \tag{5.25}$$

After expressing the acoustic pressures and velocity as the sum of right and left traveling plane waves and rearranging,

$$A_1 e^{ikL_1}\left[1 - \frac{S_1}{\left(\rho c\right)_1} Z_{12}\right] + B_1 e^{-ikL_1}\left[1 + \frac{S_1}{\left(\rho c\right)_1} Z_{12}\right] - \left(A_2 + B_2\right) = 0\,. \tag{5.26}$$

The final boundary condition was that the acoustic velocity must vanish at the rigid end-termination, which was expressed by

$$u_2\left(x_2 = L_2\right) = 0\,, \tag{5.27}$$

or

$$A_2 e^{ikL_2} - B_2 e^{-ikL_2} = 0\,. \tag{5.28}$$

Equations (5.14), (5.16), (5.18), (5.20), (5.22), (5.24), (5.26), and (5.28) are needed to find the eight unknown complex amplitudes. In addition Eq. 3.32 gives the impedance for an acoustically compact area expansion. This system of equations is nonlinear in two acoustic velocities, specifically the acoustic velocity at the area contraction and the acoustic velocity at the area expansion. Therefore, two additional constraint equations are required to solve this system of equations. These constraint equations are given by

$$\left|\frac{S_1}{(\rho c)_1}\left(A_1 e^{ikL_1} - B_1 e^{-ikL_1}\right)\right| = |u_1'| S_1 \tag{5.29}$$

and

$$\left|\frac{S_4}{(\rho c)_4}\left(A_4 e^{ikL_4} - B_4 e^{-ikL_4}\right)\right| = |u_4'| S_4, \tag{5.30}$$

where $|u_1'|$ and $|u_4'|$ were the acoustic velocities used in the nonlinear impedances $Z_{12}\left(|u_1'|\right)$ and $Z_{41}\left(|u_4'|\right)$, respectively. Physically, these constraint equations require that the acoustic velocity magnitudes used in the impedance relations be equal to acoustic velocity magnitudes obtained by solving the system of model equations above.

The results of these calculations for the magnitude and phase of the reflection coefficient measured at $x_1 = L_1$ are shown in Figure 5.10. Figure 5.11 shows the predicted magnitude and phase of the impedance of the area expansion.

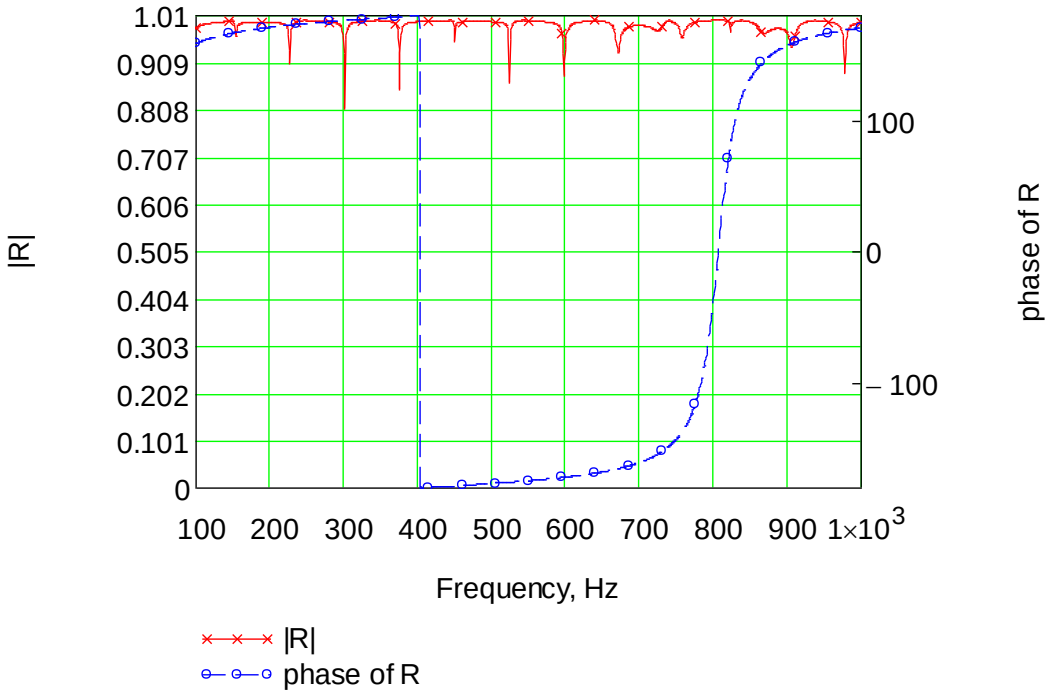

Figure 5.10: Magnitude and phase of the reflection coefficient at the area expansion vs. Frequency.

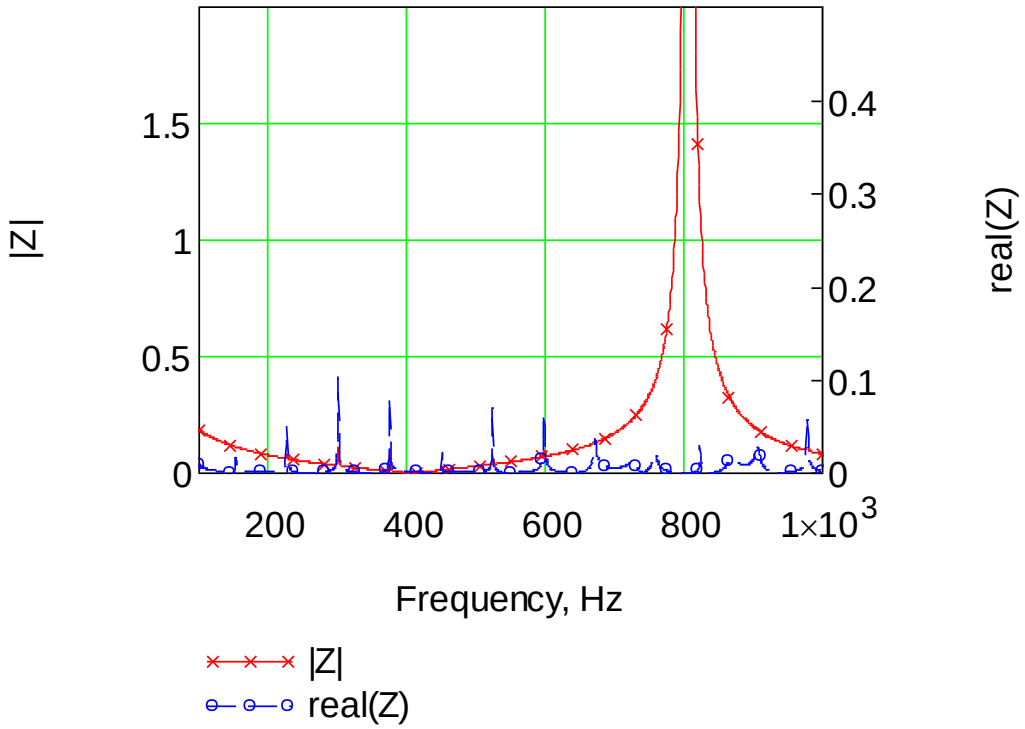

Figure 5.11: Magnitude and real part of the impedance of the area expansion vs. Frequency.

5.4 A 'Tee' junction

Figure 5.12 shows a schematic of a 'tee' junction, which joins three rigidly-terminated branch tubes having lengths L_1, L_2, and L_3, respectively. For this study, it was assumed that the area in the vicinity of the junction point (marked by a dashed box in Figure 5.12) formed an incompressible, acoustically compact region, i.e., its dimensions were much smaller than the wavelength in the relevant frequency range.

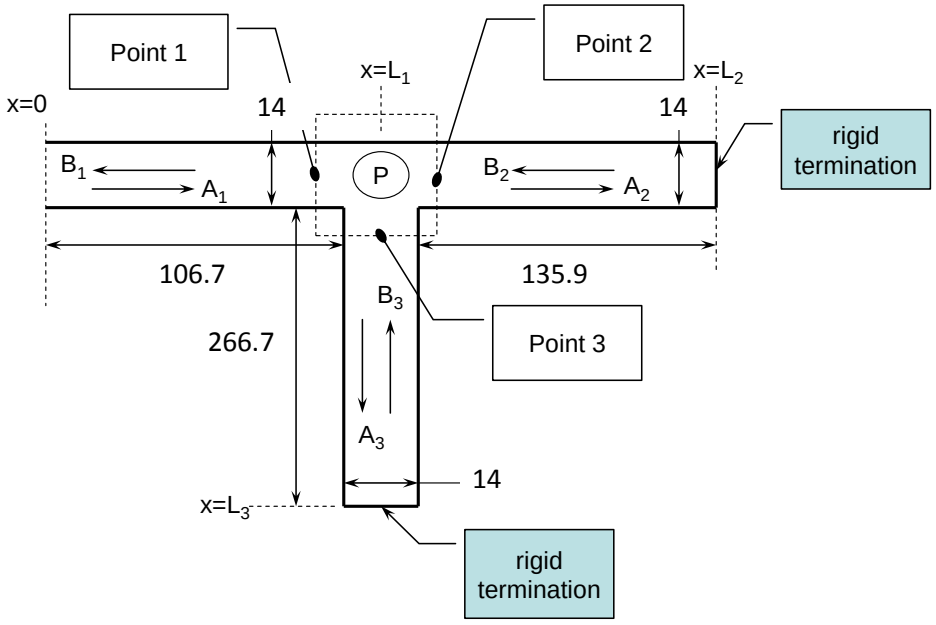

Figure 5.12: Schematic of 'tee' junction of three tubes.

The boundary condition equations were developed as follows. The pressure difference $P_1 - P$ was related to the acoustic volume velocity U_1 at $x_1 = L_1$ through the impedance as follows:

$$\frac{P_1 - P}{U_1} = Z_{1.} \tag{5.31}$$

Substituting the appropriate expressions for the acoustic pressure and volume velocity leads to

$$\frac{\left(A_1 e^{ikL_1} + B_1 e^{-ikL_1}\right) - P}{\frac{S_1}{\rho c}\left(A_1 e^{ikL_1} - B_1 e^{-ikL_1}\right)} = Z_1. \tag{5.32}$$

Similarly, the pressures and volume velocities at points 2 and 3 were related to their respective volume velocities by

$$\frac{P - \left(A_2 + B_2\right)}{\frac{S_2}{\rho c}\left(A_2 - B_2\right)} = Z_2 \tag{5.33}$$

and

$$\frac{P - \left(A_3 + B_3\right)}{\frac{S_3}{\rho c}\left(A_3 - B_3\right)} = Z_3. \tag{5.34}$$

Z_1, Z_2, and Z_3 were given by Eq. (3.14), and *P* was the acoustic pressure common to all locations in the junction of the 'tee'.

Applying continuity, the volume velocities at the three points summed to zero leading to the following equation:

$$U_1 = U_2 - U_3 \tag{5.35}$$

or

$$\frac{S_1}{(\rho c)}\left(A_1 e^{ikL_1} - B_1 e^{-ikL_1}\right) = \frac{S_2}{(\rho c)}\left(A_2 - B_2\right) + \frac{S_3}{(\rho c)}\left(A_3 - B_3\right). \tag{5.36}$$

Since the velocity was zero at $x = L_2$ and $x = L_3$ due to the presence of rigid terminations there, the following two equations must be satisfied:

$$\frac{S_2}{(\rho c)_2}\left(A_2 e^{ikL_2} - B_2 e^{-ikL_2}\right) = 0 \tag{5.37}$$

and

$$\frac{S_3}{(\rho c)_3}\left(A_3 e^{ikL_3} - B_3 e^{-ikL_3}\right) = 0. \tag{5.38}$$

Finally, since the pressure P_{ext} at $x = 0$ was imposed, it follows that

$$P_1(x = 0) = A_1 + B_1 = P_{ext} . \tag{5.39}$$

These seven equations, Eqs. (5.32)-(5.39), were solved for the six complex amplitudes and the junction pressure *P*. As with the previous examples, the solution was obtained iteratively using the procedure illustrated in Figure 5.13.

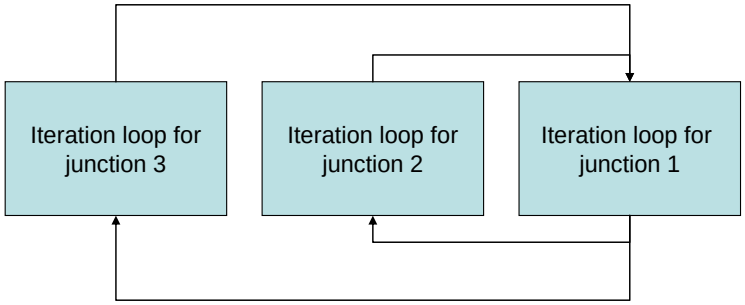

Figure 5.13: Iteration procedure for the 'tee' junction

Figure 5.14 shows a comparison between the predicted and measured reflection coefficient of a 'tee' junction whose dimensions are shown in Figure 5.12. As explained previously the experimental reflection coefficient was obtained from pressure measurements in the two-microphone impedance tube. Figure 5.14 shows that the theory predicts the phase of the reflection coefficient very precisely. Also, the theoretical model predicted the minimum of the amplitude of the reflection coefficient very well. However, there was a discrepancy of about 5% in the frequency at which the amplitude minimum occurs. This small disagreement could very likely be corrected with a more accurate choice of the effective lengths of the 'tee' junctions.

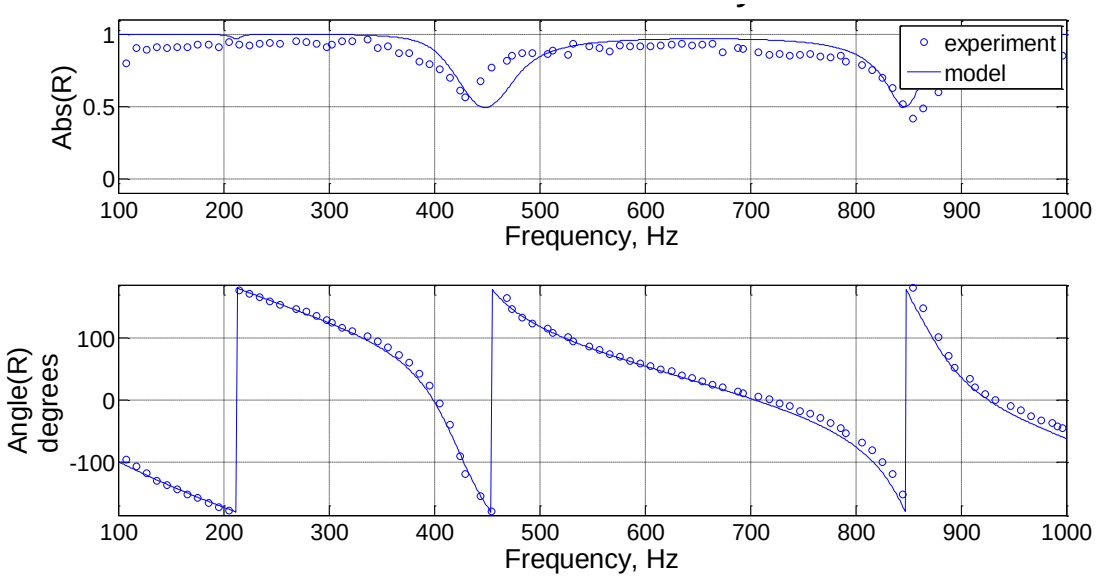

Figure 5.14: Comparison of tee model and measurements of the reflection coefficient taken in the impedance tube.

5.5 Variable area gate valve

As a final example, the gate valve shown in Figure 5.15 was modeled as a sudden area contraction followed by a sudden area expansion.

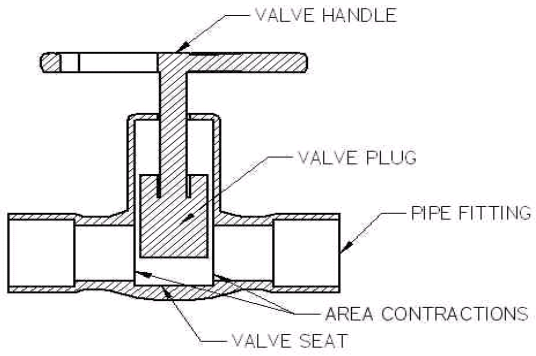

Figure 5.15: Schematic of a commercial gate valve

The system model, which included the valve in series with a rigidly terminated tube, is shown in Figure 5.16. Although the end-termination was assumed rigid, any other end-termination impedance could also be treated with this model.

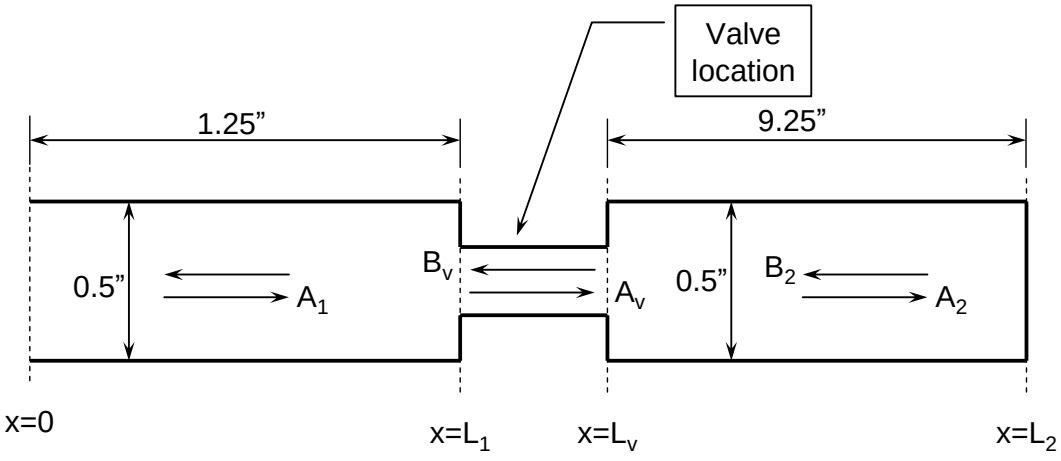

Figure 5.16: Schematic of a rigidly terminated duct section containing a gate valve located at L_v.

As in the previous examples, a fixed value for the acoustic pressure amplitude P_{ext} at $x=0$ was assumed. Using Eqs. (5.1), the pressure at $x=0$ was expressed as

$$A_1 + B_1 = P_{ext}\,. \tag{5.40}$$

The valve resistance and reactance was accounted for by using the impedance of an acoustically compact area contraction. By definition, the pressure across the acoustically compact junction at $x=L_1$ is related to the acoustic volume velocity through the acoustic impedance Z_{v1} of the junction as follows:

$$\frac{\left(A_1 e^{ikL_1} + B_1 e^{-ikL_1}\right) - \left(A_v + B_v\right)}{\frac{S_1}{(\rho c)_1}\left(A_1 e^{ikL_1} - B_1 e^{-ikL_1}\right)} = Z_{v1}\,. \tag{5.41}$$

Similarly, the pressure difference across the acoustically compact junction at $x=L_2$ was related to the acoustic volume velocity at the same location through the acoustic impedance Z_{v2} of the junction as follows:

$$\frac{\left(A_v e^{ikL_v} + B_v e^{-ikL_v}\right) - \left(A_2 + B_2\right)}{\frac{S_2}{(\rho c)_2}\left(A_2 - B_2\right)} = Z_{v2}, \tag{5.42}$$

where Z_{v1} and Z_{v2} are the impedances, which are given by appropriate forms of Eq. (3.14). By continuity, the volume velocity at $x=L_1$ equaled that at $x=L_v$, which yielded

$$\frac{S_v}{(\rho c)_v}\left(A_v e^{ikL_v} - B_v e^{-ikL_v}\right) = \frac{S_2}{(\rho c)_2}\left(A_2 - B_2\right) \tag{5.43}$$

and

$$\frac{S_1}{(\rho c)_1}\left(A_1 e^{ikL_1} - B_1 e^{-ikL_1}\right) = \frac{S_v}{(\rho c)_v}\left(A_v - B_v\right). \tag{5.44}$$

Finally, the zero velocity boundary condition at the rigid termination at $x=L_2$ required that

$$\frac{S_2}{(\rho c)_2}\left(A_2 e^{ikL_2} - B_2 e^{-ikL_2}\right) = 0\,. \tag{5.45}$$

The resulting six equations with six unknowns were solved simultaneously. Since there were only two nonlinear boundary conditions, the solution required only two "nested" iteration loops.

Figure 5.17 and Figure 5.18 show the comparisons between the predicted and measured reflection coefficient of the gate valve system having the physical dimensions shown in Figure 5.16. In Figure 5.17, the valve was completely closed, and in Figure 5.18, it was partially open. As expected, when nearly closed, the reflection magnitude was nearly unity for all frequencies.

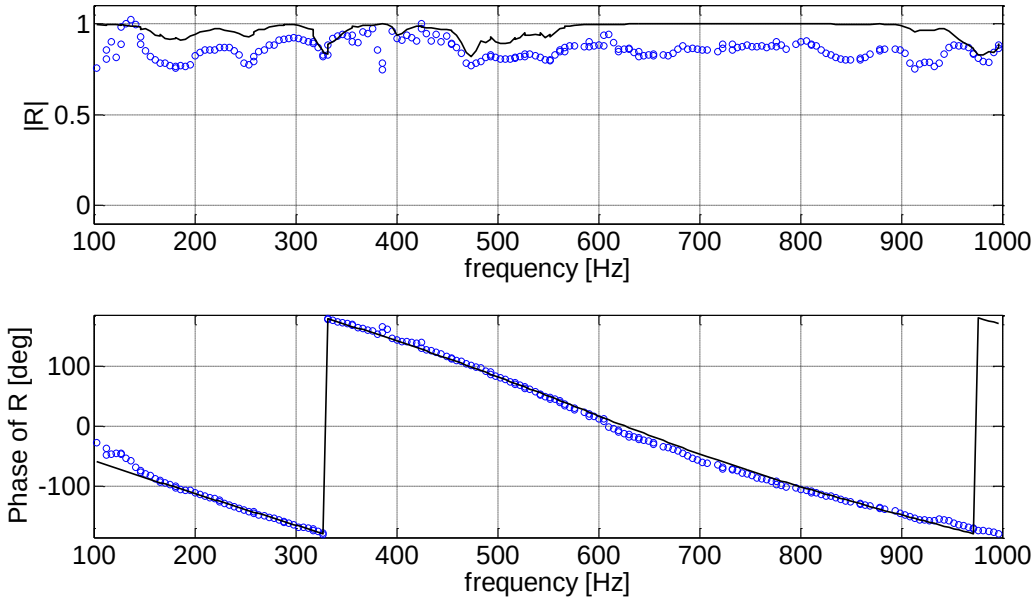

Figure 5.17: Measured (o) and predicted (-) reflection coefficient vs. Frequency for the gate valve nearly closed.

The resistive nature of the valve is clear in Figure 5.18. The variation with frequency seen is due to the fact that the acoustic velocity amplitude at the valve depends on the driving frequency due to the geometry of the system. The importance of this observation is that the model effectively captures the physical behavior of the valve.

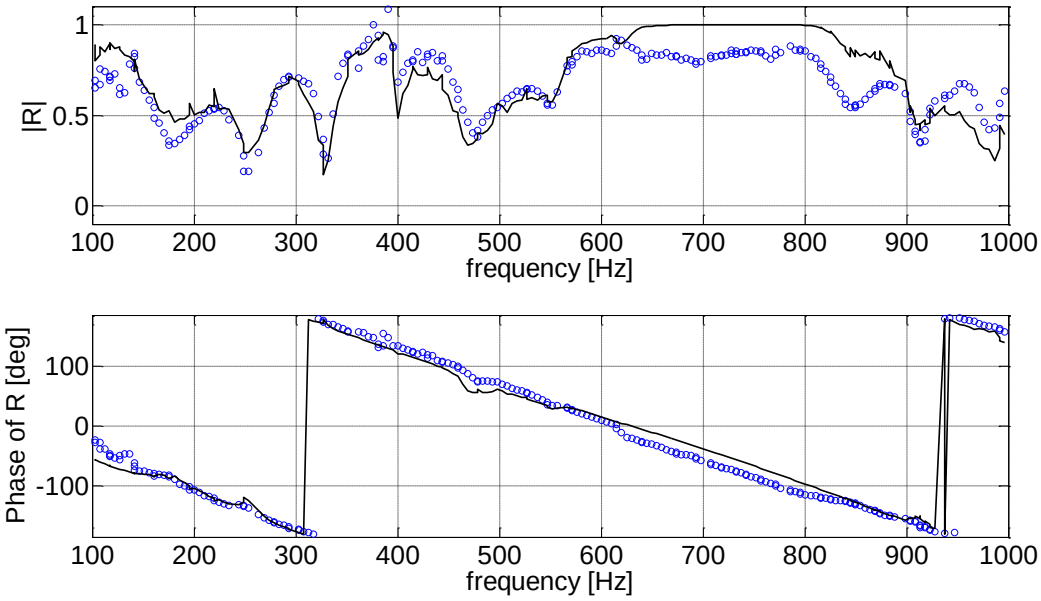

Figure 5.18: Measured (o) and predicted (-) reflection coefficient vs. Frequency for the gate valve partially open.

5.6 Combined area change and gate valve

Although the primary objective of this study was to model the entire FST, more understanding can be obtained by studying the interaction of simple combinations of resistive elements like the area contraction and the valve in an acoustic network. Therefore, this section presents the results of a network containing both an abrupt area contraction and a variable area gate valve. The system modeled is shown in Figure 5.19.

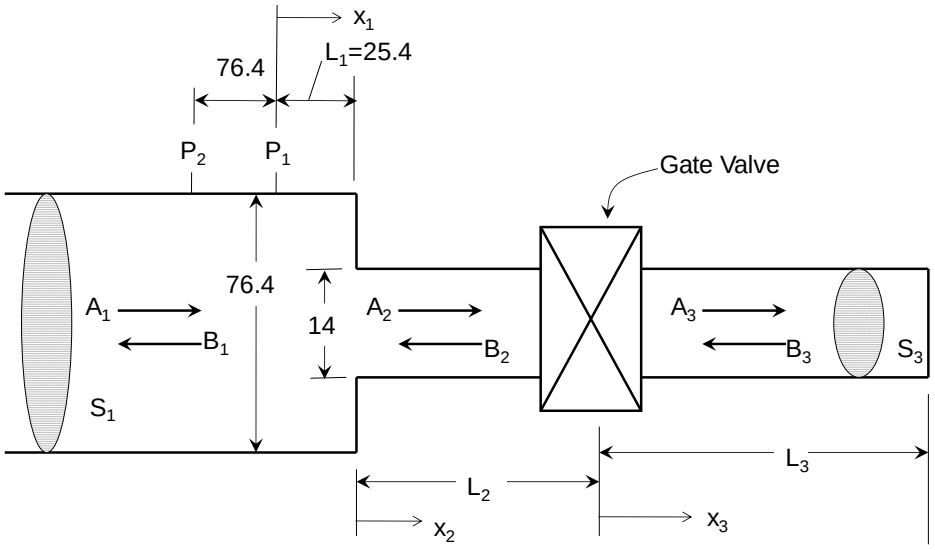

Figure 5.19: Schematic of the system including an area contraction and a variable area gate valve followed by a rigid-walled, rigidly terminated tube.

The investigated system consists of an area contraction, a short length of rigid-walled duct having a diameter of 14 mm, variable area gate valve, and a length of 14 mm diameter, rigid-walled, rigidly terminated tube connected in series. The model for this system assumed that the area contraction and the variable area gate valve were both area contractions with nonlinear acoustic impedances.

5.6.1 Model development

For comparison with the experimental data taken in the impedance tube, a model was developed taking advantage of the fact that the pressure at the location marked $x_1 = 0$ was measured. The model development proceeded as follows.

First, as noted, the pressure P_{ext} at $x_1 = 0$ was measured so that

$$p_1(x_1 = 0) = P_{ext}. \tag{5.46}$$

Expressing Eq. (5.46) in terms of right and left traveling, plane waves yielded

$$A_1 + B_1 = P_{ext}. \tag{5.47}$$

The boundary conditions at the location $x_2 = 0$ required that the volume velocity across the area contraction be conserved, which was expressed as follows

$$U_1(x_1 = L_1) = U_2(x_2 = 0), \tag{5.48}$$

or in terms of right and left traveling, plane waves

$$\frac{S_1}{(\rho c)_1}\left(A_1 e^{ikL_1} - B_1 e^{-ikL_1}\right) - \frac{S_2}{(\rho c)_2}(A_2 - B_2) = 0. \tag{5.49}$$

Also, the impedance of the area contraction required that

$$\frac{p_1(x_1 = L_1) - p_2(x_2 = 0)}{S_1 u_1(x_1 = L_1)} = Z_{12} = \frac{i\frac{\omega}{c}L_{e,12}}{S_1} + \left(\frac{|u_1'|}{2 \cdot c}\right)\frac{\left[\left(\frac{S_1}{S_2}\right)^2 - 1\right]}{S_1}. \tag{5.50}$$

Expressing the pressures and velocity in Eq. (5.50) in terms of right and left traveling plane waves and rearranging yielded

$$A_1 e^{ikL_1}\left[1 - \frac{S_1}{(\rho c)_1}Z_{12}\right] + B_1 e^{-ikL_1}\left[1 + \frac{S_1}{(\rho c)_1}Z_{12}\right] - (A_2 + B_2) = 0. \tag{5.51}$$

The same methodology was used at $x_2 = L_2$ and $x_3 = 0$ to obtain the following equations expressing the impedance and continuity of volume velocity at these two locations. First, at location $x_2 = L_2$

$$A_2 e^{ikL_2}\left[1-\frac{S_2}{(\rho c)_2}Z_{2v}\right]+B_2 e^{-ikL_2}\left[1+\frac{S_2}{(\rho c)_2}Z_{2v}\right]-(A_v+B_v)=0 \tag{5.52}$$

and

$$\frac{S_2}{(\rho c)_2}\left(A_2 e^{ikL_2}-B_2 e^{-ikL_2}\right)-\frac{S_v}{(\rho c)_v}(A_v-B_v)=0, \tag{5.53}$$

where the acoustic impedance is given by

$$Z_{v2}=\frac{i\frac{\omega}{c}L_{e,2v}}{S_2}+\left(\frac{|u_2'|}{2\cdot c}\right)\frac{\left[\left(\frac{S_2}{S_v}\right)^2-1\right]}{S_2}. \tag{5.54}$$

Next, at location $x_3 = 0$

$$A_v e^{ikL_v}\left[1-\frac{S_v}{(\rho c)_v}Z_{v3}\right]+B_v e^{-ikL_v}\left[1+\frac{S_v}{(\rho c)_v}Z_{v3}\right]-(A_3+B_3)=0 \tag{5.55}$$

and

$$\frac{S_v}{(\rho c)_v}\left(A_v e^{ikL_v}-B_v e^{-ikL_v}\right)-\frac{S_3}{(\rho c)_3}(A_3-B_3)=0, \tag{5.56}$$

where

$$Z_{v3}=\frac{i\frac{\omega}{c}L_{e,v3}}{S_v}+\left(\frac{|u_v'|}{2\cdot c}\right)\frac{\left[\left(\frac{S_v}{S_3}\right)^2-1\right]}{S_v}. \tag{5.57}$$

Finally, the acoustic velocity u_3 vanished at the rigid end-termination located at $x_3 = L_3$ requiring that

$$u_3\left(x_3 = L_3\right) = \frac{S_3}{\left(\rho c\right)_3}\left(A_3 e^{ikL_3} - B_3 e^{-ikL_3}\right) = 0\,. \tag{5.58}$$

Equations (5.47), (5.49), (5.51), (5.52) with (5.54), (5.53), (5.55) with (5.57), (5.56), and (5.58) are eight, nonlinear, algebraic equations for the eight unknown complex amplitudes.

These equation above were solved subject to the following constraint equations:

$$\left|\frac{S_2}{\left(\rho c\right)_2}\left(A_2 e^{ikL_2} - B_2 e^{-ikL_2}\right)\right| = \left|u_2'\right| S_2, \tag{5.59}$$

$$\left|\frac{S_v}{\left(\rho c\right)_v}\left(A_v e^{ikL_v} - B_v e^{-ikL_v}\right)\right| = \left|u_v'\right| S_v, \tag{5.60}$$

and

$$\left|\frac{S_1}{\left(\rho c\right)_1}\left(A_1 e^{ikL_1} - B_1 e^{-ikL_1}\right)\right| = \left|u_1'\right| S_1\,. \tag{5.61}$$

These equations express the requirement that the acoustic velocity obtained from the complex coefficients must equal the acoustic velocity used in the nonlinear acoustic impedance expressions. A linear acoustic response model was obtained from the equations above by setting Z_{12}, Z_{v2}, and Z_{v3} equal to zero.

The magnitude and phase of the reflection coefficient just upstream of the area contraction $(x_1 = L_1)$ was computed from the calculated complex coefficients assuming that the pressure at this location was constant. These calculations were made for seven valve positions ranging from completely closed to completely opened. The results of these calculations are shown in Figure 5.21.

5.6.2 Model/experiment comparison

In this section, the predictions of the developed linear and nonlinear acoustic response models are compared with acoustic response measurements. Figure 4.34 shows the predictions of a linear acoustic system model. It shows that the linear model predicted the resonances of the system but that the $|R| = 1$ for all frequencies. However, no information about the resistive properties of the system was obtained from the linear model.

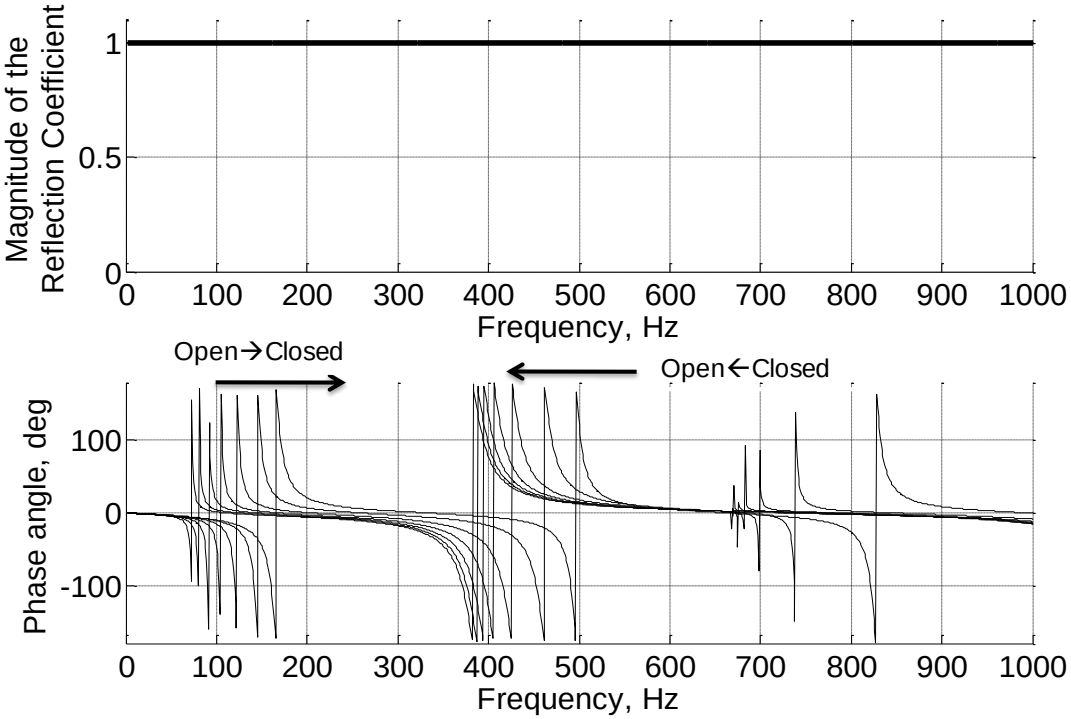

Figure 5.20: Linear model predictions for the magnitude and phase of the reflection coefficient vs. Frequency just upstream of the area contraction for seven valve positions ranging from completely closed to completely open.

Figure 5.21 and Figure 4.35 shows the nonlinear model predictions and acoustic response measurements for the reflection coefficient magnitude and phase spectrum for seven different valve settings, respectively. Comparing the two figures, it is clear that

the model accurately predicts that the $|R|$ is minimized at 180 and 480 Hz when the valve is open and that the $|R|$ is minimized at 380 Hz when the valve is closed.

When the valve was completely open (valve setting 1) or closed (valve setting 7), the source of the damping was the nonlinear resistance of the area contraction upstream of the valve. At intermediate valve positions, the total system damping was due to both the nonlinear resistance of the area contraction and the valve.

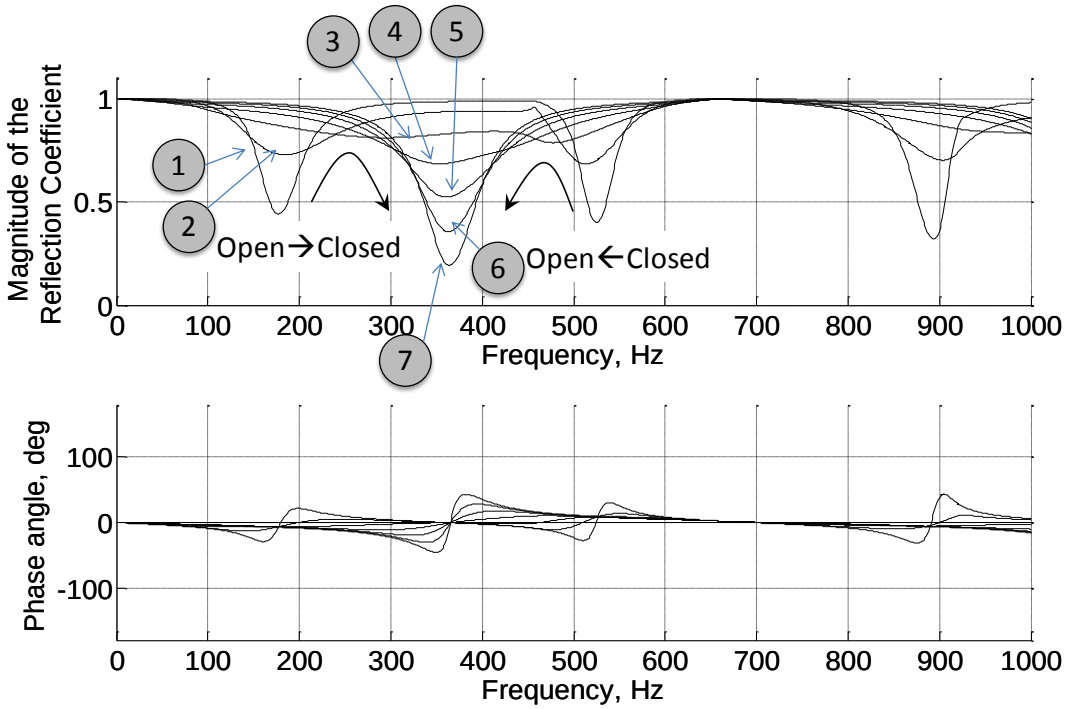

Figure 5.21: Nonlinear model predictions of the magnitude and phase of the reflection coefficient vs. frequency just upstream of the area contraction for seven valve positions ranging from completely closed to completely open.

For valve positions 3 and 4, the $|R|$ deviates significantly from one over the entire frequency range from 100 to 600 Hz. Further closing the valve causes the damping to be increasingly focused around 370 Hz.

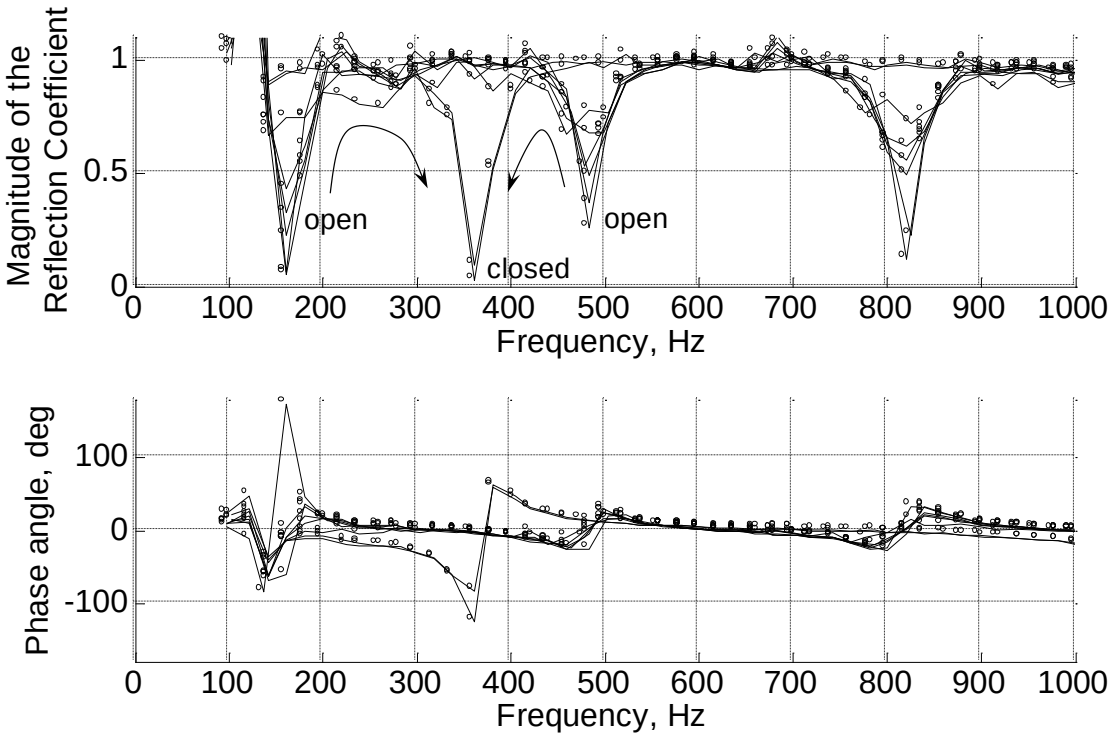

Figure 5.22: Experimental measurements of the magnitude and phase of the reflection coefficient vs. frequency for a range of valve settings.

5.6.3 Impedance tube model studies

To gain further insight into the physical behavior of the area change/valve system, a model was developed for the system shown in Figure 5.23 with $L_2 = 241.3$ mm and $L_3 = 266.7$ mm. This model is identical to the model developed in Section 5.6.2 except that it includes the impedance tube geometry as well.

In these studies, Equations (5.49), (5.51), (5.52) with (5.54), (5.53), (5.55) with (5.57), (5.56), and (5.58) along with the constraint equations still apply. The acoustic speaker diaphragm velocity u_{spkr} was specified. Therefore, Eq. (5.47) was eliminated and three additional equations were developed in order to solve for the ten unknown complex amplitudes. These additional equations were developed as follows.

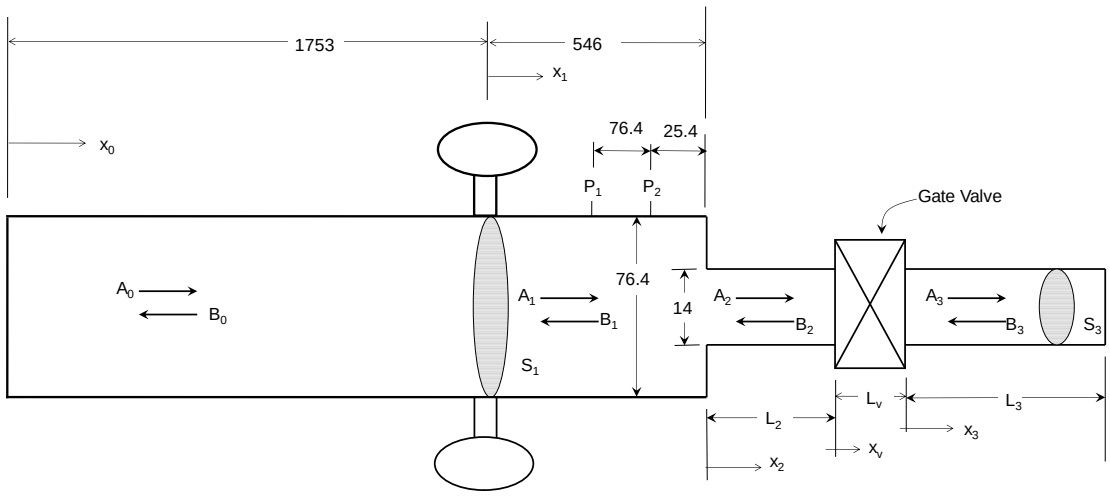

Figure 5.23: Schematic of the system including an area contraction and a variable area gate valve followed by a rigid-walled, rigidly terminated tube.

First, the rigid-termination at $x_0 = 0$ requires that the acoustic velocity there equal zero yielding

$$u_0(x_0 = 0) = (A_0 - B_0) = 0\,. \tag{5.62}$$

The two additional equations were obtained from the requirement that the sum of the volume velocities at the speaker be zero and that the pressures were equal, leading to the following two equations:

$$U_0(x_0 = L_0) - U_1(x_1 = 0) = -U_{spkr} \tag{5.63}$$

and

$$p_0(x_0 = L_0) - p_1(x_1 = 0) = 0\,. \tag{5.64}$$

Expressing the acoustic velocities and pressures in terms of right and left traveling, plane waves yielded

$$\frac{S_0}{(\rho c)_0}\left(A_0 e^{jkL_0} - B_0 e^{-jkL_0}\right) - \frac{S_1}{(\rho c)_1}(A_1 - B_1) = -S_{spkr} u_{spkr} \tag{5.65}$$

and

$$\left(A_0 e^{ikL_0} + B_0 e^{-ikL_0}\right) - \left(A_1 + B_1\right) = 0\,. \tag{5.66}$$

Equations (5.62), (5.65), and (5.66) comprised the three additional equations required to solve for the ten unknown complex amplitudes.

Recall that the acoustic impedance and phase of the acoustic impedance are related to the reflection coefficient by

$$\frac{Z}{\left(\rho c / S\right)} = \frac{1+R}{1-R} \tag{5.67}$$

and

$$\phi_Z = \tan^{-1}\left[\frac{\mathrm{Re}(Z)}{\mathrm{Im}(Z)}\right]. \tag{5.68}$$

The acoustic resistance was computed from the real part of Eq. (5.67).

Both the acoustic resistance and ϕ_Z were computed for the system downstream of the location $x_1 = L_1$ (termed 'system') and of the system downstream of the location $x_2 = L_2$ (termed 'valve') for five different valve settings. These predictions are shown in Figure 5.24 through Figure 5.33.

5.6.3.1 Effect of valve resistance on system impedance magnitude

The acoustic resistance and phase of the acoustic impedance for the valve 100%, 55%, 25%, 11%, and 0% open are shown in Figure 5.24 through Figure 5.28. In general, the acoustic resistance of the area contraction dominated while the valve was open. As the valve was gradually closed, the valve resistance increased until its resistance dominated over the resistance of the area contraction. Note that in each of the figures, the frequency dependence of the valve and area contraction is due to the fact that the local acoustic velocity, which is part of the cause of the resistance, at the valve and area contraction is also frequency dependent. Details of this behavior are given below. Also, the system is most affected when the acoustic impedance is mostly resistive. Therefore, the system is most affected by increased resistance near system resonance when the reactance is near zero.

Figure 5.24 shows that the acoustic resistance of the valve was zero and the damping was due entirely to the presence of the area contraction. The resistance of the entire system (area contraction plus the valve) in this case was as much as five times the characteristic impedance.

The valve resistance for the 55% open valve setting (see Figure 5.25) was much larger than for the 100% open case. However, its highest value was only 15% of the characteristic impedance. At 700 Hz, the resistance of the valve was 0.075. Though small, this was high enough to cause the resistance of the entire system to be 3800 times the characteristic impedance.

Figure 5.26 shows the magnitude and phase of the valve and system reflection coefficients for the case where the valve was only open 25%. At this setting, the acoustic resistance of the valve at 700 Hz, for example, was as high as 0.6. Notice,

however, that the resistance of the entire system decreased somewhat to 825. Also, the resistance of the area contraction near 325 Hz increased to 200 where it had not been significant before.

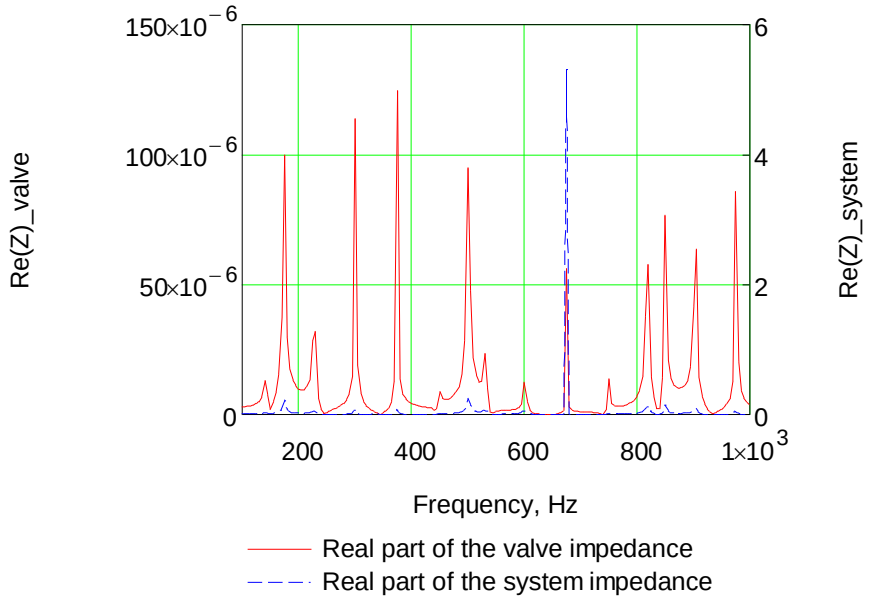

Figure 5.24: Real part of the valve and system impedances vs. Frequency when the valve was open 100%.

Closing the valve to the 11% open position, yielded the model predictions shown in Figure 5.27. They show that, compared to the previous case, the valve impedance increased by nearly an order of magnitude for most frequencies. At 700 Hz, the valve and system resistances were 12 and 185, respectively. In this case, increasing valve resistance decreased the overall system impedance at 325 and 700 Hz.

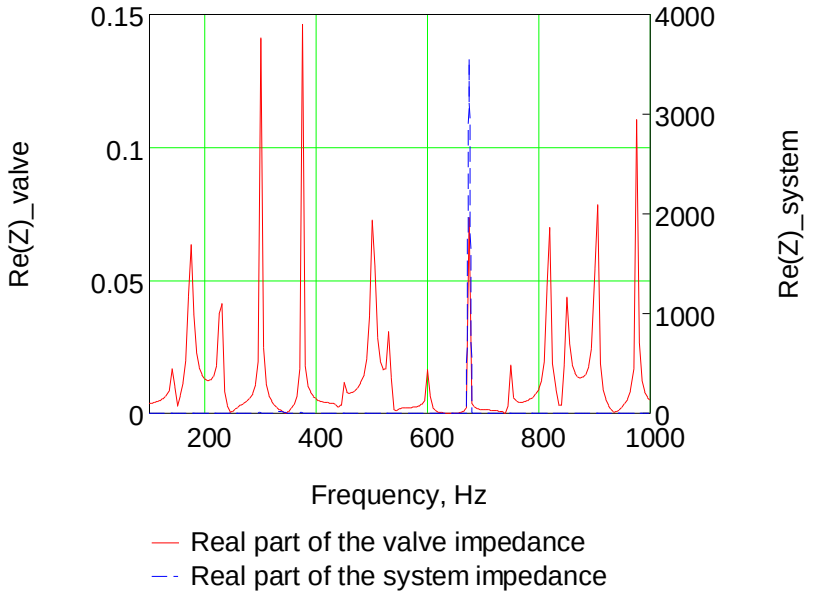

Figure 5.25: Real part of the valve and system impedances vs. Frequency when the valve was open 55%.

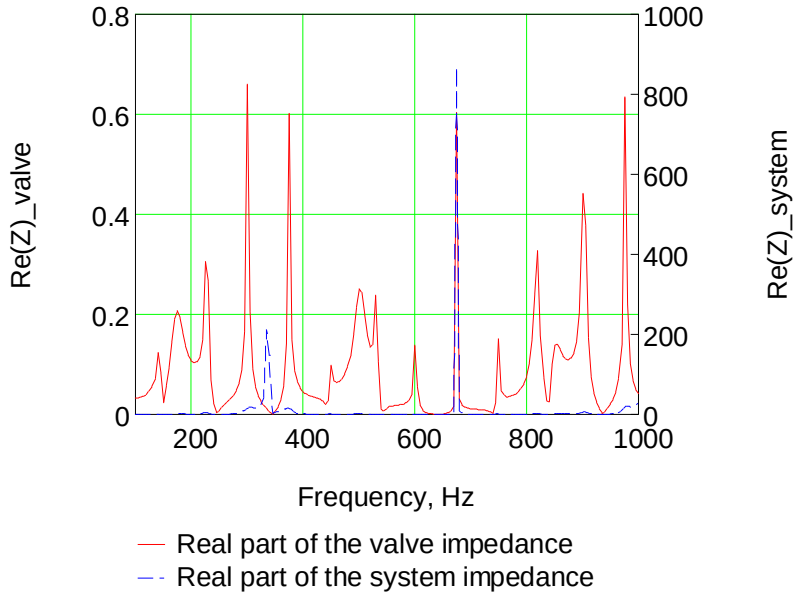

Figure 5.26: Real part of the valve and system impedances vs. Frequency when the valve was open 25%.

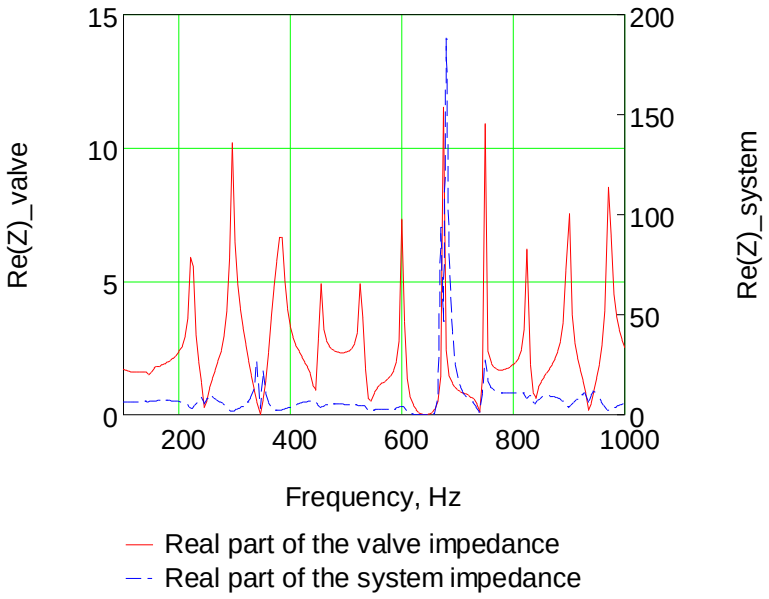

Figure 5.27: Real part of the valve and system impedances vs. Frequency when the valve was open 11%.

Figure 5.28 shows the model predicted resistance for the valve and system when the valve was completely closed. In this case, the valve resistance was, as it should be, nearly infinite. At this setting, the valve is seen by the acoustic oscillations as a rigid end-termination. Also, the resistance of the system at 700 Hz increased compared to the 11% open case.

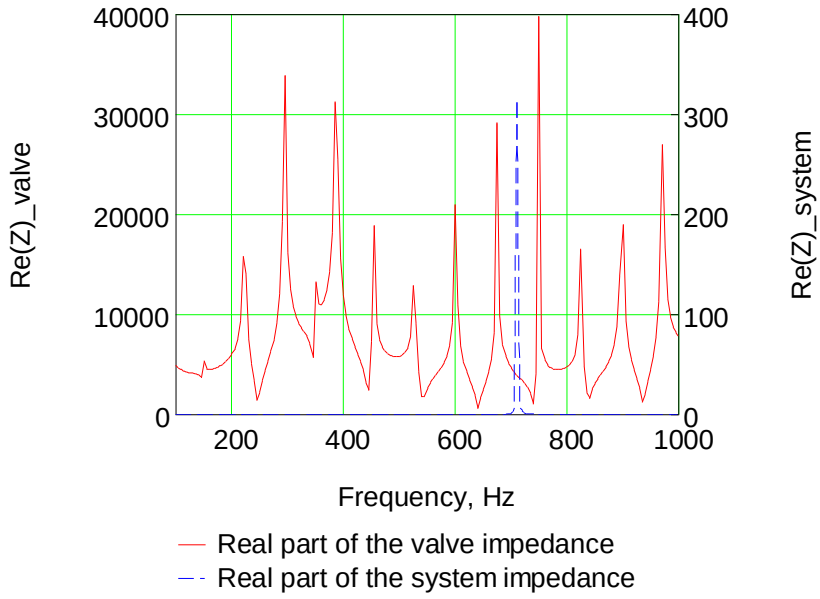

Figure 5.28: Real part of the valve and system impedances vs. Frequency when the valve was completely closed.

These results show that (1) closing the valve increases the valve resistance due to nonlinear acoustic effects, (2) the completely closed valve is effectively a rigid end-termination, (3) the open valve is effectively a short length of rigid-walled tube, (4) and (4) increasing valve resistance affects the resistance of other nonlinear elements.

5.6.3.2 Effect of valve resistance on system impedance phase

The acoustic resistance and phase of the acoustic impedance for the valve 100%, 55%, 25%, 11%, and 0% open are shown in Figure 5.29 through Figure 5.33. Recall that for systems with no damping, the magnitude of the phase is 90 degrees, and the sign of the phase changes abruptly at the resonant frequencies. Damping causes the magnitude of the phase to be less than 90 degrees, and the slope of the phase roll-off with frequency to be finite.

Figure 5.29 shows that, in this case, the damping is too small to significantly affect the phase behavior. In this case, the slope of the phase roll-off with frequency was nearly infinite for both the valve and the entire system.

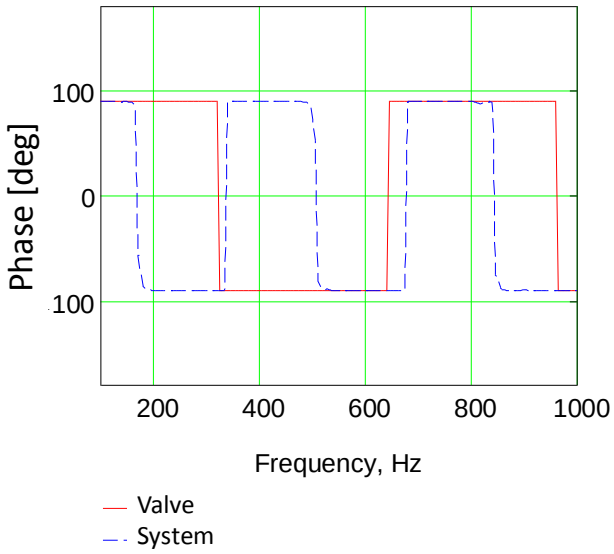

Figure 5.29: Phase of the valve and system impedances vs. Frequency when the valve was open 100%.

Closing the valve to the 55% open setting yields the predictions shown in Figure 5.30. In this case, the phase plot is beginning to be affected by the increased

valve/system resistance. However, the slope of the phase roll-off is still quite large for both.

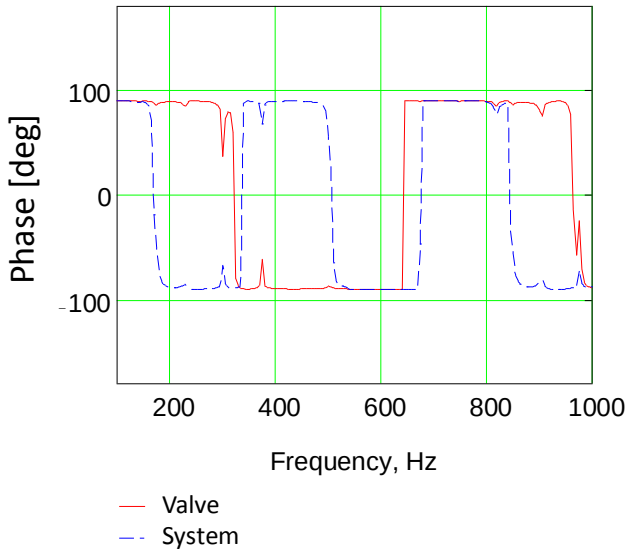

Figure 5.30: Phase of the valve and system impedances vs. Frequency when the valve was open 55%.

Figure 5.31 and Figure 5.32 show the model predictions when the valve was further closed to the 25% and 11% open settings, respectively. They show that further closing the valve, i.e., increasing the valve resistance, results in a significant reduction in the slope of the phase roll-off with frequency.

Figure 5.33 shows that closing the valve completely causes the phase of the valve impedance to be zero and the slope of the phase roll-off at the resonant frequencies for the entire system to again be infinite. Also notice that the resonant frequency shifted from 650 to 700 Hz. In this case, valve resistance is so high that it acts as a rigid wall causing the impedance of the valve to be entirely resistive yielding a phase of 0. This also causes the impedance of the system to become that of an area contraction followed by a 241.3 mm long, rigidly terminated tube.

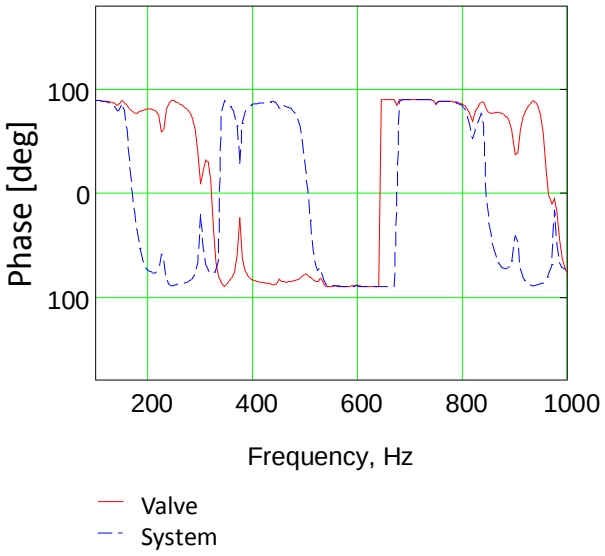

Figure 5.31: Phase of the valve and system impedances vs. Frequency when the valve was open 25%.

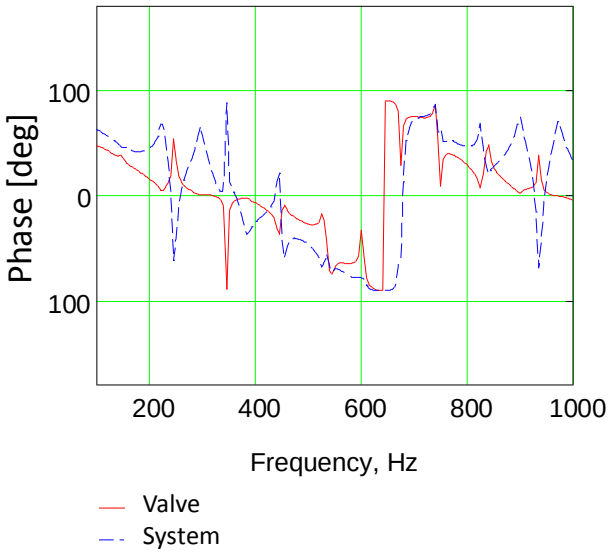

Figure 5.32: Phase of the valve and system impedances vs. Frequency when the valve was open 11%.

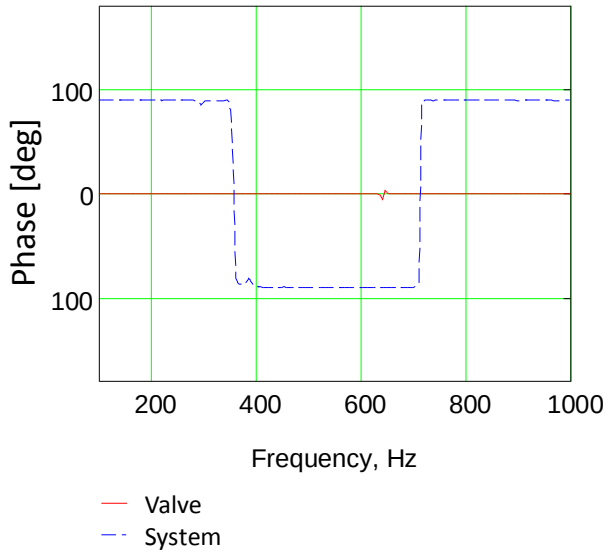

Figure 5.33: Phase of the valve and system impedances vs. Frequency when the valve was completely closed.

5.6.3.3 System tunability

The primary focus of this study is controlling the magnitude and phase of the fuel system impedance. Therefore, the tunability of the area contraction/valve system was considered. In this case, the system impedance, which was measured at the area contraction, was primarily of interest.

First, it was noted that the system resistance also depended on the frequency and valve setting. For example, the maximum value of the system resistance was quite low when the valve was completely open, and it increased as the valve was gradually closed. The exact location of the minima and maxima depended heavily on the length of the connecting tubes. Therefore at a given frequency, the value of the acoustic resistance can be controlled by changing the length of the tube connecting the valve and area contraction or by closing or opening the valve.

Comparing the phase of the impedance for each case reveals that for certain frequencies, e.g., 250 Hz, the phase of the system impedance could be changed simply by opening or closing the valve. For instance, at 250 Hz, the phase of the impedance was 90 degrees when the valve was completely open, 0 degrees when completely closed, about 10 degrees when the valve was 11% open, and nearly 90 degrees when the valve was greater than 25% open. These results could be shifted in frequency by varying the length of the tube between the area contraction and valve or between the valve and rigid end-termination.

Consequently, obtaining the system to obtain a specific magnitude and phase required adjusting the lengths of the interconnecting tubes and the valve setting. Table 5.1 shows the real part and the phase of the impedance of the system for different

lengths of the tube between the area contraction and the valve for frequencies of 250 and 400 Hz.

It shows that the phase of the impedance at 250 Hz was shifted from -25 to 30 degrees simply by varying the length of the interconnecting tube, i.e., changing the system reactance, with little change in the resistance of the system. At 400 Hz, the phase was shifted from 30 degrees to -5 degrees by the same adjustment. However, much more variation in the resistance was observed for this case than in the 250 Hz case. Moreover, adjusting the length of the tube between the valve and the rigid end-termination reduced the resistance of the system.

Table 5.1: Magnitude and phase of the system impedance at 250 and 400 Hz for different lengths of the tube between the area contraction and the valve.

	Frequency = 250 Hz		Frequency = 400 Hz	
	$\|Z_{sys}\|$	Phase of Z_{sys}	$\|Z_{system}\|$	Phase of Z_{sys}
L_2=190.5, L_3=266.7, Valve 11% open	7.6	-25.4	4.8	29.6
L_2=165, L_3=266.7, Valve 11% open	7.4	-17	6.2	39
L_2=140, L_3=266.7, Valve 11% open	7.3	-8.4	8.2	41
L_2=89, L_3=266.7, Valve 11% open	7.2	8.0	15.2	33.6
L_2=64, L_3=266.7, Valve 11% open	7.3	15.6	20	23.8
L_2=38, L_3=266.7, Valve 11% open	7.3	22.8	24.8	10.4
L_2=13, L_3=266.7, Valve 11% open	7.5	29	25	-5
L_2=33, L_3=190.5, Valve 24% open	0.252	88.2	4.9	-4.9

Using this procedure, the resistance and the phase of the system were independently adjusted. The results in the first row and the last two rows of the table illustrate this point. As an example, let the desired resistance and phase be 4.9 and -5 degrees, respectively. The first row of the table shows that the resistance value was

obtained but the phase was not. The results in the seventh row show that the phase value was obtained but the desired resistance was not. The last row shows that by adjusting the length of L_2 to 33, the length of L_3 to 190.5, and the valve to 24% open results in the desired settings.

5.6.3.4 Summary of area change/valve studies

This very simple system indicates that many combinations of system resistance and phase could be obtained by simply adjusting the valve opening and the length of the interconnecting tubes. It is noteworthy, however, that obtaining a certain setting required the adjustment of two different system elements, namely the valve setting and the length of the interconnecting tube.

In summary, these results demonstrate that the nonlinear impedance model is a useful tool for designing practical system tuners. However, it also shows that even simple combinations of such elements present significant modeling challenges, increased computational effort, and complex frequency response characteristics. Nevertheless, the developed models accurately predict the response of real systems containing nonlinear, resistive elements.

5.7 Overall FST acoustic model

The modeling methods described above were also used to develop a nonlinear, frequency response model of the FST shown in Figure 5.34. For modeling purposes, the FST was "broken down" into eight tube sections, two variable area valves, and two tees. The two variable area valves were assumed to consist of an area contraction and expansion. The two 'tees' were assumed to consist of three nonlinear area contractions and/or expansions, and the variable volume was treated as an area expansion in series with a length of rigid-walled tube. Therefore, eleven nonlinear impedance equations were required to adequately model the system.

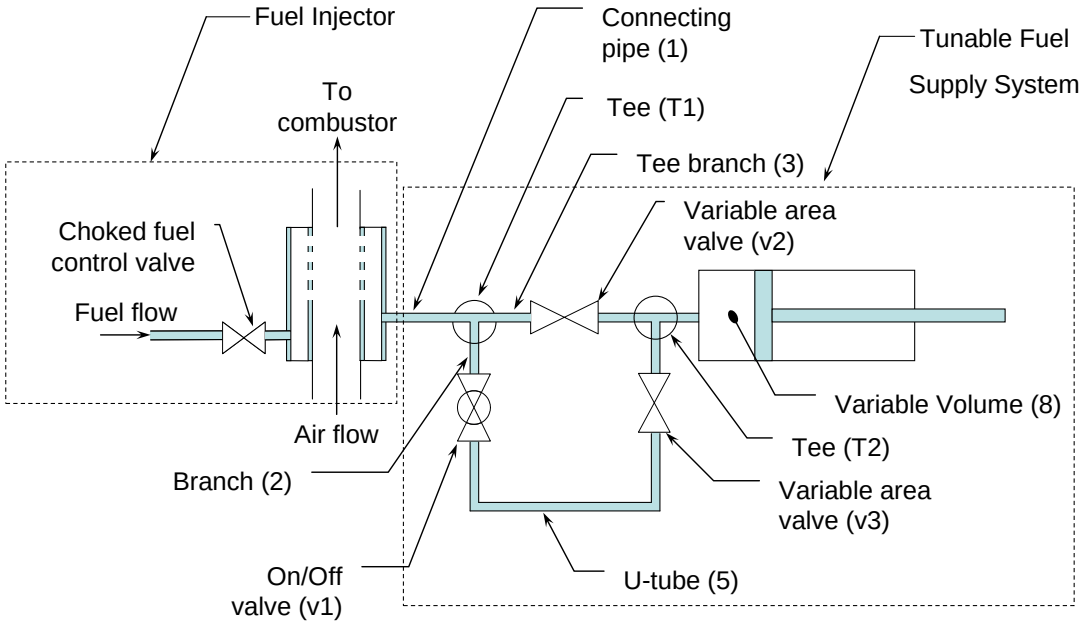

Figure 5.34: Schematic of the FST and fuel injection system.

The model for the eight tube sections were solved for the sixteen unknown complex coefficients using sixteen equations developed from the applicable boundary conditions. These boundary conditions were similar to those used in the previously described models. Impedance conditions (see, for example, Eq. (5.4)) were used at

each area contraction or expansion, and volume velocity matching conditions (see Eqs. (5.6) and (5.35)) were applied at each tube junction. Finally, at the rigid end-wall of the variable volume, the volume velocity was equal to 0.

These boundary conditions yielded sixteen equations, which were subject to eleven constraint equations similar to Eq. (5.29). As before, the constraint equations guarantee that computed acoustic velocity magnitude be equal to the velocity used in the nonlinear impedance formulation for that particular location. The sixteen unknown complex coefficients were obtained by simultaneously solving this set of equations.

The predictions of the developed model were compared with measurements of the acoustic impedance of the FST over the 150 to 1000 Hz range. Since the FST contained two valves, the area of each of which could be changed with virtually infinite resolution, and a continuously variable length 'volume' section, there were infinitely many possible settings of the FST. The FST settings chosen for investigation consisted of every combination of four gate positions for each of the two gate valves, two positions (ON and OFF) of the ball valve, and three positions of the volume section. Consequently, there were 96 FST settings for each investigated frequency.

Figure 5.35 through Figure 5.38 show comparisons of the predicted and measured impedance at four distinct settings. These particular settings, see Appendix F, were chosen as examples because each one has a significantly different frequency response. These figures show that the overall FST model accurately predicts the phase of the FST impedance for frequencies up to 600 Hz. The magnitude of the FST impedance is also well-predicted for most settings up to 600 Hz. However, Figure 5.36 shows that the phase was well-predicted while the magnitude was not for FST setting 8.

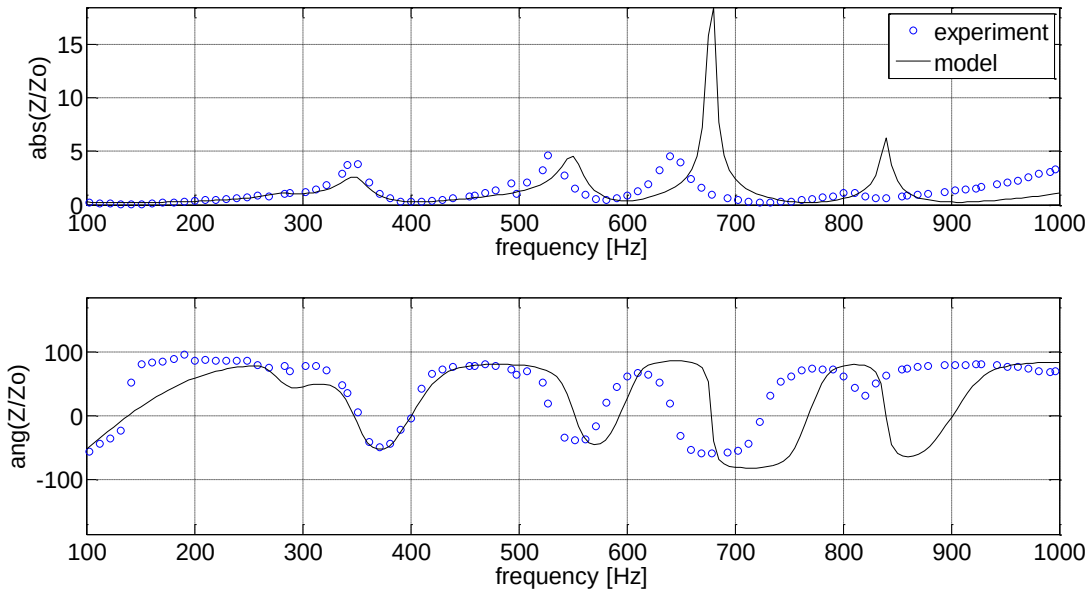

Figure 5.35: Magnitude/Phase of the FST impedance vs. Frequency for FST setting 1.

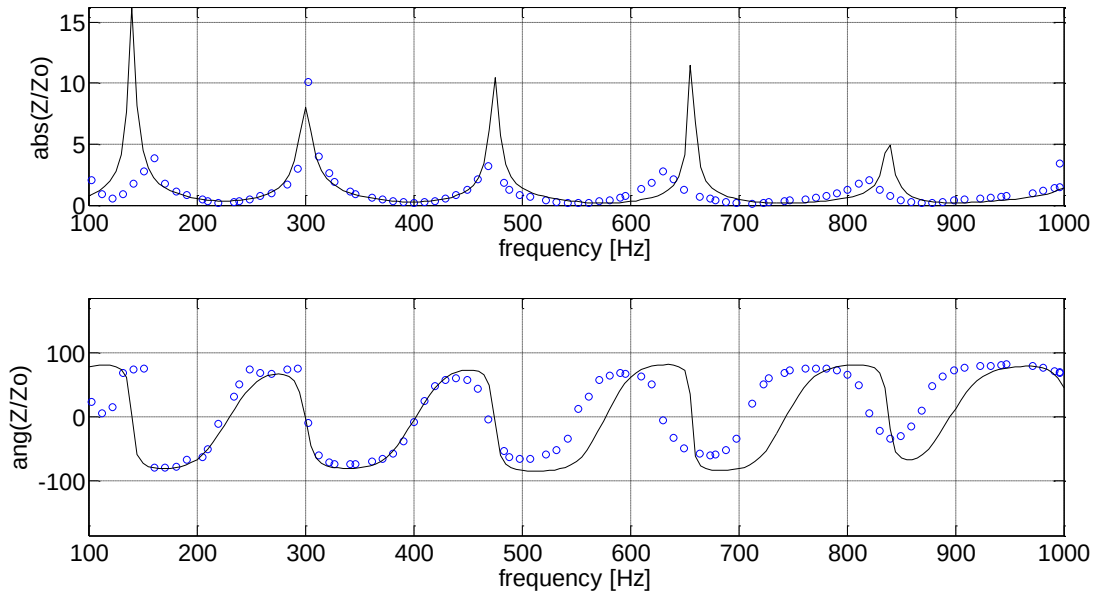

Figure 5.36: Magnitude/Phase of the FST impedance vs. Frequency for FST setting 8.

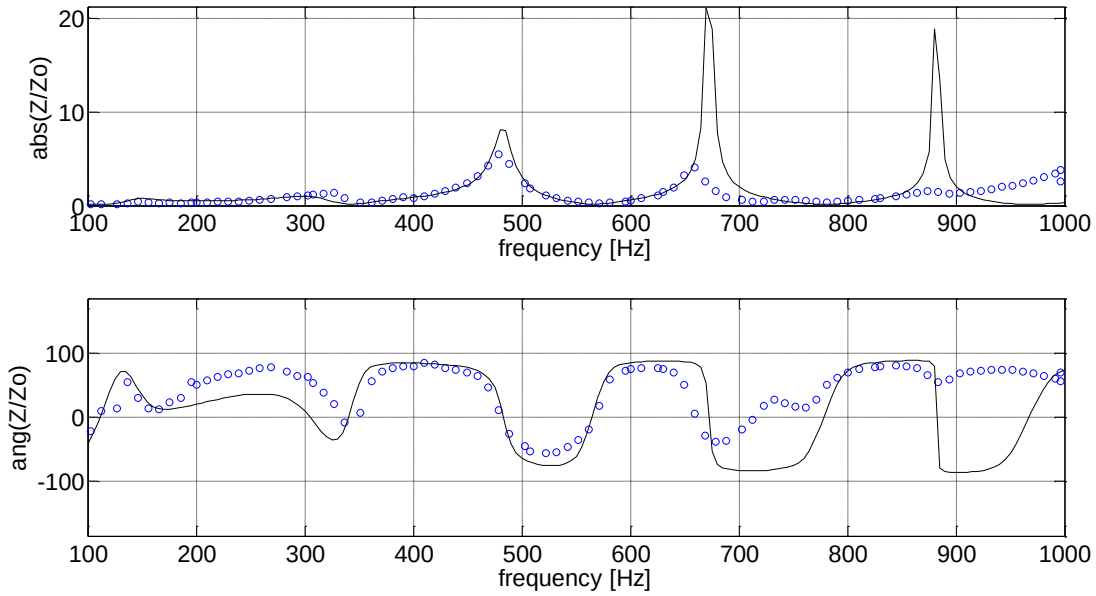

Figure 5.37: Magnitude/Phase of the FST impedance vs. Frequency for FST setting 15.

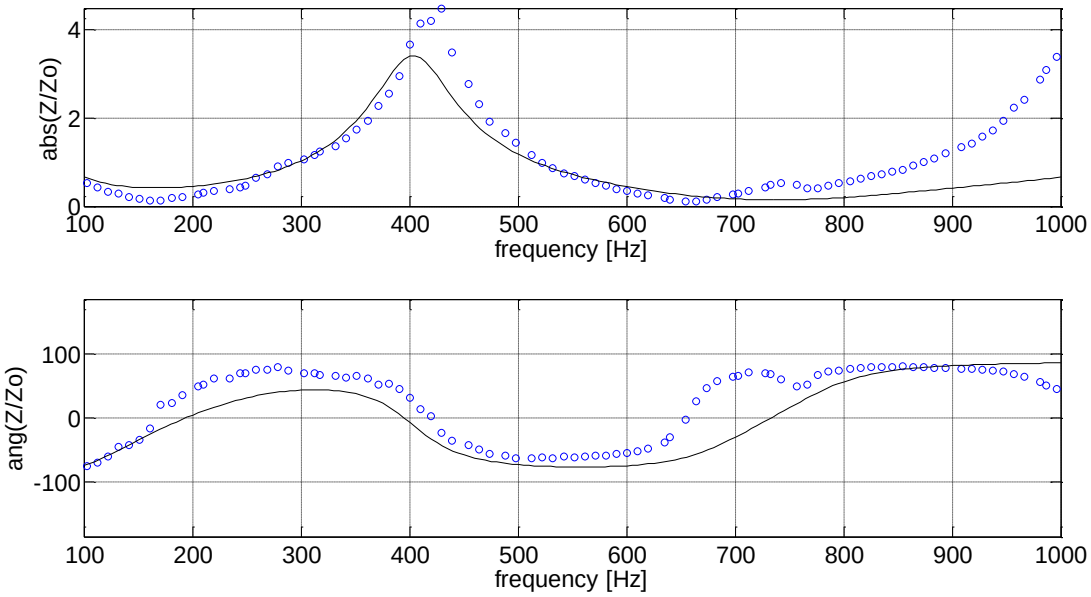

Figure 5.38: Magnitude/Phase of the FST impedance vs. Frequency for FST setting 31.

Disagreement between the measurements and theoretical predictions in the higher frequency range, i.e., above 600 Hz is attributed to the shortcomings of the rather simple theory, which neglected viscous losses and tube wall radiation effects. However,

the developed model is still useful since longitudinal combustion instabilities above 600 Hz are less common.

Most importantly, the experimental measurements and model predictions show that the FST can be tuned to obtain a wide range of impedance values for a given frequency. Therefore, the FST, when properly designed, could provide means for adjusting the impedance of a given fuel system to obtain stable combustor operation or, at least, greatly reduced thermo-acoustic oscillations.

5.8 Conclusions

In this chapter, the procedure for developing 1-D, nonlinear acoustic models for systems containing single or multiple nonlinear elements was presented. Further, the chapter shows that when significant damping is observed when the acoustic resistance dominates the acoustic impedance of the system. Therefore, it was shown that it is necessary to control both the reactive and resistive parts of the system impedance to obtain system impedance phase control. It was also shown that nonlinear elements affect the acoustic velocity field, which affects the impedance of other nonlinear elements. This complicates predicting the result of changing one nonlinear element in a system containing numerous nonlinear elements.

The overall FST modeling procedure was outlined, and model predictions for the FST impedance were presented. These results were shown to be in good agreement with the experimental results for frequencies below 600 Hz.

Finally, experimental measurements and model predictions show that the FST can be tuned to obtain a wide range of impedance values for a given frequency. Therefore, the FST, when properly designed, could provide means for adjusting the impedance of a given fuel system to obtain stable combustor operation or, at least, greatly reduced thermo-acoustic oscillations.

Chapter 6:

Combustor Model Development

6.1 Introduction

The primary purpose of this portion of the investigation was to use a thermo-acoustic model to demonstrate that the FST can be used to achieve stable, or nearly stable, combustor operation. The second objective was to investigate the sensitivity of combustor stability to FST setting for various combustor operating conditions and changes to various combustor components.

This chapter presents the development of a quasi-linear, thermo-acoustic model of a realistic combustion system similar to those used in modern gas turbine engines. This model was used to predict combustor stability and instability frequency for a wide range of FST settings. In addition, model predictions are used to better understand the effect of fuel system impedance on combustor stability. Finally, model sensitivities to combustor operating conditions are presented. The predictions of the model will be discussed further in Chapter 7 in comparison with experimental measurements.

6.2 Combustor stability analysis

Theoretically, a suitable nonlinear combustor/FST model could be used to determine the optimal FST setting that minimizes or eliminates the combustion instability with maximum stability margin. However, there are several difficulties with this approach. First, the inherent acoustic and combustion nonlinearities are difficult to model. Second, such a model would require considering hundreds of possible FST settings. Rather, to simplify the problem, linear stability analysis was performed.

Linear stability analysis, which will be described in more detail in the next section, was used to determine the growth rate of the combustion instability for a wide range of FST settings, combustor/fuel injector component geometries, and operating conditions.

The overall solution scheme is shown schematically in Figure 6.1. First, the combustor geometry, i.e., lengths and diameters, was specified along with the relevant properties of the gas in each section of the combustor and the setting of the FST being investigated. Next, the acoustic impedance of the FST was determined using an assumed pressure amplitude and the developed nonlinear FST model. Then, the system of model equations, including the FST acoustic impedance, was cast in the complex matrix form $W \cdot x = 0$.

To determine the eigenvalues, the determinant of W was set to 0 and solved for the complex wavenumber k, whose imaginary part represents system growth rate (for positive value of the imaginary part of k), or damping (for negative values of the imaginary part of k). The real part of k represents the wavenumber of the instability, which is related to the system frequency by $f = \mathrm{Re}(k) \cdot c / 2\pi$.

The solution of the eigenvalue equation yields an infinite number of values for k, each of which represented an eigenmode of the unstable combustor. In theory, the

imaginary part of k for each eigenmode must be examined to determine whether the system was stable or unstable at that particular frequency. However, this study focused on the stability of the first eigenmode. Furthermore, although there are, theoretically, an infinite number of eigenmodes for a given system, only the ones having frequencies below about 600 Hz are of real importance for longitudinal combustion instabilities in gas turbines.

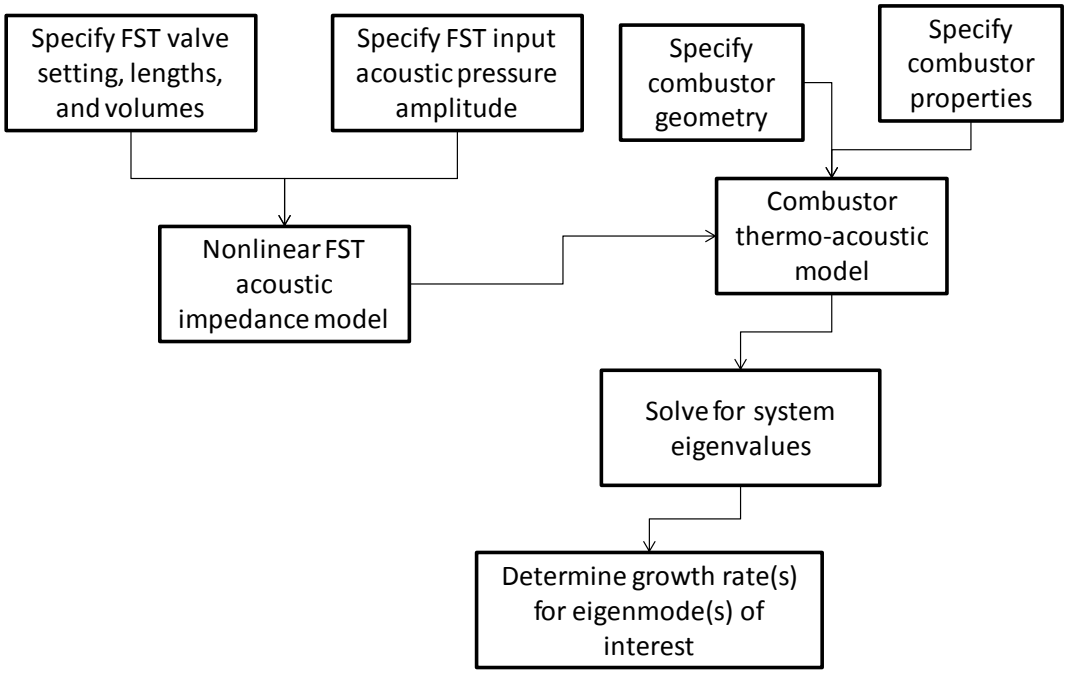

Figure 6.1: Diagram of the solution procedure used to determine the frequency and growth rate of thermo-acoustic instabilities.

These calculations yield the instability frequency and the growth rate of the instability. The results of this analysis show how the settings of the FST affect the stability of the combustor. Further, these results show how variations in combustor geometry and operating condition affect combustor stability and how these changes can be compensated for by adjusting the FST to achieve maximum stability.

The next section gives the fundamentals of stability analysis.

6.2.1 Stability analysis

Stability analysis is used to determine whether or not a given combustor will be stable. In these forms of stability analysis, the eigenvalues of the thermo-acoustic modeling equations are determined for the system of interest. The real and imaginary parts of these eigenvalues describe the frequency and growth/decay rate, respectively, of the corresponding combustion instability (see Figure 6.2). For positive growth rates, the pressure amplitude in the system grows exponentially with time.

As the pressure amplitude increases, system damping increases and driving decreases due to nonlinear effects in the acoustic impedance and combustion process, respectively. The increased system damping eventually offsets the driving so that the growth rate tends to zero, at which point the system is said to be in 'limit cycle'. At limit cycle, $\alpha=0$ and no further growth or decay in pressure amplitude occurs unless there is some change to the system geometry or operating condition. Figure 6.2 depicts this process conceptually for three different values of the growth rate.

For linear stability analysis, the key simplifying assumption is that the amplitude of the limit cycle is directly associated with the linear value of α. In other words, a large value of α means a higher limit cycle.

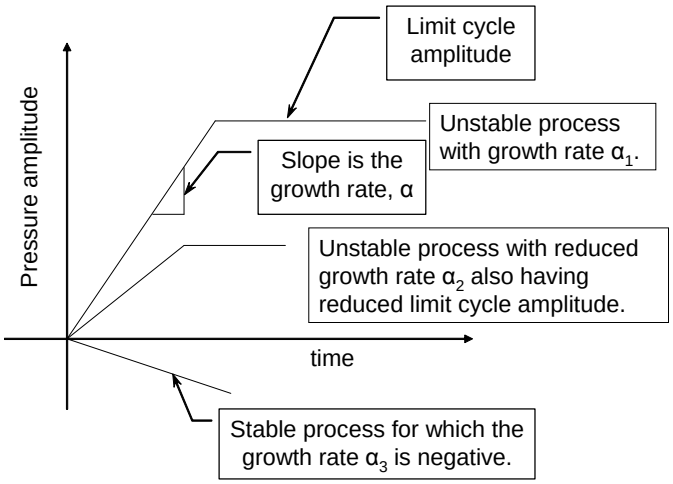

Figure 6.2: Diagram of pressure amplitude as a function of time showing the variation in saturation amplitude with linear growth rate.

In this study, it was assumed that large growth rates correspond to high combustor pressure amplitudes and that negative growth rates correspond to stable combustors. It was also assumed that the larger the growth rate, the higher the combustor pressure amplitude.

The "stability margin" is related to the magnitude of the negative growth rate. The larger the magnitude of the negative growth rate, the higher the stability margin. This means that if the growth rate was minimized by adjusting the FST, the pressure amplitude was minimized and, in the case of negative α, the stability margin was maximized. Therefore, the problem was reduced to a rather complex, but linear, stability problem in which the goal was to minimize α by adjusting the FST.

6.3 The model combustor and modeling assumptions

The modeled combustion system, which closely mirrors the combustor used in the experimental portion of this study, is shown in Figure 6.3. Combustion air entered from the right through the choked air inlet valve. It then flowed down the air inlet pipe and through a swirler, which imparted rotational motion on the air flow. The swirling air then flowed past the fuel plenum, where fuel was injected into the air. The mixture then passed through another swirler, down a short pipe section, and into the combustion chamber where the reactions occurred at the location marked Reaction Zone. The hot products flowed down the combustor tailpipe and out at the exhaust at the extreme left.

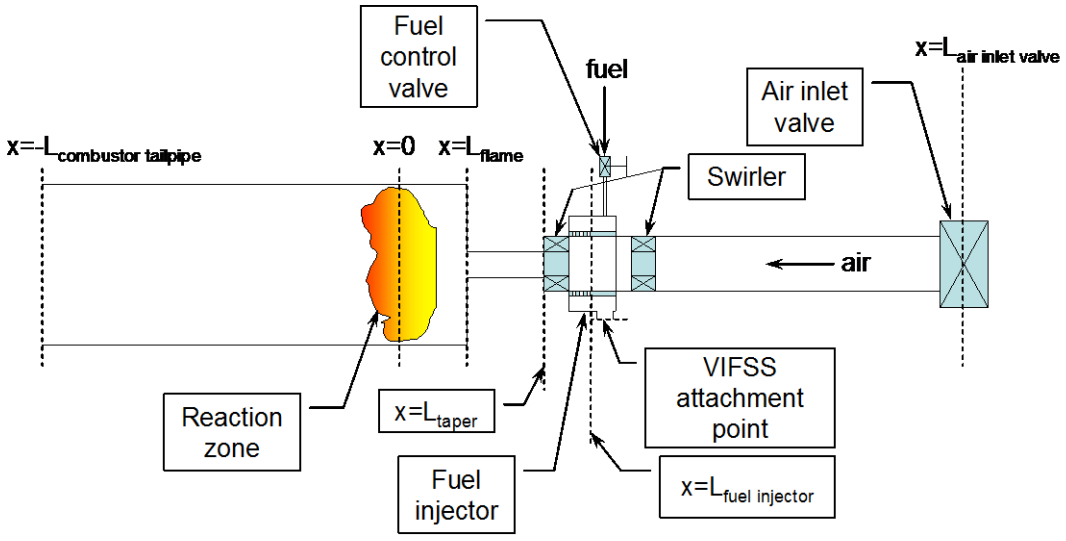

Figure 6.3: Schematic of a swirl-stabilized combustor.

6.3.1 Modeling assumptions

The basic assumptions used for the quasi-linear combustor stability models were as follows:

1. The acoustic pressure was uniform across the test-section, i.e., the oscillations 1-D.
2. The swirler impedance is purely resistive and proportional to the steady flow rate.
3. The combustion process was an infinitely thin heat release zone.
4. The combustor was adiabatic.
5. The flame response was described by the following equation, which was derived in Appendix A),

$$\frac{Q'}{Q} = \left(\frac{\rho'}{\rho} + \frac{Y_i'}{Y_i} e^{i\omega\tau_{conv}} + \frac{U'}{U} \right) e^{i\omega\tau_{chem}}. \tag{6.69}$$

6.4 Development of the thermo-acoustic model equations

In this section a system of nonlinear algebraic equations describing the thermo-acoustic response of the model combustor is developed using the nonlinear impedance relations developed in Chapter 3 and the linear heat release transfer function, which was derived in Appendix A. A schematic of the modeled combustor showing the pertinent components and locations is shown in Figure 6.4.

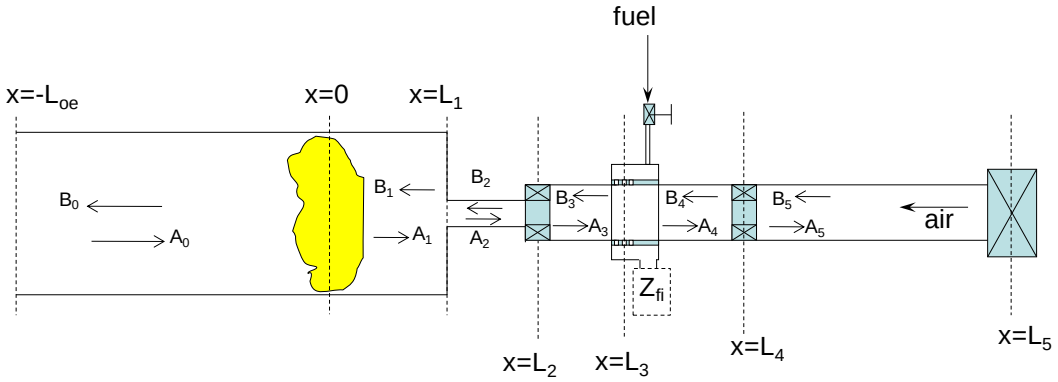

Figure 6.4: Schematic of the modeled combustor showing pertinent locations.

In what follows, the acoustic waves were assumed to be linear, harmonic, right and left traveling plane waves.

Based on this assumption, the acoustic pressure and volume velocity at a given location L_i are given by

$$p_i' = A_i e^{ik_f L_i} + B_i e^{-ik_b L_i} \tag{6.70}$$

and

$$U_i' = S_i u_i' = \frac{S_i}{(\rho c)_i}\left(A_i e^{ik_f L_i} - B_i e^{-ik_b L_i}\right), \tag{6.71}$$

respectively, where

$$k_f = \frac{\omega}{c-u} \text{ and } k_b = \frac{\omega}{c+u}. \tag{6.72}$$

6.4.1 Combustor exhaust boundary

The combustor exhaust end was located a distance L_{oe} from the flame (see Figure 6.5). At this point, the acoustic pressure dropped from the acoustic pressure just upstream of the exhaust opening to the ambient acoustic pressure, which was assumed to have zero amplitude.

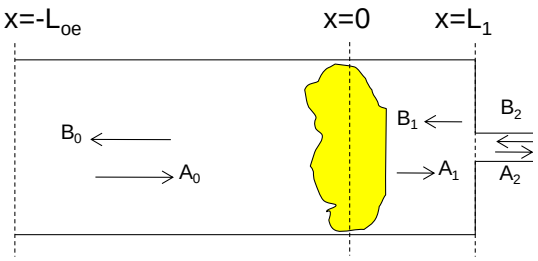

Figure 6.5: Schematic of the open-ended exhaust.

These assumptions led to the following expressions

$$\frac{p'_{oe} - p'_{amb}}{U'_{oe}} = Z_{oe} \tag{6.73}$$

and

$$U'_{oe} = U'_{amb}\,. \tag{6.74}$$

Assuming harmonic, plane waves, the acoustic pressures and volume velocities were written as the sum of right and left traveling waves so that Eqs. (6.73) and (6.74) became

$$\frac{\left(A_0 e^{-ik_f L_{oe}} + B_0 e^{ik_b L_{oe}}\right) - 0}{\frac{S_0}{(\rho c)_0}\left(A_0 e^{-ik_f L_{oe}} + B_0 e^{ik_b L_{oe}}\right)} = Z_{oe} \tag{6.75}$$

and

$$U'_{oe} = \frac{S_0}{(\rho c)_0}\left(A_0 e^{-ik_f L_{oe}} + B_0 e^{ik_b L_{oe}}\right). \tag{6.76}$$

Upon rearrangement, Eq. (6.75) became

$$A_0 e^{-ik_f L_{oe}} \left(1 - \frac{S_0}{(\rho c)_0} Z_{oe}\right) + B_0 e^{ik_b L_{oe}} \left(1 + \frac{S_0}{(\rho c)_0} Z_{oe}\right) = 0 \tag{6.77}$$

where A_0 and B_0 were the complex coefficients of the right and left traveling plane waves, S_0 was the area of the exhaust pipe, and $(\rho c)_0$ was the characteristic impedance of the exhaust gases.

6.4.2 Combustion zone

At the combustion zone, the heat release was modeled as a volume velocity source while the pressure was assumed constant across the flame. These assumptions are depicted in Figure 6.6.

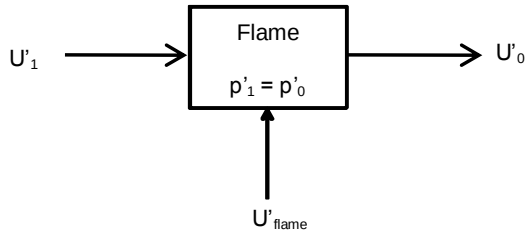

Figure 6.6: Schematic used in the development of the flame model.

The continuity equation required that

$$U_0' = U_1' + U_{flame}' \tag{6.78}$$

and constancy of acoustic pressure across the flame required that

$$p_1' = p_0' . \tag{6.79}$$

The volume velocity U_{flame}' added by the flame is given by

$$U_{flame}' = \frac{\gamma - 1}{\gamma p_1} S_1 \frac{\dot{Q}'}{Q_0} Q_0 . \tag{6.80}$$

Expressing the acoustic volume velocities and pressures as the sum of right and left traveling, harmonic, plane waves yields

$$\frac{S_0}{(\rho c)_0}(A_0 - B_0) - \frac{S_1}{(\rho c)_1}(A_1 - B_1) - \frac{\gamma - 1}{\gamma p_1}\dot{Q}' = 0 \tag{6.81}$$

and

$$(A_0 + B_0) - (A_1 - B_1) = 0\,. \tag{6.82}$$

Equation (2.10) was used to relate the unsteady heat release to the unsteady field variables as described above. Substituting Eq. (2.10) into (6.81) yields

$$\begin{aligned} &\frac{S_0}{(\rho c)_0}(A_0 - B_0) - \frac{S_1}{(\rho c)_1}(A_1 - B_1) \\ &-\frac{\gamma - 1}{\gamma p_1}\left[\left(\frac{\rho'}{\rho} + \frac{Y_i'}{Y_i}e^{i\omega\tau_{conv}} + \frac{U'}{U}\right)e^{i\omega\tau_{chem}}\right]\dot{Q}_0 = 0. \end{aligned} \tag{6.83}$$

For clarity, the terms appearing in the last term on the left hand side of Eq. (6.83) were related to the acoustic variables in the system using the relations developed in Chapter 2. First, assuming isentropic acoustic waves, the acoustic density ratio in Eq. (6.83) was rewritten using $p' = \rho' c^2$ and $\gamma p = \rho c^2$ in terms of the acoustic pressure ratio as

$$\frac{\rho_1'}{\rho_1} = \frac{p_1'}{\gamma p_1}\,. \tag{6.84}$$

Next, the acoustic volume velocity ratio were written in terms of the acoustic pressure at the flame location using the acoustic impedance to yield

$$\frac{U_1'}{U_1} = \frac{p'}{Z_1 U}\,. \tag{6.85}$$

Finally, using the relation for the fluctuating fuel mass fraction ratio developed in Appendix B and $p'/\gamma p$ for the acoustic density ratio, Y_{fuel}'/Y_{fuel} was written as

$$\frac{Y'_{fuel}}{Y_{fuel}} = \frac{p'_3}{\gamma p_{fuel}}\left(1-Y_{fuel}\right) - \frac{p'_3}{Z_{fi}U_{fuel}}\left(1-Y_{fuel}\right) - \frac{p'_3}{\gamma p_3}\left(1-Y_{fuel}\right) - \frac{p'_3}{\rho_{total}U_{total}Z_{air}}\left(\frac{\gamma p}{c^2}\right)_{air} \tag{6.86}$$

or

$$\frac{Y'_{fuel}}{Y_{fuel}} = \frac{p'_3}{\gamma p_3}\left(1-Y_{fuel}\right) - \frac{p'_{fuel}}{Z_{fi}U_{fuel}}\left(1-Y_{fuel}\right) - \frac{p'_3}{\gamma p_3}\left(1-Y_{fuel}\right) - \frac{U'_3}{\rho_{total}U_{total}}\left(\frac{\gamma p}{c^2}\right)_{air}, \tag{6.87}$$

where each term in Eq. (6.86) was evaluated at the location of the fuel injector.

Substituting Eqs. (6.84), (6.85), and (6.86) into Eq. (6.83) yields

$$\frac{S_0}{(\rho c)_0}\left(A_0 - B_0\right) - \frac{S_1}{(\rho c)_1}\left(A_1 - B_1\right) - \frac{\gamma-1}{\gamma p_1}[C_3]\dot{Q}_0 = 0 \tag{6.88}$$

where

$$C_3 = \left(\frac{p'_1}{\gamma p_1} + \begin{bmatrix} \frac{p'_3}{\gamma p_3}\left(1-Y_{fuel}\right) \\ -\frac{p'_3}{Z_{fi}U_{fuel}}\left(1-Y_{fuel}\right) \\ -\frac{p'_3}{\gamma p_3}\left(1-Y_{fuel}\right) \\ -\frac{U'_3}{\rho_{total}U_{total}}\left(\frac{\gamma p}{c^2}\right)_{air} \end{bmatrix} e^{i\omega\tau_{conv}} + \frac{U'_1}{U_1} \right) e^{i\omega\tau_{chem}} . \tag{6.89}$$

The acoustic pressures and volume velocities in Eq. (6.89) were expressed as the sum of right and left traveling plane waves at their respective locations in the system as follows:

$$p'_1 = A_1 + B_1, \tag{6.90}$$

$$U'_1 = \frac{S_1}{(\rho c)_1}\left(A_1 - B_1\right), \tag{6.91}$$

$$p'_3 = A_3 + B_3, \tag{6.92}$$

and

$$U_3' = \frac{S_3}{(\rho c)_3}(A_3 - B_3). \tag{6.93}$$

Substituting Eqs. (6.90), (6.91), (6.92), and (6.93) into Eq. (6.89) and rearranging leads to

$$\begin{aligned} C_3 = C_{1a}(A_3 + B_3) - C_{1b}\frac{S_3}{(\rho c)_3}(A_3 - B_3)\ldots \\ +C_{1c}(A_1 + B_1) + C_{1d}\frac{S_1}{(\rho c)_1}(A_1 - B_1) \end{aligned} \tag{6.94}$$

where

$$C_{1a} = e^{i\omega\tau_{conv}}\left\{\frac{(1-Y_{fuel})}{\dot{m}_{total}Y_{fuel}}\left[\frac{Y_{fuel}\dot{m}_{total}}{\gamma_{fuel}p_3} - \frac{\gamma_{fuel}p_3}{Z_{fi}c_{fuel}^2}\right] - \frac{(1-Y_{fuel})}{\gamma_{air}p_3}\right\} \tag{6.95}$$

$$C_{1b} = e^{i\omega\tau_{conv}}\frac{\gamma_{air}p_3}{\dot{m}_{total}c_{air}^2} \tag{6.96}$$

$$C_{1c} = \frac{1}{\gamma_{mix}p_1} \tag{6.97}$$

and

$$C_{1d} = \frac{\gamma_{mix}p_1}{\dot{m}_{total}c_{mix}^2}. \tag{6.98}$$

Substituting Eq. (6.94) into Eq. (6.88) gives, upon rearrangement

$$\begin{aligned} &\left[A_0\frac{S_0}{(\rho c)_0} - B_0\frac{S_0}{(\rho c)_0}\right] - A_1\left[\frac{S_1}{(\rho c)_1} + \left(C_{1c} + \frac{S_1}{(\rho c)_1}C_{1d}\right)C_{1e}\right]\ldots \\ &+B_1\left[\frac{S_1}{(\rho c)_1} - \left(C_{1c} - \frac{S_1}{(\rho c)_1}C_{1d}\right)C_{1e}\right] - A_3\left(C_{1a} - \frac{S_3}{(\rho c)_3}C_{1b}\right)C_{1e}\cdots \\ &-B_3\left(C_{1a} + \frac{S_3}{(\rho c)_3}C_{1b}\right)C_{1e} = 0 \end{aligned} \tag{6.99}$$

where

$$C_{1e} = \left[\frac{(\gamma_{mix} - 1)}{\gamma_{mix} p_1} \dot{Q} \right] e^{i\omega\tau_{chem}} . \tag{6.100}$$

The acoustic pressure across the flame was assumed constant, which gives

$$p_0' = p_1' . \tag{6.101}$$

Writing the acoustic pressures as the sum of right and left traveling plane waves yields

$$(A_0 + B_0) - (A_1 + B_1) = 0 . \tag{6.102}$$

Equations (6.99) and (6.102) were the equations used to model the effect of heat release oscillations on the acoustic response of the system.

6.4.3 Area change from duct section 1 to 2

This section describes the development of the equations used to model of the area change from duct section 1 to duct section 2 shown in Figure 6.7.

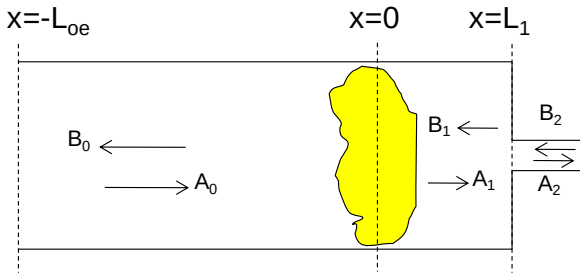

Figure 6.7: Schematic of area change from duct section 1 to 2.

According to the theory developed in Chapter 3, the impedance of the area change Z_{12} between duct sections 1 and 2 is given by

$$\frac{Z_{12}}{(\rho c)_1} = \frac{p_1' - p_2'}{(\rho c)_1 \cdot S_1 u_1'} = \frac{i\frac{\omega}{c} L_e}{S_1} + \left(\frac{u_1}{c} + \frac{|u_1'|}{2 \cdot c} \right) \frac{\left[\left(\frac{S_1}{S_2} \right)^2 + K_L - 1 \right]}{S_1} . \tag{6.103}$$

Writing the acoustic pressures and velocities in terms of right and left traveling plane waves yields

$$\frac{p_1' - p_2'}{(\rho c)_1 \cdot S_1 u_1'} = \frac{\left(A_1 e^{ik_f L_1} + B_1 e^{-ik_b L_1}\right) - \left(A_2 + B_2\right)}{\frac{S_1}{(\rho c)_1}\left(A_1 e^{ik_f L_1} - B_1 e^{-ik_b L_1}\right)} = \frac{Z_{12}}{(\rho c)_1}. \tag{6.104}$$

Equation (6.104) was rearranged to give

$$A_1 e^{ik_f L_1}\left(1 - Z_{12}\frac{S_1}{(\rho c)_1}\right) + B_1 e^{-ik_b L_1}\left(1 + Z_{12}\frac{S_1}{(\rho c)_1}\right) - \left(A_2 + B_2\right) = 0. \tag{6.105}$$

Also, according to the theory, the volume velocity across the area change was constant. This assumption yields

$$U_1' = U_2' \tag{6.106}$$

or, upon writing the volume velocities in terms of right and left traveling waves,

$$\frac{S_1}{(\rho c)_1}\left(A_1 e^{ik_f L_1} - B_1 e^{-ik_b L_1}\right) - \frac{S_2}{(\rho c)_2}\left(A_2 - B_2\right) = 0. \tag{6.107}$$

Equations (6.105), (6.107), and (6.103) were the equations used to model the acoustics of the area change from duct section 1 to 2.

6.4.4 Area change from duct section 2 to 3 with a swirler

A schematic of the transition from duct section 2 to 3 includes a swirler as shown in Figure 6.8. The area of duct section 2 was slightly smaller than that of the duct section upstream of it, and a swirler was situated between the two sections.

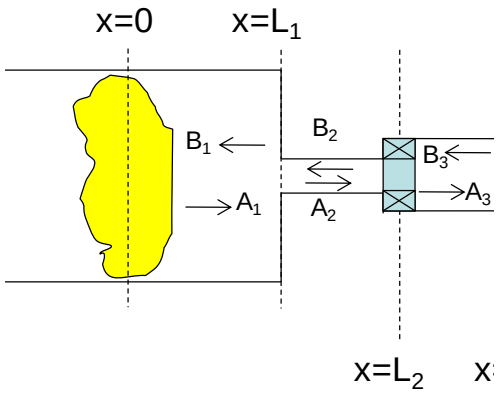

Figure 6.8: Schematic of the swirler location.

Since the area change was slight, the effect of the area change itself was negligible. However, neglecting the nonlinear effect, the swirler imparted a pressure drop proportional to its area and the amount of steady mean flow passing through it. Neglecting nonlinear effects was justified because of the small change in area between the two sections. Therefore, the following impedance model was to connect duct sections 2 and 3:

$$\frac{Z_{swirler}}{(\rho c)_2} = \frac{p_2' - p_3'}{(\rho c)_2 \cdot S_2 u_2'} = \frac{i\frac{\omega}{c}L_e}{S_2} + \left(\frac{u_2}{c}\right)\frac{\left[\left(\frac{S_2}{S_{swirler}}\right)^2 - 1\right]}{S_2}. \tag{6.108}$$

As before, continuity of volume velocity between the two duct sections requires that

$$U_2' - U_3' = 0. \tag{6.109}$$

Again, writing the acoustic pressures and volume velocities in terms of right and left traveling waves and rearranging transformed Eqs. (6.108) and (6.109) into the following equations:

$$A_2 e^{ik_f L_2}\left(1 - Z_{swirler}\frac{S_2}{(\rho c)_2}\right) + B_2 e^{-ik_b L_2}\left(1 + Z_{swirler}\frac{S_2}{(\rho c)_2}\right) - (A_3 + B_3) = 0 \qquad (6.110)$$

and

$$\frac{S_2}{(\rho c)_2}\left(A_2 e^{ik_f L_2} - B_2 e^{-ik_b L_2}\right) - \frac{S_3}{(\rho c)_3}(A_3 - B_3) = 0\,. \qquad (6.111)$$

Equations (6.110), (6.111), and (6.108) were used to model the transition between duct sections 2 and 3, including the effect of the swirler.

6.4.5 The fuel injector equations

The fuel injector was situated between duct sections 3 and 4. A schematic of this arrangement is shown in Figure 6.9.

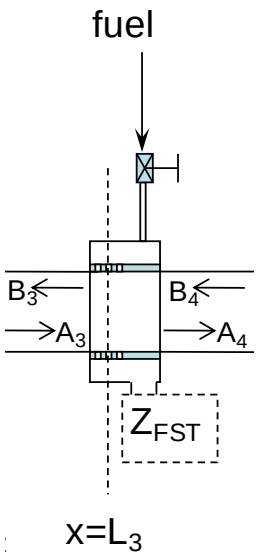

Figure 6.9: Diagram of duct sections 3 and 4 with the fuel injector.

In reality, the fuel injector consisted of an acoustic network comprised of an array of holes, a volume, and the FST, which is represented by the block labeled Z_{FST}. The injected fuel flowed through a choked control valve into a fuel plenum, i.e., a small volume. From there, it passed through a set of injector holes, which were not choked,

prior to being injected into the air stream. For reference, there were three rows of twelve injector holes. The diameter of these holes could be changed by changing a part on the fuel injector assembly.

The junction of duct section 3, the fuel injector, and duct section 4 is shown in Figure 6.10.

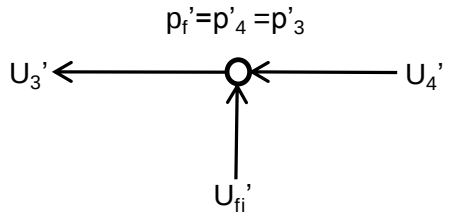

Figure 6.10: A schematic of duct sections 3 and 4 with the fuel injection.

At this junction of the three, mass conservation required that

$$U_3' = U_{fi}' + U_4', \tag{6.112}$$

where U_{fi}' is obtained using the overall impedance of the fuel injection system so that

$$U_{fi}' = \frac{p_4'}{Z_{fi}}. \tag{6.113}$$

Also, all three of the acoustic pressures at the junction were assumed equal so that

$$p_3' = p_4' = p_{fi}'. \tag{6.114}$$

Substituting Eq. (6.113) into Eq. (6.112) yields

$$U_3' = \frac{p_4'}{Z_{fi}} + U_4'. \tag{6.115}$$

Writing the acoustic pressures and volume velocities in terms of right and left traveling plane waves yields, after some algebraic manipulations, the following equations:

$$\left(A_3 e^{ik_f L_3} + B_3 e^{-ik_b L_3}\right) - \left(A_4 + B_4\right) = 0 \tag{6.116}$$

and

$$\begin{aligned} &\frac{S_3}{(\rho c)_3}\left(A_3 e^{ik_f L_3} - B_3 e^{-ik_b L_3}\right) \\ &-\left\{A_4\left[\frac{S_4}{(\rho c)_4} + \frac{1}{Z_{fi}}\right] - B_4\left[\frac{S_4}{(\rho c)_4} - \frac{1}{Z_{fi}}\right]\right\} = 0. \end{aligned} \tag{6.117}$$

The total impedance of the fuel system Z_{fi} was obtained using the network diagram shown in Figure 6.11. Using this network model, the impedance of the entire fuel injection system Z_{fi} was found to be

$$Z_{fi} = \frac{p'_4}{U'_{fi}} = Z_{holes} + \frac{Z_{volume} Z_{FST}}{Z_{volume} + Z_{FST}}. \tag{6.118}$$

It then remained only to develop models for the impedance of the holes, volume, and FST to obtain a model for the fuel injector impedance. This model was used to determine the acoustic volume velocity of the fuel flowing out of the fuel injector.

The hole array was subjected to grazing airflow, a steady bias flow of fuel, and an unsteady flow in and out of the holes due to acoustic oscillations. A linear model for the acoustic impedance of a perforated plate subjected to both grazing and steady mean flow was given by Sun et. al.[59]. A schematic of the flow patterns into and out of the perforate is shown in Figure 6.12.

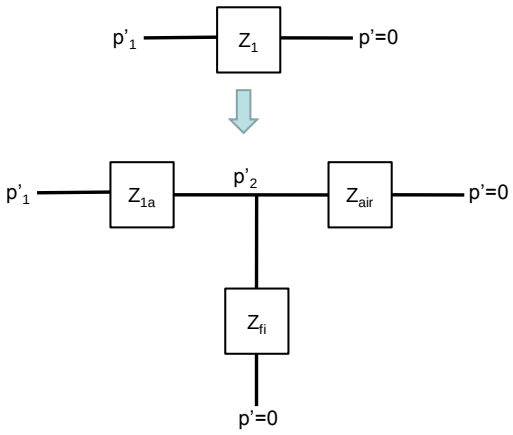

Figure 6.11: Network diagram of the fuel injector plenum, volume, and FST.

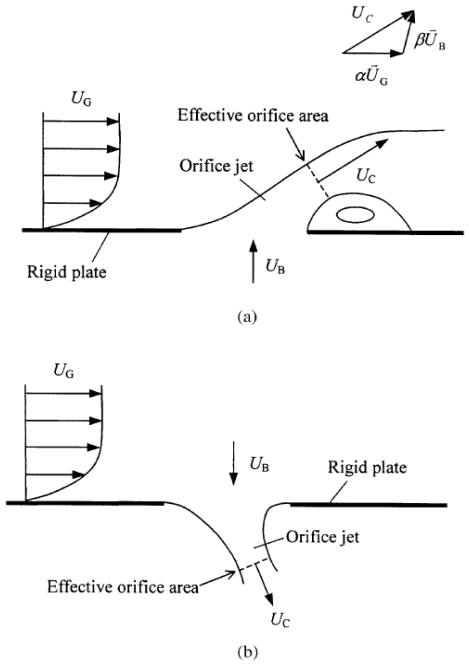

Figure 6.12: Diagram used in the grazing-bias flow interaction model[59].

In Sun's model, the effective discharge area of the perforated plate was modified by a factor involving the grazing and bias flow velocities. In Sun's model, the acoustic resistance of the perforate is given by

$$r = \frac{\Delta p'}{\rho c u'} = \frac{M_B}{\sigma C_D^2}. \tag{6.119}$$

C_D is the effective discharge coefficient, which is defined as $C_D = U_B / U_c = u_0' / u_c'$ and $u' = \sigma u_0'$. Additionally, U_c is related to the steady and grazing flows using

$$U_c = \sqrt{\beta_1 U_B^2 + \beta_2 U_B U_G + \beta_3 U_G^2}, \tag{6.120}$$

so that the effective discharge coefficient is given by

$$C_D = \frac{1}{\sqrt{\beta_1 + \frac{\beta_2}{\lambda} + \frac{\beta_3}{\lambda^2}}}, \tag{6.121}$$

where

$$\beta_1 = 2.10,\ \beta_2 = -0.332,\ \text{and}\ \beta_3 = 0.556\ \text{(for outflow)}. \tag{6.122}$$

Although accounting for grazing and bias flow, this model ignores the reactive part of the orifice impedance and neglects nonlinear effects. These effects can be included as follows. First, the reactive part of the perforate impedance was included using a simple effective length model given by

$$Z_{reactive} = \frac{i \rho c k L_{eff,holes}}{S_{holes}}, \tag{6.123}$$

where $L_{eff,holes}$ was the effective length of the holes due to the air mass oscillating within the holes.

According to the theory developed in Chapter 3, accounting for the nonlinear effect simply requires replacing the bulk flow Mach number in Eq. (6.119) with $M_B + M_B'/2$.

Thus making the suggested modifications, the final expression for the impedance of the perforated section of the fuel injector including nonlinear effects and the effect of the oscillating air mass, in terms of the acoustic network shown above, is given by

$$Z_{holes} = \frac{p'_v - p'_4}{S_{holes} u'_{fi}} = i \frac{(\rho c)_{fi} k L_{eff,holes}}{S_{holes}} + \frac{(\rho c)_{fi}}{S_{holes}} \left(\frac{1 - C_D^2}{C_D^2} \right) \left(\frac{U_{fi} + U'_{fi}/2}{c} \right). \quad (6.124)$$

The impedance of the fuel volume between the injector holes and the FST was given by

$$Z_{vol} = -i \frac{(\rho c)_{fi}}{k V_{vol}}. \quad (6.125)$$

Finally, for the purposes of this discussion, the FST impedance Z_{FST} was assumed to be a known quantity. (In actuality, it was calculated following the procedure described in Chapter 3.)

The impedance of the fuel injector Z_{fi} was obtained by substituting Eqs. (6.124) and (6.125) along with Z_{FST} into Eq. (6.118). For the purpose of calculation, Z_{FST} was determined either from the previously developed FST.

Equations (6.116), (6.117), and (6.124) were the final equations used to model the junction of duct sections 3 and 4 and the fuel injection system.

6.4.6 Area change from duct sections 4 to 5 with a swirler

The area change from duct section 4 to 5 is shown in Figure 6.13. Clearly, this section is almost identical with the one shown Figure 6.8.

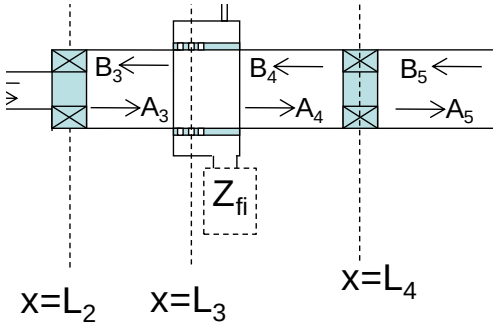

Figure 6.13: Diagram of the swirler situated between the end of duct section 4 and the beginning of duct section 5.

Therefore, the modeling equations for this section are the same as those derived in Section 6.4.4 with the exception that the location numbers were changed as follows. First, the impedance across the swirler required that

$$A_4 e^{ik_f L_4}\left(1 - Z_{swirler}\frac{S_4}{(\rho c)_4}\right) + B_4 e^{-ik_b L_4}\left(1 + Z_{swirler}\frac{S_4}{(\rho c)_4}\right) - (A_5 + B_5) = 0 \qquad (6.126)$$

and continuity of acoustic volume velocity requires that

$$\frac{S_4}{(\rho c)_4}\left(A_4 e^{ik_f L_4} - B_4 e^{-ik_b L_4}\right) - \frac{S_5}{(\rho c)_5}(A_5 - B_5) = 0\,. \qquad (6.127)$$

6.4.7 The air inlet valve

The air inlet valve was situated at the upstream end of duct section 5 as shown in Figure 6.14. Assuming that the impedance of the air inlet valve was Z_{valve}, the appropriate modeling equation was developed as follows.

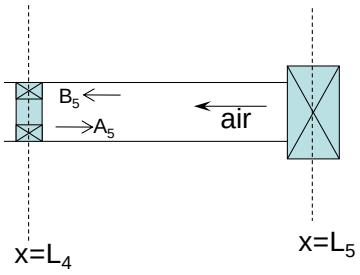

Figure 6.14: Diagram of air inlet valve situated at the upstream end of duct section 5.

The definition of the air inlet valve impedance was

$$Z_{valve} = \frac{p_5'}{U_5'}. \tag{6.128}$$

Writing the acoustic pressure and volume velocity in terms of right and left traveling plane wave yields, after some algebraic manipulation,

$$A_5 e^{ik_f L_5}\left[1 - Z_{valve}\frac{S_5}{(\rho c)_5}\right] + B_5 e^{-ik_b L_5}\left[1 + Z_{valve}\frac{S_5}{(\rho c)_5}\right] = 0. \tag{6.129}$$

Measurements in the impedance tube revealed that the reflection coefficient, and, therefore, the impedance, of the air inlet valve was dependent on the steady flowrate of air through the valve. Using these measurements, the following correlation expresses this dependence:

$$R_{\text{inlet valve}} = 1 - 1.445 \cdot 10^{-4} U_{air}. \tag{6.130}$$

The impedance of the air inlet valve in terms of the reflection coefficient was given by

$$Z_{valve} = \frac{(\rho c)_5}{S_5}\frac{(1 + R_{valve})}{(1 - R_{valve})}. \tag{6.131}$$

Equations (6.130) was substituted into Eq. (6.131) for use in Eq. (6.129), which modeled the acoustic boundary condition at the air inlet valve.

6.5 Quasi-linear thermo-acoustic model results

The model developed above was used to address the following questions. (1) Is the FST able to stabilize the combustor? (2) How do different FST settings affect stability? (3) How do model predicted combustor growth rates correlate with fuel system impedance? (4) Does the model help explain why and under what conditions the FST is effective? (5) Can these results be used to guide the development of new and better fuel systems that eliminate combustion instabilities?

Figure 6.15 shows a schematic of the modeled combustor having the various lengths and properties specified in Table 6.1. For modeling purposes, the FST shown in Figure 6.16 was considered to be attached at the location marked Z_{fi} in Figure 6.15. For each case studied, the length of the variable volume (8) and the position of the ball valve (BV) were specified. The growth rate of the instability was then computed for a range of settings of the variable area valves (V1 and V2). Also, for each of the cases studied, a baseline value for the growth rate was determined by turning the FST completely off.

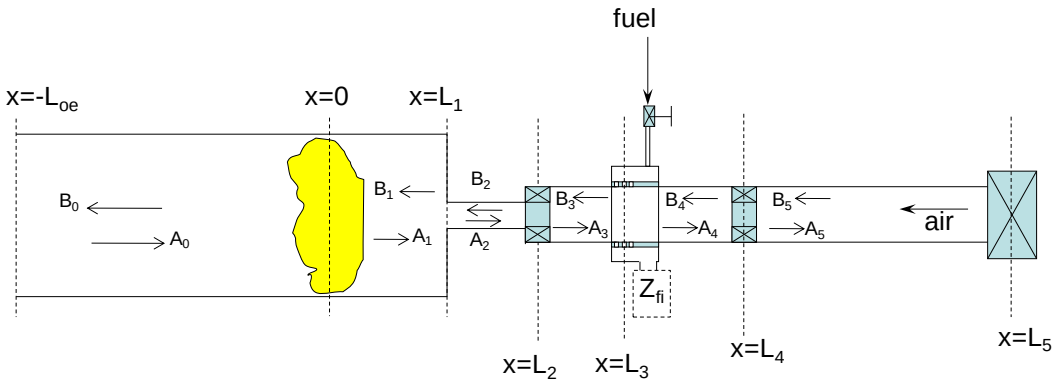

Figure 6.15: Schematic of the modeled combustor.

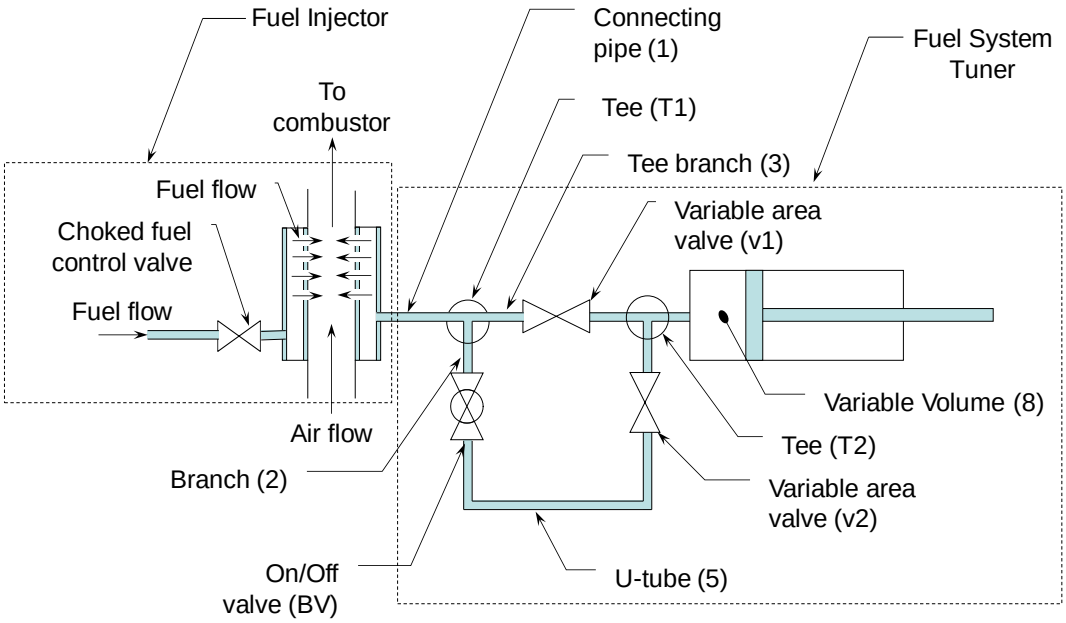

Figure 6.16: FST schematic.

Table 6.1: Combustor parameters.

	Length, [mm]	Diameter, [mm]	Fluid	Temp., [K]
L_{oe}	558.8 or 863.6	70	Products	1800
L_1	50.8	70	Reactants	300
L_2	33.9	19	Reactants	300
L_3	21.4	25.4	Reactants	300
L_4	56	25.4	Air	300
L_5	345.9	25.4	Air	300

The effect of the FST on model predicted growth rate was investigated for each of the cases shown in Table 6.2 for all 96 settings of the FST (i.e., side gate valve, top gate valve, ball valve, and volume setting) and for fuel flowrates of 0.9 and 1.9 kg/hr. In

addition, the sensitivity of the model to assumed flame location, combustor average temperature, and acoustic pressure amplitude was also investigated. For calculations other than investigations of the effect of acoustic pressure amplitude, the acoustic pressure amplitude at the inlet of the FST was taken to be 500 Pa for computing the nonlinear impedance of the fuel system.

Table 6.2: Combustor configurations tested for various FST settings.

Config.	Combustor Tailpipe Length, in. (mm)	Fuel Injector Hole Size, in. (mm)	FST U-tube Length, in. (mm)	Combustor Inlet Diameter, in. (mm)	Equiv. Ratio	Number of Power Settings Tested
1	24 (609.6)	0.125 (3.3)	21.75 (552.4)	0.70 (17.8)	0.8	5
2	36 (914.4)	0.125 (3.3)	21.75 (552.4)	0.70 (17.8)	0.8	5
3	24 (609.6)	0.125 (3.3)	21.75 (552.4)	0.70 (17.8)	0.9	5
4	24 (609.6)	0.032 (0.8)	21.75 (552.4)	0.70 (17.8)	0.8	5
5	24 (609.6)	0.125 (3.3)	42.75 (1085.9)	0.70 (17.8)	0.8	5

The following sections present the results of this study, which seeks to address the questions posed at the beginning of this section. In addition, some of these predictions will be used in the next chapter to help explain the results of experiments carried out in a combustion test facility.

6.5.1 Model predictions without the FST

To better understand model predicted FST performance, the model was first used to generate some combustor growth rate trends without the FST. All of these predictions were developed using the model for Configuration 1 from Table 6.2 assuming the FST was turned off. In particular, the sensitivity of the combustor to fuel flowrate, equivalence ratio, fuel injector hole diameter, and combustor length were considered.

Figure 6.17 shows a plot of the growth rate of the combustor versus fuel flowrate for several different fuel injector hole diameters ranging from 0.41 to 6.6 mm. Notice that the model predicts that the combustor is less stable at higher fuel flowrates than at lower ones. As predicted by the model in Chapter 2, the acoustic pressure amplitude increases with combustor power setting.

For this combustor, the fuel injector actually consists of an array of three rows of twelve holes. Since the total number of holes was the same for all cases, reducing the diameter of the holes reduces the effective area and increases the impedance of the fuel injector. As fuel injector impedance increased, fuel velocity oscillations decreased, and the contribution of fuel velocity oscillations to the total heat release oscillation decreased. However, equivalence ratio oscillations depend on both the magnitude and phase of the fuel and air velocity oscillations. Reducing the magnitude of the fuel velocity oscillations does not necessarily mean that equivalence ratio oscillations are eliminated. It simply means that the fuel flows more steadily into an oscillating air stream.

For the combustor configuration modeled here, the model predicts that larger diameter fuel injector holes lead to higher growth rates than smaller diameter ones. However, as shown in Chapter 2, this result depends on the location of the fuel injector in the air inlet, the frequency of the instability, and the fact that the fuel injector holes are not choked.

Figure 6.18 and Figure 6.19 show the effect of fuel flowrate on growth rate for a range of equivalence ratios with injectors having 0.83 and 3.3 mm hole diameters, respectively. It should be noted that although the equivalence ratio was varied, the average combustor temperature was assumed to be 1800 K for all cases.

Figure 6.18 shows that the equivalence ratio has a rather large impact on combustor stability. For example, at a fuel flowrate of 0.9 kg/hr, the combustor is nearly

stable for $\phi = 1.0$ but very unstable for $\phi = 0.5$ or 0.6. This effect is predicted to be much worse at 1.9 kg/hr where the higher equivalence ratios have negative growth rates while the lowest equivalence ratio has a growth rate of 10.

Figure 6.19 shows the effect of equivalence ratio on combustor stability for the range of fuel flowrates shown. Clearly, at 0.9 kg/hr, the model predicts that the growth rate should increase as the equivalence ratio decreases. However, the 0.8 to 1.0 equivalence ratio cases have nearly the same growth rate as do the 0.5 and 0.6 equivalence ratio cases. However, at a fuel flowrate of 1.9 kg/hr, the model predicts that the lowest growth rate corresponds to the $\phi = 0.9$ case, but the highest growth rate corresponds to the $\phi = 0.8$ case. Finally, note that the growth rate tends to increase with fuel flowrate as before.

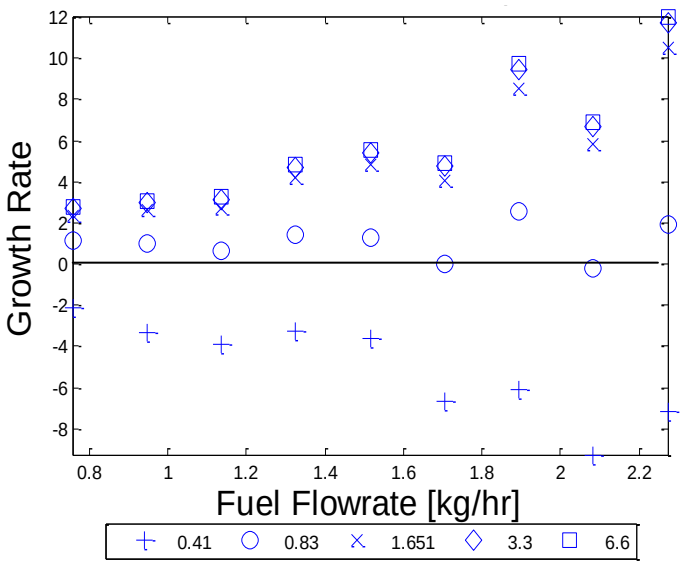

Figure 6.17: Growth rate vs. Fuel flowrate for five different fuel injector diameters. (Combustor length = 609 mm, FST off, Combustor area/Inlet area=10, Equivalence ratio=0.8).

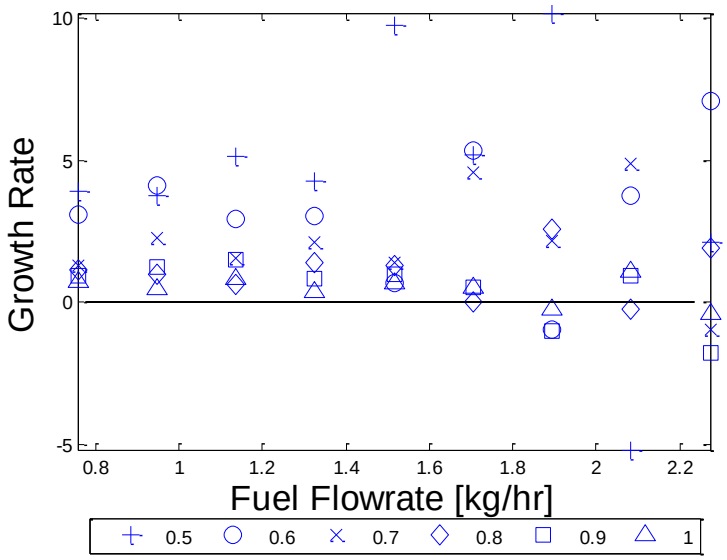

Figure 6.18: Growth rate vs. Fuel flowrate for five equivalence ratios. (Combustor length = 609 mm, FST off, Combustor area/Inlet area=10, Fuel injector hole diameter=0.83 mm)

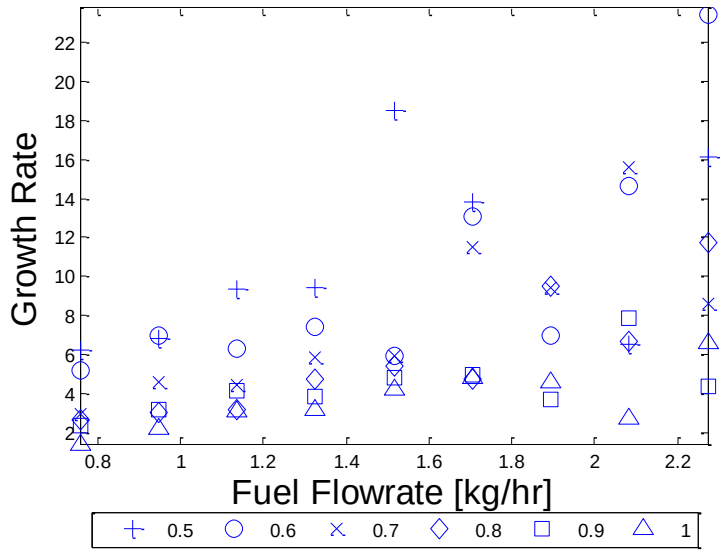

Figure 6.19: Growth rate vs. Fuel flowrate for five equivalence ratios. (Combustor length = 609 mm, FST off, Combustor to Inlet area ratio=10, Fuel injector hole diameter=3.3 mm)

Figure 6.20 shows the results of the same calculation for a 914 mm long combustor. First, notice that the growth rates for the 914 mm long combustor are much

higher than for the 609 mm long combustor. This indicates that the 914 mm long combustor is more unstable for all fuel flowrates and equivalence ratios and, therefore, should have higher acoustic pressure amplitudes. Also, notice that the growth rate increases with fuel flowrate for all but the highest fuel flowrate as before.

At 0.9 kg/hr, the growth rate decreases as the equivalence ratio increases. This indicates that lean combustors should be more unstable. At 1.9 kg/hr, the $\phi = 0.9$ case still yields the lowest growth rate, but the $\phi = 0.7$ case now produces the highest. The $\phi = 0.8$ case being about 20% lower than the $\phi = 0.7$ case.

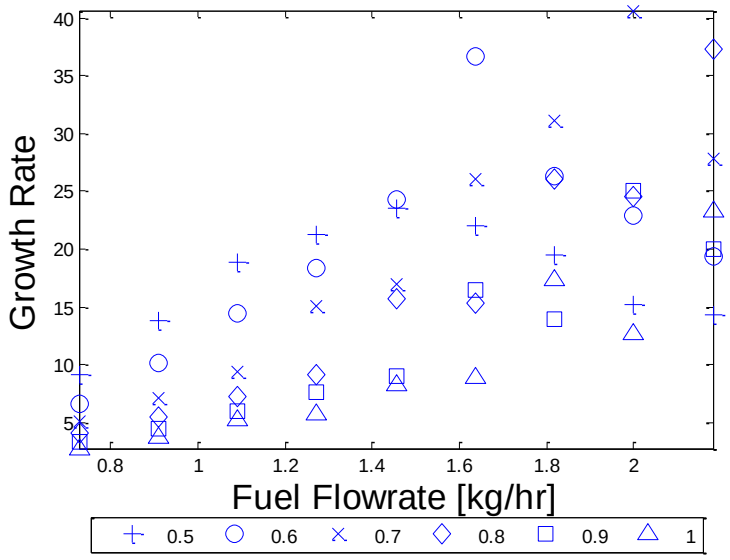

Figure 6.20: Growth rate vs. Fuel flowrate for five different equivalence ratios. (Combustor length = 914 mm, FST off, Combustor to Inlet area ratio=10, Fuel injector hole diameter=3.3 mm)

Figure 6.21 shows the model predictions for several different ratios of combustor to air inlet area. Assuming fixed combustor cross-sectional area, this ratio increases with decreasing air inlet pipe area. This gives an indication of how changing the geometry of the dump plane might affect combustor stability and how sensitive the model predictions are to choice of this ratio. The plot shows that for area ratios above

10, the growth rate of the combustor does not depend strongly on this ratio. However, the growth rate does depend on combustor power setting (i.e., fuel flowrate). For an area ratio of 5.7, the combustor is nearly stable for all power settings, and for an area ratio of 2.04, the combustor is stable for all fuel flowrates except 1.7 kg/hr. These results seem to indicate that large combustor to inlet area ratios lead to large combustion instabilities whereas smaller ones do not.

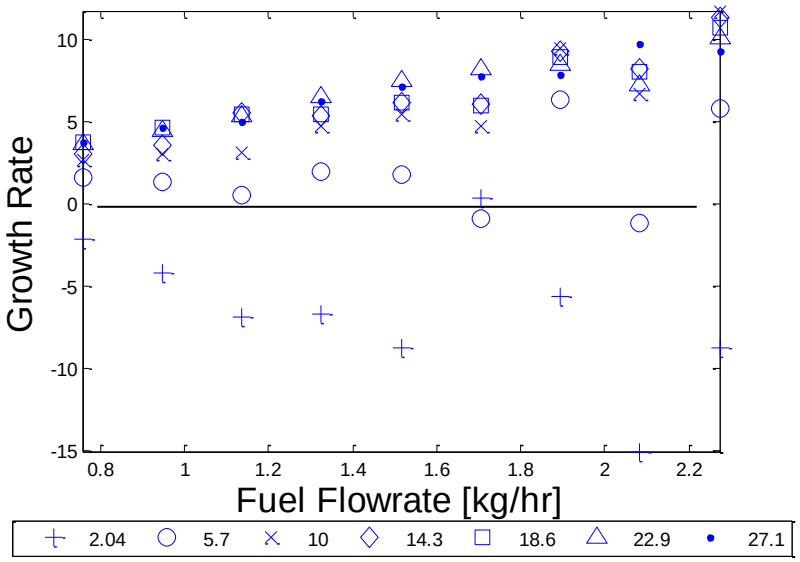

Figure 6.21: Growth rate vs. Fuel flowrate for seven different values of Combustor to Inlet area ratios. (Combustor length = 609 mm, FST off, Equivalence ratio=0.8, Fuel injector hole diameter=3.3 mm)

6.5.2 Model predictions of combustor growth rates (FST performance)

Having established some basic model predictions regarding combustor stability, the model was then used to develop some combustor stability trends with the FST tuned to a variety of settings. The model was used to accomplish three basic purposes. First, the model was used to determine which, if any, settings of the FST were predicted to result in stable combustor operation by the model. Second, the predictions of the model were used to better understand the underlying physical phenomenon responsible for the effect of the fuel system on combustor stability. Finally, the model was used to better understand the sensitivity of combustor growth rate to combustor average temperature, equivalence ratio, fuel injector hole diameter (i.e., fuel injector effective area), and FST geometry.

Model predictions for the combustor with the FST tuned to a variety of settings were obtained as follows. For each particular combustor configuration listed in Table 6.2, the model was run at the given equivalence ratio for the two different fuel flowrates (0.9 and 1.9 kg/hr). For each power setting and combustor configuration, 96 FST settings were tested. These 96 FST settings correspond to four equally spaced settings for each of the two variable area valves, two settings (ON and OFF) of the ball valve, and three equally spaced settings of the tunable volume section. (The FST settings and corresponding case numbers are shown for reference in Appendix F.) At each FST setting the combustor acoustic pressure was recorded. Using this procedure, a database of $7 \times 5 \times 96 = 3360$ data points was obtained. It should be noted that cases 20, 24, 28, 32, 52, 56, 60, 64, 84, 88, 92, and 96 were cases where the FST was effectively turned off due to the settings of the various valves. Figure 6.22 shows a plot

with each of the FST component settings as a function of its corresponding case number for reference.

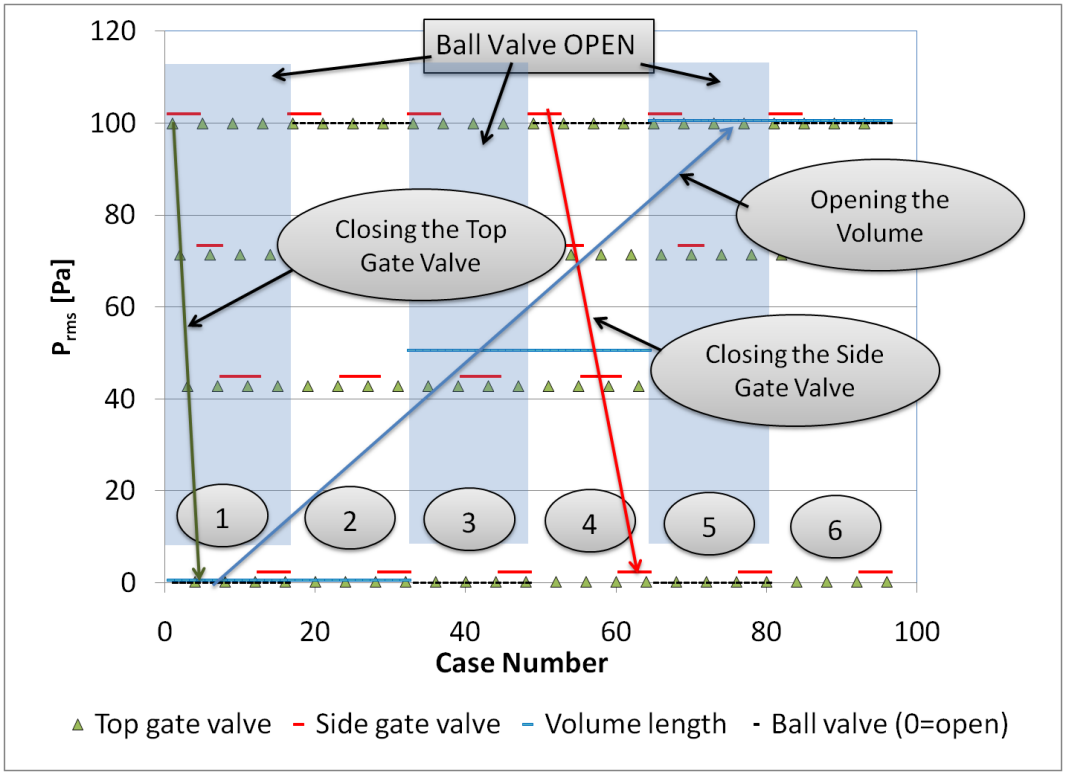

Figure 6.22: FST component % open vs. FST case number (see Appendix F) for reference.

6.5.2.1 Configuration 1

This section presents the results of model calculations for Configuration 1, which had an instability frequency with no FST of approximately 270 Hz. Of particular interest was the combustor growth rate as a function of FST setting. By assumption, the primary effect of the FST is to modify the impedance of the fuel system impedance. Therefore, to better understand why certain FST settings yielded more or less stable combustor growth rates, the correlation between model predicted fuel system impedance and combustor growth rate was investigated.

First, consider the effect of tuning the FST on the instability frequency of the combustor. Figure 6.23 shows the instability frequency of the combustor for both the 0.9 and 1.9 kg/hr fuel flowrate cases for Configuration 1. The instability frequency with no FST was 270 Hz. Clearly, the frequency of the instability was affected by tuning the FST, but the effect was generally less than +/-10% of the no FST case. Turning the heat release in the model off, revealed that the shift in frequency due to heat release was small. This effect may be partially due to the presence of the FST changing the natural frequency of the entire combustion system or because tuning the FST changes the phase of the heat release relative to the acoustic pressure oscillation at the combustion zone. Either of these effects can have an effect on the instability frequency.

Turning both the heat release and the FST OFF in the model, the natural frequency of the combustor was predicted to be 324 Hz. Turning the FST OFF but leaving the heat release ON in the model led to a predicted instability frequency of 270 Hz. With heat release OFF but the FST ON, the predicted frequencies were generally 5 to 10 Hz higher than shown in Figure 6.23 with the exception of zones 4 and 6. In these

zones, the predicted frequencies were typically 329 Hz, which is about 5 Hz higher than the natural frequency of the combustor without the FST and with no heat release.

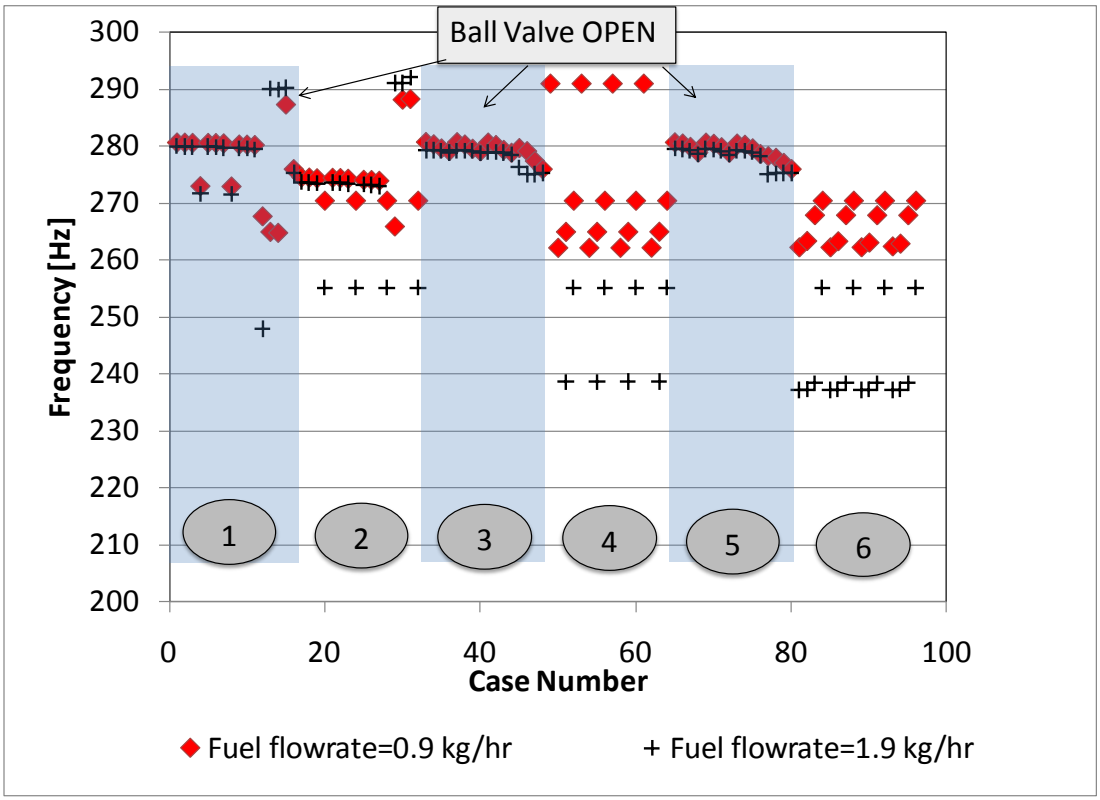

Figure 6.23: Model predicted instability frequency vs. FST setting for Configuration 1.

Figure 6.24 and Figure 6.25 show the combustor growth rate as a function of FST case number (i.e., FST setting) for fuel flowrates of 0.9 and 1.9 kg/hr, respectively. These plots show conclusively that numerous FST settings yield stable combustor growth rates and that without the FST the combustor is unstable. In particular, at a fuel flowrate of 0.9 kg/hr, zones 3 through 6 exhibit very low growth rates compared with zones 1 and 2. This trend is also seen to a lesser degree in the 1.9 kg/hr case. In zones 1 and 2, the FST volume is completely closed, so this trend indicates that the effect of the FST volume on combustor stability was significant.

Careful examination of these figures also reveals that the position of the side gate valve has little effect until the valve is closed. However, in some cases the growth rate increases on closing the side gate valve, and in some cases, the growth rate decreases depending on the volume position. Closing the top gate valve always affects combustor stability with the basic trend being that closing the top gate valve leads to higher growth rates. Some exceptions can be seen in the figure, however.

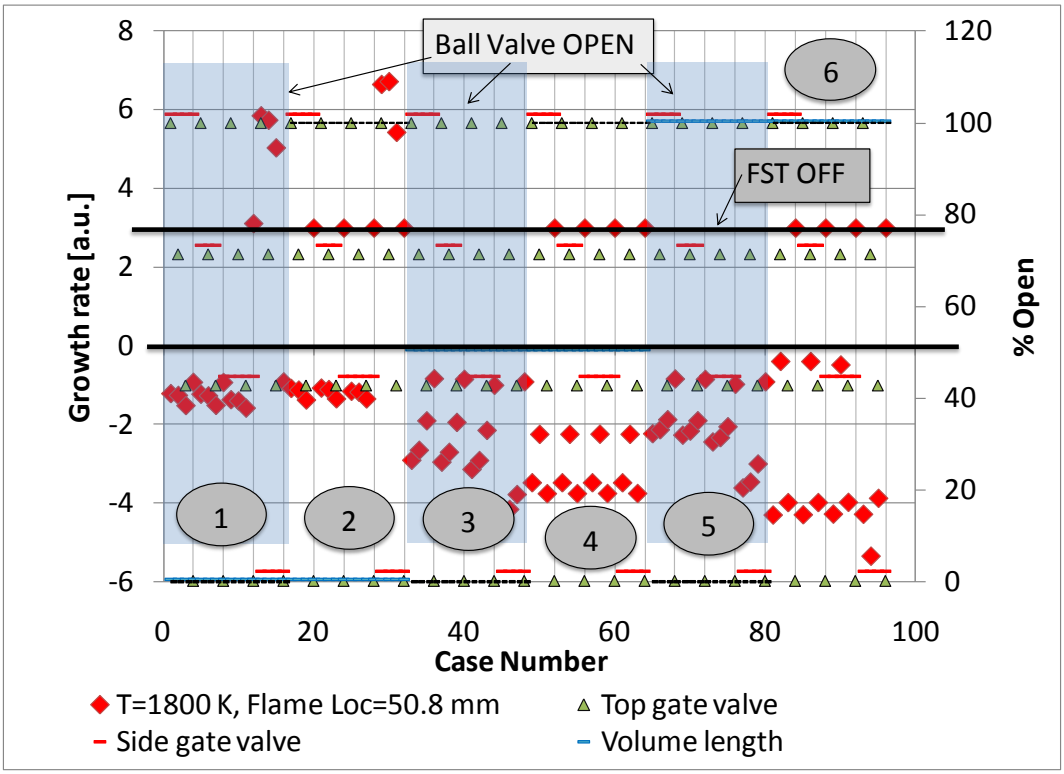

Figure 6.24: Growth rate vs. FST setting for Configuration 1 at a fuel flowrate of 0.9 kg/hr.

The position of the ball valve also plays a role in the effectiveness of the FST. Interestingly, zones 2, 4, and 6 exhibit some of the lowest predicted growth rates. However, the highest predicted growth rates also occur in these zones. Due to this tendency, the model indicates that care must be taken to avoid FST settings that result in unacceptably high growth rates.

The ability to tune the impedance of the fuel system leads to a potential problem. There are, in fact, several settings of the FST that lead to growth rates that are much higher than those with no FST. However, these regions appear to be confined to FST settings in which the volume is completely closed.

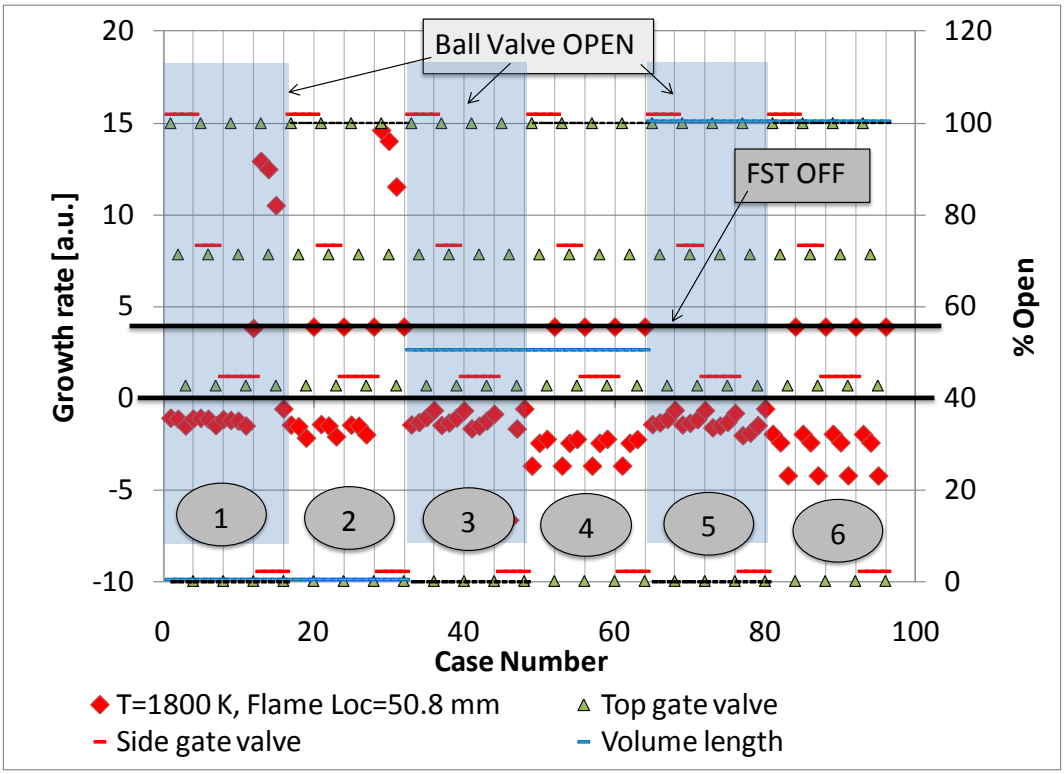

Figure 6.25: Growth rate vs. FST setting for Configuration 1 at a fuel flowrate of 1.9 kg/hr.

Figure 6.26 and Figure 6.27 show the combustor growth rate and the magnitude and phase of the fuel system impedance for Configuration 1 as a function of FST case number. In these plots, the magnitude of the impedance was normalized as follows:

$$\text{Normalized } |Z_{fi}| = \frac{|Z_{fi}|}{10\dfrac{(\rho c)_{air}}{S_{air}}}100. \qquad (6.132)$$

Careful examination of these figures reveals that there are negative growth rates associated with Normalized $|Z_{fi}| > 20\%$ as long as the $phase(Z_{fi})$ is not near +/-90 degrees. The figures also show that when Normalized $|Z_{fi}| < 20\%,$ the growth rate is always positive, indicating an unstable combustor.

When the Normalized $|Z_{fi}| < 20\%,$ the fuel injection rate oscillation is very large compared with the air inlet pipe pressure oscillations. In this case, the heat release oscillations due to the fuel-air ratio oscillations can be large enough to dominate other sources of heat release oscillations. With proper phasing, i.e., $phase(Z_{fi}) \neq \pm 90$ degrees, the gain due to the oscillating fuel-air ratio can be quite large. In fact, the model predicts that it can lead to growth rates larger than for combustors with no tuning system at all.

These plots also show that most of the stable operating points occur at FST case numbers that yield a $phase(Z_{fi})$ between -60 and 60 degrees. When the $phase(Z_{fi})$ is near +/- 90 degrees the predicted growth rate is the same as the growth rate for a fuel system with no FST at all. This is understandable considering that when fuel is injected 90 degrees out of phase with the air inlet pipe acoustic pressure, the heat release due to the fuel oscillation at the combustion zone is 90 degrees out of phase with the pressure there. Therefore, in this case the oscillating heat release due to the fuel-air ratio oscillation has no effect on combustor stability.

In addition, the plots show that when the Normalized $|Z_{fi}| > 90\%,$ the $phase(Z_{fi})$ has very little effect on combustor stability. The reason for this is that the amplitude of the fuel injection rate oscillations is very small compared to the acoustic pressure amplitude when Normalized $|Z_{fi}| > 90\%.$ Under these conditions, the combustor is either stable or it is not, but because the amplitude of the fuel flowrate

oscillations are so small, their contribution to the overall heat release oscillation is negligible. This effect was also predicted by the model of Chapter 2 (see Figure 2.5).

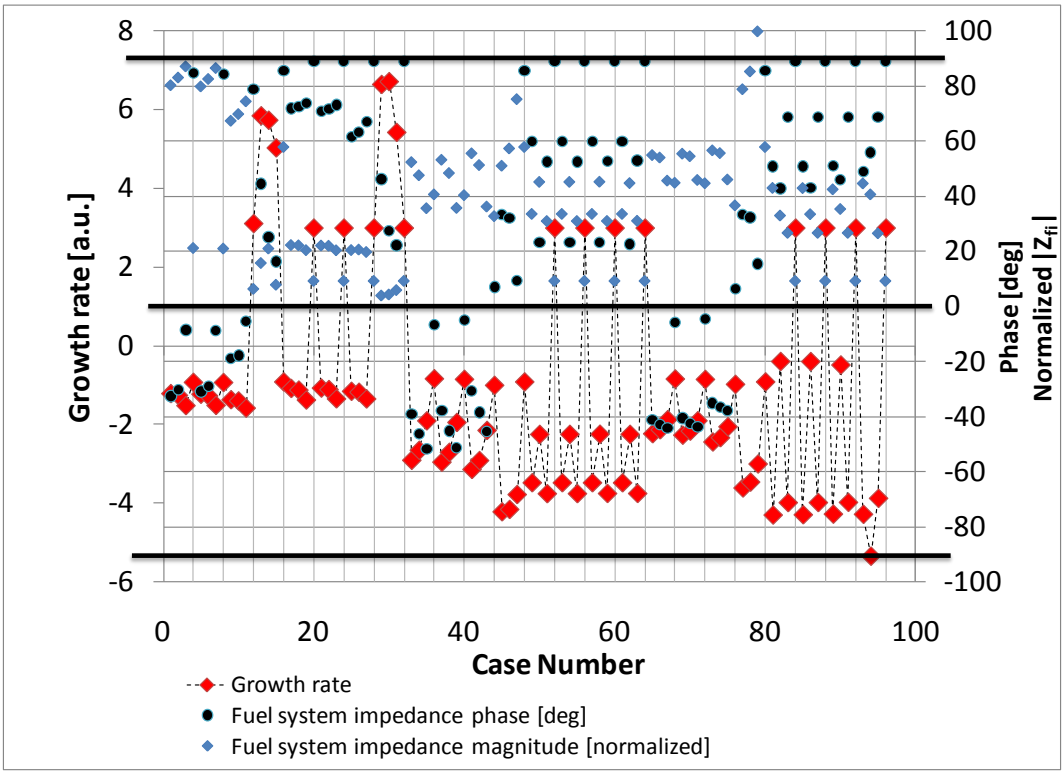

Figure 6.26: Growth rate vs. fuel system impedance (magnitude and phase) setting for Configuration 1 at a fuel flowrate of 0.9 kg/hr.

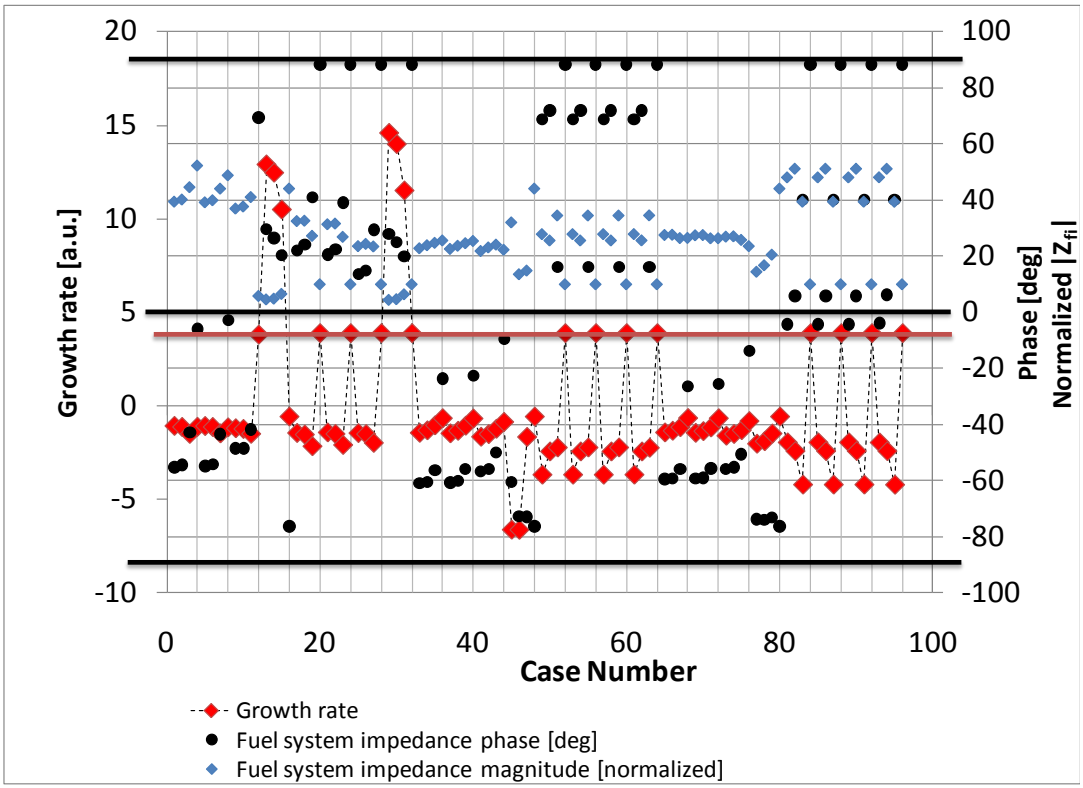

Figure 6.27: Growth rate vs. fuel system impedance (magnitude and phase) for Configuration 1 at a fuel flowrate of 1.9 kg/hr.

In summary, the model predictions for Configuration 1 predict that the FST should be able to stabilize the combustor at a number of different settings. In addition, the model indicates that the most stable operation will occur at FST settings having a Normalized $|Z_{fi}| > 20\%$ and a $phase(Z_{fi})$ between -60 and 60 degrees. Operating points having a Normalized $|Z_{fi}| < 20\%$ may exhibit unstable operation even worse than with no FST, and when the $phase(Z_{fi}) = \pm 90$ degrees, the combustor will operate as if the FST were not present.

6.5.2.2 Configuration 2

To investigate the sensitivity of FST operation to frequency, the model was used to predict the stability of a combustor having a natural frequency near 170 Hz. The model predictions for Configuration 2 for fuel flowrates of 0.9 and 1.9 kg/hr are shown in Figure 6.30 through Figure 6.32. These figures show that the model does not predict good performance of the FST except in zones 1, 3, and 5. In zones 3 and 5, only a few settings are predicted to give low combustor acoustic pressure amplitudes.

Comparing the results for Configuration 2 to those for Configuration 1 at the same fuel flowrate, it is apparent that the growth for Configuration 2 is much larger than for Configuration 1 with no FST. This is consistent with the predictions of Figure 6.20 and is an indication that Configuration 2 is potentially a more unstable combustor than Configuration 1.

Figure 6.30 and Figure 6.31 show plots of the growth rate and the magnitude and phase of the fuel system impedance as a function of FST case number for flowrates of 0.9 and 1.9 kg/hr, respectively. The same basic trends that were noted in regard to Configuration 1 apply to Configuration 2, i.e., very low impedance magnitudes lead to very high growth rates and the FST is ineffective when $phase(Z_{fi}) = \pm 90$. Growth rates appear to be lowest when $phase(Z_{fi})$ is between -80 and -40 degrees with Normalized $|Z_{fi}| > 20\%$. However, Case numbers 77 and 78 for the 1.9 kg/hr case have Normalized $|Z_{fi}| < 10\%$ that are very stable. For these cases the $phase(Z_{fi})$ is very near 0 degrees.

These results suggest that a fuel system tuner having Normalized $|Z_{fi}|$ between 20% and 60% with the ability to vary the phase between +/- 90 degrees should be

adequate to stabilize the combustor. Of course, the ability to tune the FST to the frequency of the instability is a must.

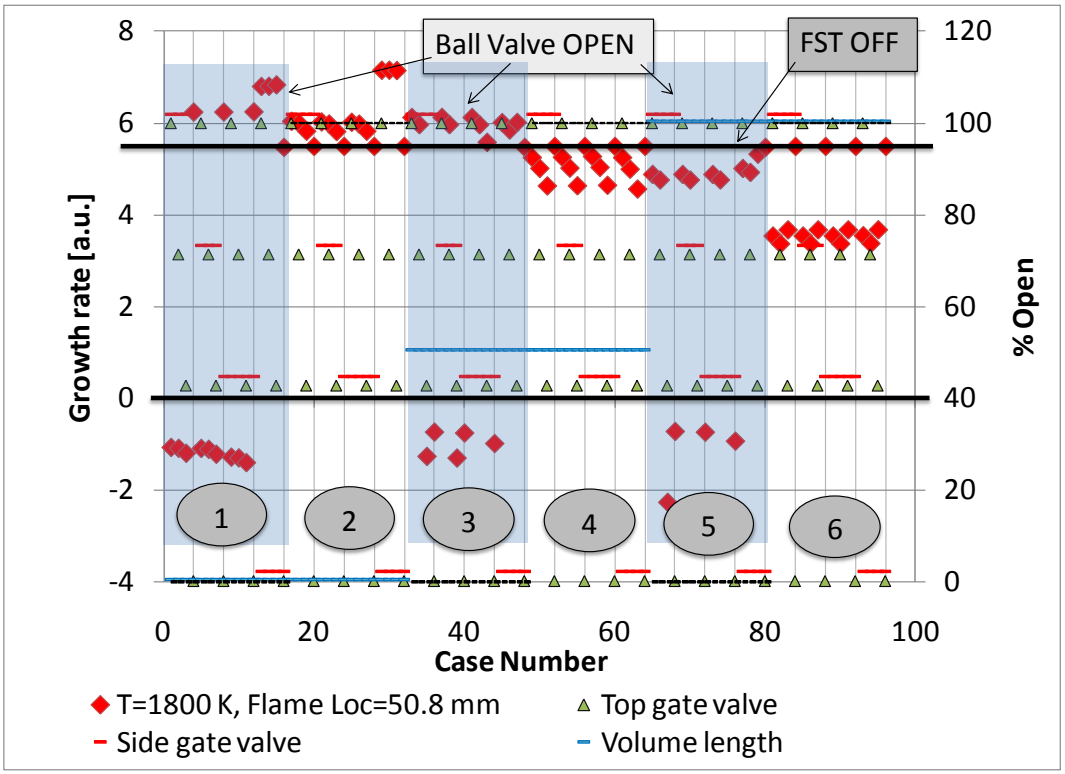

Figure 6.28: Growth rate vs. FST setting for Configuration 2 at a fuel flowrate of 0.9 kg/hr.

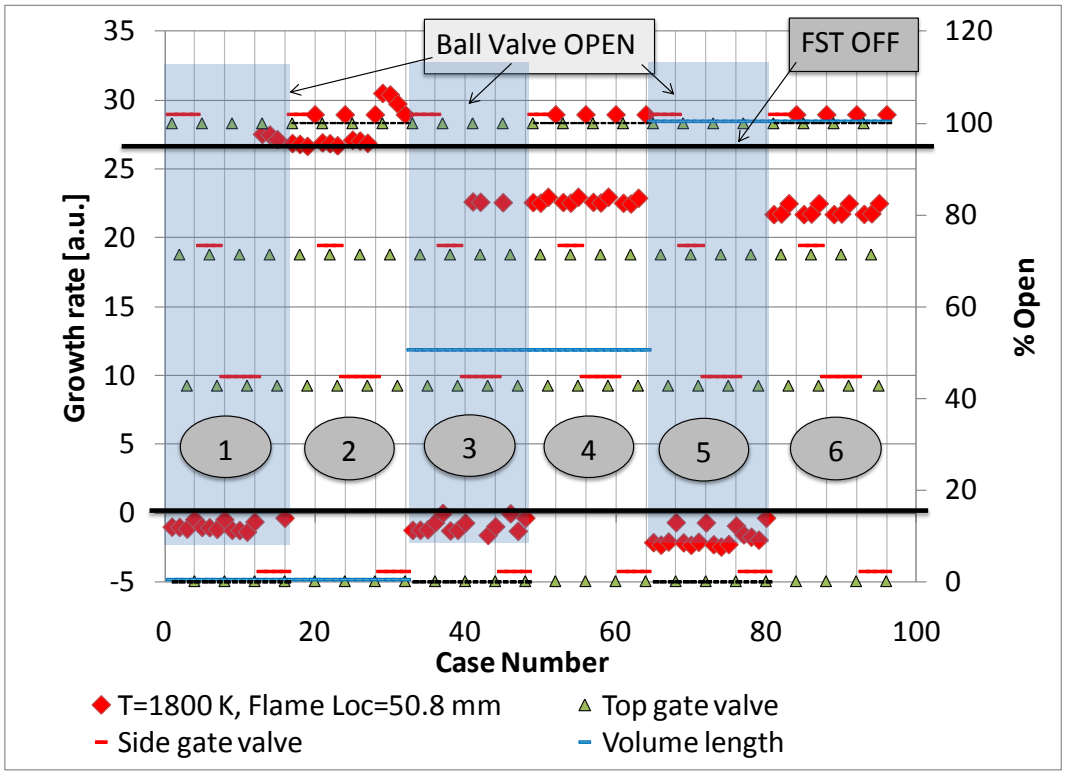

Figure 6.29: Growth rate vs. FST setting for Configuration 2 at a fuel flowrate of 1.9 kg/hr.

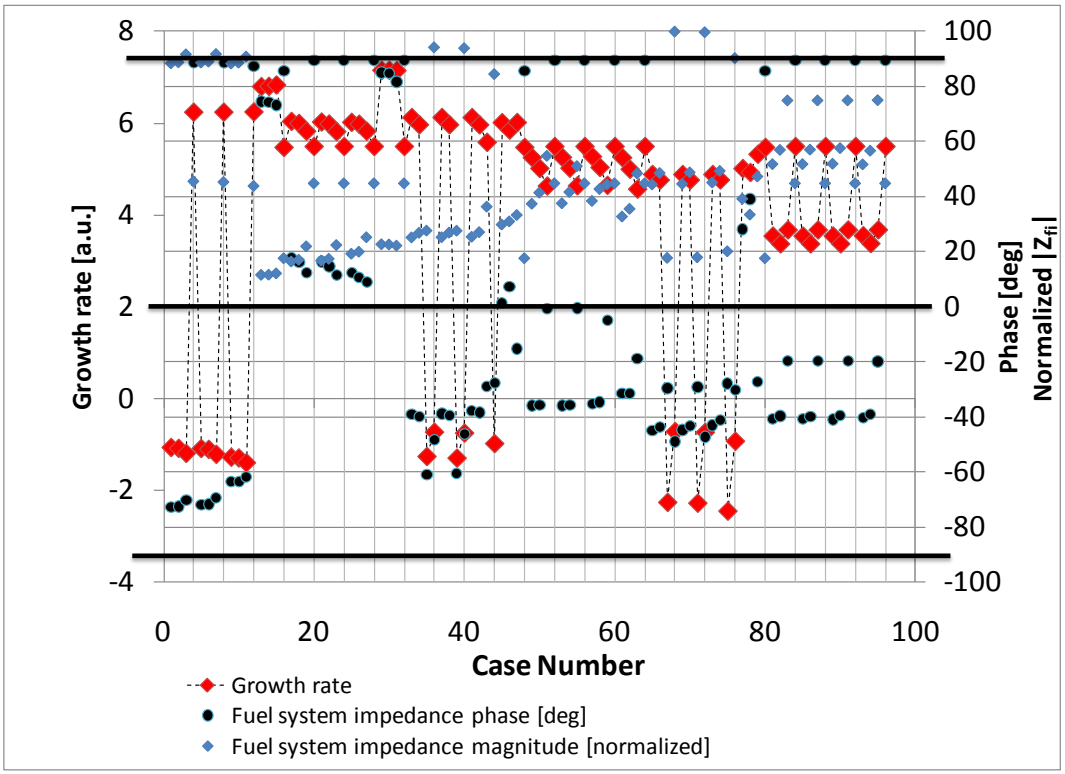

Figure 6.30: Growth rate vs. fuel system impedance (magnitude and phase) for Configuration 2 at a fuel flowrate of 0.9 kg/hr.

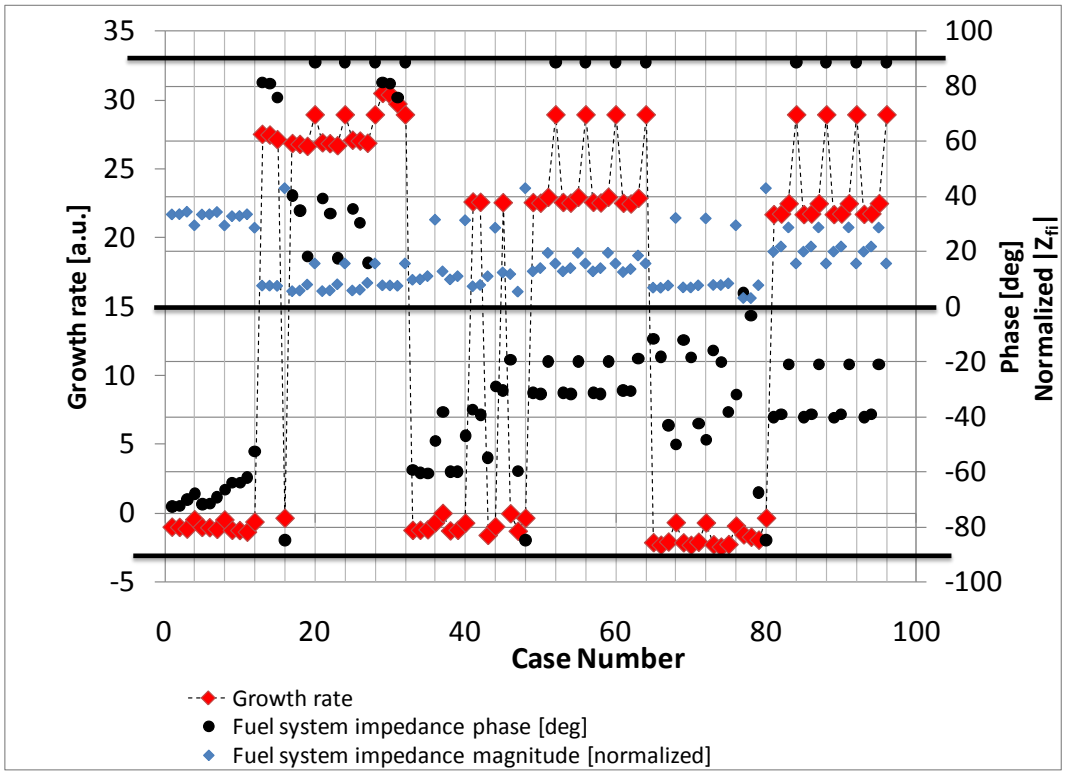

Figure 6.31: Growth rate vs. fuel system impedance (magnitude and phase) for Configuration 2 at a fuel flowrate of 1.9 kg/hr.

6.5.2.3 Model sensitivity to flame location

In practical gas turbine combustors, the flame is neither uniform nor infinitely thin. In many cases, the location of the 'center of heat release', i.e., the first moment of the heat release, is not well-known. Also, the average flame location tends to move closer to or further away from the combustor dump plane depending on whether the acoustic pressure amplitude is high or low, respectively. In addition, the flame position can shift due to other factors, such as overall power setting, inlet air temperature, and equivalence ratio. The purpose of this section is to briefly examine the sensitivity of the model predictions to the estimated flame location.

Figure 6.32 through Figure 6.35 show the model predictions for Configuration 1 and Configuration 2 for the several different flame locations noted. In general, the model predicted growth rate is smaller and less sensitive to FST setting when the flame is located 70.2 mm from the dump plane. In fact, when the flame is located 25.4 mm from the dump plane, the growth rate is most sensitive to variations in FST setting.

Based on the discussion above, the flame location that best predicts experimental results will probably depend on the acoustic pressure amplitude assuming all other factors remain constant. In other words, when the model predicts very large or very small growth rates, the best model predictions will be those in which the flame location was assumed to be very close to or farther from the dump plane, respectively.

In the absence of experimental data on flame position, the procedure was as follows. Model stability predictions were generated using several assumed flame locations. These calculations were used to place an upper and lower bound on combustor growth rate at each FST setting.

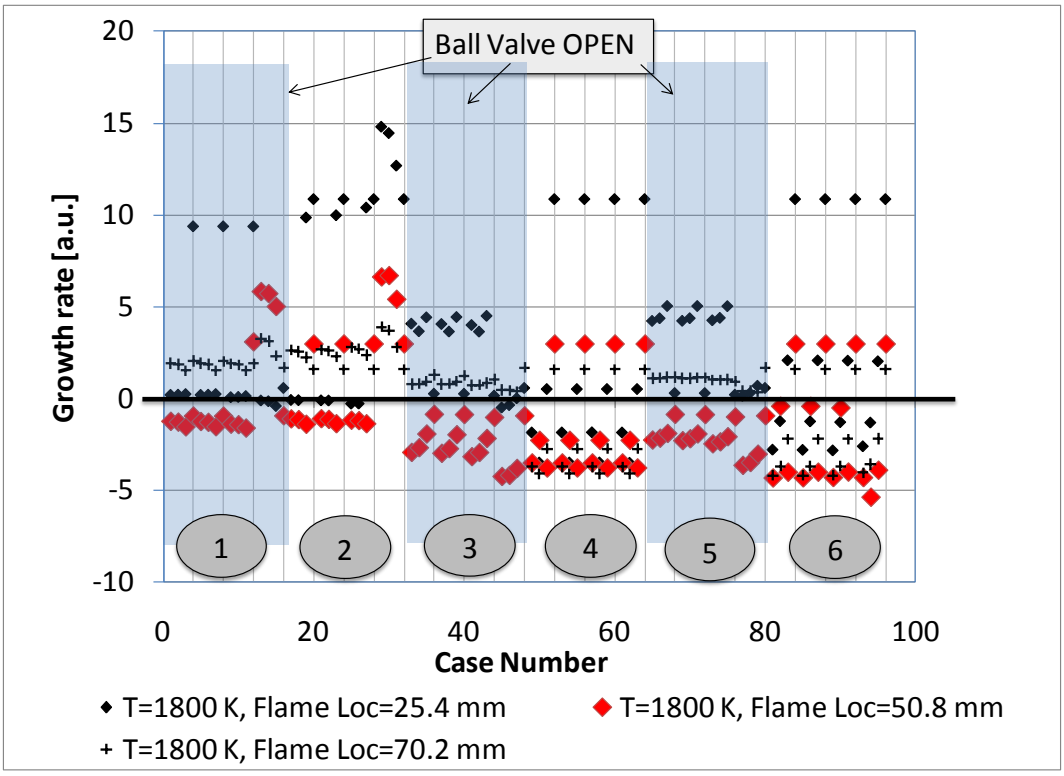

Figure 6.32: Growth rate vs. FST setting for Configuration 1 at a fuel flowrate of 0.9 kg/hr at flame locations of 25.4, 50.8, and 70.2.

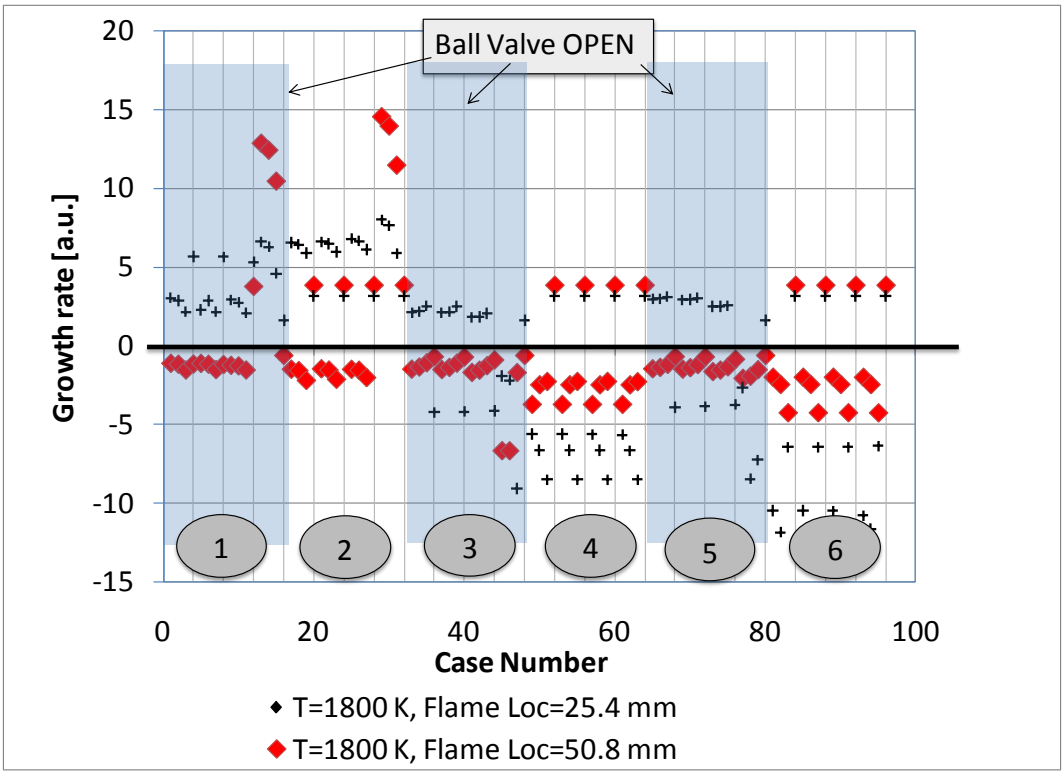

Figure 6.33: Growth rate vs. FST setting for Configuration 1 at a fuel flowrate of 1.9 kg/hr at flame locations of 25.4, and 50.8 mm.

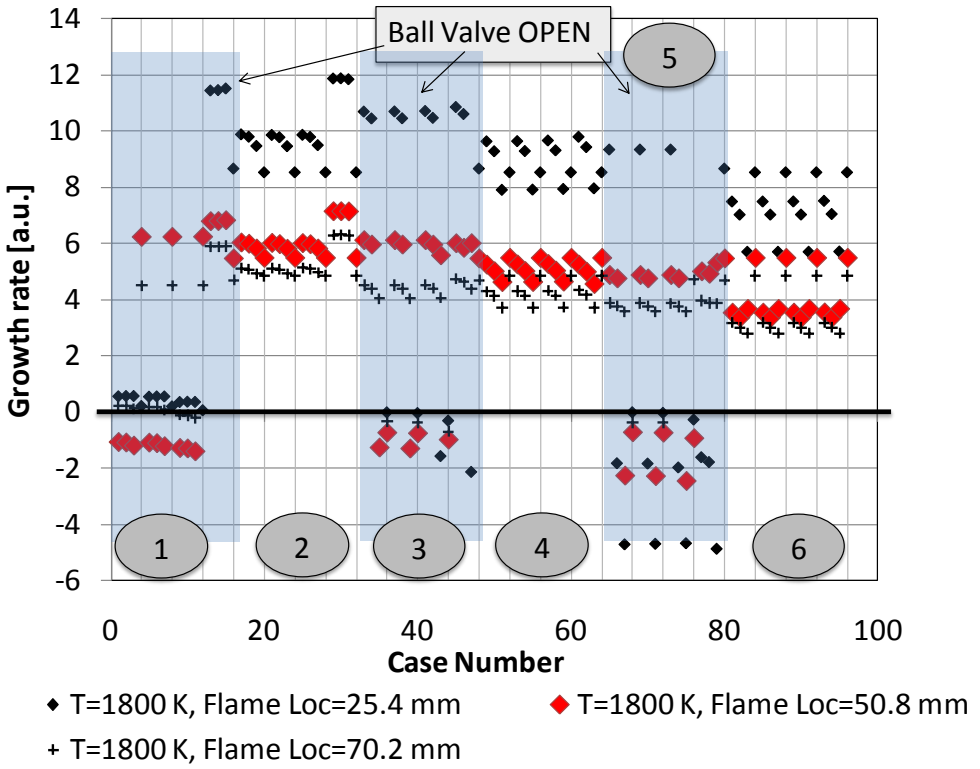

Figure 6.34: Growth rate vs. FST setting for Configuration 2 at a fuel flowrate of 0.9 kg/hr at flame locations of 25.4, 50.8, and 70.2.

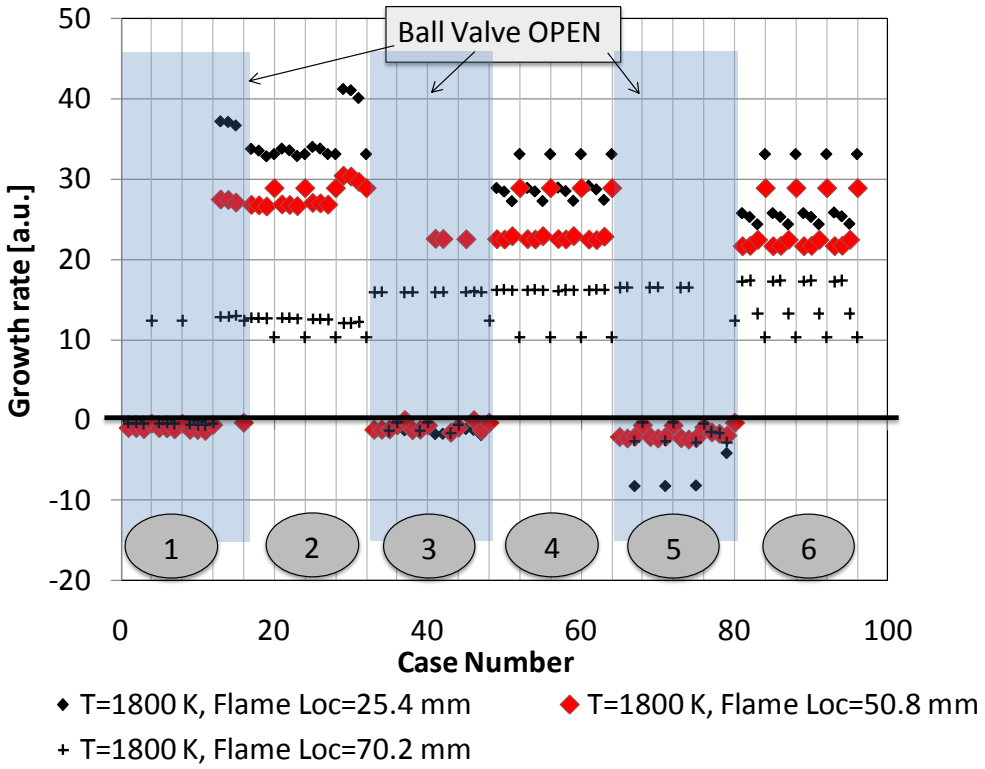

Figure 6.35: Growth rate vs. FST setting for Configuration 2 at a fuel flowrate of 1.9 kg/hr at flame locations of 25.4, 50.8, and 70.2.

6.5.2.4 Model sensitivity to combustor average temperature

As with flame location, the actual combustor average temperature depends on many factors. Among these are equivalence ratio, combustor power setting, and radiative and convective heat losses. In addition, the model assumes that the average temperature in the combustor after the flame is both uniform and constant. For this model, the primary effect of the combustor temperature is to shift the instability frequency as shown in Figure 6.36 through Figure 6.38.

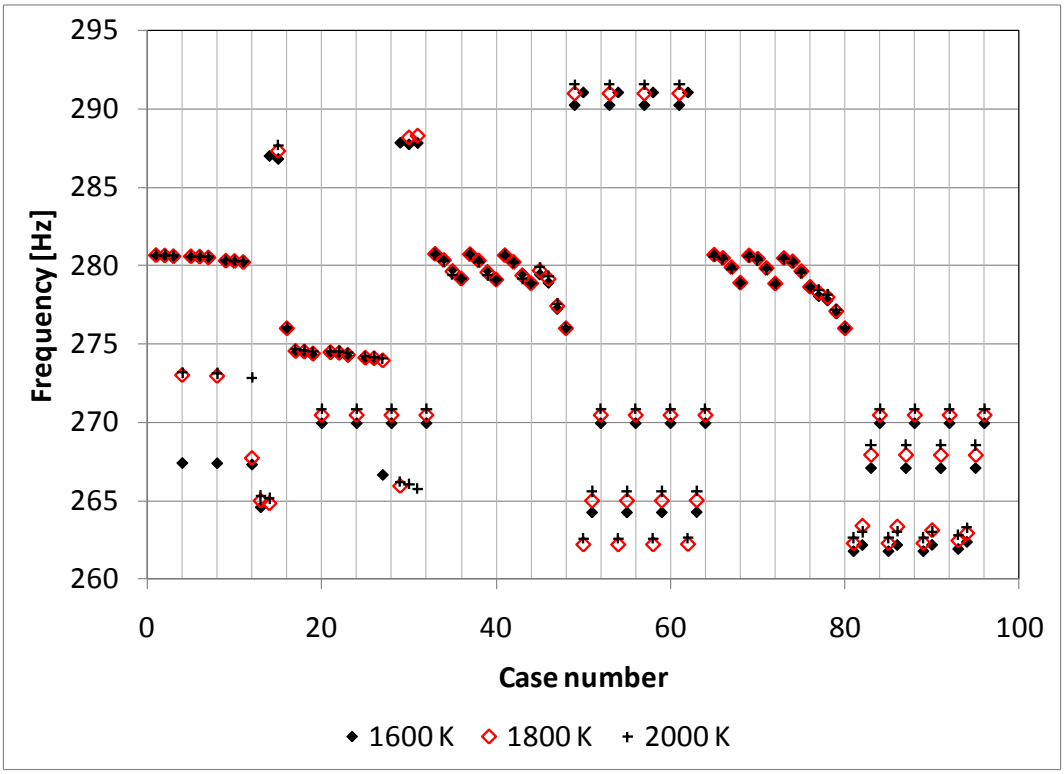

Figure 6.36: Instability frequency vs. FST setting for Configuration 1 at a fuel flowrate of 0.9 kg/hr for average combustor temperatures of 1600, 1800, and 2000 K.

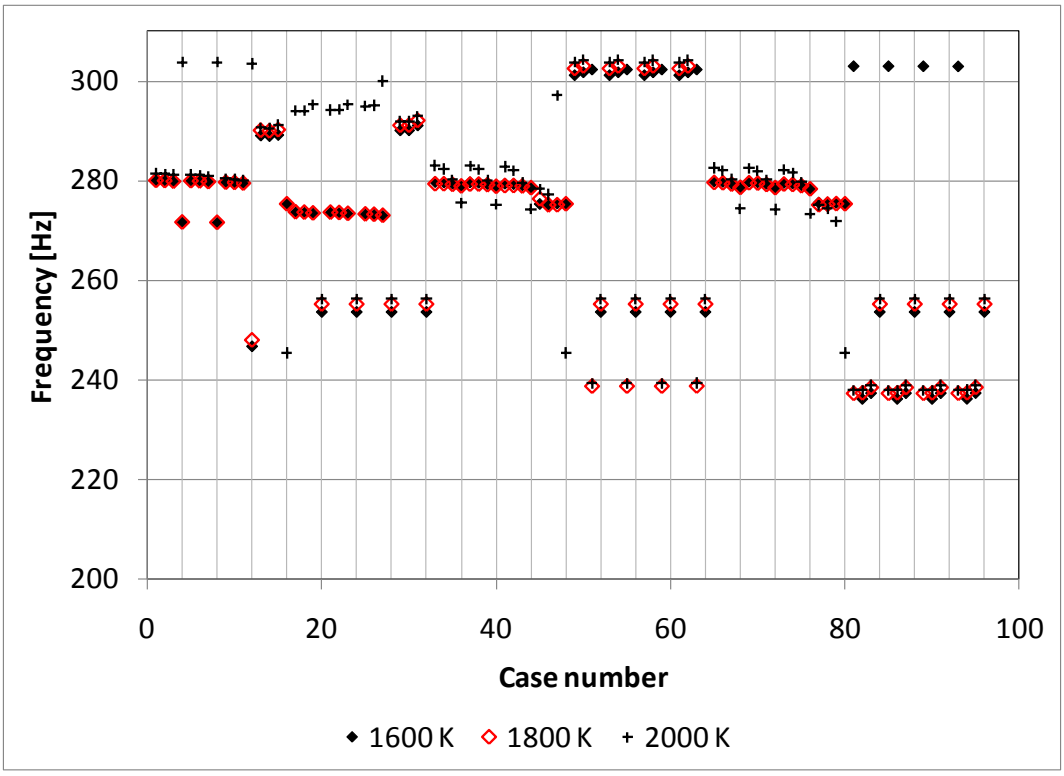

Figure 6.37: Instability frequency vs. FST setting for Configuration 1 at a fuel flowrate of 1.9 kg/hr for average combustor temperatures of 1600, 1800, and 2000 K.

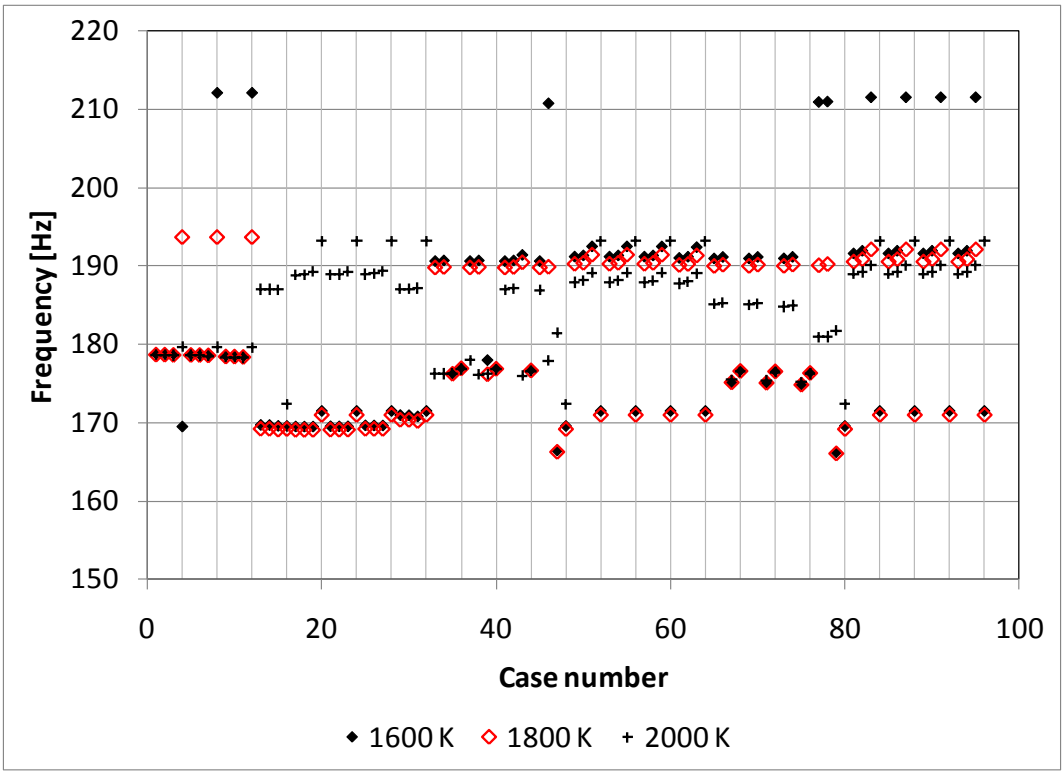

Figure 6.38: Instability frequency vs. FST setting for Configuration 2 at a fuel flowrate of 0.9 kg/hr for average combustor temperatures of 1600, 1800, and 2000 K.

Figure 6.39 and Figure 6.40 show the model growth rate predictions for Configuration 1, and Figure 6.41 shows the 0.9 kg/hr fuel flowrate case for Configuration 2. Examining Case numbers 20, 24, 28, and 32 reveals that the sensitivity is quite small for Configuration 1 as long as the FST is off. When the FST is on, the sensitivity of predicted growth rate to combustor average temperature is greater for the Configuration 1 case shown in Figure 6.40. In fact, Figure 6.36 exhibits very low sensitivity to combustor average temperature for any FST setting. As was the case for instability frequency, the model is more sensitive to combustor average temperature for the Configuration 2 case shown in Figure 6.41.

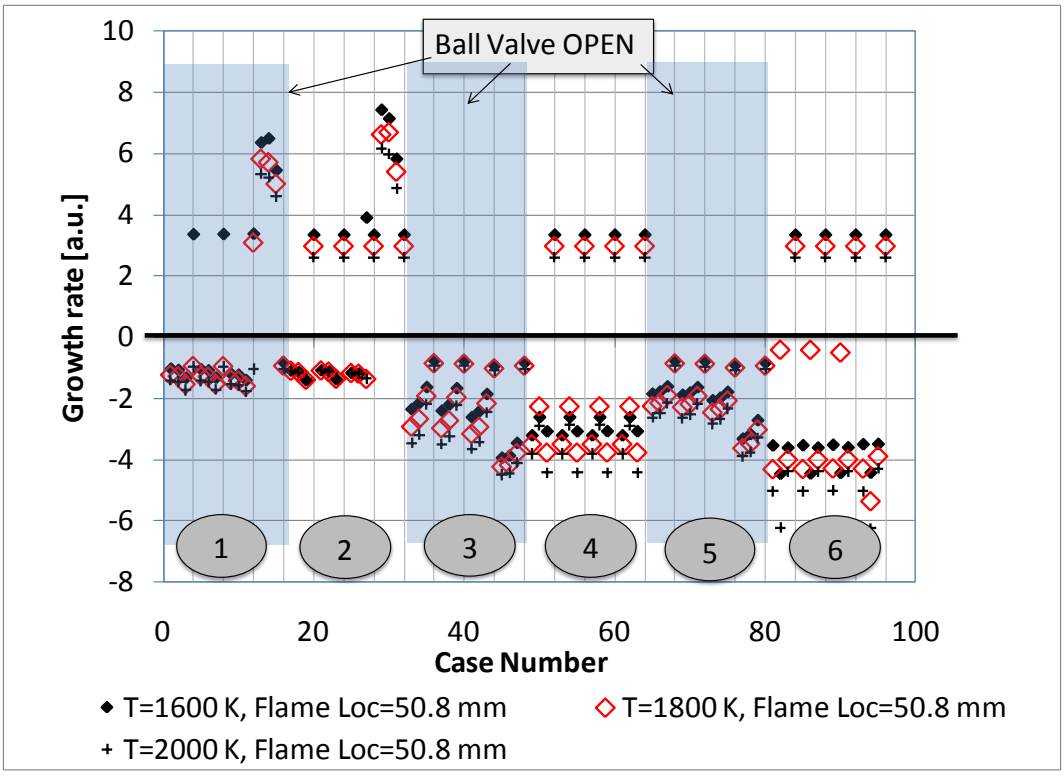

Figure 6.39: Growth rate vs. FST setting for Configuration 1 at a fuel flowrate of 0.9 kg/hr for average combustor temperatures of 1600, 1800, and 2000 K.

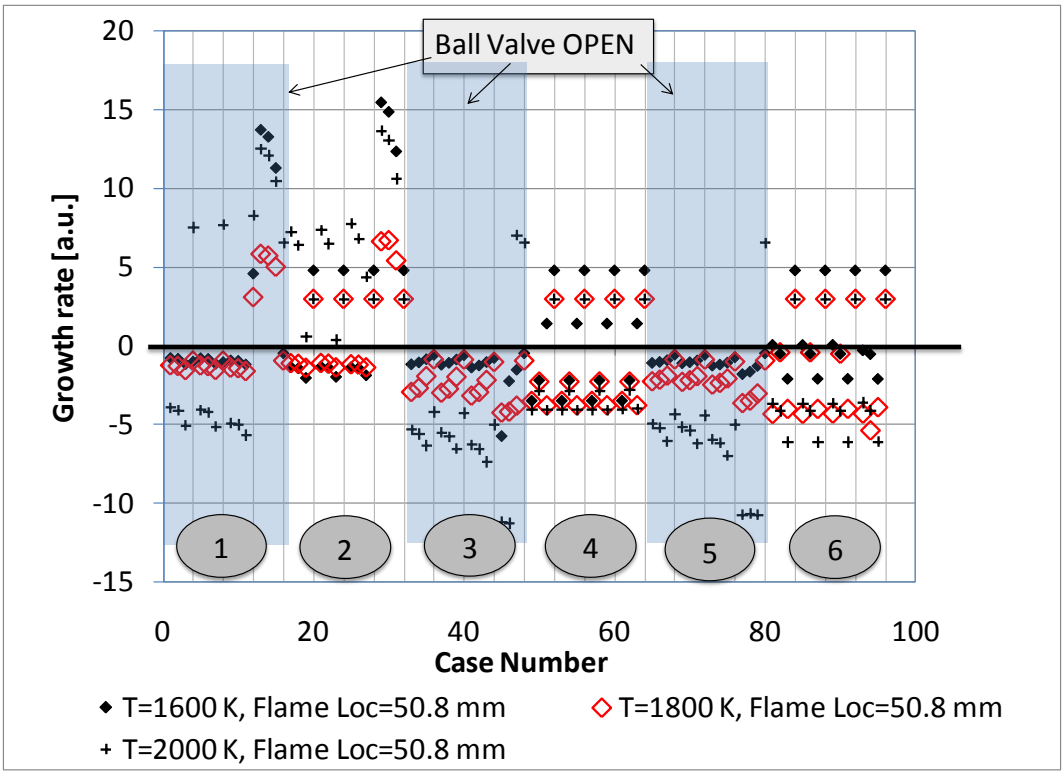

Figure 6.40: Growth rate vs. FST setting for Configuration 1 at a fuel flowrate of 1.9 kg/hr for average combustor temperatures of 1600, 1800, and 2000 K.

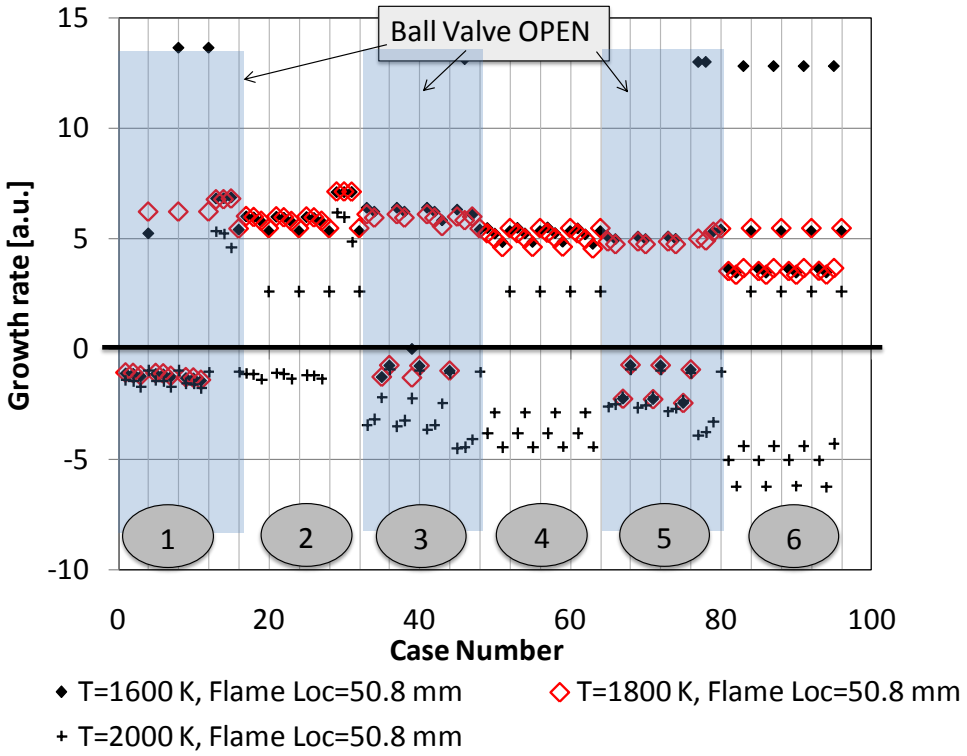

Figure 6.41: Growth rate vs. FST setting for Configuration 2 at a fuel flowrate of 0.9 kg/hr for average combustor temperatures of 1600, 1800, and 2000 K.

6.5.2.5 Model sensitivity to acoustic pressure amplitude

As has been shown, combustor acoustic pressure amplitude depends on the impedance of the fuel supply system. However, given the acoustically nonlinear elements in the FST, the impedance of the fuel supply system depends on the acoustic pressure amplitude at the inlet of the fuel supply system. Therefore, it is important to understand the sensitivity of model predicted growth rates to FST input acoustic pressure amplitude.

Due to the complexity of the fuel supply system, no simple relationship exists between the acoustic pressure amplitude and the fuel system impedance. However, the effect can be illustrated by providing the model with different acoustic pressure

amplitudes and examining the model predicted growth rate for those different input pressures.

Figure 6.42 shows the results of these calculations for Configuration 1 at the 0.9 kg/hr fuel flowrate setting. The results show a large difference in model predicted growth rates when the acoustic pressure is changed from 500 Pa to 2500 Pa, but the effect is much less pronounced when the pressure was increased from 2500 Pa to 4000 Pa. In spite of the pronounced sensitivity of the system to acoustic pressure amplitude, it is interesting to note that for all acoustic pressure amplitudes tested, there are FST system that yield stable growth rates.

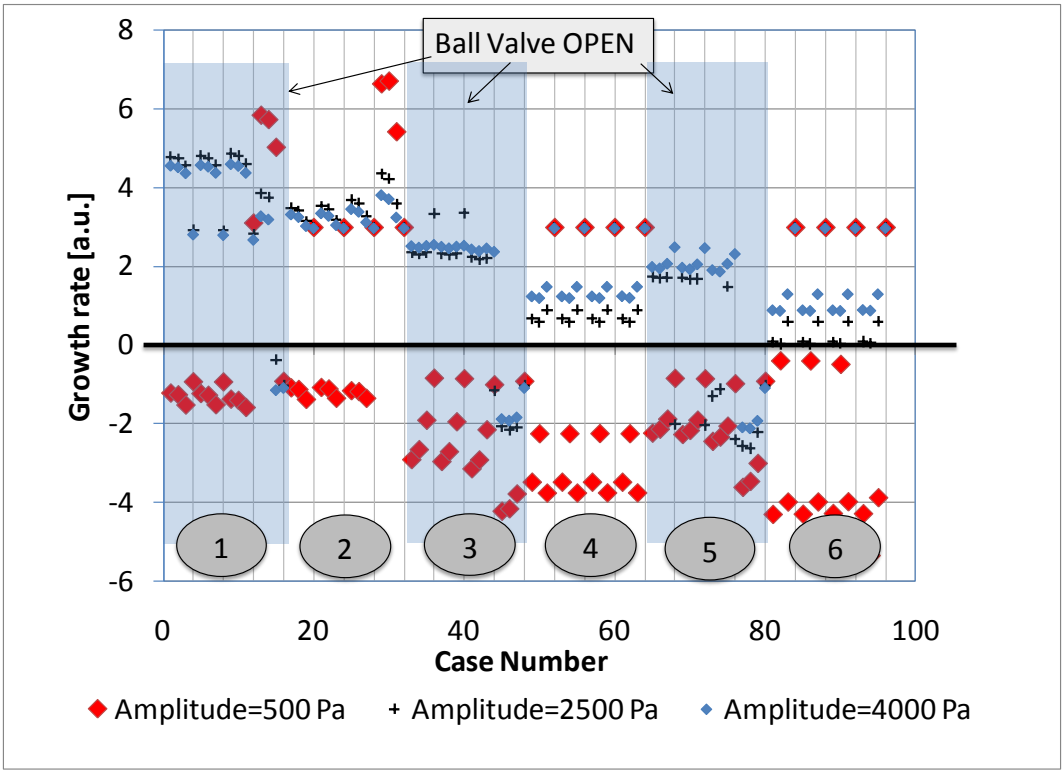

Figure 6.42: Growth rate vs. FST setting for Configuration 1 at a fuel flowrate of 0.9 kg/hr for acoustic pressure amplitudes at the fuel injector of 500, 2500, and 4000 Pa.

It is clear from these results that accurate predictions of the actual stability condition of the combustor depends on accurate knowledge of the acoustic pressure

amplitude at the fuel injector. However, since the fuel system impedance affects combustor stability, the problem is actually a coupled, non-linear problem. The best way to solve the problem is to iterate on the combustor acoustic pressure until the model predicted growth rate is zero, as mentioned in the introduction to the chapter.

6.6 Conclusions

The development of a thermo-acoustic model of a lean, premixed combustor similar to those used in modern gas turbine engines was presented. The model for the combustor fuel supply system included the developed nonlinear FST impedance model. A flame transfer function was used to model the combustion process. The combustor/FST thermo-acoustic model was used to predict the instability frequency and growth rate of the model combustor for two different combustor configurations. Further, the sensitivity of combustor growth rate to combustor average temperature, FST input pressure, and flame location was also investigated for a wide range of FST settings.

The model predictions indicate that large FST impedances can lead to either stable or unstable combustor operation depending on the combustor, but that phase control has no effect on combustor stability in this case. In addition, model predictions show that fuel system tuning, i.e., phase control, is very important and effective when the magnitude of the FST impedance is very small. However, in this case, care must be taken when tuning the fuel system due to extreme sensitivity of the combustor to the phase of the fuel system impedance. In some instances, destructive combustor pressure oscillations were predicted. The model predictions indicate that the best performance is obtained for magnitudes of fuel system impedance between 20-80% of $10\frac{(\rho c)_{fuel}}{S_{fi}}$. In this range, the combustor responds well to changes in the impedance of the fuel supply system without the danger of excessive combustor pressure oscillations at off-design FST settings. The results obtained here were shown to be consistent with predictions of the model developed in Chapter 2. Additional model predictions will be

presented in Chapter 7 as needed to clarify, explain, and compare with the experimental results presented therein.

Chapter 7:

Experimental Evaluation of the FST

7.1 Introduction

This chapter describes an experimental investigation of the effect of the FST on the stability of a lean, premixed combustor developed to simulate the characteristics of dry, low NOx gas turbine combustors. These results demonstrate that the FST was able to significantly reduce the amplitude of the self-excited acoustic oscillations in the combustor. Next, the experimental measurements were used to validate the predictions of the combustor model developed in Chapter 6. Model prediction in conjunction with the experimental measurements were used to show that stable combustor operation strongly depends on FST setting and, more importantly, on overall fuel system impedance. Finally, the FST was tested on several configurations of the combustor. These results show that the FST was capable of adapting to changes in system architecture.

The developed experimental setup is shown schematically in Figure 7.1. It consists of an air inlet section, a fuel injection section, a mixing section, and a combustion chamber. For this study, the fuel injection section was retrofitted with a FST.

Air was supplied to the combustor through a choked air control valve. This air flowed down the inlet pipe through a swirler with a 45˚ vane angle. Fuel was injected into the air flow through a perforated fuel injector sleeve located just downstream of the air swirler. It included a second swirler (not shown) downstream of the fuel injection holes, which were located upstream of the combustion section. The air and fuel mixed as they flowed from the fuel injector to the dump plane where combustion was stabilized

in the recirculation zone. The combustion products were discharged to the surrounding atmosphere through the open end of the combustor.

The combustor air and fuel flow rates were measured using variable area flowmeters (i.e., rotameters). Acoustic pressures were measured with Kistler 211B5 pressure transducers in the three following locations: (1) in the combustor tube just downstream of the cooling cap, (2) in the volume just behind the fuel injector and (3) in the air inlet duct downstream the fuel injector. Combustor lengths of 914 and 609 mm were tested, which produced longitudinal instabilities with frequencies of 170 and 270 Hz, respectively.

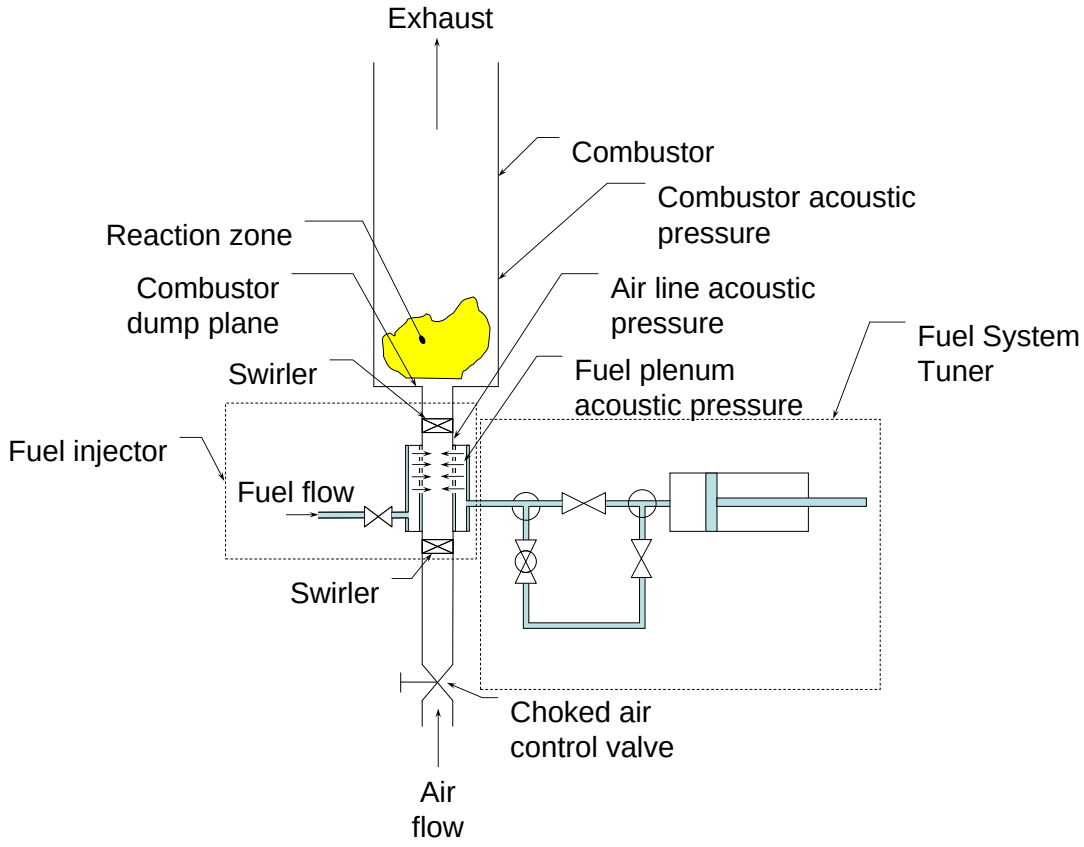

Figure 7.1: A schematic of the natural gas fueled, atmospheric pressure, swirl-stabilized combustor.

7.2 FST Performance Mapping

Using the developed combustor, the effect of the FST on combustor stability for a range of combustor configurations and operating conditions was determined for the test configurations listed in Table 7.1. These five configurations were chosen because they illustrate important factors affecting the performance of the FST. Specifically, Configuration 1 will be considered a baseline case. Configurations 2 and 3 show the effect of changing the instability frequency and equivalence ratio, respectively. Configuration 4 shows that changing the resistance of the fuel system, e.g., by reducing the fuel injector effective area, affects FST performance, and Configuration 5 demonstrates the effect of changing the geometry of the adjustable u-tube length.

The database used for performance evaluation was established as follows. For each particular configuration listed in the table, the combustor was operated at the given equivalence ratio for the five different power settings, i.e., fuel flowrates, shown. For each power setting, 96 FST settings were tested. These 96 FST settings correspond to four equally spaced settings for each of the two variable area valves, two settings (ON and OFF) of the ball valve, and three equally spaced settings of the tunable volume section. (The FST settings and corresponding case numbers are shown for reference in Appendix F.) At each FST setting the combustor acoustic pressure was recorded. Using this procedure, a database of $7 \times 5 \times 96 = 3360$ data points was obtained. It should be noted that cases 20, 24, 28, 32, 52, 56, 60, 64, 84, 88, 92, and 96 were cases where the FST was effectively turned OFF due to the settings of the various valves.

The data are presented in two ways. First, the acoustic pressure amplitudes are shown for all 96 FST settings tested for the 0.9 and 1.9 kg/hr fuel flowrate cases. Then, the data are shown in a single summary plot.

Table 7.1: Combustor configurations tested for various FST settings.

Config.	Combustor Tailpipe Length, in. (mm)	Fuel Injector Hole Size, in. (mm)	FST U-tube Length, in. (mm)	Combustor Inlet Diameter, in. (mm)	Equiv. Ratio	Number of Power Settings Tested
1	24 (609.6)	0.125 (3.3)	21.75 (552.4)	0.70 (17.8)	0.8	5
2	36 (914.4)	0.125 (3.3)	21.75 (552.4)	0.70 (17.8)	0.8	5
3	24 (609.6)	0.125 (3.3)	21.75 (552.4)	0.70 (17.8)	0.9	5
4	24 (609.6)	0.032 (0.8)	21.75 (552.4)	0.70 (17.8)	0.8	5
5	24 (609.6)	0.125 (3.3)	42.75 (1085.9)	0.70 (17.8)	0.8	5

The plots containing the data for all 96 FST settings will be shown on a plot similar to Figure 7.2 (in this figure, the acoustic pressures have been removed for clarity). Using this type of plot, the combustor acoustic pressure amplitude for all 96 FST settings can be shown on a single figure for each power setting. The plot shows six zones of FST operation. In zones 1 and 2, 3 and 4, and 5 and 6 the FST volume was completely closed, 50% open (volume length of 101.6 mm), and 100% open (volume length of 203.2 mm) respectively. In zones 1, 3, and 5, the FST ball valve was open, and in zones 2, 4, and 6, the ball valve was closed. In each zone, for each FST side gate valve setting, the top gate valve setting ranged from completely open to completely closed in 4 steps, i. e., 100%, 71%, 43%, and 0% open. This was repeated in each zone for side gate valve settings of 100%, 71%, 43%, and 0% open.

The summary plots were developed as follows. First, for comparison, the acoustic pressure with the FST turned OFF is shown. Then, the following three cases were considered: (1) the FST settings when the FST was tuned for maximum attenuation at each power setting, (2) the single FST setting that produced the lowest overall average acoustic pressure, and (3) the single FST setting that produced the highest overall average acoustic pressure.

For the first case, the database was searched for the FST setting that provided the lowest amplitude pressure oscillations at each power setting. Each point on these curves represents a different FST setting. These points, which are the bottom-most curves in the summary plots, show that significant attenuation could be realized for all configurations. This level of performance could only be obtained by adjusting the FST as the power setting of the combustor changed.

Case (2) is the fixed FST setting that yielded the best performance (i.e., lowest acoustic pressure amplitude) over all power settings for a given configuration. Overall performance was determined by averaging the RMS pressure level over the five points of operation for each FST setting. The setting that yielded the lowest overall pressure level was chosen as the 'best fixed' FST setting. Finally, case (3) was the FST setting that yielded the highest overall average acoustic pressure amplitude.

The instability frequency for each of the combustor configurations and all FST settings was calculated from the measured acoustic pressures. For Configuration 2, which used a 914 mm long combustor, the instability frequency was approximately 170 Hz. For the other configurations, the instability frequency was approximately 270 Hz. These measured instability frequencies compared well with those predicted by the model for the 914 mm and 609 mm long combustors, which were 185 and 285 Hz, respectively.

In the remainder of the chapter, the overall performance of the FST will be presented for each configuration shown above. For Configuration 1, model predictions are compared with the experimental measurements. Finally, the relationship between FST performance and the impedance of the fuel injection system is discussed.

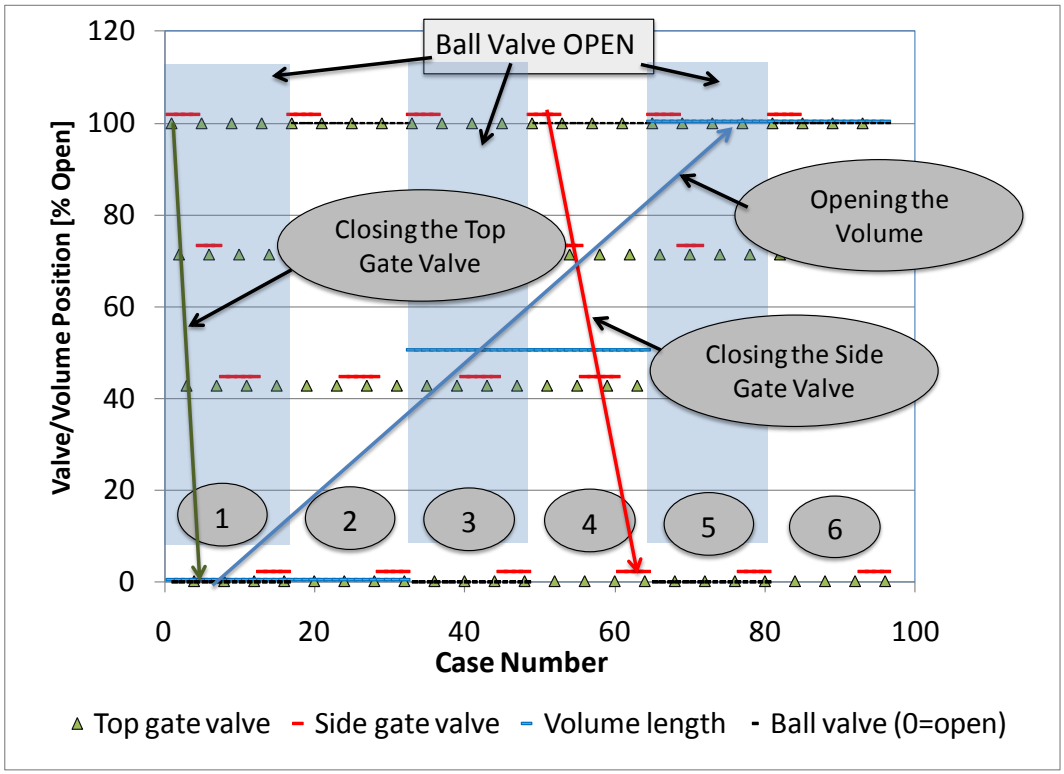

Figure 7.2: FST component % open vs. FST case number (see Appendix F) for reference.

7.2.1 Configuration 1: a baseline case

The first configuration under consideration, which will be considered the baseline case, is Configuration 1 from Table 1. Figure 7.3 and Figure 7.4 show the aggregate plots for fuel flowrates of 0.9 and 1.9 kg/hr, respectively. When the FST was OFF, the acoustic pressure for both fuel flowrate cases was 4193 and 4000 Pa, respectively. The experimental results for Configuration 1 were quite repeatable and consistent. The average acoustic pressure amplitude for Configuration 1 operating at 0.9 kg/hr when the FST was OFF was 4164 Pa with a standard deviation of 42 Pa. The acoustic pressure amplitude average and standard deviation for the 1.9 kg/hr case was 3998 and 88 Pa, respectively.

Figure 7.3 shows that the acoustic pressure for most FST settings was better than when the FST was turned OFF. Notably, cases 4, 8, and 12 exhibited slightly elevated acoustic pressures. However, the acoustic pressure amplitude was reduced to 1240 Pa (nearly the background combustor noise level) in zones 1, 3, 4, 5, and 6. It should be noted that measuring the background noise level with a long combustor is difficult due to the tendency of the combustor to be unstable at its resonant frequency. Therefore, the background noise level in all cases was estimated from the lowest observed acoustic pressure amplitude for a given configuration.

Figure 7.4 shows the aggregate plot for a fuel flowrate of 1.9 kg/hr. In contrast to the previous case, the FST was much less effective at reducing the acoustic pressure amplitude in this case. Zone 2, once again, exhibited the worst performance, but zones 1, 3, and 5 were only slightly more effective. In this case, The FST only reduced the acoustic pressure amplitude to an approximate average of 3000 Pa.

Zone 4, and to a lesser degree zone 6, was quite effective for all settings of the side gate valve when the top gate valve was 43% open. At these settings, the acoustic

pressure amplitude was reduced to 1800 Pa, which accounting for the higher background noise level at the higher power setting was quite good.

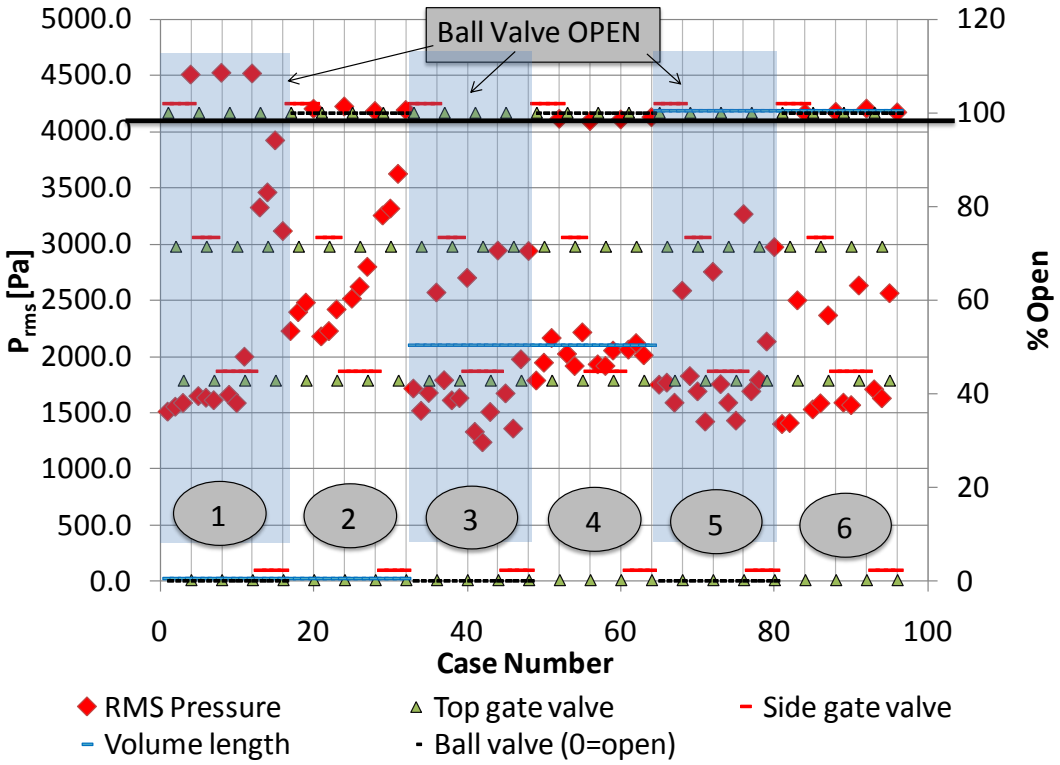

Figure 7.3: Acoustic pressure amplitude vs. FST setting for Configuration 1 at a fuel flowrate of 0.9 kg/hr.

The reduced effectiveness at the higher flowrates may be due to the fact that the higher fuel flowrates caused the fuel injector holes to have a higher acoustic resistance (see Chapter 6) than lower fuel flowrates. This higher resistance serves to cut-off communication between the inlet air pipe and the FST, thereby reducing the effectiveness of the FST.

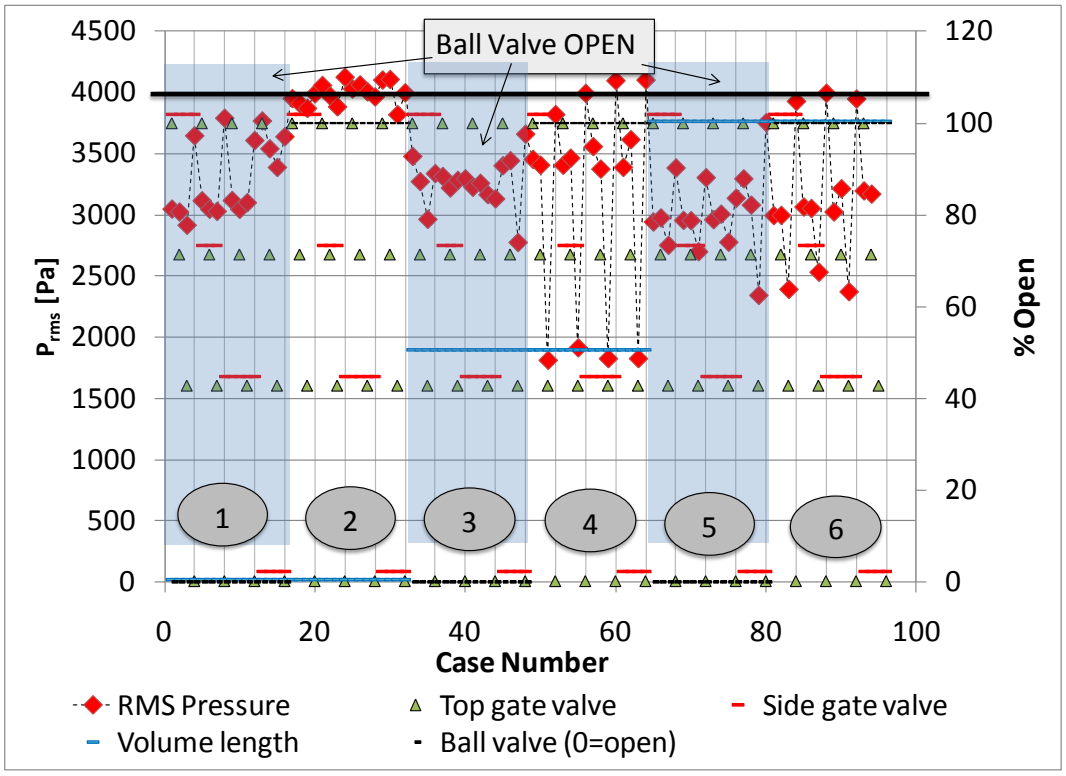

Figure 7.4: Acoustic pressure amplitude vs. FST setting for Configuration 1 at a fuel flowrate of 1.9 kg/hr.

Figure 7.5 shows the summary plot for Configuration 1. For this case, the FST setting that produced the highest overall average acoustic pressure was little different than the baseline, i.e., "FST OFF" case, except at the highest power setting. However, the single optimal FST setting that produced the overall lowest acoustic pressure amplitude yielded more than a 50% reduction in the acoustic pressure amplitude. Selecting the optimal FST setting at each power setting resulted in an even greater reduction in the acoustic pressure amplitude. In this case, the pressure amplitude was reduced to near the level of the background combustion noise. Appendix F gives the settings for the individual FST components corresponding to the optimal FST settings shown in Figure 7.5.

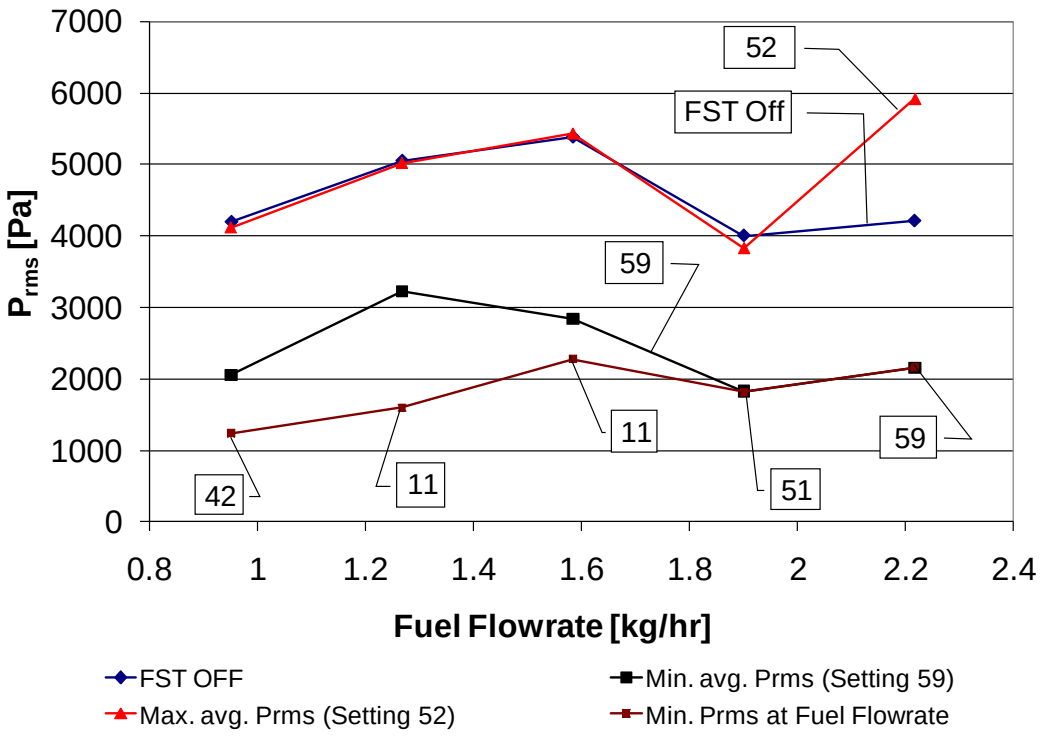

Figure 7.5: P_{rms} vs. Fuel Flowrate for Configuration 1.

Both model predictions from Chapter 6 and experimental results presented earlier in this chapter demonstrate conclusively the effectiveness of the FST. The next two sections seek to better understand why the FST is effective. To this end, the model will first be compared directly with experimental measurements. Then, the connection between the experimental results with model predicted fuel system impedance will be discussed. It will also be shown that these results are consistent with the more general predictions of Chapter 2.

7.2.1.1.1 Model validation

The model validation for Configuration 1 proceeds as follows. The acoustic pressure amplitude for each fuel flowrate was plotted against FST setting (or Case number). The model predicted growth rate for that FST setting is also shown on each figure. Recall that large positive growth rates should correspond to high acoustic pressure amplitudes, and smaller positive growth rates should correspond to lower acoustic pressure amplitudes. Negative growth rates correspond to stable combustors with zero acoustic pressure amplitude. Due to the presence of background combustion noise, the acoustic pressure amplitude never attains a value of 0, so stable operation corresponds to acoustic pressure amplitudes at or near the level of the background acoustic pressure amplitude.

Two cases were considered for Configuration 1. For modeling purposes, Case 1 assumed that the average combustor gas temperature was 1800 K and the flame location was 25.4 mm from the combustor dump plane. Case 2 assumed that the average combustor gas temperature was also 1800 K but that the flame was located 50.8 mm from the combustor dump plane. In each plot, a red line marks the baseline case (i.e., FST OFF) and background acoustic pressure amplitude. The black line indicates zero growth rate.

The experiment/model comparison plots for all configurations at a fuel flowrate of 0.9 and 1.9 kg/hr are shown in Figure 7.6 and Figure 7.7. The reader is referred to Figure 7.2, which shows the FST's component settings for each case number.

In zone 1, Cases 1 and 2 accurately predict that the measured acoustic pressure amplitude is low when the side gate valve is 100%, 71%, and 43% open. However, Case 2 fails to predict the high amplitude spike that occurs at each of these side gate

valve settings when the top gate valve is completely closed. Case 2 more accurately predicts the experimental results when the side gate valve is completely closed.

In zones 2, 4, and 6, Case 2 predictions were more consistent with the experimental results except when the pressure amplitude was very high. However, Case 1 seems to capture these pressure amplitude peaks quite well.

In zone 3 and 5, Case 2 predicts that the pressure amplitude should be very low for all valve settings. In general, the experiment follows these predictions except when the top gate valve is completely closed. In this case, Case 1 seems to do a better job than Case 2.

As mentioned earlier, the flame tends to sit much closer to the combustor dump plane when the acoustic pressure amplitude is very high. When the combustor is quieter, the flame tends to move away from the combustor dump plane. Therefore, Case 1 should more accurately predict combustor acoustic pressure amplitude in this case.

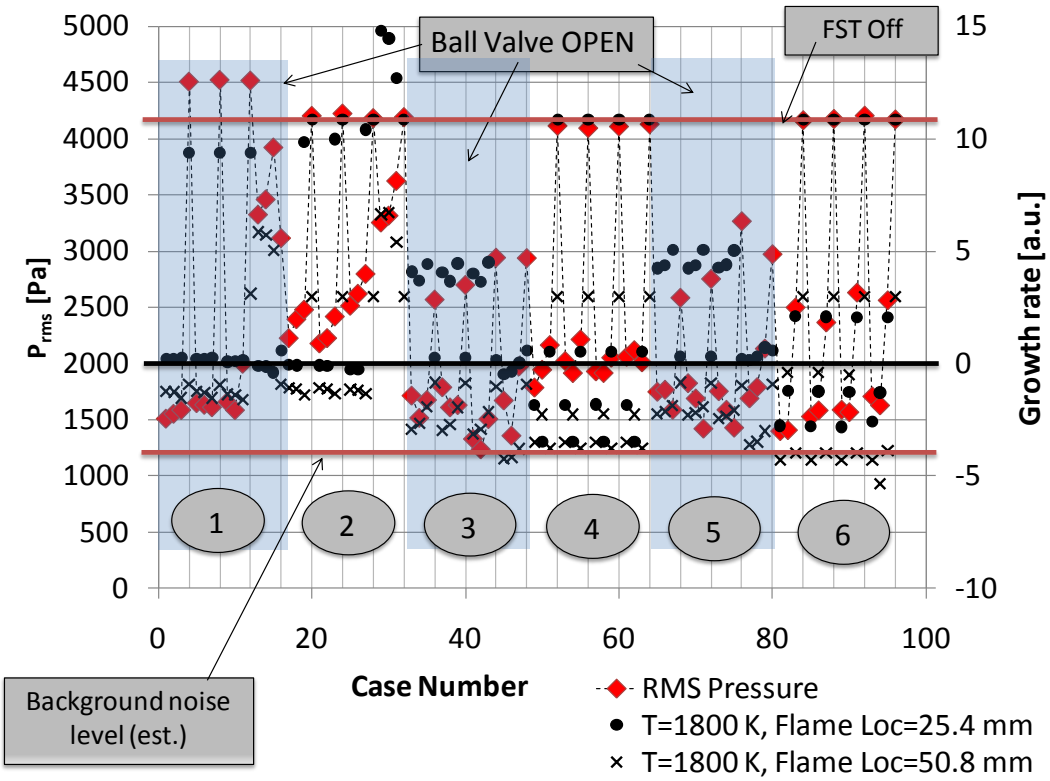

Figure 7.6: Model/Experiment comparison vs. FST setting for Configuration 1 at a fuel flowrate of 0.9 kg/hr.

Figure 7.7 shows the model predictions and experimental results for Configuration 1 at 1.9 kg/hr fuel flowrate. The baseline acoustic pressure amplitude for this case was 4000 Pa. In zones 1, 3, and 5, the model predicts low acoustic pressure amplitudes except when the side gate valve is completely closed, and in these zones, the experimentally measured acoustic pressure amplitude is on average much lower than the baseline. In zone 2, the model completely misses the behavior of the combustor. In zones 4 and 6, the model once again captures the behavior of the combustor well except when the top gate valve is completely open.

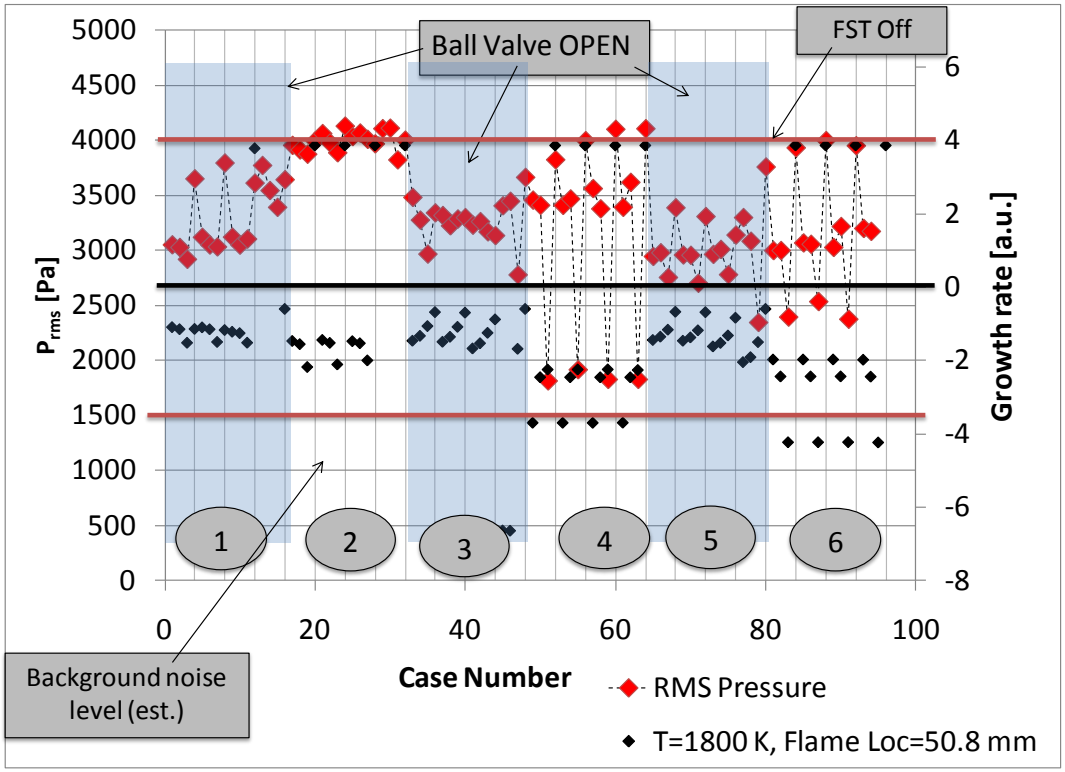

Figure 7.7: Model/Experiment comparison vs. FST setting for Configuration 1 at a fuel flowrate of 1.9 kg/hr.

The next section makes use of model predicted fuel system impedances and experimentally measured acoustic pressure amplitude data to help explain why and under what conditions the FST is effective.

7.2.1.1.2 The dependence of combustor stability on fuel system impedance

The fuel supply system impedance determines the magnitude and timing of the fuel injected into the air flowing into the combustor. Therefore, it plays a critical role in determining the stability of a typical combustor used for power generation. This section shows that combustor stability depends on both the magnitude and phase of the fuel system impedance and that it does so in a predictable fashion. These results greatly enhance our understanding of the critical role played by the fuel system impedance on combustor stability.

It is important to note that here it is the fuel system impedance, not the FST impedance, that matters. It is the overall impedance of the fuel supply system that is critical to combustor stability. The FST's role is simply to provide a way to predictably modify the fuel supply system impedance. The effects discussed below were demonstrated by the model results presented in Chapter 2.

Recall that the impedance of the fuel system is defined as the ratio of the acoustic pressure (in the air duct at the location of the fuel system) to the acoustic volume velocity of the fuel flowing from the fuel injector into the air stream. Therefore, a phase of 90 degrees means that the fuel injection is out of phase with the acoustic pressure at the fuel injector, and a phase of 0 degrees means that they are exactly in-phase.

The magnitude of the impedance is considered large or small when it is much larger or smaller than the characteristic impedance of the air inlet pipe $(\rho c)_{air}/S_{air}$.

Fuel injection rate oscillations are very small when fuel system impedance is large. In this case, the equivalence ratio oscillations are not due to fuel flowrate oscillations

because the fuel system is effectively choked, and, therefore, tuning the phase of the fuel system impedance can have no effect on combustor stability.

It should be noted that very large fuel system impedance does not necessarily imply an unstable combustor. It also does not imply that equivalence ratio oscillations are not present. They can be present due to air flowrate oscillations even when the fuel flowrate is constant. A very large fuel system impedance simply means that whether stable or unstable, changing the phase of the fuel system has no effect on combustor stability.

The converse is true for very small fuel system impedance magnitudes. In this case, equivalence ratio oscillations may well be the dominating source of heat release oscillations, in which case, the phase of the fuel injection rate oscillations is the determining factor in combustor stability. As was shown in Chapter 2, very small fuel system impedances lead to very high heat release oscillations. These oscillations have the potential for very large combustor growth rates (both positive and negative). Due to the magnitude of these growth rates, combustor stability is very sensitive to adjustments in fuel system phase. A small change in phase may result in a stable combustor becoming suddenly very unstable, which is not a desirable situation.

For the reasons given above, practically speaking, neither very large nor very small fuel system impedance is desirable for combustor stability control. Therefore, intermediate fuel system impedances, i.e., those on the order of $(\rho c)_{air}/S_{air}$, were expected to yield the best overall results.

Figure 7.8 and Figure 7.9 show the model predicted magnitude and phase of the fuel system impedance along with the experimentally measured acoustic pressure

amplitude for the 96 FST settings tested at fuel flowrates of 0.9 and 1.9 kg/hr. Here the magnitude of the impedance is shown as a percentage of $10\frac{(\rho c)_{air}}{S_{air}}$.

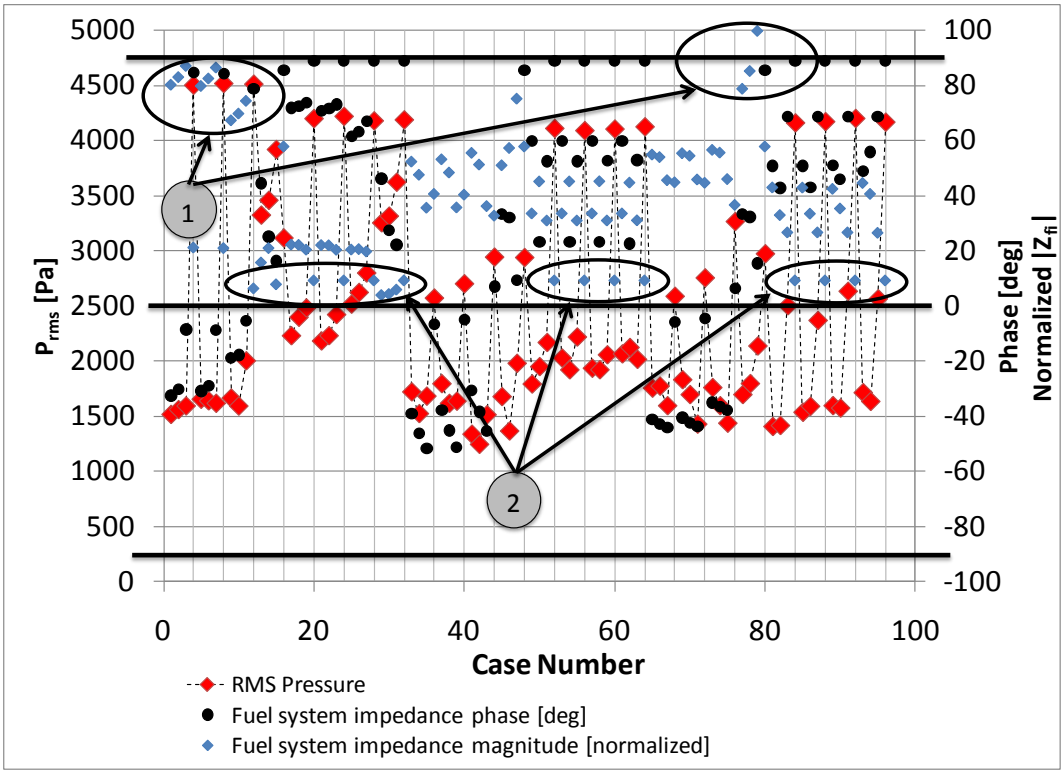

Figure 7.8: Acoustic pressure amplitude and Fuel system impedance (magnitude and phase) vs. FST setting for Configuration 1 at a fuel flowrate of 0.9 kg/hr.

In both figures, the number 1 indicates fuel system impedance magnitudes that are within 60-100% of $10(\rho c)_{air}/S_{air}$. These fuel system impedance magnitudes are considered large compared to $(\rho c)_{air}/S_{air}$, and in this case, result in very stable combustor operation. The number 2 indicates normalized impedance magnitudes that are between 0 and 10% of $10(\rho c)_{air}/S_{air}$, which are considered small. Typically, these small impedance settings exhibit quite a bit of variation in combustor acoustic pressure amplitude depending on the phase of the fuel system impedance. It is interesting to note

that most of the best FST settings have normalized impedance magnitudes that are between 20 and 60% of $10(\rho c)_{air}/S_{air}$.

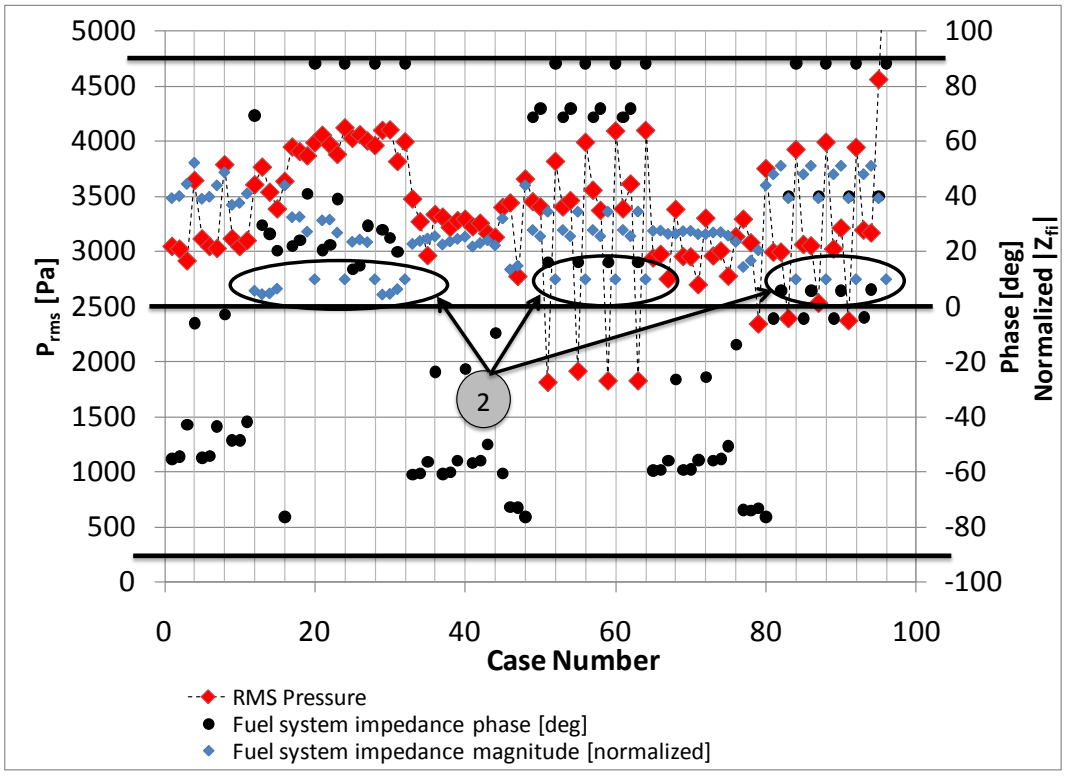

Figure 7.9: Acoustic pressure amplitude and Fuel system impedance (magnitude and phase) vs. FST setting for Configuration 1 at a fuel flowrate of 1.9 kg/hr.

In general, the fuel system phase required to achieve good combustor stability depends on the magnitude of the fuel system impedance as well. Figure 7.10 and Figure 7.11 show the normalized magnitude and phase of the fuel system impedance plotted against the measured combustor acoustic pressure amplitude for the 0.9 and 1.9 kg/hr fuel flowrate cases. Figure 7.10 shows that the lowest acoustic pressure amplitudes occur at the two distinct regions marked, i.e., when the phase of the fuel system impedance was near -40 or 50 degrees. The magnitude of the fuel system

impedance for both cases was approximately 40 and 80-100% of maximum, respectively.

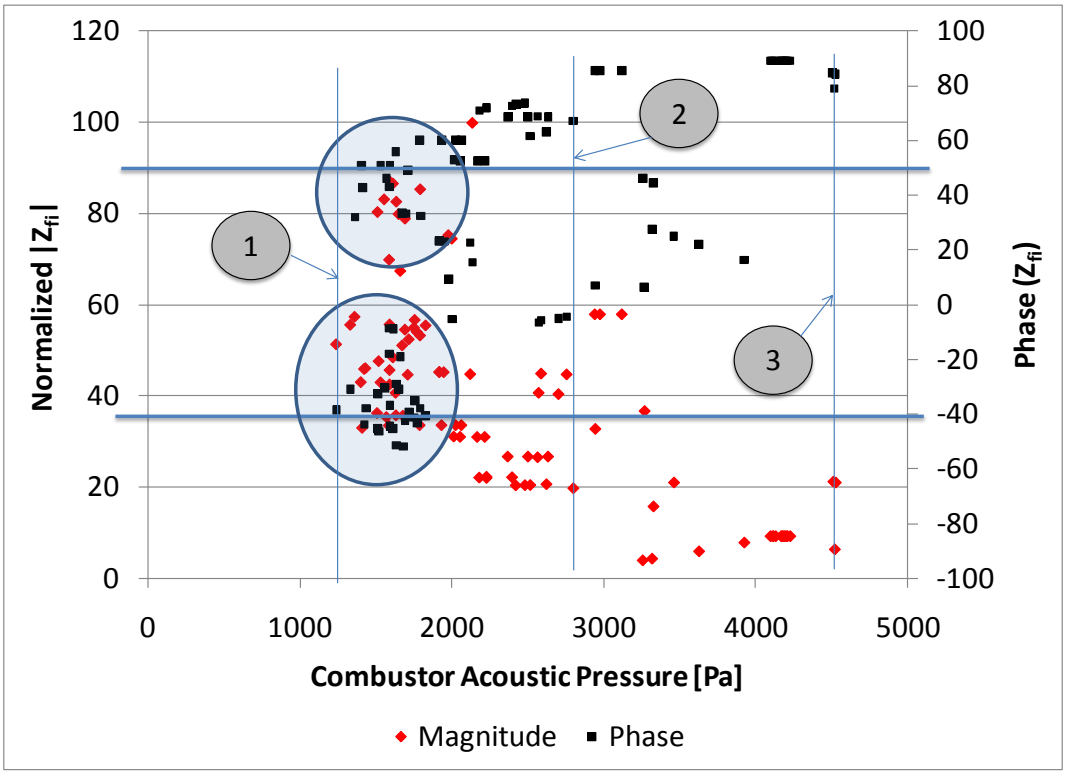

Figure 7.10: Fuel system impedance (magnitude and phase) vs. Experimental acoustic pressure amplitude for Configuration 1 operating at a fuel flowrate of 0.9 kg/hr.

The optimal phase for the 1.9 kg/hr case appears to be between -50 and -70 degrees. However, good performance was observed for phases of 20 and 40 degrees as well.

The increased phase lag observed in the 1.9 kg/hr case is consistent with time-lag theory, which says that the time-delay for stable operation should be shifted by an additional 36 degrees for the 1.9 kg/hr case compared with the 0.9 kg/hr case. Using the -40 and 50 degree phases from the 0.9 kg/hr case, time-lag theory predicts that the

optimal phases for stable operation at 1.9 kg/hr would be -76 and 16 degrees, respectively.

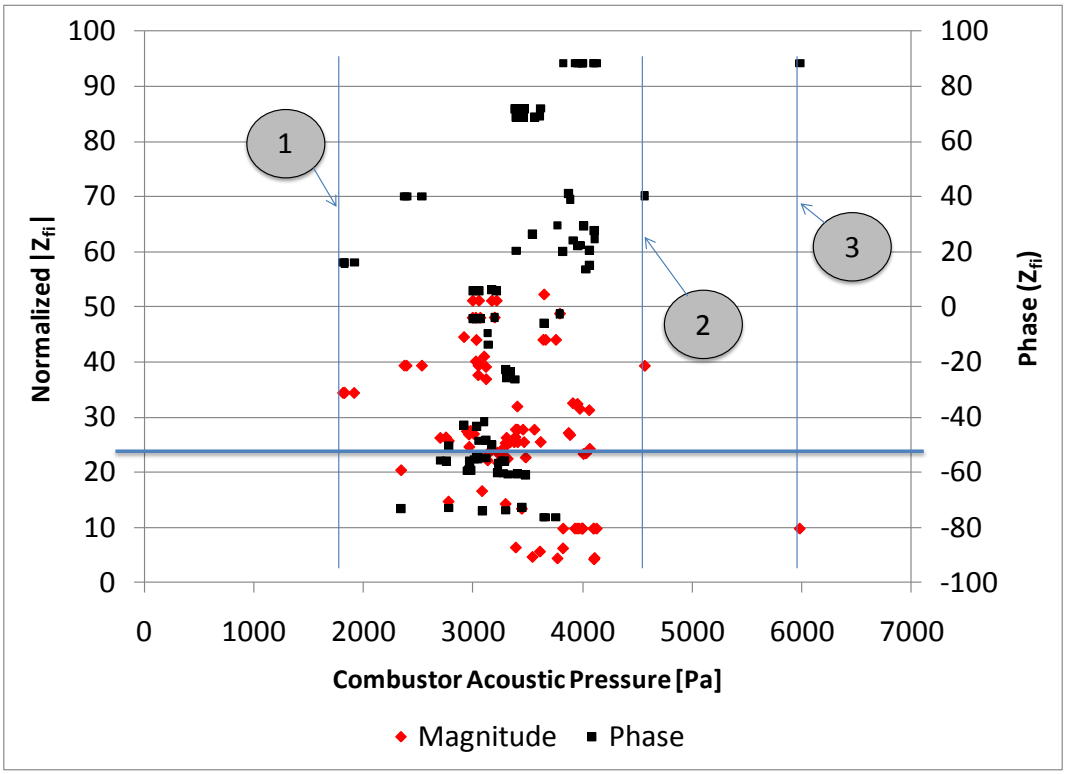

Figure 7.11: Fuel system impedance (magnitude and phase) vs. Experimental acoustic pressure amplitude for Configuration 1 at a fuel flowrate of 1.9 kg/hr.

The results for Configuration 1 show that the FST was able to stabilize the combustor for the range of operating conditions tested. In addition, actual combustor performance with the FST was well-predicted by the model. Model predictions in conjunction with experimental measurements show that the FST performed best when the fuel system impedance was between 20 and 60% of $10(\rho c)_{air}/S_{air}$, and when the phase was not near +/- 90 degrees. These results were also shown to be consistent with the predictions of the model developed in Chapter 2.

7.2.2 Configuration 2: the effect of combustor length

Combustor Configuration 2 yielded an average instability frequency of 170 Hz. Using this configuration, the performance of the FST in a combustor having a lower instability frequency could be observed.

The experimental results for Configuration 2 exhibited more variability than was observed for Configuration 1. At a fuel flowrate of 0.9 kg/hr, the average acoustic pressure amplitude for Configuration 2, when the FST was OFF, was 3919 Pa with a standard deviation of 450 Pa. The average and standard deviation for the 1.9 kg/hr case was 6443 and 329 Pa, respectively.

The conclusions of the model studies presented in Chapter 6 are briefly summarized here. In Section 6.5.1, it was shown that the 914 mm combustor had higher predicted growth rates than the shorter 609 mm combustor, and it also predicted higher growth rates at higher combustor power setting. Section 6.5.2.2 presented the results of model calculations with the FST. Comparing the 0.9 and 1.9 kg/hr fuel flowrate cases, higher growth rates were predicted for higher power settings. Comparing the various FST settings tested, the results of the study showed that stable operation could be expected in zones 1, 3, and 5. It also showed that a slight reduction in acoustic pressure amplitude could be expected in zones 4 and 6.

The aggregate plots for Configuration 2 are shown in Figure 7.12 and Figure 7.13, and, in general, the results are similar to those for the 609 mm long combustor in that the FST was quite effective at the lower fuel flowrates and less effective at the higher fuel flowrates.

Figure 7.12 shows the data for the 0.9 kg/hr case. Clearly, the FST was not effective in zone 1, but was somewhat more effective in zone 2. As in Configuration 1,

the FST was most effective in zones 3, 5, and 6. In these cases, certain FST settings reduced the acoustic pressure amplitude as low as 2000 Pa, which was nearly 2000 Pa lower than with the FST turned OFF.

As was noted previously, a number of cases correspond to the FST being turned OFF, and, as such, should have the same acoustic pressure amplitude. Examination of the data reveals that with the 914 mm combustor this was not always the case. The black line in Figure 7.12 marks the expected acoustic pressure amplitude for these cases. Clearly, only Case number 60 comes close to this value. The reason for the lack of repeatability in this case is not clear except that it was noted that during operation, the combustor acoustic pressure amplitude was not stable.

Several settings of the FST in zones 1, 2, and 4, yielded acoustic pressure amplitudes far greater than with the FST turned OFF. Since these settings are in zones that do not contain the lowest acoustic pressure amplitudes, e.g., zone 3, 5, and 6, there is little danger of accidentally tuning the FST to one of these settings while trying to minimize the combustor acoustic pressure amplitude.

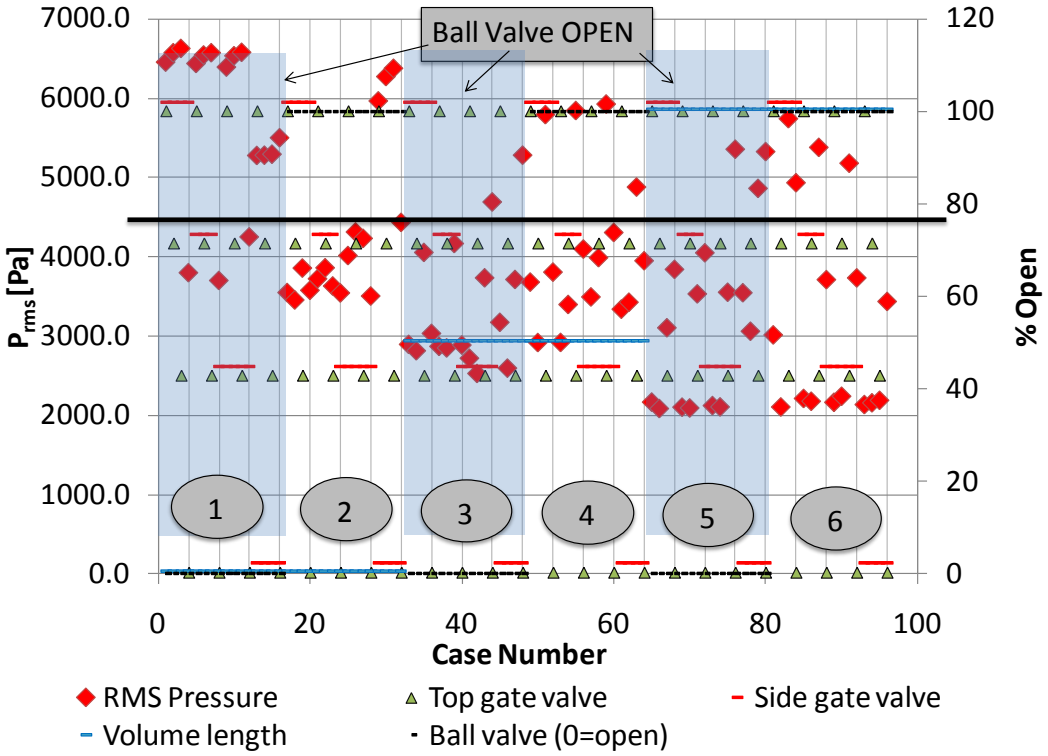

Figure 7.12: Acoustic pressure amplitude vs. FST setting for Configuration 2 at a fuel flowrate of 0.9 kg/hr.

Figure 7.13 shows that only zones 1 and 5 were effective at the 1.9 kg/hr fuel flowrate setting. The acoustic pressure amplitude was 6380 Pa with the FST OFF, and the minimum acoustic pressure amplitude achieved was 3704 Pa in zone 1. It is interesting to note that certain settings in zones 1, 2, and 3 resulted in acoustic pressures amplitudes in excess of 8000 Pa.

In contrast to the 0.9 kg/hr fuel flowrate case, the FST settings corresponding to extremely high acoustic pressure amplitudes are in the same zones as the optimal FST settings. Therefore, care must be taken when tuning the combustor to avoid these settings.

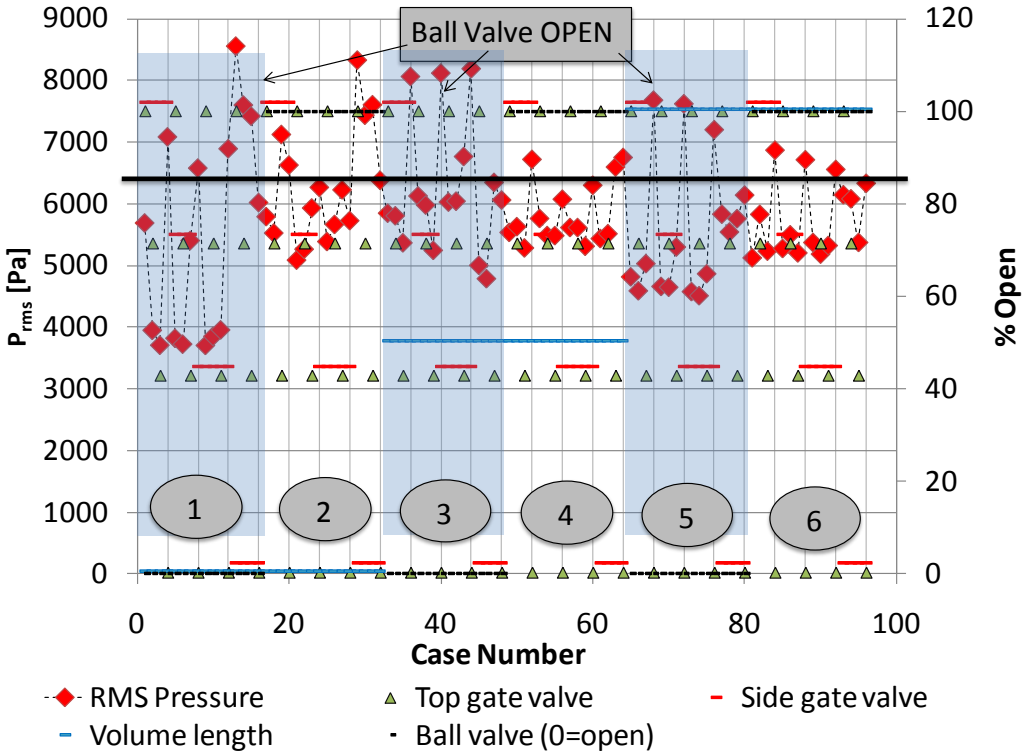

Figure 7.13: Acoustic pressure amplitude vs. FST setting for Configuration 2 at a fuel flowrate of 1.9 kg/hr.

Figure 7.14 shows the summary plot for Configuration 2. As noted, in this case the instability frequency was 170 Hz. Clearly, the overall optimal FST setting (73) significantly reduced the acoustic pressure amplitude. However, in this case the best performance was obtained by tuning the FST at each power setting since no single setting yielded very low acoustic pressure amplitudes.

As noted in the discussion above, FST setting 31 significantly increased the acoustic pressure amplitude over the baseline for all but the highest power setting. Appendix H shows plots of model predicted fuel system impedance and experimental combustor acoustic pressure amplitude as a function of FST setting.

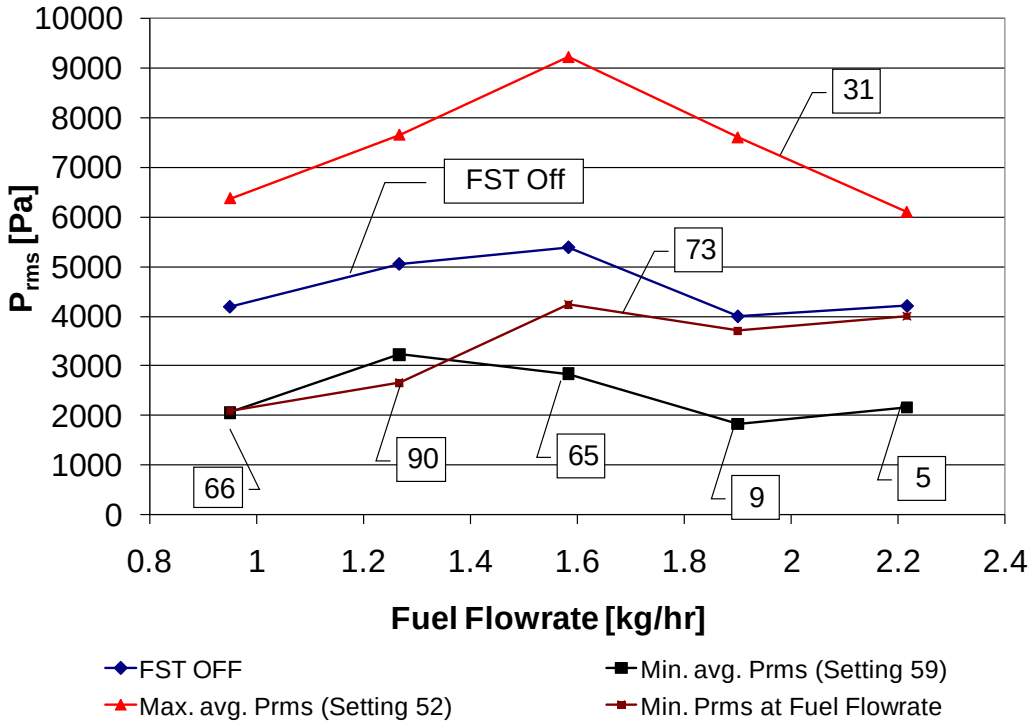

Figure 7.14: P_{rms} vs. Fuel Flowrate for Configuration 2.

7.2.3 Configuration 3: The effect of equivalence ratio

In an actual engine, the combustor overall equivalence ratio is well-known, being computed from actual fuel and air flowrate measurements. Also, changing the mean equivalence ratio changes the combustor operating pressure and average combustor temperature in addition to changing the gas composition in the combustor.

According to the model assumptions, changing the equivalence ratio changes only the steady fuel-air ratio, but it does not automatically change the combustor average temperature as it would in an actual combustor. Therefore, the primary effect of changing the equivalence ratio in the model is to scale the portion of the heat release oscillations that are due to equivalence ratio fluctuations.

Figure 7.15 and Figure 7.16 show model growth rate predictions for Configuration 1 at the three equivalence ratios noted. As was noted in Section 6.5.1, the model predicts that the growth rate varies more with equivalence ratio at a fuel flowrate of 0.9 kg/hr than for the 1.9 kg/hr case. For both cases, settings corresponding to the FST being turned OFF (Settings 20, 24, 28, 32, 52, 56, 60, 64, 84, 88, 92, and 96) exhibited the trends shown in Section 6.5.1, as expected.

It is interesting to note that the ordering of equivalence ratios from lowest to highest growth rate at each FST setting is not always the same. For instance, in zone 1, the ordering is 0.8, 0.9, and 0.7, and in zone 3 the ordering is 0.8, 0.7, and 0.9. In essence, there was a certain mean equivalence ratio that resulted in the most stable operation for a given FST setting, and depending on the FST setting, the mean equivalence ratio might be slightly higher or lower than some other FST setting.

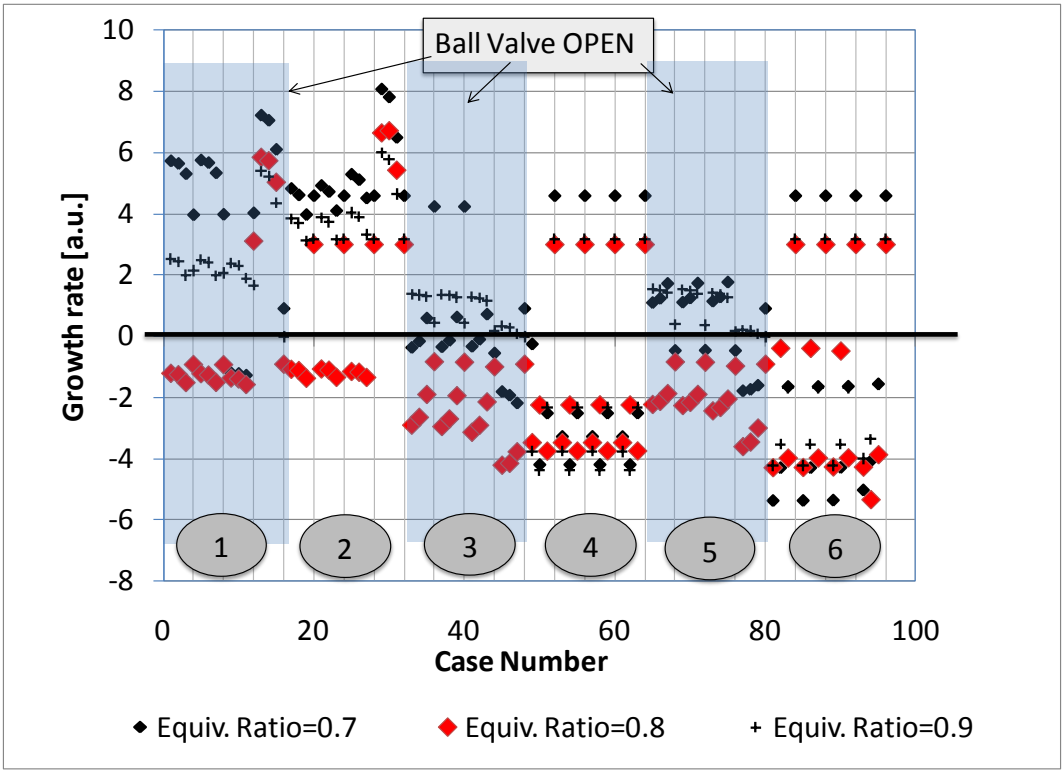

Figure 7.15: Growth rate vs. FST setting for Configuration 1 at a fuel flowrate of 0.9 kg/hr. Shown are model predictions for equivalence ratios of 0.7, 0.8, and 0.9.

Since, by assumption, combustor mean temperature was not dependent on equivalence ratio in this model, the only effect of increasing the equivalence ratio was to increase the contribution of equivalence ratio oscillations to the total heat release. This means that increasing the equivalence ratio leads to higher amplitude fuel-air ratio oscillations.

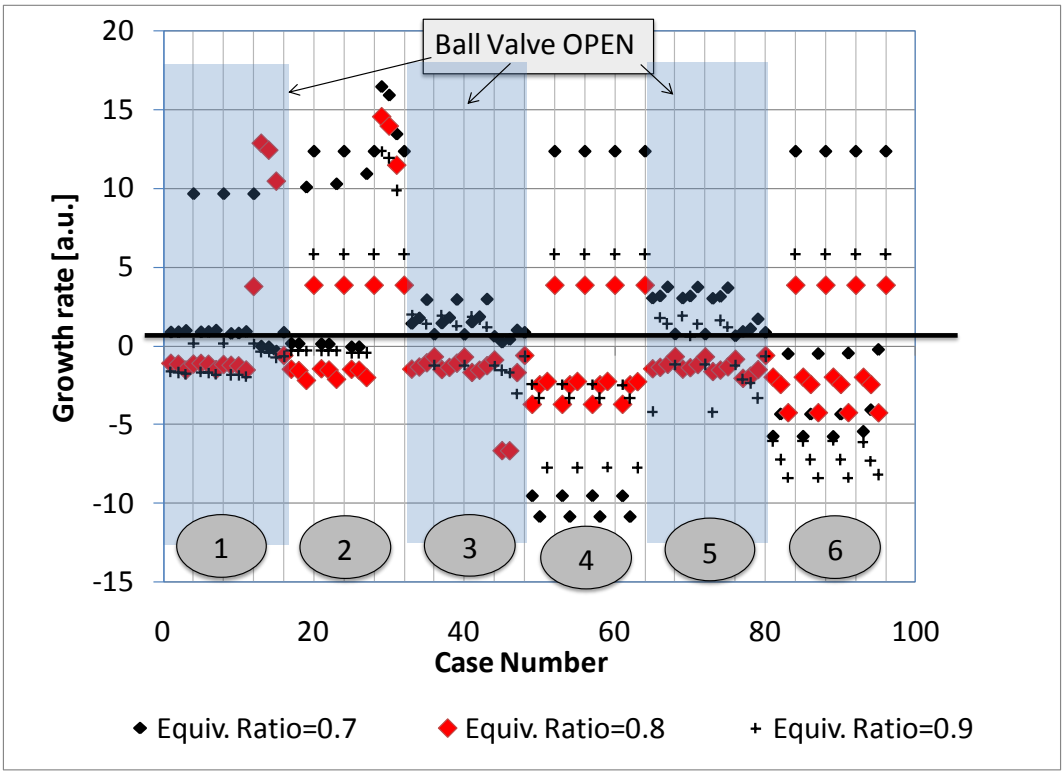

Figure 7.16: Growth rate vs. FST setting for Configuration 1 at a fuel flowrate of 1.9 kg/hr. Shown are model predictions for equivalence ratios of 0.7, 0.8, and 0.9.

Experimentally, Configuration 3 was used to investigate FST performance for an equivalence ratio of 0.9. The aggregate plots for this configuration are shown in Figure 7.17 and Figure 7.18 for fuel flowrates of 0.9 and 1.9 kg/hr, respectively. Figure 7.17 shows that the FST was quite effective in all zones except zone 2 with zone 1 and zone 4 exhibiting the lowest combustor acoustic pressure amplitude of 1244 Pa, which was much lower than the 3600 Pa observed with the FST turned OFF. All FST settings in zones 3 and 5 exhibited lower than baseline (FST OFF) acoustic pressure amplitudes, and only six settings exhibited higher acoustic pressure amplitudes than the baseline.

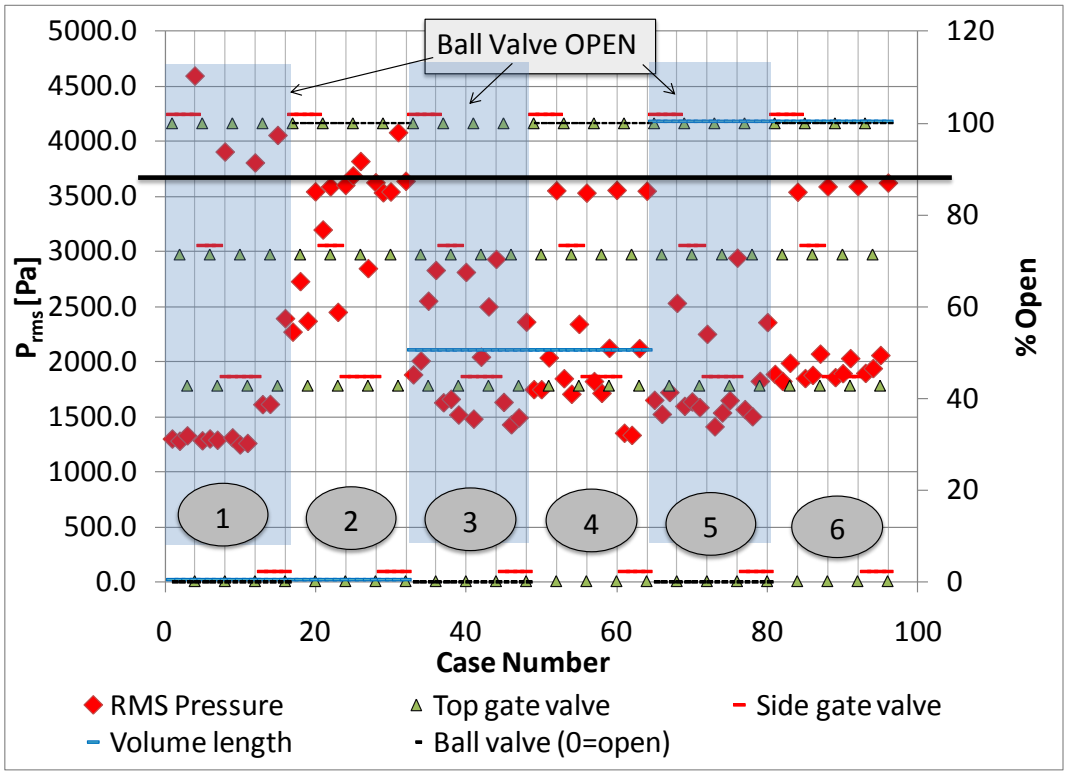

Figure 7.17: Acoustic pressure amplitude vs. FST setting for Configuration 3 at a fuel flowrate of 0.9 kg/hr.

The results shown in Figure 7.18 are similar in that only three FST settings (zone 4) yielded higher acoustic pressure amplitudes than the baseline case, and zones 1, 3, and 5 yielded the lowest acoustic pressure amplitudes. At the 1.9 kg/hr fuel flowrate, the lowest acoustic pressure amplitude of 3700 Pa was observed in all of zones 1, 3, and 5. Zones 2, 4, and 6 were only nearly as effective as zones 1, 3, and 5 but also contained settings having acoustic pressure amplitudes that were equal to or greater than the baseline.

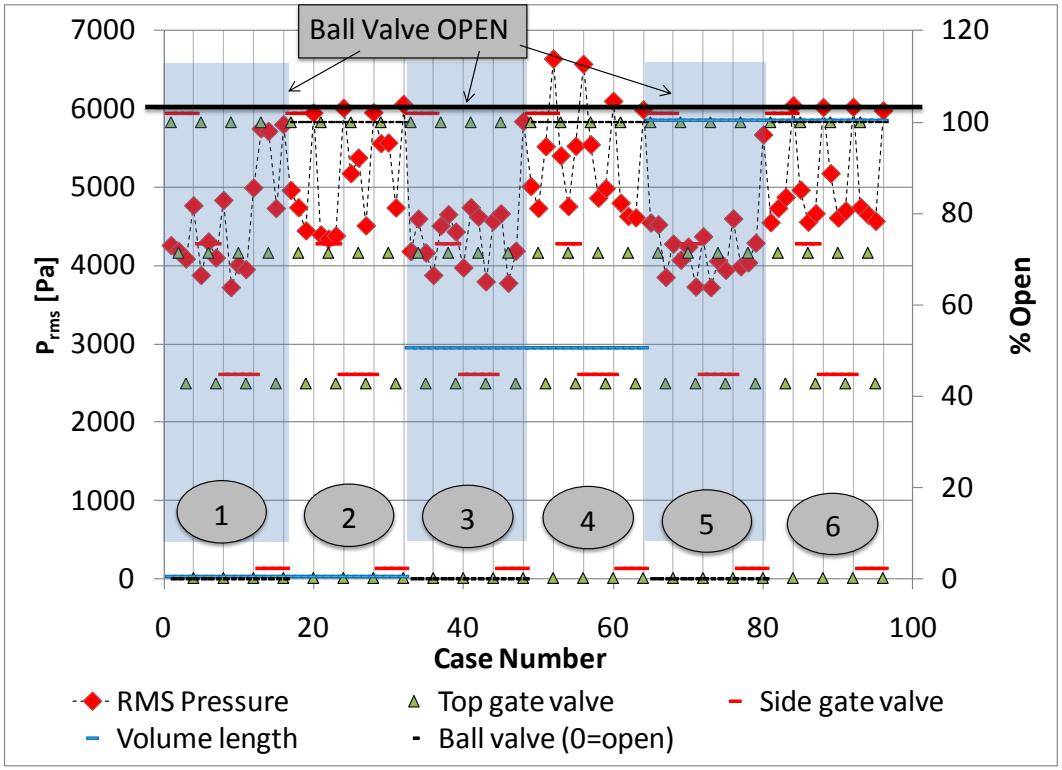

Figure 7.18: Acoustic pressure amplitude vs. FST setting for Configuration 3 at a fuel flowrate of 1.9 kg/hr.

Since the only change between Configuration 1 and Configuration 3 was to increase the equivalence ratio from 0.8 to 0.9, these figures may be compared to Figure 7.3 and Figure 7.4, respectively.

At a fuel flowrate of 0.9 kg/hr, Configuration 3 yielded a higher baseline acoustic pressure amplitude than Configuration 1. However, the minimum acoustic pressure amplitude achieved with the FST was the same for both cases. Also in these cases, zone 2 was the only zone that did not perform well. In addition, neither Configuration 1 nor Configuration 3 had FST settings that yielded significantly higher than baseline acoustic pressure amplitudes, and in both cases the absolute maximum observed acoustic pressure amplitude was the same (4500 Pa).

For the 1.9 kg/hr fuel flowrate case, several differences between Configuration 3 and Configuration 1 were noted. First, Configuration 3 exhibited a higher baseline acoustic pressure amplitude than Configuration 1 (6000 Pa vs. 4000 Pa). Second, the lowest acoustic pressure amplitude achievable with the FST was only slightly lower than the baseline for Configuration 1. However, the general response of the combustor to tuning the FST remained basically the same with the exception of zone 4.

The experimental results for Configuration 3 are seen in Figure 7.19. The overall optimal FST setting reduced the pressure amplitude to 30% of its baseline value at low power settings. However, the pressure amplitude at higher power settings was only reduced to about 60% of baseline. Though not insignificant, this reduction was somewhat less than achieved at lower equivalence ratios. Tuning the FST at each power setting resulted in the pressure amplitude being about 44% of baseline. Clearly, finding the optimal FST setting resulted in much greater attenuation.

The reduced effect of the FST at higher equivalence ratios was most probably due to the fact that the FST creates fuel flowrate oscillations in response to the acoustic pressure field at its inlet. At low equivalence ratios, these fluctuations remain entirely on the lean side resulting in significant fluctuations in heat release rate. However, at high overall average equivalence ratios, these oscillations may range from lean to rich. Since the heat release rate is a maximum near an equivalence ratio of one, fluctuations near an equivalence ratio of one do not produce the same level of heat release oscillations as fluctuations entirely in the lean regime. Therefore, the FST loses some of its effectiveness near an equivalence ratio of one.

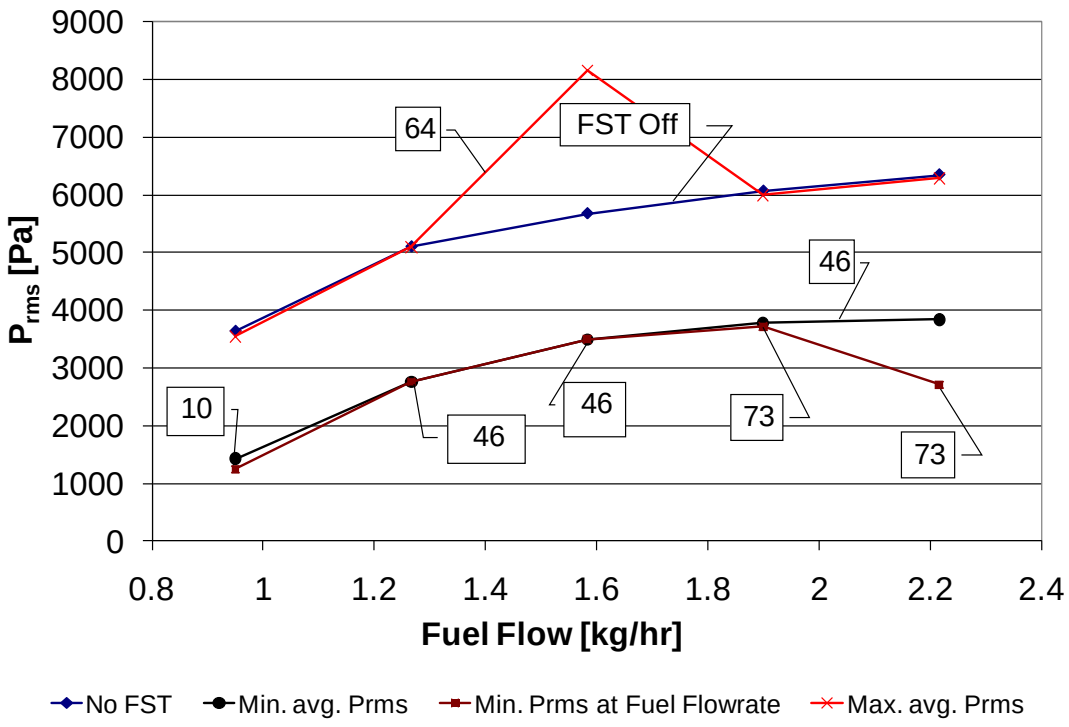

Figure 7.19: P_{rms} vs. Fuel Flowrate for Configuration 3.

These figures show that, with the FST in its best fixed setting, the pressure level was always lower than when the FST was turned OFF and was nearly as low as the 'Min. avg. P_{rms}' setting. It is clear that in this case the FST could be adjusted to produce significantly higher sound pressure levels than the baseline (FST OFF) case. These figures also show that the performance of the FST was not extremely sensitive to changes in combustor configuration or operating condition as long as the FST was adjusted to account for these changes.

7.2.4 Configuration 4: The effect of fuel injector effective area

This section presents the experimental results for Configuration 4, which differs from Configuration1 in that it has a fuel injector with three rows of twelve 0.8 mm fuel injection holes. (Configuration 1 had three rows of twelve 3.2 mm holes.) This change amounts to a 62% reduction in fuel injector effective area.

Obviously, making the fuel injector effective area very small would be the same as removing the FST completely, as was shown in Chapter 2. In fact, Figure 2.4 shows that the FST has no effect at all with a vanishingly small injector effective area. However, as Figure 2.5 and Figure 2.6 show, increasing the fuel injector effective area increases the sensitivity of the combustor to FST setting. This increases the probability of the FST stabilizing the combustor.

The flow resistance due to the fuel injector holes is related to the square of the flow velocity through the holes. Therefore, very high flow velocities are expected to effectively cut-off communication between the air inlet pipe and the FST. The flow velocity of the natural gas through the 0.8 mm fuel injector holes at a fuel flowrates of 0.9 and 1.9 kg/hr is 20.7 and 43.7 m/s, respectively. These velocities are 16 times higher than the velocities for Configuration 1, which for 0.9 and 1.9 kg/hr are 1.3 and 2.7 m/s, respectively. However, the velocities for Configuration 4 are still far from sonic, and therefore, communication between the air inlet pipe and the FST was still possible.

Figure 7.20 and Figure 7.21 show the model predicted growth rate for this case. At the lower fuel flowrate of 0.9 kg/hr, the model predictions shown in Figure 7.20 indicate that FST performance with the smaller effective area fuel injector should be very similar to that with the larger effective area except in zones 2 and 3. In the other zones, the amplitude of the predicted growth rate is lower for the smaller fuel injector, consistent

with the predictions from Section 6.5.1. This is easily seen for settings where the FST is OFF.

Figure 7.21 compares the model predicted growth rate for the two different injectors at the higher flowrate of 1.9 kg/hr. For all zones at this higher flowrate case, the model predicted growth rate is lower for the smaller injector for all settings where the FST is OFF, again consistent with Section 6.5.1 predictions. In zone 1, performance was the same for both injectors except when the side gate valve was OFF, in which case, the smaller injector had the smaller growth rate. In zone 2 and 3, the predicted growth rate was higher for the smaller injector. Zones 4, 5, and 6 contained the most promising FST settings for stable combustor operation with the smaller fuel injector.

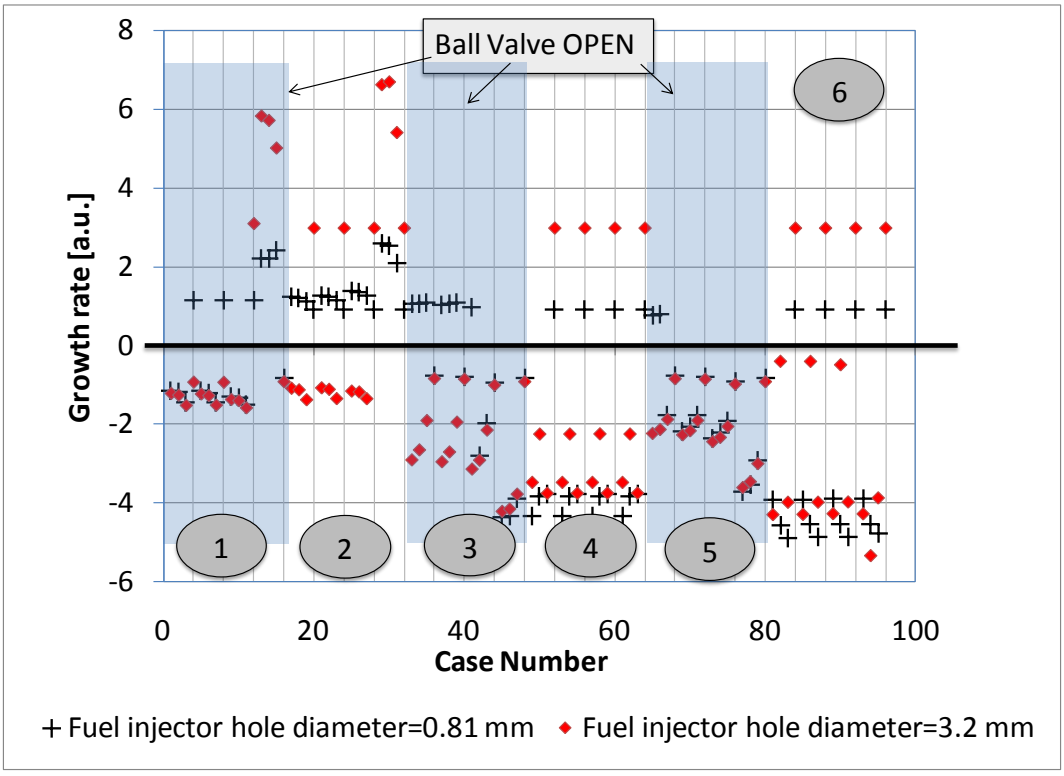

Figure 7.20: Growth rate vs. FST setting for Configuration 4 at a fuel flowrate of 0.9 kg/hr. Shown are model predictions for fuel injector hole diameters of 0.81 and 3.2 mm.

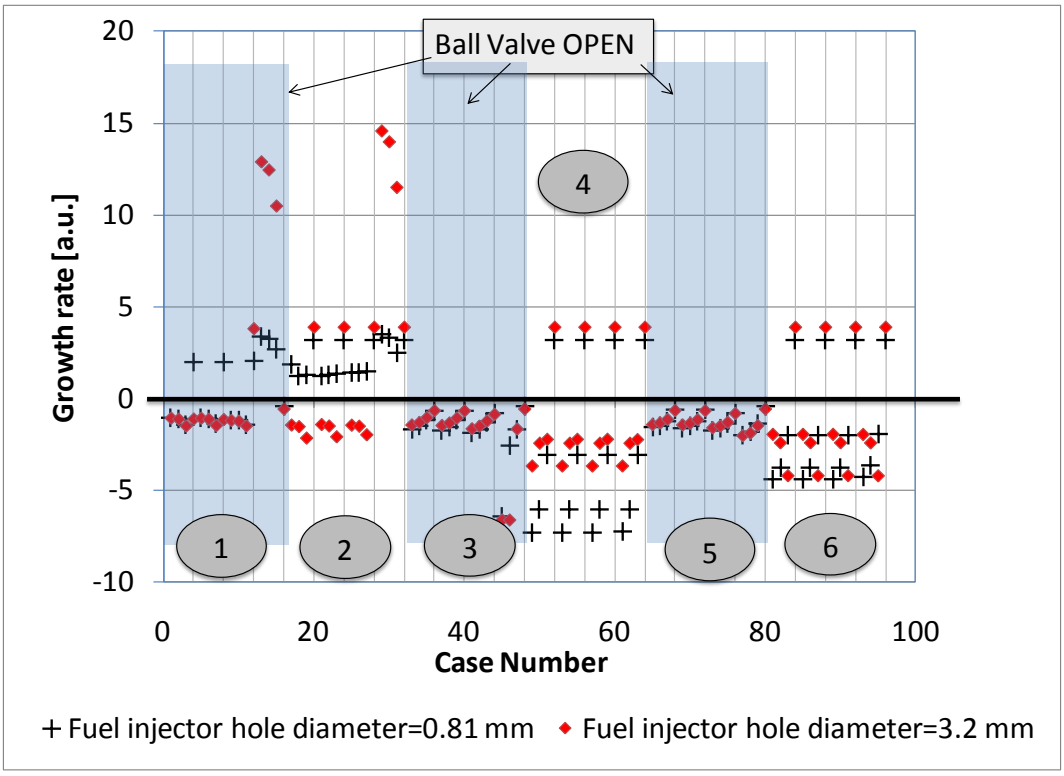

Figure 7.21: Growth rate vs. FST setting for Configuration 4 at a fuel flowrate of 1.9 kg/hr. Shown are model predictions for fuel injector hole diameters of 0.81 and 3.2 mm.

To summarize, the thermo-acoustic model calculations presented here and in Chapter 6 (see Section 6.5.1) predict the following. (1) The combustor will not be stable for either the 0.8 or the 1.3 mm fuel injector hole diameters without the FST, but (2) that the baseline (no FST) acoustic pressure amplitude should decrease with a smaller fuel injector area. (3) The combustor should be stable over a wide range of FST valve settings with either fuel injector effective area. (4) The highest pressure amplitude achievable by adjusting the FST should be higher with the larger effective area fuel injector. (5) The most stable FST setting would be for Configuration 1 in zones 3, 4, and 6.

Figure 7.22 and Figure 7.23 show the acoustic pressure amplitude for all 96 FST settings tested at fuel flowrates of 0.9 and 1.9 kg/hr, respectively. The baseline (i.e., FST OFF) acoustic pressure amplitude for the 0.9 kg/hr fuel flowrate case was 4000 Pa, which was slightly lower than the baseline for Configuration 1. Figure 7.22 shows that only a few FST settings in zones 3 and 4 are able to reduce the acoustic pressure amplitude as low as 1717 Pa. This is in contrast to the results for Configuration 1 in Figure 7.3, which shows that zones 1, 3, 5, and 6 have several settings capable of achieving acoustic pressures less than 1500 Pa. Zones 4 and 6 show some improved performance, with zone 4 having similar acoustic pressure amplitudes as in Configuration 1. Zone 6, although better than the baseline (i.e., FST OFF case), only reduces the acoustic pressure amplitude to around 3000 Pa.

The baseline acoustic pressure amplitude for the 1.9 kg/hr fuel flowrate case was 3819 Pa, which was also somewhat lower than the 4000 Pa baseline that resulted for Configuration 1 operating at a fuel flowrate of 1.9 kg/hr. Figure 7.23 reveals that in zones 1 and 3, the acoustic pressure amplitudes were lower than for Configuration 1 shown in Figure 7.3. In fact, settings in zone 3 yielded the best performance in this case. In zone 2, the results were the same for both configurations. In zones 4, 5, and 6, better performance was observed for Configuration 1. As an example, in zone 4 the lowest acoustic pressure amplitude achievable with the FST for Configuration 1 operating at a fuel flowrate of 1.9 kg/hr was 1813 Pa, while for the same case for Configuration 4, it was 1993 Pa.

It seems that in most cases, the reduction in fuel injector effective area reduced the effectiveness of the FST. This is most likely due to the fact that the increased flow velocity through the smaller fuel injector holes increased the acoustic resistance of the

holes, thereby reducing somewhat the communication between the air inlet pipe and the FST.

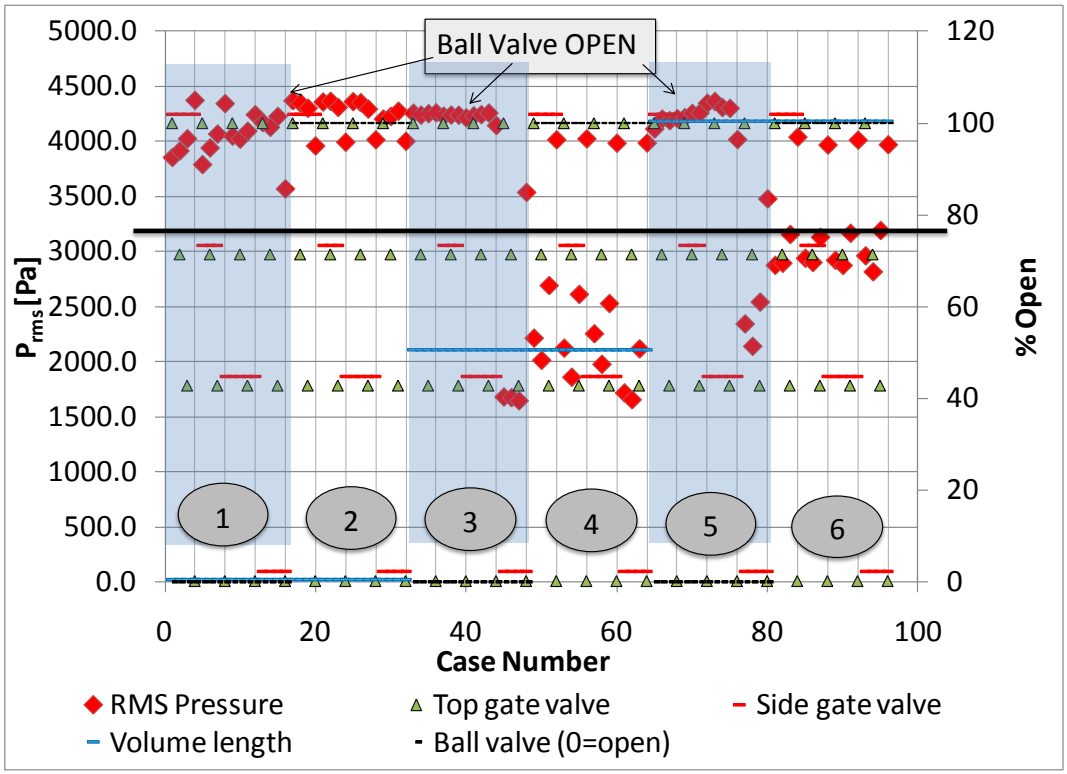

Figure 7.22: Acoustic pressure amplitude vs. FST setting for Configuration 4 at a fuel flowrate of 0.9 kg/hr.

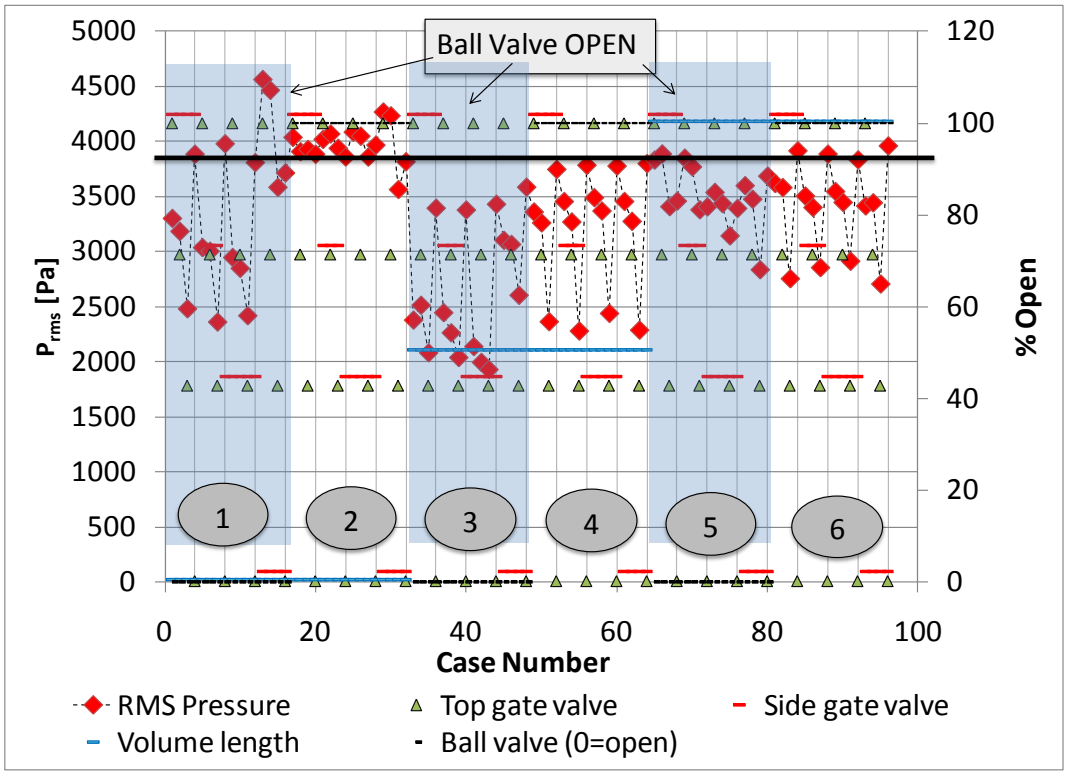

Figure 7.23: Acoustic pressure amplitude vs. FST setting for Configuration 5 at a fuel flowrate of 1.9 kg/hr.

Figure 7.24 shows the summarized experimental results for configuration 4. As noted, in spite of this reduction in flow area, the fuel injector holes were not choked. Therefore, the fuel system and the FST were able to communicate acoustically with the main combustor through the air inlet system. As shown, the baseline acoustic pressure amplitude was 4000 Pa. The FST was able to reduce the acoustic pressure near the level of the background noise for only the 0.9 and 1.9 kg/hr fuel flowrates. At the other fuel flowrates, the reduction in pressure amplitude was 50%. No significant increase in acoustic pressure amplitude was noted as the combustor power setting was increased.

Comparing Figure 7.24 with Figure 7.5 reveals that the combustor was unstable in both cases without the FST, and that the baseline pressure amplitude was smaller for the case with the smaller fuel injector effective area (i.e., hole size). In addition, Figure

7.5 and Figure 7.24 show that the FST was very effective in reducing the acoustic pressure amplitude in the combustor. In most cases, the reduction in pressure amplitude was better than 50% for both cases across the range of operating conditions.

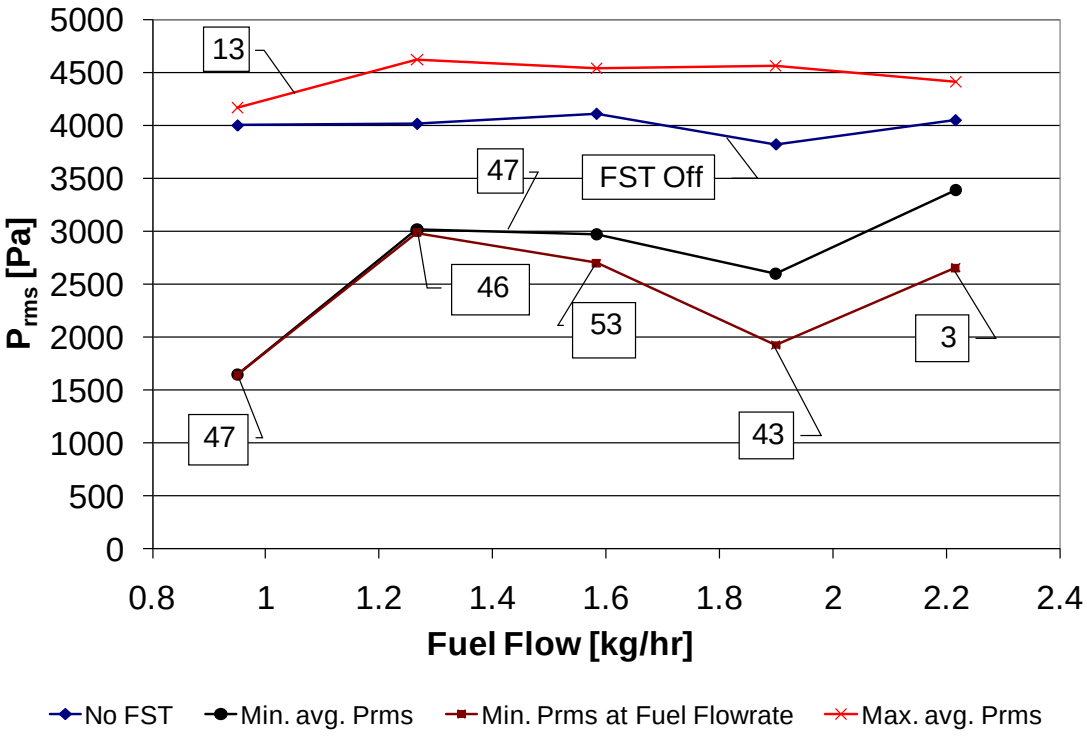

Figure 7.24: P_{rms} vs. Fuel Flowrate for Configuration 4.

7.2.5 Configuration 5: The effect of FST 'u-tube' length

This section presents the results of combustor performance measurements made with an FST having a u-tube overall length of 1.08 m. The results obtained from these tests are compared with results obtained for Configuration 1, in which the FST's u-tube was 0.55 m. In the low-frequency limit, lengthening a section of the FST would be the same is increasing the effective mass in a mass-spring-damper system. However, at higher-frequencies, the effect is more complex, and there is no simple analog for understanding how lengthening or shortening a given section will affect the impedance of the FST. Therefore, to understand the effect of changing the length of one of the FST sections, model calculations were performed for u-tube lengths of 0.10 and 1.08 m, in addition to the 0.55 m case already studied.

Model predictions for Configuration 5 at 0.9 and 1.9 kg/hr fuel flowrates are shown in Figure 7.25 and Figure 7.26, respectively. Model predictions for the 0.55 and 1.08 m cases show little change in combustor growth rate with some notable exceptions in zones 1, 3, and 5. Also shown in these figures are the results for a much-shortened u-tube having a length of 0.10 m. The model predicts much improved FST performance with the 0.10 m long u-tube for FST settings in zones 1 and 5. However, the model predicts higher growth rates for FST settings in zone 2 with the shorter u-tube.

The studies on Configuration 1 indicate that for this particular combustor very large and very small fuel system impedances lead to very small and very large combustor growth rates, respectively. Model calculations for the 0.10 m long u-tube (not shown) reveal that the fuel system impedance is very large for most settings in zones 1, 3, and 5 and very small in zone 2. In the other zones, the magnitude of the fuel system

impedance is small enough that combustor stability also depends on the phase of the fuel system impedance.

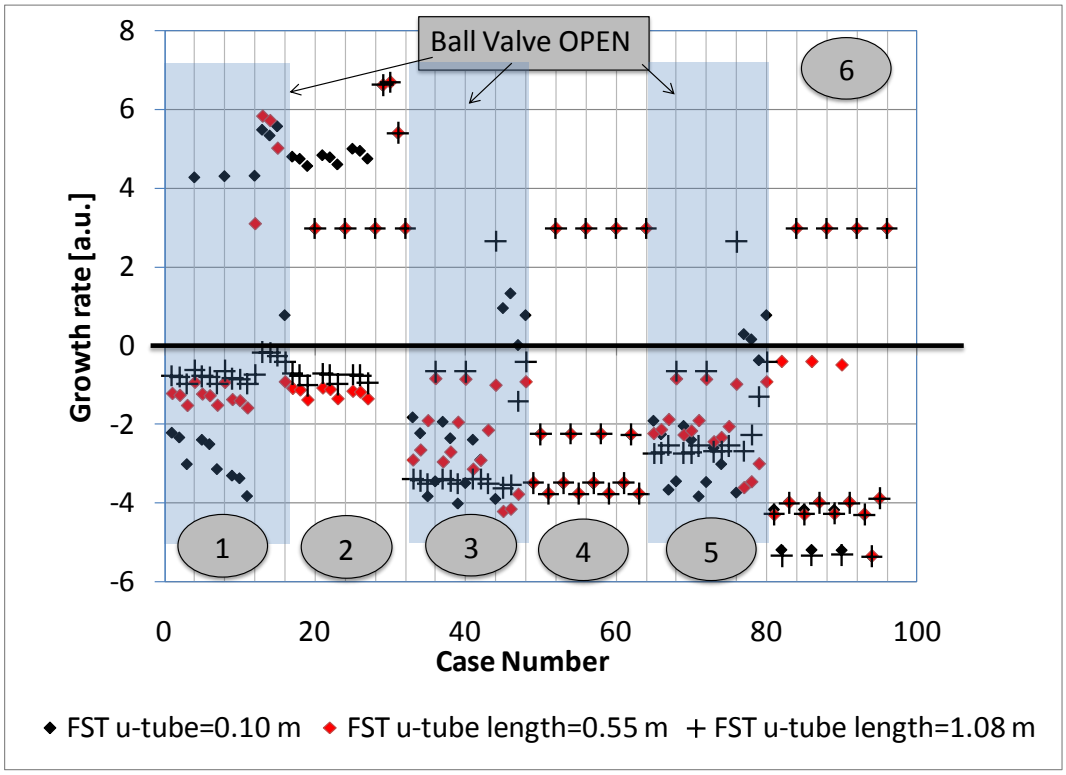

Figure 7.25: Growth rate vs. FST setting for Configuration 5 at a fuel flowrate of 0.9 kg/hr. Shown are model predictions for FST u-tube lengths of 0.10, 0.55 and 1.08 m.

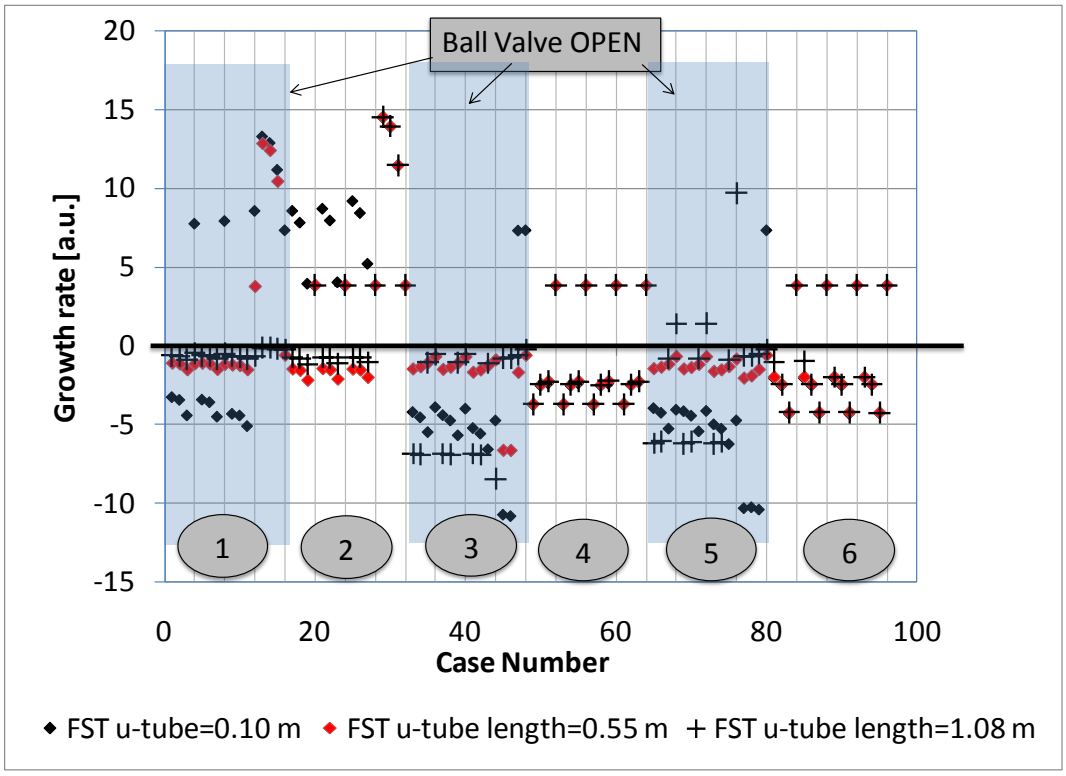

Figure 7.26: Growth rate vs. FST setting mm for Configuration 5 at a fuel flowrate of 1.9 kg/hr. Shown are model predictions for FST u-tube lengths of 0.10, 0.55 and 1.08 m.

Figure 7.27 and Figure 7.28 show the aggregate experimental results for Configuration 5 at fuel flowrates of 0.9 and 1.9 kg/hr, respectively. Examining Figure 7.27 reveals that the baseline acoustic pressure amplitude was 4281 Pa, which was very close to the baseline for Configuration 1 (see Figure 7.3). This should be the case since there was no difference between the two configurations with the FST turned OFF. As was the case for Configuration 1, the acoustic pressure amplitudes for Configuration 5 were lowest in zones 3, 4, 5, and 6. However, there were fewer FST settings in each zone yielding low acoustic pressure amplitudes in Configuration 5. The biggest difference between the results for Configuration 1 and Configuration 5 is seen in zone 1 where Configuration 5 shows no reduction in acoustic pressure amplitude. In contrast,

Zone 1 for Configuration 1 yielded some of the lowest acoustic pressure amplitudes observed for that case. Figure 7.28 shows the results for Configuration 5 at a fuel flowrate of 1.9 kg/hr were virtually the same as those for Configuration 1 at the same fuel flowrate.

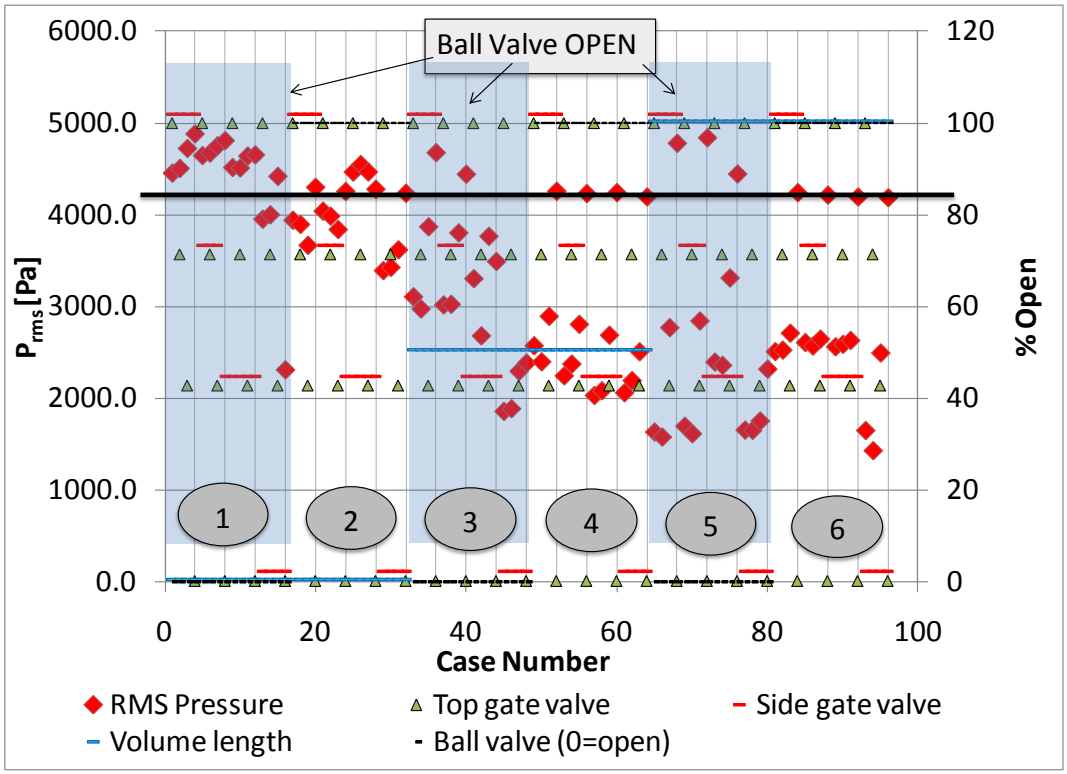

Figure 7.27: Acoustic pressure amplitude vs. FST setting for Configuration 5 at a fuel flowrate of 0.9 kg/hr.

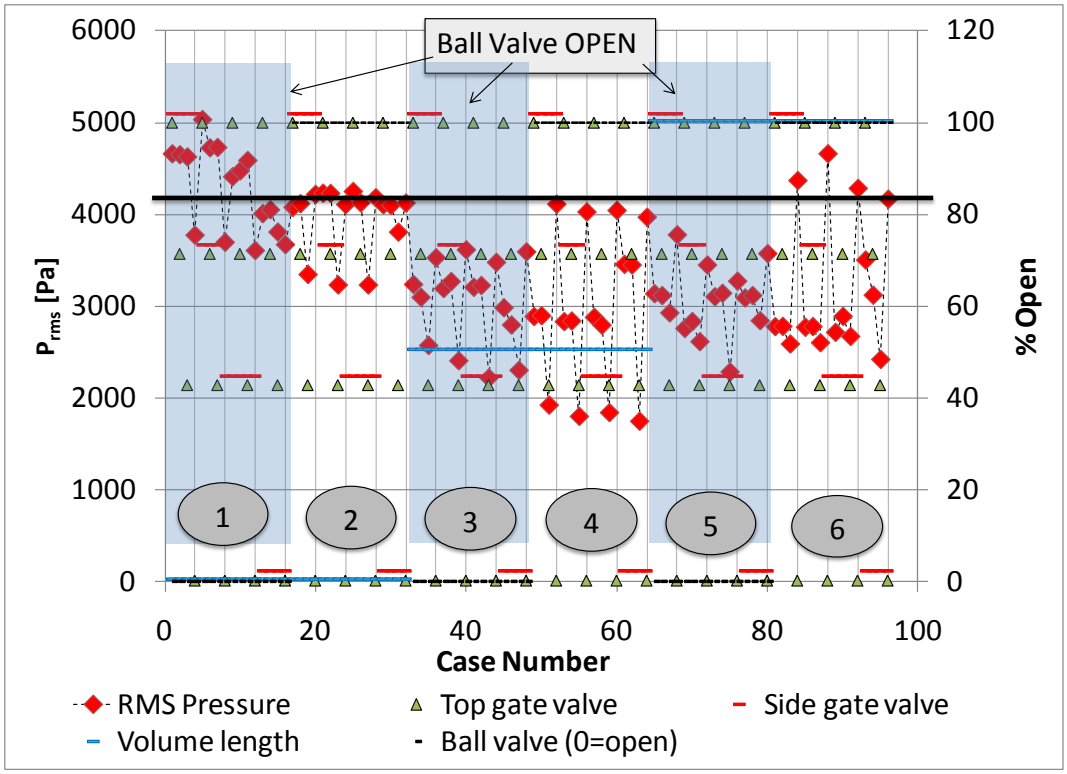

Figure 7.28: Acoustic pressure amplitude vs. FST setting for Configuration 5 at a fuel flowrate of 1.9 kg/hr.

Figure 7.29 shows the summary plot for Configuration 5. As predicted by the model, there were FST settings that resulted in stable combustor operation for each power setting. However, the FST had to be adjusted to achieve stable operation as the combustor operation condition was changed. There was no single FST setting that resulted in completely stable combustor operation. However, FST Case 58 had the lowest average combustor acoustic pressure over all operating conditions.

The model predicted that there were some settings that should yield higher than baseline combustor acoustic pressures. Experimentally, this was found to be the case as well. In fact, FST Case 5 was found to have the highest overall combustor acoustic pressure amplitude, which was significantly higher than the baseline of 4000 Pa. Figure

7.27 and Figure 7.28 also show that a number of settings had significantly higher combustor acoustic pressure amplitudes than the baseline.

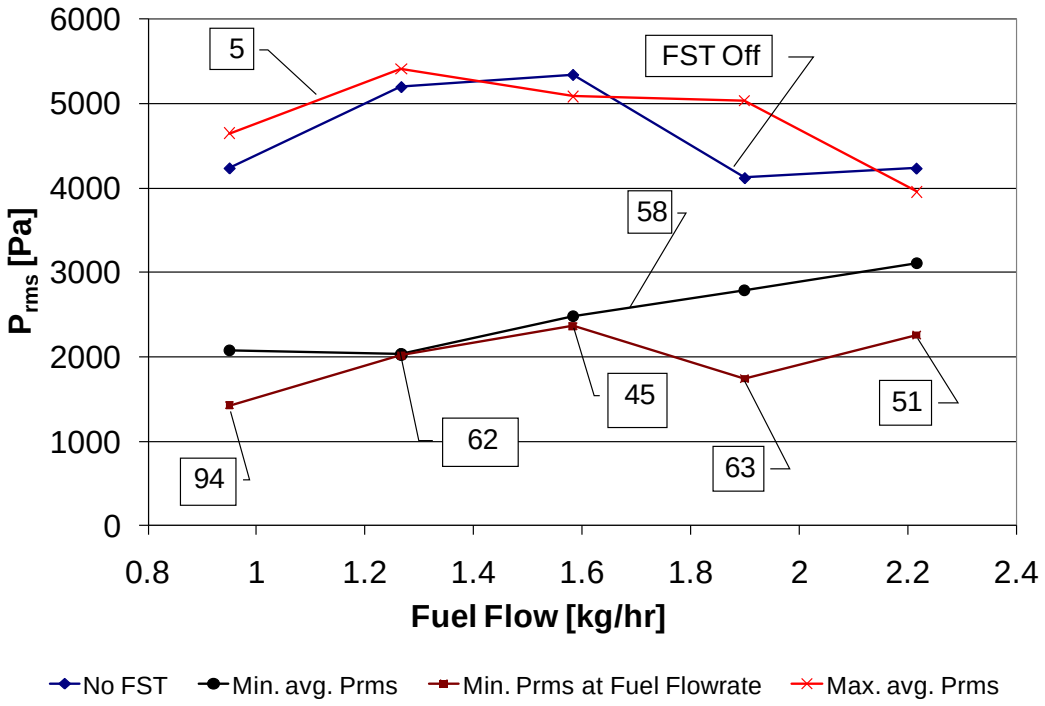

Figure 7.29: P_{rms} vs. Fuel Flowrate for Configuration 5.

7.3 Conclusions

The FST was tested on an acoustically unstable, lean, premixed, swirl-stabilized combustor developed for this purpose. The results of these tests, which were presented in Chapter 7, show that the FST significantly reduced the amplitude of the self-excited acoustic oscillations in the combustor. These results also showed that certain FST settings increased the amplitude of the thermo-acoustic oscillations.

The performance of the FST proved somewhat sensitive to changes in combustor configuration and operating condition, but the FST was adjusted to account for these changes to yield low acoustic pressure amplitudes in the combustor. These results are consistent with the predictions of the model developed in Chapter 6. These model predictions in conjunction with the experimental results were used to gain further insight into why certain fuel system impedances lead to stable/unstable combustor operation. In addition, both the predictions and the experimental measurements were used to develop some basic guidelines for designing fuel system tuner. It was shown that there is, in fact, an optimal range for the magnitude of the fuel system impedance. Consistent with predictions developed in Chapter 2, fuel system impedances much larger than the characteristic impedance of the air supply system $(\rho c)_{air}/S_{air}$ prevent communication between the fuel system and the air inlet pipe. Further, very large fuel system impedances result in such small fuel velocity oscillations that fuel system phase control has little effect on the phase of the total heat release oscillation and, therefore, combustor stability. Conversely, fuel flowrate oscillations can dominate the total heat release oscillation when the fuel system impedance is very small. In this case, combustor stability is so sensitive to the phase of the fuel system impedance that small shifts in the phase of the fuel system impedance results in unstable combustor

operation. Therefore, most of the FST settings resulting in stable combustor operation were those yielding fuel system impedances on the order of $(\rho c)_{air} / S_{air}$.

These results demonstrate that the FST was able to significantly reduce the amplitude of the self-excited acoustic oscillations in the combustor, and the FST was tested on several configurations of the combustor showing that the FST is capable of adapting to changes in system architecture.

Chapter 8:

Conclusions

8.1 Introduction

The focus of this dissertation was the development of a rational technique for designing a fuel system tuner capable of reducing or eliminating thermo-acoustic instabilities in gas-turbine combustors. In the course of the study, it proved necessary to account for certain nonlinear acoustic effects when modeling combustion systems. Therefore, a portion of this dissertation also concentrates on the effect of high-amplitude acoustic velocity oscillations on the impedance of fuel supply systems and how this affects the stability characteristics of combustion systems commonly used in lean, non-premixed, swirl-stabilized gas turbine engines.

8.2 Discussion

Chapter 1 introduced the problem of combustion instabilities in gas turbine engines, followed by a survey of techniques used to control these instabilities. The literature states that the stability of a given combustor depends, at least in part, on the impedance of the fuel supply system and that various passive control devices and tunable fuel injectors have been successfully used to stabilize combustion systems. Noting that a properly designed FST could theoretically be used to adjust the impedance of the fuel supply system to attain stable combustor operation, a novel Fuel System Tuner (FST) was proposed. However, a systematic, rational method for developing a tunable fuel supply system was needed.

The development and predictions of a feasibility study using a form of Rayleigh's criterion was presented in Chapter 2. This analysis is straightforward to use but is capable of making important predictions about the effect of fuel system impedance on combustor stability. In this study, it yielded the following important conclusions about the use of fuel system tuners and combustor stability. First, the fuel system impedance is critical to combustor stability for acoustically open fuel systems, and that control of combustor instabilities can be accomplished using a variable impedance fuel supply system. Second, the magnitude of the fuel system impedance controls the sensitivity of combustor response to fuel system impedance. Third, restricting the fuel injector diameter, i.e., choking the fuel supply system, limits the ability of the variable impedance fuel supply system to control combustion instabilities. Fourth, the response of the combustor to changes in fuel system impedance depends on the location of the fuel system in the air supply system. Finally, and most importantly, fuel system impedance must be considered when developing new combustion systems. Otherwise, modifications will need to be made after the fact to allow for stable combustor operation.

Based on the results of these predictions, the best design for a tunable fuel system would center on keeping the fuel system impedance as low as possible while incorporating a mechanism for adjusting the fuel system resistance. In practice, the lowest fuel system impedance is obtained by tuning the fuel system to resonance at the frequency of the expected combustor instability frequency, which minimizes the imaginary part of the fuel system impedance. By varying the fuel system resistance from 0 to a value much larger than the imaginary part of the fuel system impedance, the phase of the impedance can be varied from 0 to +/- 90 degrees.

Larger fuel system impedance magnitudes can be obtained by tuning slightly away from resonance to increase the imaginary part while keeping the resistive part

essentially constant. This also changes the phase of the fuel system impedance, so some adjustment to the fuel system resistance may be needed to retain the same phase as before.

Chapter 3 presented the development of nonlinear acoustic impedance models for acoustically compact area contractions and expansions. These models captured the important trends and provided a convenient relationship for correlating experimental data. In addition, the developed models can be conveniently incorporated into acoustic network models. Finally, the development and predictions of an acoustic response model of an acoustic network containing an area contraction were presented.

Chapter 4 presented the development, sensitivity analysis, and validation of a two-microphone impedance tube used to measure the impedance of the various area contractions and valves critical to the construction and performance of the FST. The measurements presented in this chapter accomplished the following. First, the measurements extended those made by previous researchers to higher acoustic pressure and velocity amplitudes. Specifically, the acoustic resistance of an area contraction was measured over the range of acoustic velocity amplitudes from 0.25 to 110 m/s. In addition, these measurements show that the nonlinear impedance model developed in Chapter 3 correctly predicts a linear relationship between acoustic resistance and acoustic velocity amplitude for simple area contractions. However, these measurements show that the slope of the linear dependence was not constant. In fact, the measurements show that the slope changed discretely at acoustic Reynolds numbers of 15,000, 32,000, 60,000 and 100,000. It was also found that a Reynolds number scaling, or power law, model yielded good agreement with the data over the range of acoustic velocities tested.

The measurements presented also revealed that the acoustic resistance of a simple ‘tee’ junction was also nonlinear with acoustic velocity amplitude. Although typically modeled as a linear acoustic duct element, these results show that a nonlinear model for the ‘tee’ junction impedance is required to achieve accurate predictions.

The acoustic resistance of a simple gate valve was also shown to be nonlinear and that its resistance increased as the valve was closed. However, closing the valve to its 100% closed position showed that, in this case, the acoustic resistance of the valve was infinite and, therefore, dissipated no acoustic power. These results also show that the frequency response of the system containing the valve depends on valve setting. The important conclusion from this part of the study is that achieving an accurate prediction of valve resistance is critical to predicting the acoustic impedance of the overall system.

Finally, the reflection coefficient of a combination of an area contraction, a gate valve, and a rigid-walled tube was measured for frequencies between 100 and 1000 Hz. These results show that the behavior of simple acoustic networks containing nonlinear elements have a complex acoustic response that cannot be captured by linear models.

In Chapter 5, the procedure for developing 1-D, nonlinear acoustic models for systems containing single or multiple nonlinear elements was presented. Further, the chapter shows that significant damping is observed when the acoustic resistance dominates the acoustic impedance of the system. Therefore, it was shown that it is necessary to control both the reactive and resistive parts of the system impedance to obtain system impedance phase control. It was also shown that nonlinear elements affect the acoustic velocity field, which, in turn, affects the impedance of other nonlinear elements. This complicates predicting the result of changing one nonlinear element in a system containing numerous nonlinear elements.

The overall FST modeling procedure was outlined, and model predictions for the FST impedance were presented. These results were shown to be in good agreement with the experimental results for frequencies below 600 Hz.

Finally, experimental measurements and model predictions show that the FST can be tuned to obtain a wide range of impedance values for a given frequency. Therefore, the FST, when properly designed, could provide means for adjusting the impedance of a given fuel system to obtain stable combustor operation or, at least, greatly reduced thermo-acoustic oscillations.

Chapter 6 presented the development of a thermo-acoustic model of a lean, premixed combustor similar to those used in modern gas turbine engines. The model for the combustor fuel supply system included the developed nonlinear FST impedance model. A flame transfer function was used to model the combustion process. The combustor/FST thermo-acoustic model was used to predict the instability frequency and growth rate of the model combustor for two different combustor configurations. Further, the sensitivity of combustor growth rate to combustor average temperature, FST input pressure, and flame location was also investigated for a wide range of FST settings.

The model predictions indicate that large FST impedances can lead to either stable or unstable combustor operation depending on the combustor, but that phase control has no effect on combustor stability in this case. In addition, model predictions show that fuel system tuning, i.e., phase control, is very important and effective when the magnitude of the FST impedance is very small. However, in this case, care must be taken when tuning the fuel system due to extreme sensitivity of the combustor to the phase of the fuel system impedance. In some instances, destructive combustor pressure oscillations were predicted. The model predictions indicate that the best performance is obtained for magnitudes of fuel system impedance between 20-80% of

$10\frac{(\rho c)_{fuel}}{S_{fi}}$. In this range, the combustor responds well to changes in the impedance of the fuel supply system without the danger of excessive combustor pressure oscillations at off-design FST settings. The results obtained here were shown to be consistent with predictions of the model developed in Chapter 2.

The FST was tested on an acoustically unstable, lean, premixed, swirl-stabilized combustor developed for this purpose. The results of these tests, which were presented in Chapter 7, show that the FST significantly reduced the amplitude of the self-excited acoustic oscillations in the combustor. These results also showed that certain FST settings increased the amplitude of the thermo-acoustic oscillations.

The performance of the FST proved somewhat sensitive to changes in combustor configuration and operating condition, but the FST was adjusted to account for these changes to yield low acoustic pressure amplitudes in the combustor. These results are consistent with the predictions of the model developed in Chapter 6. These model predictions in conjunction with the experimental results were used to gain further insight into why certain fuel system impedances lead to stable/unstable combustor operation. In addition, both the predictions and the experimental measurements were used to develop some basic guidelines for designing the fuel system tuner. It was shown that there is, in fact, an optimal range for the magnitude of the fuel system impedance. Consistent with predictions developed in Chapter 2, fuel system impedances much larger than the characteristic impedance of the air supply system $(\rho c)_{air}/S_{air}$ prevent communication between the fuel system and the air inlet pipe. Further, very large fuel system impedances result in such small fuel velocity oscillations that fuel system phase control has little effect on the phase of the total heat release oscillation and, therefore, combustor stability. Conversely, fuel flowrate oscillations can

dominate the total heat release oscillation when the fuel system impedance is very small. In this case, combustor stability is so sensitive to the phase of the fuel system impedance that small shifts in the phase of the fuel system impedance results in unstable combustor operation. Therefore, most of the FST settings resulting in stable combustor operation were those yielding fuel system impedances on the order of $(\rho c)_{air} / S_{air}$.

Finally, these results demonstrate that the FST was able to significantly reduce the amplitude of the self-excited acoustic oscillations in the combustor, and the FST was tested on several configurations of the combustor showing that the FST is capable of adapting to changes in system architecture

8.3 Important contributions

This dissertation presented a comprehensive study of the development and performance of a novel Fuel System Tuner for the control of combustion instabilities in gas turbine engines. Acoustic models for the subcomponents of the FST were developed, and these models were experimentally verified using a two-microphone impedance tube. Models useful for designing, analyzing, and predicting the performance of the FST were developed and used to demonstrate the effectiveness of the FST in a model combustor. The FST was tested and shown to reduce the acoustic pressure amplitude for a wide range of operating conditions and combustor configurations. Combustor acoustic pressure amplitude measurements were used in conjunction with model predicted fuel system impedances to determine the optimal magnitude and phase of the fuel system impedance for stable combustor operation.

The FST concept and design methodology presented in this dissertation can be used on existing gas turbine combustors to reduce, or eliminate altogether, thermo-

acoustic oscillations. Furthermore, the concepts presented here can be used in the initial combustor design process to develop tunable fuel systems including the necessary controls to prevent, or eliminate, thermo-acoustic oscillations.

The important contributions of this study are

(1) A nonlinear, acoustic response modeling methodology was developed and the acoustic impedance was measured for the FST and its components. The measurements and models agreed reasonably well for the conditions tested.

(2) A stability model based on Rayleigh's criterion was developed that proves the importance of fuel system impedance to stable gas turbine engine operation. The model was also used to develop guidelines for designing fuel system tuners, and allows designers to predict engine stability. In fact, predictions by this model have been used to develop a simpler embodiment of the fuel system tuner.

(3) A thermo-acoustic combustor model incorporating the FST acoustic response model was developed that predicted stable operating settings of the FST in a test combustor, predicts the sensitivity of combustor stability to changes in FST setting and combustor operating condition, and forms a basis for a FST control system.

8.4 Future work

The research presented here indicates that nonlinear acoustic effects play an important role in the physical behavior of acoustical systems, particularly in the performance of lean, premixed gas turbine combustors. However, much work remains in this area. Some topics for future research include:

(1) Investigating nonlinear acoustic effects in the flame transfer function and experimentally investigating the importance of these effects, in particular, the nonlinear interaction between fuel-air ratio and acoustic velocity (see Appendix A).

(2) Extending the thermo-acoustic model developed here to include nonlinear effects into a nonlinear combustor model capable of predicting saturation pressure amplitudes.

(3) Explaining the modal dependence of the area contraction acoustic resistance on acoustic Reynolds number. This translates into studying the major flow features of the acoustically forced flow field in the vicinity of area contractions and expansions.

(4) Investigating (using both models and experiments) the effect of and proper positioning for the FST on combustors having azimuthal, as well as, longitudinal acoustic instabilities.

(5) Developing and testing new FST designs using the design rules developed in this investigation.

Appendix A:

Heat Release Transfer Function Development

A.1 Introduction

In order to predict the effect of the tunable fuel supply system on combustion instabilities, a heat release transfer function was needed to link the acoustic combustor model with the fuel supply system acoustic model. The model described in this section captures, in a global manner, the salient effects simply and efficiently.

It is well known that combustion instabilities may couple with the acoustics of the system through several mechanisms, which depend on system design. These include fluctuations in the flame area, flame speed, unburned gas density, unburned gas flowrate, and fuel mass fraction. In the next section, each of these fluctuations will be related to the acoustical properties of the combustion chamber, air plenum and fuel injector.

A.2 Linear heat release transfer function development

Starting with the equation for heat release due to combustion, given by

$$\dot{Q} = Y_f \left(\rho u A\right)_{air} \delta H_c \,, \tag{A.1}$$

and assuming that each term, except the enthalpy of combustion, in this equation may be written as the sum of a steady and oscillating component, the following equation for the total heat release was obtained

$$\left(\dot{Q}_0 + \dot{Q}'\right) = \left(\rho + \rho'\right)\left(U + U'\right)\left(Y_f + Y_f'\right)\delta H_c \,. \tag{A.2}$$

Multiplying the right hand side out, subtracting the steady state component from both sides, and dividing both sides by $\dot{Q}_0$ yields the following equation for the nonlinear form of the heat release transfer function

$$\frac{\dot{Q}'}{\dot{Q}_0} = \underbrace{\left(\frac{U'}{U} + \frac{\rho'}{\rho} + \frac{Y_f'}{Y_f}\right)}_{\text{term 1}} + \underbrace{\left(\frac{U'}{U}\frac{\rho'}{\rho} + \frac{U'}{U}\frac{Y_f'}{Y_f} + \frac{Y_f'}{Y_f}\frac{\rho'}{\rho}\right)}_{\text{term 2}} + \underbrace{\frac{U'}{U}\frac{\rho'}{\rho}\frac{Y_f'}{Y_f}}_{\text{term 3}}. \tag{A.3}$$

The linear heat release transfer function

$$\frac{\dot{Q}'}{\dot{Q}_0} = \frac{U'}{U} + \frac{\rho'}{\rho} + \frac{Y_f'}{Y_f} \tag{A.4}$$

is obtained from Eq. (A.3) by retaining term 1 and neglecting all terms involving the products of differentials, which are generally assumed negligible.

Equation (A.4) shows that the actual magnitude and phase of the heat release oscillation occurring at the flame is a function of the magnitude and timing of disturbances in the mixture ratio (or equivalence ratio), the density, and the acoustic volume velocity at the flame.

At the fuel injector, “packets” of fuel and air having a time varying fuel-air ratio are produced continuously. Because the fuel is injected upstream of the combustion zone, there is a time delay τ_{conv} between when these packets are produced and when they arrive at the reaction zone. This time delay was accounted for in Eq. (A.4) by including a time delay τ_{conv} of $\omega L/v$ as follows:

$$\frac{Q'}{Q} = \frac{\rho'}{\rho} + \frac{Y_i'}{Y_i} e^{i\omega\frac{L}{v}} + \frac{U'}{U}. \tag{A.5}$$

There is also a delay between the arrival of a packet at the combustion zone and when that packet is actually consumed. This was accounted for by including a chemical time delay τ_{chem} so that Eq. (A.5) becomes

$$\frac{Q'}{Q} = \left(\frac{\rho'}{\rho} + \frac{Y_i'}{Y_i} e^{i\omega\tau_{conv}} + \frac{U'}{U} \right) e^{i\omega\tau_{chem}} . \tag{A.6}$$

Equation (A.6) relates the heat release fluctuation at the combustion zone to the acoustical properties of combustion system and fuel supply system. It shows explicitly that the heat release fluctuations depend on fluctuations in the unburned gas density, mixture ratio and volume velocity, as well as, the timing of the arrival and consumption of reactants.

A.2.1 Nonlinear heat release transfer function development

The expression for the linear heat release transfer function was obtained by neglecting the second and third terms in Eq. (A.3). Usually, these terms are assumed to be second and third order terms, respectively. This section investigates the validity of this assumption.

First, the ratio of the acoustic to the steady velocity is, for the velocities encountered in many combustors, of order one. Next, the ratio of the steady fluctuating density to the mean density can be re-written in the following form

$$\frac{\rho'}{\rho} = \frac{\frac{p'}{c^2}}{\frac{\gamma p}{c^2}} = \frac{p'}{\gamma p} . \tag{A.7}$$

For sound pressure levels of 170 dB ($p' = 5000\ Pa$), Eq. (A.7) yields a value of $\rho'/\rho = 0.035$, which is two orders of magnitude smaller than the acoustic velocity ratio.

However, the ratio of the fluctuating mass fraction to the mean mass fraction is another matter. An estimate for the ratio of the fluctuating mass fraction to the mean mass fraction Y'/Y was obtained as follows. First, assume that (1) the operating equivalence ratio for most lean, premixed combustors is around 0.75, (2) the lean

blowout limit is at an equivalence ratio of 0.5, and (3) that the highest equivalence ratio achievable is 1.0.

To estimate the order of magnitude of the acoustic fuel mass fraction, the following expression was used

$$Y_{fuel} = \frac{\dot{m}_{fuel}}{\dot{m}_{fuel} + \dot{m}_{air}} = \frac{\Psi}{1+\Psi}. \tag{A.8}$$

The acoustic mass fraction ratio was obtained by assuming that each of these may be written as the sum of mean and oscillating components, i.e., small perturbations, as follows:

$$\bar{Y}_{fuel} + Y'_{fuel} = \frac{\bar{\Psi} + \Psi'}{1+\bar{\Psi}+\Psi'}. \tag{A.9}$$

After some algebraic manipulation, Eq. (A.9) yields

$$\frac{Y_{fuel}{}'}{\bar{Y}_{fuel}} = \frac{\Psi'}{\bar{\Psi}\left(1+\bar{\Psi}\right)}. \tag{A.10}$$

From the definition of the equivalence ratio $\Psi = \Phi \cdot \Psi_{stoich}$, the actual fuel-air ratio was computed from the equivalence ratio. Assuming that the nominal average fuel-air ratio is $\bar{\Psi}$ and the actual fuel air ratio at any given time is Ψ, the maximum fluctuation in fuel-air ratio Ψ' is computed from

$$\Psi' = \frac{\bar{\Psi} - \Psi}{\bar{\Psi}} = \frac{\bar{\Phi} - \Phi}{\bar{\Phi}}. \tag{A.11}$$

At blowout and at stoichiometric conditions, this equation yields, respectively,

$$\begin{aligned} \Psi'_{blowout} &= \frac{0.75 - 0.5}{0.75} = 0.33 \\ \Psi'_{stoich} &= \frac{0.75 - 1.0}{0.75} = -0.33 \end{aligned}. \tag{A.12}$$

And Eq. (A.10) yields for these same conditions, respectively,

$$\frac{Y'_{fuel}}{\bar{Y}_{fuel}} = \frac{\pm 0.33}{(1+1/18)\cdot 1/18} = \pm 5.63. \tag{A.13}$$

Clearly, the ratio of fluctuating to steady mass fractions is of order 1.

From the preceding analysis, we see that the acoustic density fluctuations are negligible compared to either the acoustic velocity ratio or oscillating fuel mass fraction ratio. In addition, Y'/Y and $(Y'/Y)(U'/U)$ are both of order 1. These conclusions lead to the following simplified expression for the nonlinear heat release transfer function

$$\frac{\dot{Q}'}{\dot{Q}_0} = \frac{U'}{U}\left(1+\frac{Y'_f}{Y_f}\right)+\frac{Y'_f}{Y_f}. \tag{A.14}$$

As discussed above, Eq. (A.14) neglects only the very small acoustic density ratio fluctuations while retaining the non-negligible product of the acoustic velocity and fuel mass fraction fluctuation. Although more precise, this nonlinear expression introduces some modeling difficulties, and the nonlinear term may have to be neglected for simplicity. However, it is important to be aware of the assumption breaks down anytime the acoustic velocity ratio nears unity.

Appendix B:

Development of heat release fluctuation parameters

It is convenient in many cases to write the acoustic density ratio, volume velocity ratio, and mass fraction fluctuation ratio in terms of the acoustic properties of the system. This appendix gives the steps required to cast the heat release transfer function in a form convenient for use in the analyses presented in this thesis.

First, the acoustic density ratio at the flame location in Eq. (A.6) was written using $p' = \rho' c^2$ and $\gamma p = \rho c^2$ to obtain an expression in terms of the acoustic pressure ratio as

$$\frac{\rho'}{\rho} = \frac{p_1'}{\gamma p_1}. \tag{B.1}$$

Next, the acoustic volume velocity ratio was written in terms of the acoustic pressure as follows

$$\frac{U'}{U} = \frac{p_1'}{Z_1 U_1} = \frac{U_1'}{U_1}, \tag{B.2}$$

using the definition of the acoustic impedance.

Finally, consider the oscillating fuel mass fraction ratio. The oscillating mass fraction may be thought of as packets of fuel and air having time-varying composition. These packets originate at the fuel injector and travel toward the combustion zone at the speed of the steady flow. Therefore, the fuel-air ratio of each packet must be calculated at the fuel injector, and the time delay between the packets creation and its arrival at the combustion zone must be accounted for.

An expression for the acoustic mass fraction ratio Y'/Y can be obtained from

$$Y_f = \frac{\dot{m}_{fuel}}{\dot{m}_{fuel} + \dot{m}_{air}} = \frac{\psi}{\psi + 1} \tag{B.3}$$

by multiplying both sides by $\left(\dot{m}_{air}+\dot{m}_{fuel}\right)$ and replacing each term by the sum of its mean and oscillating component as follows

$$\left[\left(\dot{m}_{0,air}+\dot{m}'_{air}\right)+\left(\dot{m}_{0,fuel}+\dot{m}'_{fuel}\right)\right]\left(Y_{0,f}+Y_f'\right)=\left(\dot{m}_{0,fuel}+\dot{m}'_{fuel}\right). \tag{B.4}$$

Multiplying out the terms on the left hand side, neglecting products of differentials (i.e., prime quantities), dividing both sides by $Y_f\dot{m}_{total}=Y_f\left(\dot{m}_{air}+\dot{m}_{fuel}\right)$, and rearranging yields

$$\frac{Y_f'}{Y_f}=\frac{\dot{m}_{0,fuel}}{Y_f\dot{m}_{total}}+\frac{\dot{m}'_{fuel}}{Y_f\dot{m}_{total}}-\frac{\dot{m}'_{fuel}}{\dot{m}_{total}}-\frac{\dot{m}'_{air}}{\dot{m}_{total}}-1. \tag{B.5}$$

The first term on the right hand side is identically equal to one by the definition of the fuel mass fraction and cancels with the one on the right hand side, yielding

$$\frac{Y_f'}{Y_f}=\frac{\dot{m}'_{fuel}}{\dot{m}_{total}}\left(\frac{1-Y_f}{Y_f}\right)-\frac{\dot{m}'_{air}}{\dot{m}_{total}}. \tag{B.6}$$

Replacing $\dot{m}'_{fuel}$ with $\left(\rho'_{fuel}U_{fuel}+\rho_{fuel}U'_{fuel}\right)$ and $\dot{m}'_{air}$ with $\left(\rho'_{air}U_{air}+\rho_{air}U'_{air}\right)$ and rearranging yields

$$\frac{Y_f'}{Y_f}=\frac{\rho'_{fuel}U_{fuel}}{\dot{m}_{total}}\left(\frac{1-Y_f}{Y_f}\right)+\frac{\rho_{fuel}U'_{fuel}}{\dot{m}_{total}}\left(\frac{1-Y_f}{Y_f}\right)-\frac{\rho'_{air}U_{air}}{\dot{m}_{total}}-\frac{\rho_{air}U'_{air}}{\dot{m}_{total}}. \tag{B.7}$$

Upon replacing $\dot{m}_{total}$ with $\rho_{total}U_{0,total}$, $Y_f\dot{m}_{total}$ with $\dot{m}_{fuel}=\rho_{fuel}U_{0,fuel}$, $\rho_{total}U_{total}$ with $\frac{\rho_{total}U_{air}}{\left(1-Y_f\right)}$, and ρ_{air} with $\gamma p/c^2$, Eq. (B.7) becomes

$$\frac{Y_f'}{Y_f}=\frac{\rho'_{fuel}}{\rho_{fuel}}\left(1-Y_f\right)+\frac{U'_{fuel}}{U_{fuel}}\left(1-Y_f\right)-\frac{\rho'_{air}}{\rho_{total}}\left(1-Y_f\right)-\frac{U'_{air}}{\rho_{total}U_{total}}\frac{\gamma_{air}p_{air}}{{c_{air}}^2}. \tag{B.8}$$

In what follows, the mixture specific heat ratio γ, density, and speed of sound are assumed to have the same value as for air. Assuming that the impedances of the

fuel injector Z_{fi} and the air system at the fuel injector Z_{air} are known and substituting $p'/\gamma p$ for the acoustic density ratios, Eq. (B.8) can be written as

$$\frac{Y_f'}{Y_f} = \frac{p'_{fuel}}{\gamma_{fuel} p_{fuel}}(1-Y_f) - \frac{p'_{fuel}}{Z_{fi} U_{fuel}}(1-Y_f) - \frac{p'_{air}}{\gamma_{air} p_{total}}(1-Y_f) - \frac{p'_{air}}{\rho_{total} U_{total} Z_{air}} \frac{\gamma_{air} p_{air}}{c_{air}^2} \quad \text{(B.9)}$$

or as

$$\frac{Y_f'}{Y_f} = \frac{p'_{fuel}}{\gamma p_{fuel}}(1-Y_f) + \frac{U'_{fuel}}{U_{fuel}}(1-Y_f) - \frac{p'_{air}}{\gamma p_{total}}(1-Y_f) - \frac{U'_{air}}{\rho_{total} U_{total}} \frac{\gamma_{air} p_{air}}{c_{air}^2}, \quad \text{(B.10)}$$

where each term in Eq. (B.12) must be evaluated at the location of the fuel injector.

Assuming that the impedances of the fuel injector Z_{fi} and the air system at the fuel injector Z_{air} are known and substituting $p'/\gamma p$ for the acoustic density ratios, Eqs. (B.9) and (B.10) can be written as

$$\frac{Y_f'}{Y_f} = \frac{p'_{fuel}}{\gamma p_{fuel}}(1-Y_f) - \frac{p'_{fuel}}{Z_{fi} U_{0,fuel}}(1-Y_f) - \frac{p'_{air}}{\gamma p_{total}}(1-Y_f) - \frac{p'_{air}}{\rho_{total} U_{total} Z_{air}} \frac{\gamma_{air} p_{air}}{c_{air}^2} \quad \text{(B.11)}$$

and

$$\frac{Y_f'}{Y_f} = \frac{p'_{fuel}}{\gamma p_{fuel}}(1-Y_f) + \frac{U'_{fuel}}{U_{fuel}}(1-Y_f) - \frac{p'_{air}}{\gamma p_{total}}(1-Y_f) - \frac{U'_{air}}{\rho_{total} U_{total}} \frac{\gamma_{air} p_{air}}{c_{air}^2}, \quad \text{(B.12)}$$

respectively.

Appendix C:

The Transfer Matrix

The heat release transfer function developed in Appendix A, involves acoustic pressure and volume velocity terms at both the flame location and at the fuel injector location. In order to develop a useful expression, all terms in the heat release transfer function need to be related to the acoustic pressure at the flame location. This is done using a concept called the "transfer matrix".

The transfer matrix was used to relate the acoustic pressure and velocity at one location in a duct system to the pressure and velocity at another location. Typically, the matrix equation takes the following form:

$$\begin{bmatrix} p_2' \\ u_2' \end{bmatrix} = T \begin{bmatrix} p_1' \\ u_1' \end{bmatrix}, \tag{C.1}$$

where T is the transfer matrix. As an example, the transfer matrix relating the acoustic pressure and velocity between two points separated by a distance L in a straight, rigid-walled duct section is

$$T_{\delta L} = \begin{bmatrix} \frac{1}{2}\left(e^{ik\delta L} + e^{-ik\delta L}\right) & \frac{1}{2}\frac{\rho c}{S}\left(e^{ik\delta L} - e^{-ik\delta L}\right) \\ \frac{1}{2}\frac{S}{\rho c}\left(e^{ik\delta L} - e^{-ik\delta L}\right) & \frac{1}{2}\left(e^{ik\delta L} + e^{-ik\delta L}\right) \end{bmatrix}. \tag{C.2}$$

And the transfer matrix relating the acoustic pressure and velocity across an arbitrary impedance Z_i is given by

$$T_{Z_i} = \begin{bmatrix} 1 & -Z_i \\ 0 & 1 \end{bmatrix}. \tag{C.3}$$

The transfer matrix relating the acoustic pressure and velocity between two points separated by a distance L and an impedance Z_i is given by the product of the transfer matrices $T_{\delta L_1}$, $T_{\delta L_2}$, and T_{Z_i} as follows:

$$\begin{bmatrix} p_2' \\ u_2' \end{bmatrix} = T_{\delta L_1} T_{Z_i} T_{\delta L_2} \begin{bmatrix} p_1' \\ u_1' \end{bmatrix}, \tag{C.4}$$

where for this case,

$$\begin{aligned} T &= T_{\delta L_1} T_{Z_i} T_{\delta L_2} \\ &= \begin{bmatrix} T_a & T_b \\ T_c & T_d \end{bmatrix} \\ &= \begin{bmatrix} T_{a,1}T_{a,2} + T_{c,2}\left(T_{b,1} - ZT_{a,1}\right) & T_{d,2}\left(T_{b,1} - ZT_{a,1}\right) + T_{a,1}T_{b,2} \\ T_{c,1}T_{a,2} + T_{c,2}(T_{d,1} - ZT_{c,1}) & T_{d,2}\left(T_{d,1} - ZT_{c,1}\right) + T_{c,1}T_{b,2} \end{bmatrix}, \end{aligned} \tag{C.5}$$

$$T_{\delta L_1} = \begin{bmatrix} T_{a,1} & T_{b,1} \\ T_{c,1} & T_{d,1} \end{bmatrix} = \begin{bmatrix} \frac{1}{2}\left(e^{ikL_1} + e^{-ikL_1}\right) & \frac{1}{2}\frac{(\rho c)_1}{S_1}\left(e^{ikL_1} - e^{-ikL_1}\right) \\ \frac{1}{2}\frac{S_1}{(\rho c)_1}\left(e^{ikL_1} - e^{-ikL_1}\right) & \frac{1}{2}\left(e^{ikL_1} + e^{-ikL_1}\right) \end{bmatrix}, \tag{C.6}$$

and

$$T_{\delta L_2} = \begin{bmatrix} T_{a,2} & T_{b,2} \\ T_{c,2} & T_{d,2} \end{bmatrix} = \begin{bmatrix} \frac{1}{2}\left(e^{ikL_2} + e^{-ikL_2}\right) & \frac{1}{2}\frac{(\rho c)_2}{S_2}\left(e^{ikL_2} - e^{-ikL_2}\right) \\ \frac{1}{2}\frac{S_2}{(\rho c)_2}\left(e^{ikL_2} - e^{-ikL_2}\right) & \frac{1}{2}\left(e^{ikL_2} + e^{-ikL_2}\right) \end{bmatrix}. \tag{C.7}$$

Therefore, if the transfer matrices were known, the acoustic pressure and velocity at any point in the system could be related to the acoustic pressure and velocity at any other point in the system. Defining the total transfer matrix T_{total} between points 1 and 2 as

$$T_{total} = \prod_i T_i = \begin{bmatrix} T_a & T_b \\ T_c & T_d \end{bmatrix}, \tag{C.8}$$

the acoustic pressure at location 2 was obtained from the acoustic pressure and velocity at location 1 by

$$p_2' = T_a p_1' + T_c u_1' = p_1' \left(T_a + \frac{T_c}{Z_1} \right), \tag{C.9}$$

where Z_1 is the acoustic impedance at location 1, the combustion zone.

Appendix D:

Development of the Combustor Impedance Expressions

Figure 2.1 shows as schematic of the combustion system analyzed in Chapter 2. The analysis presented there requires an expression relating Z_1 (see Fig. 2.1) to the upstream impedances $Z_{1a}, Z_{fi}, and\ Z_{air}$ (see Fig. 2.1).

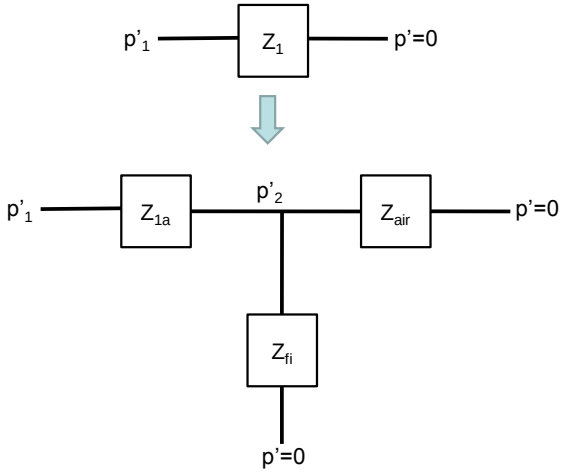

Figure D.1: Acoustic network model.

The impedance of the system at the flame location Z_1 inherently includes the impedance of the fuel injector Z_{fi}, the impedance of the air line between the flame and the fuel injector Z_{1a}, and the impedance of the air line upstream of the fuel injector Z_{air}. However, the impedance at the flame location Z_1 can be written in terms of Z_{air} and Z_{fi} by considering the acoustic network shown in Figure D.1. $Z_{fi}\ and\ Z_{air}$ are in parallel with each other and in series with Z_{1a}; therefore, the equivalent impedance of this network is given by

$$Z_1 = Z_{1a} + \frac{Z_{fi} Z_{air}}{Z_{fi} + Z_{air}}. \tag{D.1}$$

Applying Eq. (D.1) to the system required determining the value of Z_1 , which also involves Z_{1a} and Z_{air} . The impedance Z_{1a} was determined from the transfer matrix as follows. First, the transfer matrix equation between the flame and the fuel injector is given by

$$\begin{bmatrix} p_3' \\ u_3' \end{bmatrix} = \begin{bmatrix} T_a & T_b \\ T_c & T_d \end{bmatrix} \begin{bmatrix} p_1' \\ u_1' \end{bmatrix}, \tag{D.2}$$

so that

$$p_3' = T_a p_1' + T_b u_1'. \tag{D.3}$$

The acoustic impedance Z_{1a} is given by

$$Z_{1a} = \frac{p_1' - p_3'}{u_1'} = \frac{p_1' - \left(T_a p_1' + T_b u_1'\right)}{u_1'} = Z_1\left(1 - T_a\right) - T_b. \tag{D.4}$$

And substituting Eq. (D.1) for Z_{1a} in Eq. (D.4) obtained the following:

$$Z_{1a} = \frac{\frac{Z_{fi} Z_{air}}{Z_{fi} + Z_{air}}\left(1 - T_a\right) - T_b}{T_a}. \tag{D.5}$$

The impedance Z_{air} of the air inlet pipe from the fuel injector to the air inlet valve was obtained as follows. First, the air inlet valve was assumed to be acoustically rigid so that $R = e^{2ikL_3}$. The impedance Z_{air} was defined as

$$Z_{air} = \frac{p_3'}{u_3'},. \tag{D.6}$$

where both p_3' and u_3' are evaluated at the location of the fuel injector. Using the transfer matrices and substituting for the acoustic pressure and velocities yields

$$Z_{air} = \frac{\left(1+e^{2ikL_3}\right)}{\frac{S_3}{\left(\bar{\rho}c\right)_3}\left(1-e^{2ikL_3}\right)}. \tag{D.7}$$

Substituting Eq. (D.7) into Eq. (D.5) gives for Z_{1a}

$$Z_{1a} = \frac{Z_{fi}\frac{\left(1+e^{2ikL_3}\right)}{\frac{S_3}{\left(\bar{\rho}c\right)_3}\left(1-e^{2ikL_3}\right)}\left(1-T_a\right)-T_b}{T_a\left(Z_{fi}+\frac{\left(1+e^{2ikL_3}\right)}{\frac{S_3}{\left(\bar{\rho}c\right)_3}\left(1-e^{2ikL_3}\right)}\right)}. \tag{D.8}$$

Finally, substituting Eqs. (D.8) and (D.7) into Eq. (D.1) and rearranging yields

$$Z_1 = \frac{Z_{fi}\left[\frac{\left(1+e^{2ikL_3}\right)}{\frac{S_3}{\left(\bar{\rho}c\right)_3}\left(1-e^{2ikL_3}\right)}\right]}{Z_{fi}+\left(\frac{\left(1+e^{2ikL_3}\right)}{\frac{S_3}{\left(\bar{\rho}c\right)_3}\left(1-e^{2ikL_3}\right)}\right)}\left[\frac{\left(1-T_a\right)}{T_a}+1\right]-\frac{T_b}{T_a}. \tag{D.9}$$

In Eq. (D.9), the appropriate expressions for T_a and T_b are

$$\begin{aligned} T_a &= T_{a,1}T_{a,2}+T_{c,2}\left(T_{b,1}-ZT_{a,1}\right) \\ T_b &= T_{d,2}\left(T_{b,1}-ZT_{a,1}\right)+T_{a,1}T_{b,2} \end{aligned} \tag{D.10}$$

where $Z_{\delta A}$ is the impedance of the area change from duct section 2 to 1, i.e., from the fuel-air inlet duct to the combustor.

Appendix E:

Supplemental Area Contraction Impedance Results

This appendix reports the results of impedance measurements for several additional area contractions that were not included in the main thesis for brevity.

E.1 Area contraction from 50.8 mm to 25.4 mm diameter extension tube

In this section, an area contraction ratio of 4 was considered. In this case, an extension tube 270 mm long and 25.4mm in diameter was attached to the 50.8 mm diameter impedance tube. The acoustic pressure amplitude was varied from 100 dB to 150 dB, resulting in acoustic velocities in the impedance tube at the area change of 0.06 m/s to nearly 5.5 m/s. The acoustic velocity in the smaller tube at the location of the area change was varied from 0.24 m/s nearly 22 m/s.

Figure E.1 shows that the frequency response for this case closely resembled that of the 270 mm long, 14 mm diameter extension tube. The |R| for the 25.4 mm diameter tube dropped to 0.57 at 160 Hz and to 0.8 at 310 Hz. For the 14 mm diameter extension tube, it dropped to 0.46 at 160 Hz and to 0.29 at 310 Hz. As before, when the acoustic velocity was high, the |R| deviated significantly from one and the power dissipation was high. When the acoustic velocity was zero, the |R| was one and the power dissipation was zero, as it should be. Though not shown, the same trends (though at different frequencies) were observed when the 10.5 inch long extension tube was replaced with a 20 inch long extension tube.

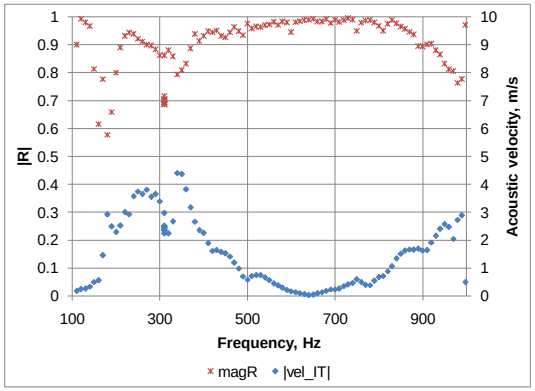

Figure E.1: Frequency response of the area change at the junction of the 50.8 mm to 25.4 mm diameter tubes with a 270 mm long extension tube attached.

The peak acoustic velocity at 310 Hz was higher for this case than for the 14 mm diameter extension tube, although the driving voltage to the speakers was the same for both cases. The reason for this was that the losses were lower for the 25.4 mm diameter tube even though the acoustic velocity was larger by nearly a factor of two. This was because the losses depended directly on the acoustic velocity but inversely with the square of the area ratio. Therefore, the theory presented in Chapter 3 indicates that in order for the losses to be the same between for both the 14 mm and 25.4 mm diameter tubes, the acoustic velocity for the 25.4 mm case must be a factor of 8 larger. Clearly, this was not the case. Therefore, the reflection coefficient showed this reduction in acoustic power dissipation by shifting toward unity.

Figure E.2 shows the normalized real and imaginary parts of the area change impedance for the 270 mm long, 25.4 mm diameter extension tube. (The squared area ratio for this case was 16.) At low Reynolds' numbers, the real part of the impedance increased very rapidly, but at moderate Reynolds' numbers, the real part of the normalized impedance was nearly linear up to a Reynolds' number of about 18,000.

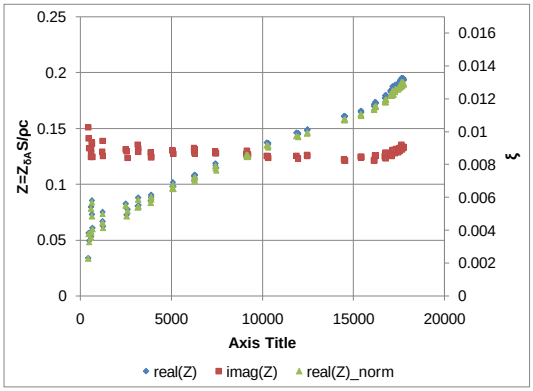

Figure E.2: Normalized real part and imaginary part of the impedance of the area change at the 50.8 mm to 25.4 mm diameter tube junction.

Other tests at even higher forcing amplitudes showed similar results. For example, Figure E.3 shows results for Reynolds' numbers up to 40,000. Even at these much higher Reynolds' numbers, the variation in the real part of the impedance was linear. However, results from the 14 mm diameter extension tube indicate that any change in slope would only occur for Reynolds' numbers greater than 60,000.

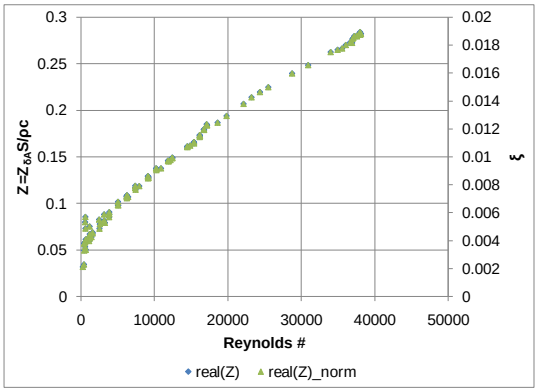

Figure E.3: Real part of the impedance of the area change at the 50.8 mm to 25.4 mm diameter tube junction.

Figure E.4 shows a plot of the loss coefficient, discharge coefficient, and effective length for this case. The loss coefficient was nearly constant at 29 for Reynolds' numbers greater than 2,500 while the discharge coefficient was seen to be smoothly varying from about 0.025 to nearly 0.125 over the entire range.

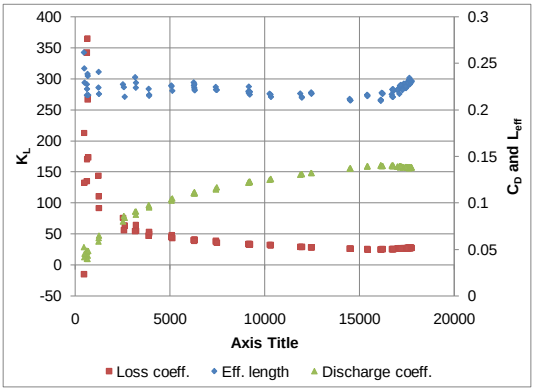

Figure E.4: Loss coefficient, effective length, and discharge coefficient for the area change at the 50.8 mm to 25.4 mm diameter tube junction with a 270 mm long extension tube.

The effective length was about 5.7 mm compared to a theoretical value of 7.7 mm. The effective length calculation is very sensitive to measurement of the length of the extension tube, and, although the effective length obtained from measurements differed somewhat from the theoretical value, some of this difference may be attributed to errors in measuring the length of the extension tube.

E.2 Area contraction from 50.8 mm to 19 mm diameter extension tube

Figure E.5 shows similar results for the reduction from the 50.8 mm impedance tube to the 19 mm diameter 270 mm long extension tube. (The squared area ratio for this case was 51.) The acoustic pressure amplitude was varied from 106 dB to 152 dB resulting in acoustic velocities in the impedance tube at the area change of 0.08 m/s to nearly 5.4 m/s. The acoustic velocity in the smaller tube at the location of the area change was varied from 5.7 m/s to nearly 38 m/s.

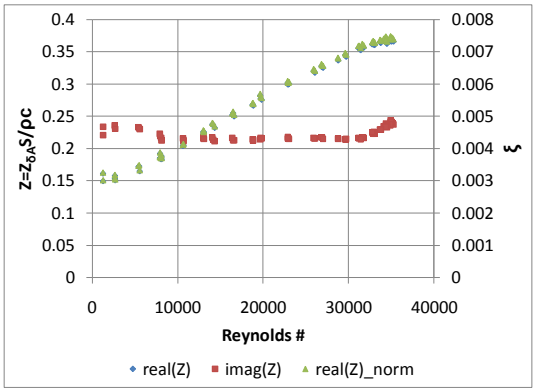

Figure E.5: Normalized real part and imaginary part of the impedance of the area change at the 50.8 mm to 19 mm diameter tube junction.

As before, the slope of the real part of the impedance was nearly constant up to a Reynolds' number of about 35,000. Figure E.6 shows a similar plot for an extended acoustic velocity range. In this case, the Reynolds' number ranges to nearly 80,000. This plot shows that the real part of the impedance was linear up to a Reynolds' number of about 50,000 at which point there was a distinct change of slope. Both plots show that the linear real part of the impedance Z was 0.15, which was close to the result for the 14 mm diameter extension tube and higher than the result for the 25.4 mm diameter extension tube.

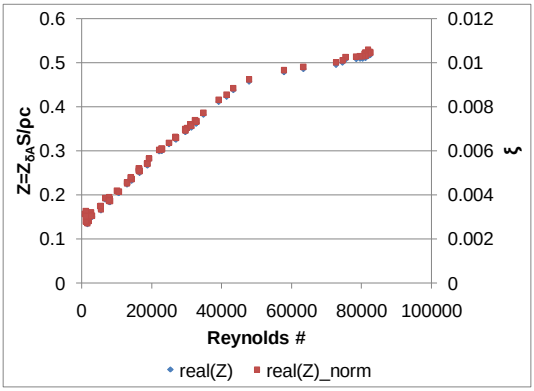

Figure E.6: Normalized real part and imaginary part of the impedance of the area change at the 50.8 mm to 19 mm diameter tube junction.

Figure E.7 shows a plot of the loss coefficient, the discharge coefficient, and the effective length for the 19 mm tube. The loss coefficient for Reynolds' numbers below 50,000 was nearly constant at a value of about 25.2 before decreasing slowly at higher Reynolds' numbers. The measured value of the loss coefficient at low Reynolds' numbers was quite close to the value obtained for the 25.4 mm diameter tube. The average effective length was about 5.41 mm (0.213 inches), which was very close to the theoretical value of 5.81 mm (0.228 inches). The discharge coefficient shows a smooth variation with Reynolds' number very similar to the 25.4 mm diameter tube case.

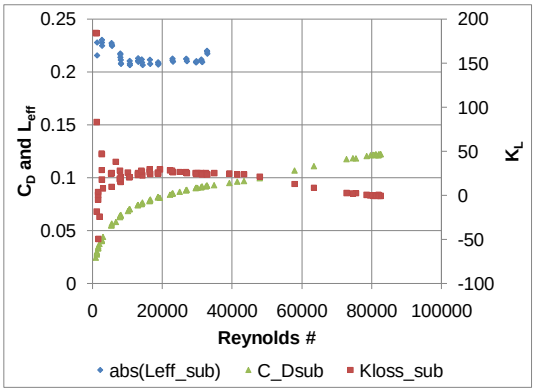

Figure E.7: Loss coefficient, discharge coefficient, and effective length of the area change at the 50.8 mm to 19 mm diameter tube junction.

E.3 Area contraction from 50.8 mm to 9.5 mm diameter extension tube

Figure E.8 shows the results for the area change at the junction of the 50.8 mm and 9.5 mm diameter tubes. (The area ratio squared for this case was 809.) Here again, the real part of the impedance exhibited a clear increase with Reynolds' number with a change in slope occurring at a Reynolds' number of about 75,000. Below this Reynolds' number, the slope of the real part was essentially constant. Above this Reynolds' number, the slope was considerably smaller. The imaginary part of the impedance exhibited far more variation than for the smaller area ratio cases, decreasing significantly at low and high Reynolds' numbers.

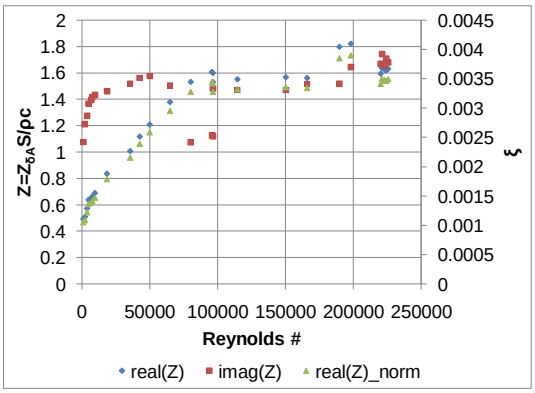

Figure E.8: Normalized real part and imaginary part of the impedance of the area change at the 50.8 mm to 9.5 mm diameter tube junction.

E.4 Area contraction from 50.8 mm to 6.35 mm diameter extension tube

Finally, Figure E.9 shows the results for the area change at the junction of the 50.8 mm and 6.35 mm diameter tubes. The area ratio squared for this case was 4096. In this case, the linear portion at low Reynolds' numbers appears to be present up to a Reynolds' number of 25,000. However, the data was somewhat noisy in this region and considerable variability was observed. The imaginary part varied quite a bit with Reynolds' number.

Although not observed for the range of Reynolds' numbers tested, it was certainly possible that the larger tubes exhibit the same saturation in the real part of the impedance similar to the behavior to the smaller tubes at very high Reynolds' numbers. However, it was very difficult to obtain extremely high Reynolds' numbers in the larger tubes due to the large diameter of the tube and the difficulty in obtaining very high sound pressure levels with these tubes attached.

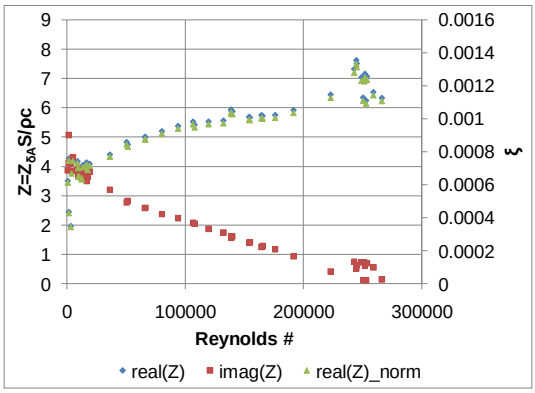

Figure E.9: Normalized real part and imaginary part of the impedance of the area change at the 2 inch to 1/4 inch diameter tube junction.

Appendix F: Key to FST Settings

Settings are given in percent of full open.

FST Setting Number	Top Gate Valve	Side Gate Valve	Ball Valve	Volume
1	100	100	0	0
2	71	71	0	0
3	43	43	0	0
4	0	0	0	0
5	100	100	0	0
6	71	71	0	0
7	43	43	0	0
8	0	0	0	0
9	100	100	0	0
10	71	71	0	0
11	43	43	0	0
12	0	0	0	0
13	100	100	0	0
14	71	71	0	0
15	43	43	0	0
16	0	0	0	0
17	100	100	100	0
18	71	71	100	0
19	43	43	100	0
20	0	0	100	0
21	100	100	100	0
22	71	71	100	0
23	43	43	100	0
24	0	0	100	0
25	100	100	100	0
26	71	71	100	0
27	43	43	100	0
28	0	0	100	0
29	100	100	100	0
30	71	71	100	0
31	43	43	100	0
32	0	0	100	0

FST Setting Number	Top Gate Valve	Side Gate Valve	Ball Valve	Volume
33	100	100	0	50
34	71	71	0	50
35	43	43	0	50
36	0	0	0	50
37	100	100	0	50
38	71	71	0	50
39	43	43	0	50
40	0	0	0	50
41	100	100	0	50
42	71	71	0	50
43	43	43	0	50
44	0	0	0	50
45	100	100	0	50
46	71	71	0	50
47	43	43	0	50
48	0	0	0	50
49	100	100	100	50
50	71	71	100	50
51	43	43	100	50
52	0	0	100	50
53	100	100	100	50
54	71	71	100	50
55	43	43	100	50
56	0	0	100	50
57	100	100	100	50
58	71	71	100	50
59	43	43	100	50
60	0	0	100	50
61	100	100	100	50
62	71	71	100	50
63	43	43	100	50
64	0	0	100	50

FST Setting Number	Top Gate Valve	Side Gate Valve	Ball Valve	Volume
65	100	100	0	100
66	71	71	0	100
67	43	43	0	100
68	0	0	0	100
69	100	100	0	100
70	71	71	0	100
71	43	43	0	100
72	0	0	0	100
73	100	100	0	100
74	71	71	0	100
75	43	43	0	100
76	0	0	0	100
77	100	100	0	100
78	71	71	0	100
79	43	43	0	100
80	0	0	0	100
81	100	100	100	100
82	71	71	100	100
83	43	43	100	100
84	0	0	100	100
85	100	100	100	100
86	71	71	100	100
87	43	43	100	100
88	0	0	100	100
89	100	100	100	100
90	71	71	100	100
91	43	43	100	100
92	0	0	100	100
93	100	100	100	100
94	71	71	100	100
95	43	43	100	100
96	0	0	100	100

Appendix G:

Model/Experiment Comparisons for Configurations 2 through 5

G.1 Configuration 2

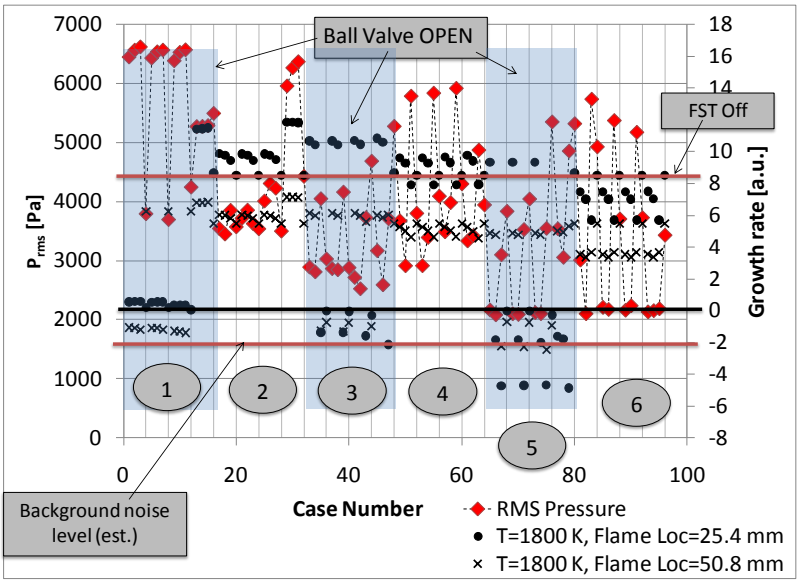

Figure G.1: Model/Experiment comparison vs. FST setting for Configuration 2 at a fuel flowrate of 0.9 kg/hr.

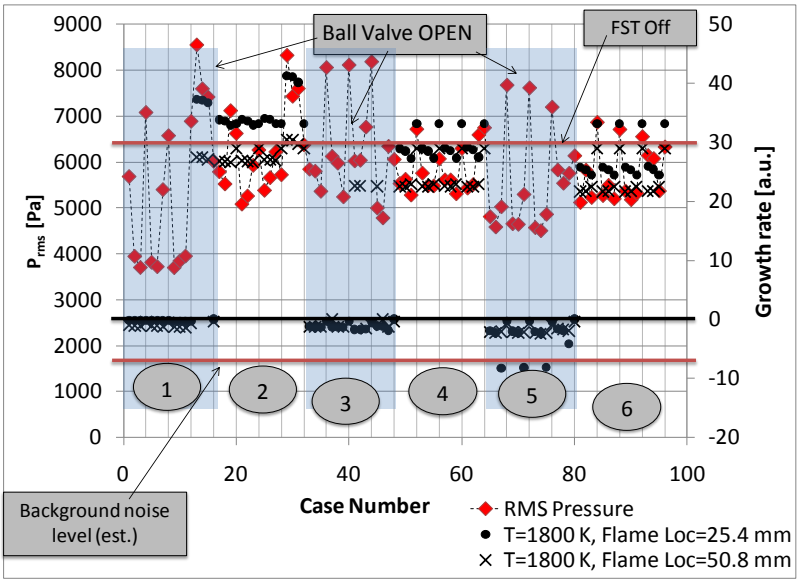

Figure G.2: Model/Experiment comparison vs. FST setting for Configuration 2 at a fuel flowrate of 1.9 kg/hr.

G.2 Configuration 3

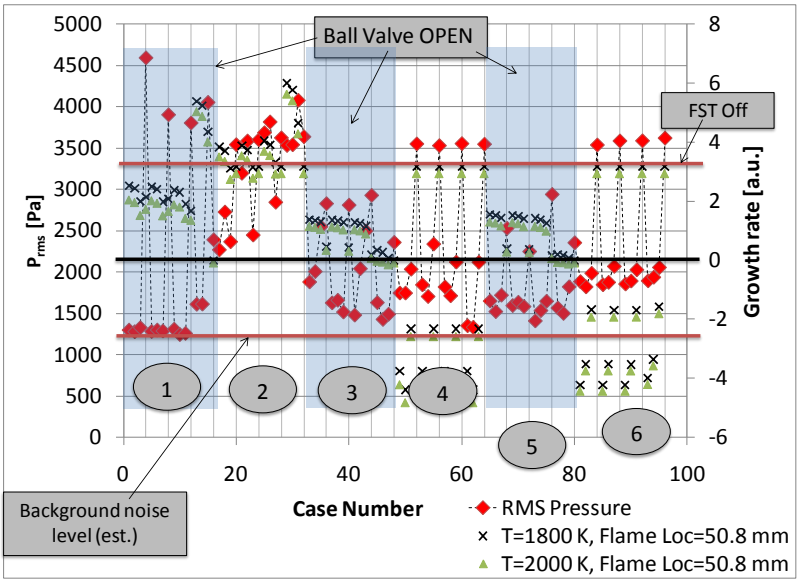

Figure G.3: Model/Experiment comparison vs. FST setting for Configuration 3 at a fuel flowrate of 0.9 kg/hr.

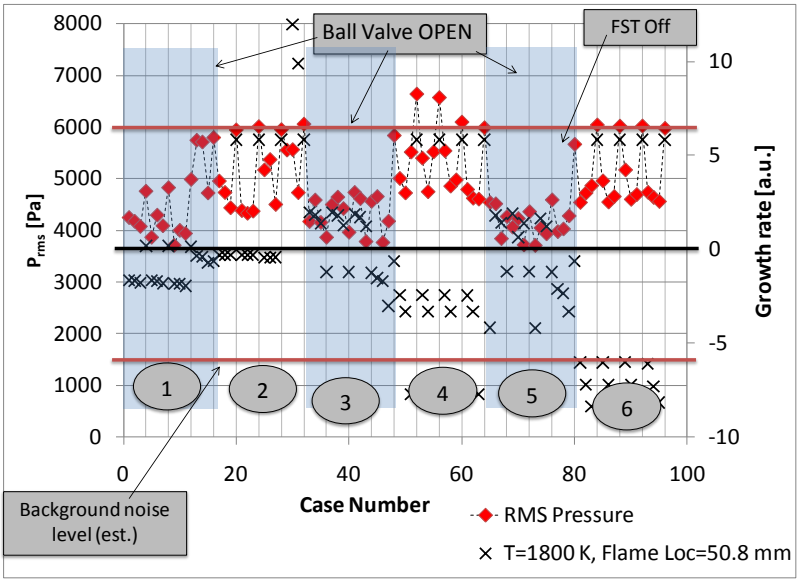

Figure G.4: Model/Experiment comparison vs. FST setting for Configuration 3 at a fuel flowrate of 1.9 kg/hr.

G.3 Configuration 4

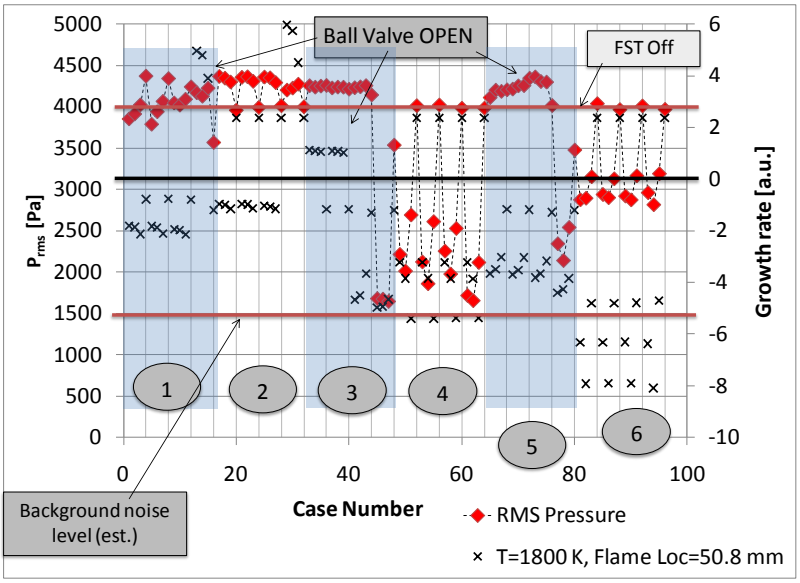

Figure G.5: Model/Experiment comparison vs. FST setting for Configuration 4 at a fuel flowrate of 0.9 kg/hr.

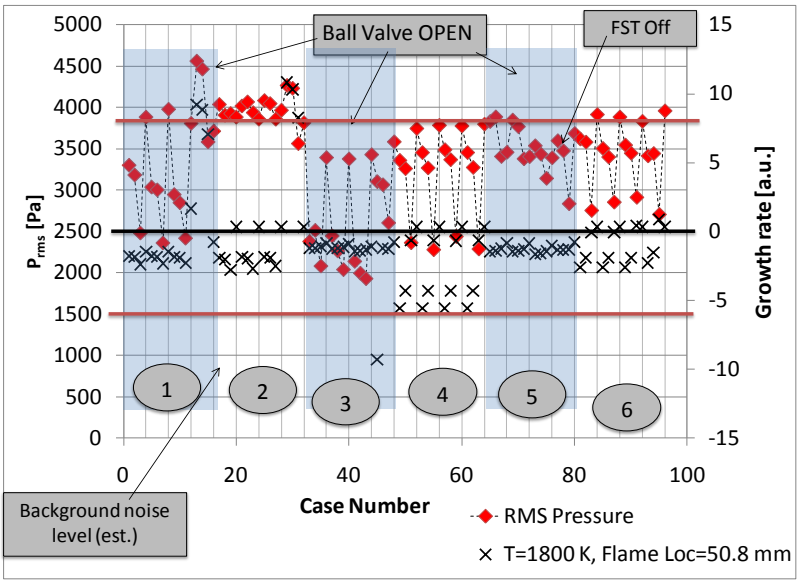

Figure G.6: Model/Experiment comparison vs. FST setting for Configuration 4 at a fuel flowrate of 1.9 kg/hr.

G.4 Configuration 5

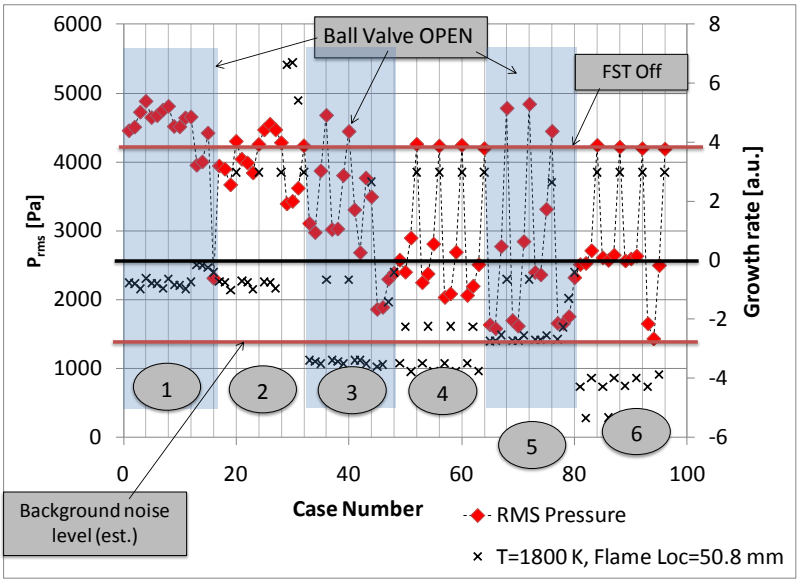

Figure G.7: Model/Experiment comparison vs. FST setting for Configuration 5 at a fuel flowrate of 0.9 kg/hr.

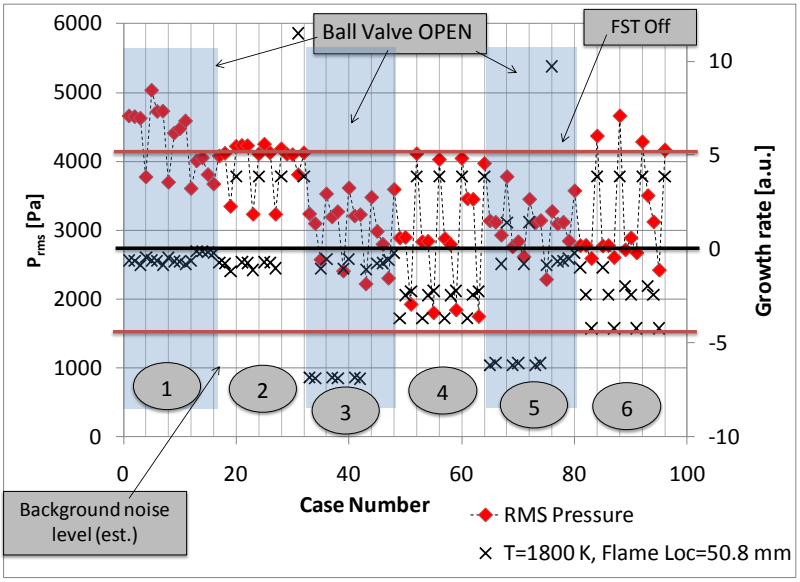

Figure G.8: Model/Experiment comparison vs. FST setting for Configuration 5 at a fuel flowrate of 1.9 kg/hr.

Appendix H:

Plots of Fuel System Impedance and Experimental Data for all FST Settings for Configurations 2 through 5

H.1 Configuration 2

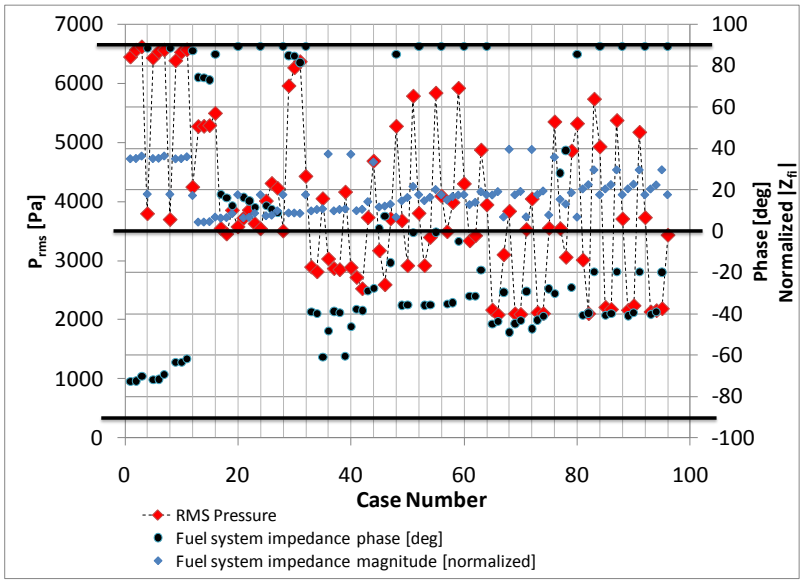

Figure H.1: Model/Experiment comparison vs. FST setting for Configuration 2 at a fuel flowrate of 0.9 kg/hr.

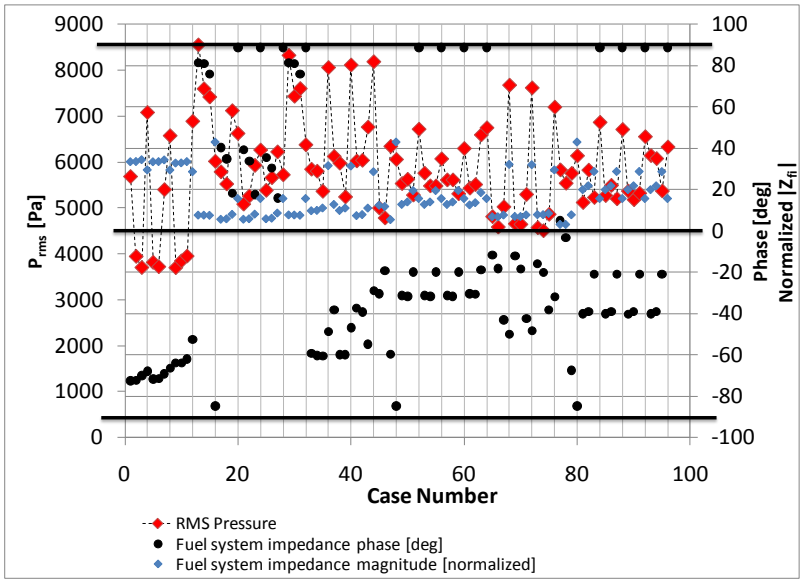

Figure H.2: Model/Experiment comparison vs. FST setting for Configuration 2 at a fuel flowrate of 1.9 kg/hr.

H.2 Configuration 3

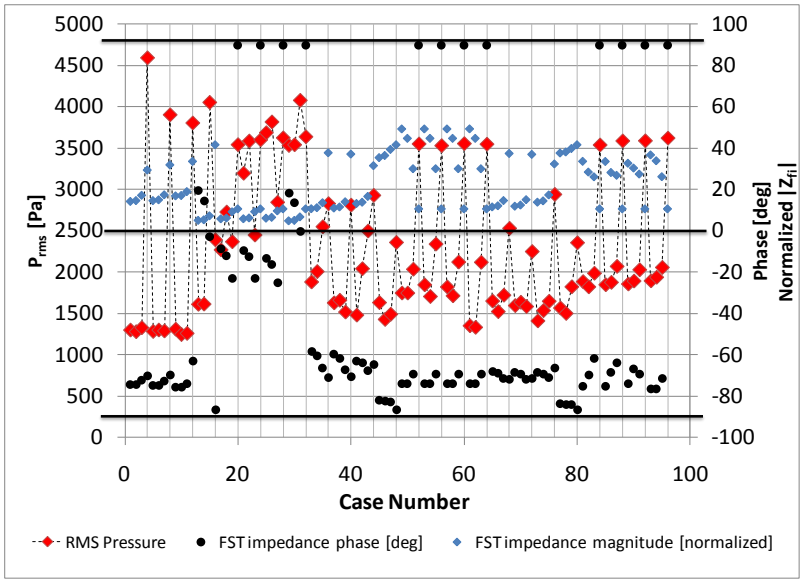

Figure H.3: Model/Experiment comparison vs. FST setting for Configuration 3 at a fuel flowrate of 0.9 kg/hr.

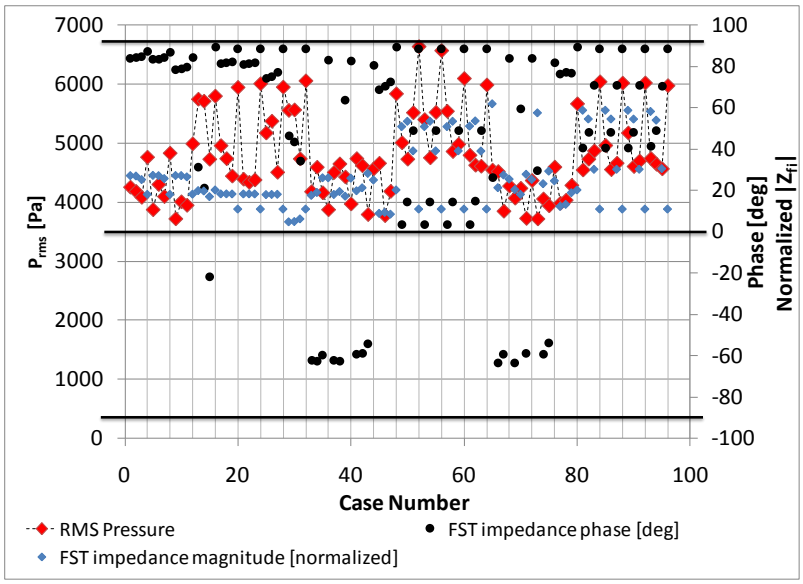

Figure H.4: Model/Experiment comparison vs. FST setting for Configuration 3 at a fuel flowrate of 1.9 kg/hr.

H.3 Configuration 4

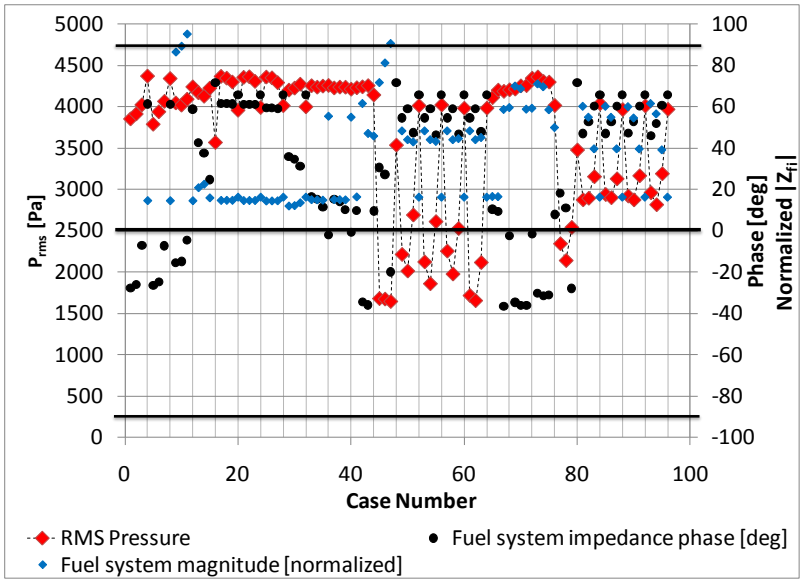

Figure H.5: Model/Experiment comparison vs. FST setting for Configuration 4 at a fuel flowrate of 0.9 kg/hr.

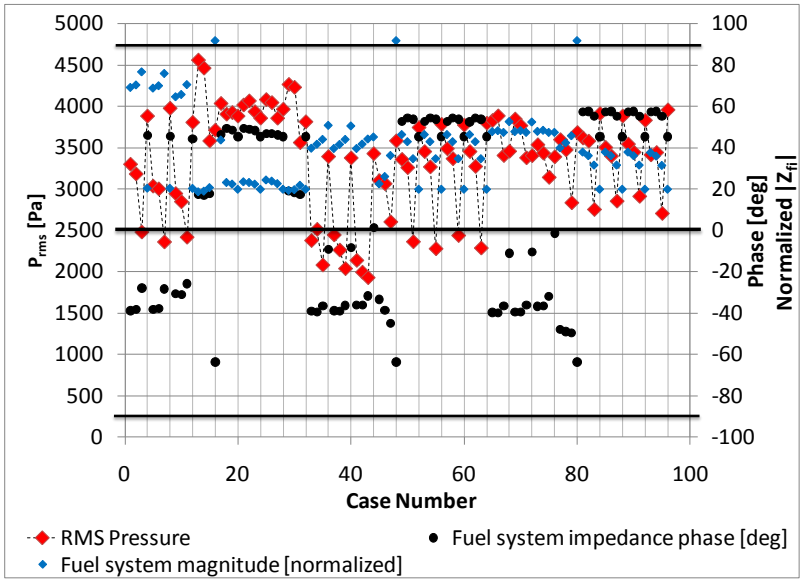

Figure H.6: Model/Experiment comparison vs. FST setting for Configuration 4 at a fuel flowrate of 1.9 kg/hr.

H.4 Configuration 5

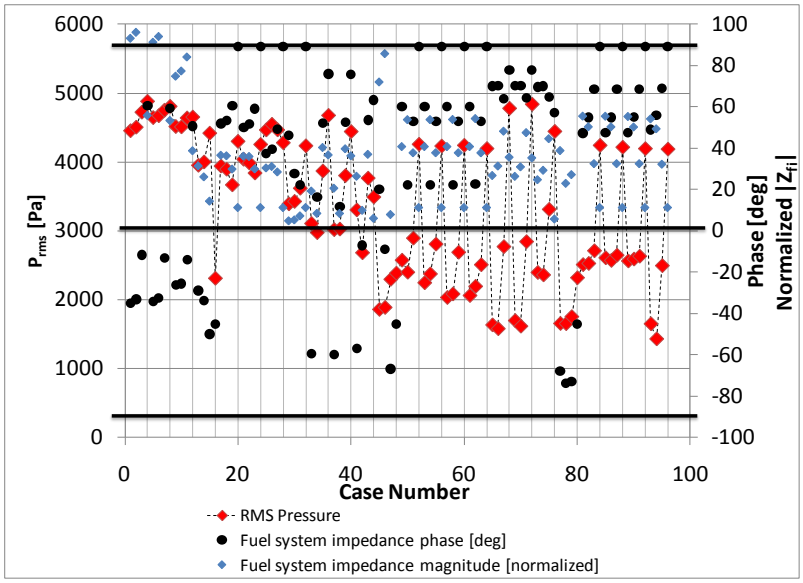

Figure H.7: Model/Experiment comparison vs. FST setting for Configuration 5 at a fuel flowrate of 0.9 kg/hr.

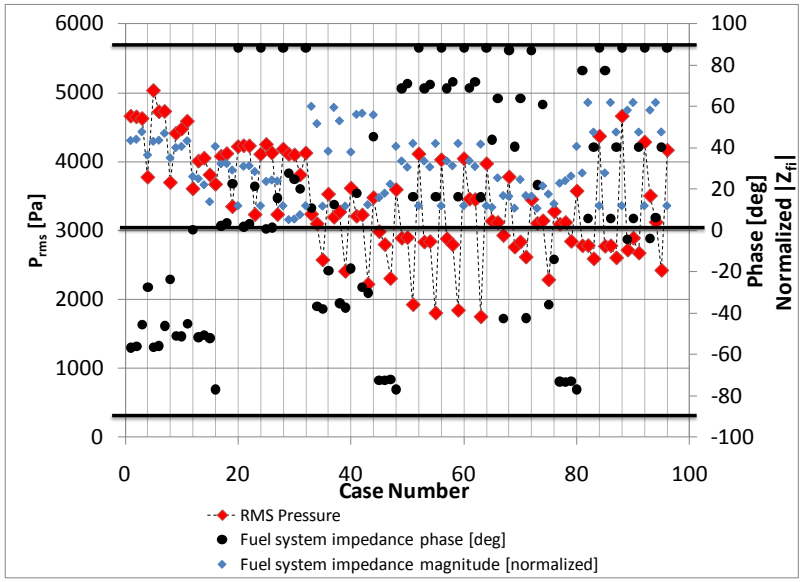

Figure H.8: Model/Experiment comparison vs. FST setting for Configuration 5 at a fuel flowrate of 1.9 kg/hr.

References

[1] J. W. S. Rayleigh, *Theory of Sound, vol. II*, 1896, replublished 1945 by Dover Publications Inc., Toronto, Ontario, p. 226.

[2] K. McManus, T. Poinsot, S. Candel, “A Review of Active Control of Combustion Instabilities”, Progress in Energy and Combustion Science, Vol. 19, 1993, pp. 1-29.

[3] R. Steel, L. Cowell, S. Cannon, C. Smith, “Passive Control of Combustion Instability in Lean Premixed Combustors”, Journal of Engineering for Gas Turbines and Power, 2000, Vol. 122, pp. 412-419.

[4] A. Dean, “Combustor Tuning”, U. S. Patent, 2001, U. S. Patent No.: 6,272,842.

[5] T. Scarinci, C. Freeman, I. Day, “Passive Control of Combustion Instability in a Low Emissions Aeroderivative Gas Turbine”, ASME Turbo Expo 2004, June 2004, Vol. 1, pp. 487-499.

[6] W. Polifke, J. Kopitz, A. Serbanovic, “Impact of the Fuel Time Lag Distribution in Elliptical Premix Nozzles on Combustion Instability”, AIAA Aeroacoustics Conference, 2001, AIAA 2001-2104.

[7] W. Krebs, S. Bethke, J. Lepers, P. Flohr, B. Prade, C. Johnson, and S. Sattinger, “Thermoacoustic Design Tools and Passive Control: Siemens Power Generation Approaches”, Progress in Astronautics and Aeronautics, Vol. 210, pp. 89-112.

[8] N. Joshi, M. Epstein, S. Durlak, S. Marakovits, P. Sabla, “Development of a Fuel-Air Premixer for Aero-derivative Dry Low Emissions Combustors”, ASME, 94-GT-253, 1994.

[9] T. Scarinci, J. L. Halpin, “Industrial Trent Combustor – Combustion Noise Characteristics”, ASME, paper 99-GT-9, 1999.

[10] D. James, “A Solution for Noise Associated with a Series Staged DLE Combustion System”, *Proceedings of the 4th International Pipeline Conference*, 29 Sept to 3 Oct. 2002.

[11] W. Mick, M. Cohen, “Method for staging fuel in a turbine in the premixed operating mode” , U. S. Patent, 1996, U. S. Patent No.: 5,551,228.

[12] R. Tuthill;W. Bechtel II; J Arthur, S. Black, R. Bland, G. DeLeonardo, S. Meyer, J. Taura, J. Battaglioli, ”Swozzle based burner tube premixer including inlet air conditioner for low emissions combustion”, U. S. Patent, 2002, U. S. Patent No.: 6,438,961.

[13] L. Davis Jr., D. Fitts, W. Mick, M. Sciocchetti, M. Cohen, “Method for Staging Fuel in a Turbine between Diffusion and Premixed Operations”, U. S. Patent, 1996, U. S. Patent No.: 5,491,970.

[14] E. Gutmark, K. Schadow, “Suppression of Combustion Instability by Geometrical Design of the Bluff-body Stabilizer”, Journal of Propulsion and Power, Vol. 11 No. 3, 1995, pp. 456-463.

[15] C. Brossard, S. Lee, C. Mordaunt, J. Broda, R. Santoro, “Effect of Swirl Injector Design and Other Important Parameters on Gas Turbine Combustor Instabilities”, AIAA 2000-3122.

[16] M. Linck, M. Armani, A. Gupta, “Passive Control of Unstable Combustion in a Swirl-Stabilized Spray Combustor”, 42nd AIAA Aerospace Sciences Meeting and Exhibit, Reno, NV, 2004.

[17] C. Paschereit, E. Gutmark, “Control of Combustion Instability and Emissions by Burner’s Exit Geometry Modifications”, AIAA 2004-0636.

[18] G. Sims, R. Copplestone, J. Tilston, “Performance Studies of Passive Damping Techniques used to Suppress Combustion Oscillations in LPP Combustors”, Proceedings of the ASME Turbo Expo, 2003 June 16-19, Atlanta, GA, GT2003-38194.

[19] V. Bellucci, P. Flohr, C. Paschereit, F. Magni, “On the Use of Helmholtz Resonators for Damping Acoustic Pulsations in Industrial Gas Turbines”, Journal of Engineering for Gas Turbines and Power, 2004, pp. 271-275.

[20] G. Sims, R. Copplestone, J. Tilston, “Performance Studies of Passive Damping Techniques used to Suppress Combustion Oscillations in LPP Combustors”, Proceedings of the ASME Turbo Expo, 2003 June 16-19, Atlanta, GA, GT2003-38194.

[21] F. Culick, V. Yang, “Overview of Combustion Instabilities in Liquid-Propellant Rocket Engines”, Progress in Astronautics and Aeronautics, Vol. 169, p. 8.

[22] D. Hobson, J. Fackrell, G. Hewitt, “Combustion Instabilities in Industrial Gas Turbines – Measurements on Operating Plant and Thermoacoustic Modeling”, Journal of Engineering for Gas Turbines and Power, Vol. 122, 2000, pp. 420-428.

[23] T. Lieuwen, B. Zinn, “The Role of Equivalence Ratio Oscillations in Driving Combustion Instabilities in Low NO_x Gas Turbines”, 27th Combustion Symposium, 1998, pp. 1809-1816.

[24] G. Richards, D. Straub, “Control of Combustion Dynamics Using Fuel supply system Impedance”, Proceedings of the ASME Turbo Expo 2003, 16-19 June 2003, Atlanta GA.

[25] G. Richards, R. Gemmen, ”Combustor Oscillation Attenuation via the Control of Fuel-supply Line Dynamics“, U. S. Patent, 1998, U. S. Patent No.: 5,809,769.

[26] G. Richards, E. Robey, “Effect of Fuel supply system Impedance Mismatch on Combustion Dynamics”, ASME Turbo Expo 2005, June 2005, GT 2005-68386.

[27] S. Black, “Apparatus for Reducing Fuel/Air Concentration Oscillations in Gas Turbine Combustors”, U. S. Patent, 1993, U. S. Patent No.: 5,211,004.

[28] K. McManus, S. Sanderson, J. Goldmeer, “Acoustic Impedance-Matched Fuel Nozzle Device and Tunable Fuel Injection Resonator Assembly”, U. S. Patent, 2004, U. S. Patent No.: 6,820,431.

[29] A. H. Lefebvre, *Gas Turbine Combustion*, Taylor and Francis, New York, 1999,p. 265

[30] J. Goldmeer, S. Sanderson, G. Myers, J. Stewart, “Passive Control of Dynamic Pressures in a Dry, Low NO_x Combustion System Using Fuel Gas Circuit Impedance Optimization”, Proceedings of the ASME Turbo Expo 2005, 2005-GT-68605.

[31] G. Swift, *Thermoacoustic: A Unifying Perspective for Some Engines and Refrigerators, Fifth Draft*, Los Alamos National Laboratory, 29 May 2001.

[32] A. Dowling, S. Stow, “Acoustic Analysis of Gas Turbine Combustors”, Journal of Propulsion and Power, Vol. 19, No. 5, 2003, pp. 751-764.

[33] P. Morse, U. Ingard, *Theoretical Acoustics*, Princeton University Press, Princeton, New Jersey , 1968, p. 758-759.

[34]P. A. Davidson, *Turbulence: An Introduction for Scientists and Engineers*, Oxford University Press, 2004, New York

[35] L. J. Sivian, Acoustic Impedance of Small Orifices, J. Acoustical Society of America, Vol. 7, 1935, pg. 94-101.

[36] U. Ingard, S. Labate, Acoustic Circulation Effects and the Nonlinear Impedance of Orifices, J. Acoustical Society of America, Vol. 22 No. 2, 1950, pg. 211-218.

[37] Ingard U., “On the theory and design of acoustical resonators”, Journal of the Acoustical Society of America, Vol. 25, 1953, pp. 1037-1061.

[38] U. Ingard, H. Ising, “Acoustic Nonlinearity of an Orifice”, J. Acoustical Society of America, Vol. 42 No. 1, 1967, pg. 8-17.

[39] B. T. Zinn, “A Theoretical Study of Nonlinear Damping by Helmholtz Resonators”, J. Sound and Vibration, Vol. 13 No. 3, 1970.

[40] J. P. Johnston, W. E. Schmidt, “Measurement of Acoustic Reflection from an Obstruction in a Pipe with Flow”, J. Acoustical Society of America, Vol. 63 No. 5, 1978, pp. 1455-1460.

[41] T. H. Melling, “The Acoustic Impedance of Perforates at Medium and High Sound Pressure Levels”, J. Sound and Vibration, Vol. 29, 1–65, 1973.

[42] A. Cummings, W. Eversman, “High Amplitude Acoustic Transmission Through Duct Terminations: Theory”, J. of Sound and Vibration, Vol. 94, No. 4, 1983, pp. 503-518.

[43] P. Morse, U. Ingard, *Theoretical Acoustics*, Princeton University Press, Princeton, New Jersey , 1968, p. 248.

[44] J. W. S. Rayleigh, *Theory of Sound, Vol. 2*, Re-printed by Dover Publications, New York, 1945, p. 172.

[45] Munson, Young, Okiishi, *Fundamentals of Fluid Mechanics*, John Wiley & Sons Inc., New York, 1990, p. 147.

[46] P. Morse, U. Ingard, *Theoretical Acoustics*, Princeton University Press, Princeton, New Jersey, 1968, p. 760.

[47] Munson, Young, Okiishi*, Fundamentals of Fluid Mechanics*, John Wiley & Sons Inc., New York, 1990, p. 505.

[48] U. Ingard, ‘On the Theory and Design of Acoustic Resonators”, The Journal of the Acoustical Society of America, Vol. 25, No. 6, 1953, pp. 1037-1061.

[49] U. Ingard, S. Labate, “Acoustic Circulation Effects and the Nonlinear Impedance of Orifices”, The Journal of the Acoustical Society of America, Vol. 22, No. 2, 1950, pp. 211-218.

[50] A. Cummings, “Acoustic Nonlinearities and Power Losses at Orifices”, AIAA Journal, Vol. 22, No. 6, 1983, pp.786-792.

[51] A. Cummings, W. Eversman, “High Amplitude Acoustic Transmission Through Duct Terminations”, Journal of Sound and Vibration, Vol. 91, No. 4, 1983, pp. 503-518.

[52] M. Salikuddin, “Acoustic Behavior of Orifice Plates and Perforated Plates with Reference to Low-Frequency Sound Absorption”, Journal of Sound and Vibration, Vol. 139, No. 3, 1990, pp. 361-381.

[53] M. Salikuddin, W. H. Brown, “Non-linear Effects in Finite Amplitude Wave Propagation Through Orifice Plate and Perforated Plate Terminations”, Journal of Sound and Vibration, Vol 139, No. 3, 1990, pp. 383-405.

[54] M. Salikuddin, K. K. Ahuja, “Acoustic Power Dissipation on Radiation Through Duct Terminations: Experiments”, Journal of Sound and Vibration, Vol. 91, No. 4, 1983, pp. 479-502.

[55] Munjal, Acoustics of Ducts and Mufflers With Application to Exhaust and Ventilation System Design, Wiley Interscience (1987).

[56] J. Y. Chung, D. A. Blaser, “Transfer Function Method of Measuring In-duct Acoustic Properties. I. Theory”, J. Acoustical Society of America, Vol. 68 No. 3 (1980).

[57] D. T. Blackstock, *Fundamentals of Physical Acoustics*, Wiley Interscience, Danvers MA, 2000, p. 133.

[58] J. P. Moeck, M. R. Bothien, and C. O. Paschereit, “An Active Control Scheme for Tuning Acoustic Impedances”, 13th AIAA/CEAS Aeroacoustics Conference, 28th AIAA Aeroacoustics Conference, 2007.

[59] X. Sun, X. Jing, H. Zhang, and Y. Shi, “Effect of Grazing-Bias Flow Interaction on Acoustic Impedance of Perforated Plates.”, Journal of Sound and Vibration, Vol. 254 No. 3, 2002, pp. 557-573.